Capillary oscillations and stability of a charged, viscous drop in a viscous dielectric medium

A. I. Grigor'ev, S. O. Shiryaeva, and V. A. Koromyslov

Yaroslavl State University, 150000 Yaroslavl, Russia
(Submitted March 28, 1997)
Zh. Tekh. Fiz. **68**, 1–8 (September 1998)

The scalarization method is used to obtain a dispersion relation for capillary oscillations of a charged, conducting drop in a viscous, dielectric medium. It is found that the instability growth rate of the charged interface depends substantially on the viscosity and density of the surrounding medium, dropping rapidly as they are increased. In the subcritical regime the influence of the viscosity and density of both media leads to a nonmonotonic dependence of the damping rate of the capillary motions of the liquid on the viscosity or density of the external medium for a fixed value of the viscosity or density of the internal medium. The falloff of the frequencies of the capillary motions with growth of the viscosity or density of the external medium is monotonic in this case.
[S1063-7842(98)00109-3]

INTRODUCTION

A study of the electrostatic instability of a charged drop of viscous liquid suspended in another viscous liquid is of significant interest in connection with numerous applications in which such an object figures: in technological applications involving the uniform mixing of immiscible liquids, in practical applications involving the combustion of liquid fuels in regard to the mixing of the fuel and oxidizer, and in geophysical experiments (see, e.g., Refs. 1–4 and the literature cited therein). Nevertheless, many questions associated with this problem have so far been only scantily investigated because of the complicated technique of the experiments and the difficulty of the theoretical calculations. This also pertains to the effect of the viscosity and density of the media on regularities of realizations of the instability of the charged surface of such drops.

1. We consider a system consisting of two immiscible incompressible liquids with densities $\rho^{(1)}$ and $\rho^{(2)}$ and kinetic viscosities $\nu^{(1)}$ and $\nu^{(2)}$. As a result of the action of the forces of surface tension, whose coefficient we denote as σ, the inner liquid, to which we assign the index (1), takes the form of a spherical drop with radius R. The outer liquid, identified by the index (2), is assumed to be unbounded. A charge Q is found on the interface of the two liquids. Further we assume that the liquid in the drop is a perfect conductor, and the liquid of the medium is a perfect insulator with dielectric constant ε. We will find the spectrum of normal vibrations of the interface of the two liquids.

In the spherical coordinate system r, θ, φ with origin at the center of the unperturbed drop the equation of the interface of the two liquids has the form $r=R+\xi(\theta,\varphi,t)$. The system of hydrodynamic equations, linearized about the equilibrium spherical state, consists of the Navier–Stokes equation

$$\frac{\partial \mathbf{u}^{(\alpha)}}{\partial t}=-\frac{1}{\rho^{(\alpha)}}\nabla p^{(\alpha)}+\nu^{(\alpha)}\Delta \mathbf{u}^{(\alpha)};\quad \alpha=1,2, \tag{1}$$

(where Δ is the Laplacian operator), the equation of continuity, reduced in the case of an incompressible liquid to the condition

$$\nabla\cdot\mathbf{u}^{(\alpha)}=0, \tag{2}$$

kinematic boundary conditions at the interface of the two liquids $r=R$ for the tangent components

$$u_\theta^{(1)}=u_\theta^{(2)}, \tag{3}$$

$$u_\varphi^{(1)}=u_\varphi^{(2)}, \tag{4}$$

and normal component

$$u_r^{(1)}=u_r^{(2)}=\frac{\partial \xi}{\partial t} \tag{5}$$

of the velocity field, dynamic boundary conditions for the tangent components

$$\rho^{(1)}\nu^{(1)}\left[\frac{1}{r}\frac{\partial u_r^{(1)}}{\partial\theta}+\frac{\partial u_\theta^{(1)}}{\partial r}-\frac{1}{r}u_\theta^{(1)}\right]=\rho^{(2)}\nu^{(2)}\left[\frac{1}{r}\frac{\partial u_r^{(2)}}{\partial\theta}+\frac{\partial u_\theta^{(2)}}{\partial r}-\frac{1}{r}u_\theta^{(2)}\right], \tag{6}$$

$$\rho^{(1)}\nu^{(1)}\left[\frac{1}{r\cdot\sin\theta}\frac{\partial u_r^{(1)}}{\partial\varphi}+\frac{\partial u_\varphi^{(1)}}{\partial r}-\frac{1}{r}u_\varphi^{(1)}\right]=\rho^{(2)}\nu^{(2)}\left[\frac{1}{r\cdot\sin\theta}\frac{\partial u_r^{(2)}}{\partial\varphi}+\frac{\partial u_\varphi^{(2)}}{\partial r}-\frac{1}{r}u_\varphi^{(2)}\right], \tag{7}$$

and normal component

$$-p^{(1)}+2\rho^{(1)}\nu^{(1)}\frac{\partial u_r^{(1)}}{\partial r}+p_\sigma-p_E$$

$$=-p^{(2)}+2\rho^{(2)}\nu^{(2)}\frac{\partial u_r^{(2)}}{\partial r} \tag{8}$$

of the stress fields, the condition of constant volume of the two liquids

$$\int_\Omega \xi(\theta,\varphi,t)d\Omega=0 \tag{9}$$

and the condition of immobility of the center of mass of the system relative to the chosen system of coordinates

$$\int_\Omega \xi(\theta,\varphi,t)\mathbf{e}_r d\Omega=0. \tag{10}$$

Here ξ, $\mathbf{u}$, and p denote the perturbations of the shape of the interface, the velocity field, and pressure field, respectively; p_σ is the perturbation of the pressure of the surface tension forces

$$p_\sigma(\xi)=-\frac{\sigma}{R^2}(2+\Delta_\Omega)\xi, \tag{11}$$

p_E is the perturbation of the pressure of the electric field associated with capillary deformation of the interface (see Appendix A)

$$p_E(\xi)=-\frac{Q^2}{2\pi\varepsilon}\xi + \frac{Q^2}{4\pi\varepsilon}\sum_{m=0}^{\infty}(m+1)P_n(\mu)\int_{-1}^{1}\xi P_n(\mu)d\mu, \tag{12}$$

Δ_Ω is the angular part of the Laplace operator in spherical coordinates, $P_n(\mu)$ are the eigenfunctions of the operator Δ_Ω, and $d\Omega$ is the solid angle element.

In order to simplify the solution of the problem, it is useful to transform from the MTL-dimensional basis, where M, L, and T represent units of mass, length, and time, respectively, to another, more suitable basis which decreases the number of parameters of the problem. It is convenient to choose the $\rho R\sigma$ basis. The formulas connecting these two bases have the form

$$[\rho]=ML^{-3},\quad [R]=L,\quad [\sigma]=MT^{-2},$$

$$[M]=\rho R^3,\quad [L]=R,\quad [T]=R^{3/2}\rho^{1/2}\sigma^{-1/2}.$$

We write the dimensions of quantities in the old and in the new basis

$$[r]=[\xi]=L=R,\quad [p]=ML^{-1}T^{-2}=R^{-1}\sigma,$$

$$[u]=LT^{-1}=R^{-1/2}\rho^{-1/2}\sigma^{1/2},$$

$$[\nu]=L^2T^{-1}=R^{1/2}\rho^{-1/2}\sigma^{1/2},$$

$$[t]=T=R^{3/2}\rho^{1/2}\sigma^{-1/2}.$$

To transform to the $\rho R\sigma$ basis, it is sufficient to set the radius of the drop R, the coefficient of surface tension σ, and one of the densities or a combination of them with the units of density equal to unity in all the equations of the system. We set $R=1$ and $\sigma=1$ at once, but we will choose the quantity with dimensions of density later from considerations of convenience. To transform back to the old basis, it is necessary to divide each quantity encountered in the equation by its corresponding dimensionality.

2. We now scalarize the problem using a procedure described in detail in Ref. 5. The velocity field $\mathbf{u}$, as an arbitrary vector field, can expanded into a sum of three orthogonal fields

$$\mathbf{u}(\mathbf{r},t)=\hat{\mathbf{N}}_1\Psi_1(\mathbf{r},t)+\hat{\mathbf{N}}_2\Psi_2(\mathbf{r},t)+\hat{\mathbf{N}}_3\Psi_3(\mathbf{r},t), \tag{13}$$

where Ψ_i (i=1,2,3) are scalar fields. By virtue of orthogonality of the fields $\hat{\mathbf{N}}_i\Psi_i$

$$\int_V(\hat{\mathbf{N}}_i\Psi_i)^*\cdot(\hat{\mathbf{N}}_j\Psi_j)dV=0 \quad (i\neq j),$$

where the symbol * denotes the complex conjugate, and the integral is taken over all space, the vector operators should satisfy the relations $\hat{\mathbf{N}}_i^+\cdot\hat{\mathbf{N}}_j=0$(for $i\neq h$), where $\hat{\mathbf{N}}_i^+$ is the Hermitian conjugate of the operator $\hat{\mathbf{N}}_j$. For the problem under consideration, it is convenient to choose these operators in the form

$$\hat{\mathbf{N}}_1=\nabla,\quad \hat{\mathbf{N}}_2=\nabla\times\mathbf{r},\quad \hat{\mathbf{N}}_3=\nabla\times(\nabla\times\mathbf{r}),$$

$$\hat{\mathbf{N}}_1^+=-\nabla,\quad \hat{\mathbf{N}}_2^+=\mathbf{r}\times\nabla,\quad \hat{\mathbf{N}}_3^+=(\mathbf{r}\times\nabla)\times\nabla.$$

Substituting expansion (13) into the condition of incompressibility (2), we obtain

$$\Delta\Psi_1^{(\alpha)}=0. \tag{14}$$

Substituting expansion (13) into the Navier–Stokes equation (1), allowing for commutativity of the operators $\hat{\mathbf{N}}_i$ and Δ, gives

$$\hat{\mathbf{N}}_1\left(\frac{\partial\Psi_1^{(\alpha)}}{\partial t}-\nu^{(\alpha)}\Delta\Psi_1^{(\alpha)}+\frac{1}{\rho^{(\alpha)}}p^{(\alpha)}\right)+\hat{\mathbf{N}}_2\left(\frac{\partial\Psi_2^{(\alpha)}}{\partial t}-\nu^{(\alpha)}\Delta\Psi_2^{(\alpha)}\right)+\hat{\mathbf{N}}_3\left(\frac{\partial\Psi_3^{(\alpha)}}{\partial t}-\nu^{(\alpha)}\Delta\Psi_3^{(\alpha)}\right)=0.$$

Acting on this equation successively with the operators $\hat{\mathbf{N}}_i^+$, we obtain three independent equations

$$\hat{\mathbf{N}}_i^+\cdot\hat{\mathbf{N}}_i\left(\frac{1}{\rho(\alpha)}p^{(\alpha)}\delta_{1i}+\frac{\partial\Psi_i^\alpha}{\partial t}-\nu^{(\alpha)}\Delta\Psi_i^{(\alpha)}\right)=0, \tag{15}$$

where δ_{ij} is the Kronecker delta.

Since the operators $\hat{\mathbf{N}}_i^+\cdot\hat{\mathbf{N}}_i$ and Δ commute, they possess a general system of eigenfunctions. Here the eigenvalues of these operators corresponding to one or another eigenfunction are, general speaking, different. Equation (15) implies that either the fields $p\delta_{1i}$ and Ψ_i should be expanded in the eigenfunctions corresponding to the zero eigenvalue of the operators $\mathbf{N}_i^+\cdot\mathbf{N}_i$ or the following equation is valid:

$$\frac{1}{\rho^{(\alpha)}}p^{(\alpha)}\delta_{1i}+\frac{\partial\Psi_i^{(\alpha)}}{\partial t}-\nu^{(\alpha)}\Delta\Psi_i^{(\alpha)}=0. \tag{16}$$

It is obvious that the first possibility would be to great a restriction; therefore we assume that Eq. (16) follows from Eq. (15). Taking condition (14) into account, we obtain the scalar analog of Eqs. (1) and (2), which consists of the following set of independent scalar equations of the fields $\Delta\Psi_i^{(\alpha)}$,

$$\Delta\Psi_i^{(\alpha)}-(1-\delta_{1i})\frac{1}{\nu^{(\alpha)}}\frac{\partial\Psi_i^{(\alpha)}}{\partial t}=0 \tag{17}$$

and an expression for the pressure field p

$$p^{(\alpha)}=-\rho^{(\alpha)}\frac{\partial\Psi_1^{(\alpha)}}{\partial t}. \tag{18}$$

We now substitute expansion (13) into boundary conditions (3) and (4). We obtain two equations

$$\frac{1}{r}\frac{\partial}{\partial\theta}\left\{\left[\Psi_1^{(1)}+\frac{\partial}{\partial r}r\Psi_3^{(1)}\right]-\left[\Psi_1^{(2)}+\frac{\partial}{\partial r}r\Psi_3^{(2)}\right]\right\}$$

$$+\frac{1}{\sin\theta}\frac{\partial}{\partial\varphi}\{\Psi_2^{(1)}-\Psi_2^{(2)}\}=0, \tag{19}$$

$$\frac{1}{r\sin\theta}\frac{\partial}{\partial\varphi}\left\{\left[\Psi_1^{(1)}+\frac{\partial}{\partial r}r\Psi_3^{(1)}\right]-\left[\Psi_1^{(2)}+\frac{\partial}{\partial r}r\Psi_3^{(2)}\right]\right\}$$

$$-\frac{\partial}{\partial\theta}\{\Psi_2^{(1)}-\Psi_2^{(2)}\}=0. \tag{20}$$

We act on Eq. (19) with the operator

$$\frac{1}{\sin\theta}\frac{\partial}{\partial\theta}\sin\theta,$$

and on Eq. (20) with the operator

$$\frac{1}{\sin\theta}\frac{\partial}{\partial\varphi}$$

and add them. As a result we obtain

$$\Delta_\Omega\left\{\left[\Psi_1^{(1)}+\frac{\partial}{\partial r}r\Psi_3^{(1)}\right]-\left[\Psi_1^{(2)}+\frac{\partial}{\partial r}r\Psi_3^{(2)}\right]\right\}=0. \tag{21}$$

We act now on Eq. (19) with the operator

$$\frac{1}{\sin\theta}\frac{\partial}{\partial\varphi},$$

and on Eq. (20) with the operator

$$\frac{1}{\sin\theta}\frac{\partial}{\partial\theta}\sin\theta$$

and subtract the second equation from the first. As a result we obtain

$$\Delta_\Omega\{\Psi_2^{(1)}-\Psi_2^{(2)}\}=0. \tag{22}$$

Equations (21) and (22) can be satisfied by choosing the eigenfunctions corresponding to the zero eigenvalue of the operator $\Delta_\Omega=-\hat{\mathbf{N}}_2^+\cdot\hat{\mathbf{N}}_2$. However, as in the case of Eq. (15), this would be too great a restriction. Therefore we choose the second possibility, in which the expressions in braces vanish, i.e.,

$$\left[\Psi_1^{(1)}+\frac{\partial}{\partial r}r\Psi_3^{(1)}\right]-\left[\Psi_1^{(2)}+\frac{\partial}{\partial r}r\Psi_3^{(2)}\right]=0, \tag{23}$$

$$\Psi_2^{(1)}-\Psi_2^{(2)}=0. \tag{24}$$

Conditions (23) and (24) give the scalar analog of boundary conditions (3) and (4). After applying the identical procedure we obtain the scalar analog of boundary conditions (6) and (7)

$$\rho^{(1)}\nu^{(1)}\left[2\frac{\partial}{\partial r}\frac{\Psi_1^{(1)}}{r}+\frac{\partial^2\Psi_3^{(1)}}{\partial r^2}-\frac{(2+\Delta_\Omega)}{r^2}\Psi_3^{(1)}\right]-\rho^{(2)}\nu^{(2)}$$

$$\times\left[2\frac{\partial}{\partial r}\frac{\Psi_1^{(2)}}{r}+\frac{\partial^2\Psi_3^{(2)}}{\partial r^2}-\frac{(2+\Delta_\Omega)}{r^2}\Psi_3^{(2)}\right]=0, \tag{25}$$

$$\rho^{(1)}\nu^{(1)}\left[r\frac{\partial}{\partial r}\frac{\Psi_2^{(1)}}{r}\right]-\rho^{(2)}\nu^{(2)}\left[r\frac{\partial}{\partial r}\frac{\Psi_2^{(1)}}{r}\right]=0. \tag{26}$$

The scalar analogs of boundary conditions (5) and (8) follow at once after substitution of expansion (13) and the expression for the pressure field (18)

$$\frac{\partial\Psi_1^{(1)}}{\partial r}-\frac{1}{r}\Delta_\Omega\Psi_3^{(1)}=\frac{\partial\Psi_1^{(2)}}{\partial r}-\frac{1}{r}\Delta_\Omega\Psi_3^{(2)}=\frac{\partial\xi}{\partial t}, \tag{27}$$

$$\left[\rho^{(1)}\frac{\partial\psi_1^{(1)}}{\partial t}+2\rho^{(1)}\nu^{(1)}\frac{\partial^2\Psi_1^{(1)}}{\partial r^2}-2\rho^{(1)}\nu^{(1)}\Delta_\Omega\frac{\partial}{\partial r}\frac{\Psi_3^{(1)}}{r}\right]$$

$$+p_\sigma-p_E=\left[\rho^{(2)}\frac{\partial\Psi_1^{(2)}}{\partial t}+2\rho^{(2)}\nu^{(2)}\frac{\partial^2\Psi_1^{(2)}}{\partial r^2}\right.$$

$$\left.-2\rho^{(2)}\nu^{(2)}\Delta_\Omega\frac{\partial}{\partial r}\frac{\Psi_3^{(2)}}{r}\right]. \tag{28}$$

The condition of constant volume (9) remains unchanged, and from the condition of immobility of the center of mass (10), upon expanding the spherical basis vector $\mathbf{e}_r$ in the constant basis vectors of the Cartesian coordinate system, we obtain

$$\int_\Omega\xi\cos\theta d\Omega=0,\quad \int_\Omega\xi\sin\theta\cos\varphi d\Omega=0,$$

$$\int_\Omega\xi\sin\theta\sin\varphi d\Omega=0,$$

or, what is the same thing,

$$\int_\Omega\xi Y_{1n}d\Omega=0, \tag{29}$$

where Y_{mn} are the spherical harmonics — the eigenfunctions of the operator Δ_Ω — corresponding to the eigenvalues $-m(m+1)$, $m=0,1,2,\ldots,-m\leqslant n\leqslant m$.

From the obtained system of equations we see that the field Ψ_2 has no effect on the variation of the shape of the surface since the problem of finding it does not depend on Ψ_1, Ψ_3, or ξ and it does not enter into the equations determining Ψ_1, Ψ_3, and ξ.

3. Let us go on now to the solution of the ordinary scalar boundary-value problem. We seek the solution of Eqs. (17) and the function ξ in the form of a spherical harmonic expansion

$$\Psi_i^{(\alpha)}=\sum_{m,n}\Psi_i^{(\alpha)}(r)Y_{mn}\exp(St),$$

$$\xi=\sum_{m,n}ZY_{mn}\exp(St). \tag{30}$$

We drop the indices n and m of the quantities $\Psi_i^{\alpha}(r)$ and Z for the sake of simplicity. From conditions (9) and (29) we obtain that $m\neq 0$ and $m\neq 1$; therefore in what follows we assume that $m=2,3,\ldots,\ -n\leqslant m\leqslant n$. The pressure of the forces of surface tension (11) now take the form

$$p_\sigma=\sum_{m,n}(m-1)(m+2)ZY_{mn}\exp(St). \tag{31}$$

The pressure of the electric field (12) now takes the form

$$p_E=\frac{Q^2}{4\pi\varepsilon}\sum_{m,n}(m-1)ZY_{mn}\exp(St). \tag{32}$$

Substituting expansions (30) into Eqs. (17), we obtain equations for the radial functions

$$\frac{a^2\Psi_i^{(\alpha)}(r)}{dr^2}+\frac{2}{r}\frac{d\Psi_i^{(\alpha)}(r)}{dr}-\left[\frac{S}{\nu^{(\alpha)}}(1-\delta_{1i})+\frac{m(m+1)}{r^2}\right]\Psi_i^{(\alpha)}(r)=0. \tag{33}$$

Substituting Eqs. (30)–(32) into Eqs. (23)–(28), we obtain boundary conditions for the functions $\Psi_i^{(\alpha)}(r)$

$$\left[\Psi_1^{(1)}(r)+\frac{\partial}{\partial r}r\Psi_3^{(1)}(r)\right]-\left[\Psi_1^{(2)}(r)+\frac{\partial}{\partial r}r\Psi_3^{(2)}(r)\right]=0,$$

$$\rho^{(1)}\nu^{(1)}\left[2\frac{\partial}{\partial r}\frac{\Psi_1^{(1)}(r)}{r}+\frac{\partial^2\Psi_3^{(1)}(r)}{\partial r^2}+(m-1)(m+2)\Psi_3^{(1)}(r)\right]-\rho^{(2)}\nu^{(2)}\times\left[2\frac{\partial}{\partial r}\frac{\Psi_1^{(2)}(r)}{r}+\frac{\partial^2\Psi_3^{(2)}(r)}{\partial r^2}+(m-1)(m+2)\Psi_3^{(2)}(r)\right]=0,$$

$$\left[\frac{\partial\Psi_1^{(1)}(r)}{\partial r}+m(m+1)\Psi_3^{(1)}(r)\right]-\left[\frac{\partial\Psi_1^{(2)}(r)}{\partial r}+m(m+1)\Psi_3^{(2)}(r)\right]=0,$$

$$\frac{\partial\Psi_1^{(1)}(r)}{\partial r}+m(m+1)\Psi_3^{(1)}(r)-SZ=0,$$

$$\rho^{(1)}\left[S\Psi_1^{(1)}(r)+2\nu^{(1)}\frac{\partial^2\Psi_1^{(1)}(r)}{\partial r^2}+2\nu^{(1)}m(m+1)\frac{\partial}{\partial r}\frac{\Psi_3^{(1)}(r)}{r}\right]-\rho^{(2)}\left[S\Psi_1^{(2)}(r)+2\nu^{(2)}\frac{\partial^2\Psi_1^{(2)}(r)}{\partial r^2}+2\nu^{(2)}m(m+1)\frac{\partial}{\partial r}\frac{\Psi_3^{(2)}(r)}{r}\right]+\left[(m-1)(m+2)-\frac{Q^2}{4\pi\varepsilon}(m-1)\right]Z=0, \tag{34}$$

$$\Psi_2^{(1)}(r)-\Psi_2^{(2)}(r)=0,$$

$$\rho^{(1)}\nu^{(1)}\left[\frac{\partial}{\partial r}\frac{\Psi_2^{(1)}(r)}{r}\right]-\rho^{(2)}\nu^{(2)}\left[\frac{\partial}{\partial r}\frac{\Psi_2^{(2)}(r)}{r}\right]=0. \tag{35}$$

The solutions of Eqs. (33) have the form

$$\Psi_1^1(r)=b_1r^m,\quad \Psi_1^2(r)=c_1r^{-(m+1)},$$

$$\Psi_2^1(r)=b_2\frac{i_m(x_1r)}{i_m(x_1)},\quad \Psi_2^2(r)=c_2\frac{k_m(x_2r)}{k_m(x_2)},$$

$$\Psi_3^1(r)=b_3\frac{i_m(x_1r)}{i_m(x_1)},\quad \Psi_3^2(r)=c_3\frac{k_m(x_2r)}{k_m(x_2)}, \tag{36}$$

where $x_1=\sqrt{S/\nu_1}$, $x_2=\sqrt{S/\nu_2}$; $i_m(x)$, and $k_m(x)$ are the modified Bessel functions of the first and third kind, respectively.

We now substitute the solutions for the radial functions $\Psi_i^{(\alpha)}(r)$ (36) into the system of boundary conditions (34). Employing the following recursion formulas

$$\frac{i_m'(x)}{i_m(x)}=\frac{i_{m+1}(x)}{i_m(x)}+\frac{m}{x},$$

$$\frac{i_m''(x)}{i_m(x)}=-\frac{2}{x}\frac{i_{m+1}(x)}{i_m(x)}+\left[1+\frac{m(m-1)}{x^2}\right],$$

$$\frac{k_m'(x)}{k_m(x)}=-\frac{k_{m-1}(x)}{k_m(x)}-\frac{m+1}{x},$$

$$\frac{k_m''(x)}{k_m(x)}=-\frac{2}{x}\frac{k_{m-1}(x)}{k_m(x)}+\left[1+\frac{(m+1)(m+2)}{x^2}\right] \tag{37}$$

for the modified spherical Bessel functions, after some transformations we obtain a homogeneous system of linear equations in the coefficients b_1, c_1, b_3, c_3, and Z

$$b_1+b_3\left[x_1\frac{i_{m+1}(x_1)}{i_m(x_1)}+(m+1)\right]-c_1+c_3\left[x_2\frac{k_{m-1}(x_2)}{k_m(x_2)}+m\right]=0,$$

$$\rho_1\nu_1\left\{2(m-1)b_1+b_3\left[-2x_1\frac{i_{m+1}(x_1)}{i_m(x_1)}+x_1^2+2(m-1)\times(m+1)\right]\right\}-\rho_2\nu_2\left\{-2(m+2)c_1+c_3\left[2x_2\frac{k_{m-1}(x_2)}{k_m(x_2)}+x_2^2+2m(m+2)\right]\right\}=0,$$

$$mb_1+m(m+1)b_3+(m+1)c_1-m(m+1)c_3=0,$$

$$mb_1+m(m+1)b_3-SZ=0,$$

$$\rho_1\left\{(S+2\nu_1m(m-1))b_1+b_32\nu_1m(m+1)\times\left[x_1\frac{i_{m+1}(x_1)}{i_m(x_1)}+(m-1)\right]\right\}-\rho_2\left\{(S+2\nu_2(m+1)\times(m+2))c_1+c_32\nu_2m(m+1)\left[x_2\frac{k_{m-1}(x_2)}{k_m(x_2)}+(m+2)\right]\right\}+\left[(m-1)(m+2)-\frac{Q^2}{4\pi\varepsilon}(m-1)\right]Z=0.$$

The given system has a nontrivial solution only if the determinant of the matrix of coefficients of the unknowns b_1, c_1, b_3, c_3, and Z is equal to zero

$$\det\begin{vmatrix} a_{11} & a_{12} & a_{13} & a_{14} & a_{15}\\ a_{21} & a_{22} & a_{23} & a_{24} & a_{25}\\ a_{31} & a_{32} & a_{33} & a_{34} & a_{35}\\ a_{41} & a_{42} & a_{43} & a_{44} & a_{45}\\ a_{51} & a_{52} & a_{53} & a_{54} & a_{55}\end{vmatrix}=0, \tag{38}$$

where

$$a_{11}=1,\quad a_{12}=-1,\quad a_{13}=x_1\frac{i_{m+1}(x_1)}{i_m(x_1)}+(m-1),$$

$$a_{14}=x_2\frac{k_{m-1}(x_2)}{k_m(x_2)}+m,\quad a_{15}=0,$$

$$a_{21}=2(m-1)\rho_1\nu_1,$$

$$a_{22}=2(m+2)\rho_2\nu_2,$$

$$a_{23}=\rho_1\nu_1\left[-2x_1\frac{i_{m+1}(x_1)}{i_m(x_1)}+x_1^2+2(m-1)(m+1)\right],$$

$$a_{24}=-\rho_2\nu_2\left[2x_2\frac{k_{m-1}(x_2)}{k_m(x_2)}+x_2^2+2m(m+2)\right],$$

$$a_{25}=0,\quad a_{31}=m,\quad a_{32}=(m+1),$$

$$a_{33}=m(m+1),\quad a_{34}=-m(m+1),\quad a_{35}=0,$$

$$a_{41}=m,\quad a_{42}=0,\quad a_{43}=m(m+1),\quad a_{44}=0,$$

$$a_{45}=-S,$$

$$a_{51}=\rho_1S+2m(m-1)\rho_1\nu_1,$$

$$a_{52}=-\rho_2S-2(m+1)(m+2)\rho_2\nu_2,$$

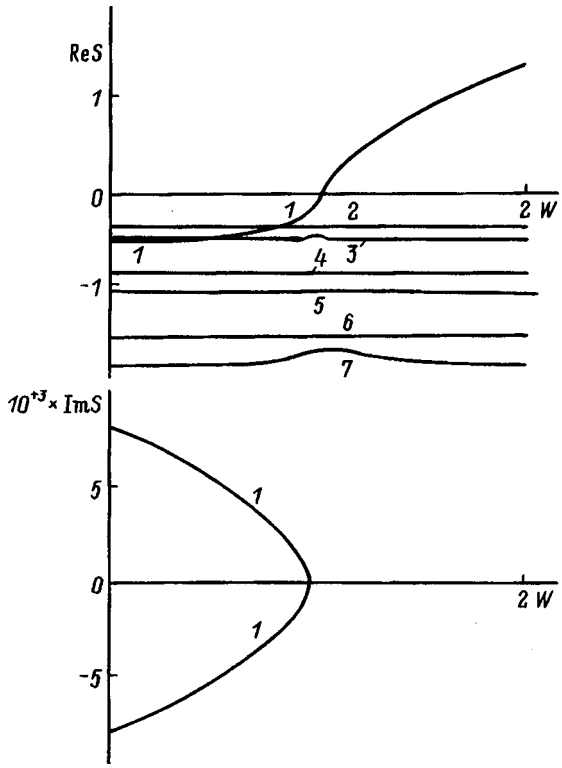

FIG. 1. $\mathrm{Re}\,S=\mathrm{Re}\,S(W)$ and $\mathrm{Im}\,S=\mathrm{Im}\,S(W)$ plotted as functions of W. $m=2$, $\nu_1=0.01$, $\nu_2=0.1$, $\rho_1=1$, $\rho_2=1.5$.

$$a_{53}=\rho_1\nu_12m(m+1)\left[x_1\frac{i_{m+1}(x_1)}{i_m(x_1)}+(m-1)\right],$$

$$a_{54}=\rho_2\nu_22m(m+1)\left[x_2\frac{k_{m-1}(x_2)}{k_m(x_2)}+(m+2)\right],$$

$$a_{55}=(m-1)(m+2)-\frac{Q^2}{4\pi\varepsilon}(m-1). \tag{39}$$

4. Numerical calculations of the determinant (38) taking relations (39) into account lead to the trends illustrated in Fig. 1, which plots the dependence of the real part $\mathrm{Re}\,S=\mathrm{Re}\,S(W)$ and imaginary part $\mathrm{Im}\,S=\mathrm{Im}\,S(W)$ of the frequency for the second mode on the Rayleigh parameter $W\equiv Q^2/(16\pi\varepsilon\sigma R^3)$: the growth rate (branch *2*) for $\mathrm{Re}\,S>0$ and damping rates for $\mathrm{Re}\,S<0$ of the damped periodic (branches *1*) and aperiodic (branch *3*) capillary motions of the drop in the medium. The branches of the dispersion relation with numbers *4–7*, etc. correspond, according to Refs. 5 and 6, to dissipation of the energy of the vortical poloidal motions.

Figures 2 and 3 plot the dependence of the real part $\mathrm{Re}\,S=\mathrm{Re}\,S(\nu_2)$ and imaginary part $\mathrm{Im}\,S=\mathrm{Im}\,S(\nu_2)$ of the complex frequency of the capillary motions of the liquid in the drop and of the liquid surrounding it as functions of the dimensionless viscosity of the medium ν_2 in the subcritical regime in the absence of charge on the interface $W=0$ (Fig. 2) and in the supercritical regime for $W=2$ (Fig. 3). Note that the critical value of the Rayleigh parameter is $W=1$.

Figures 4 and 5 plot the dependence of the real part $\mathrm{Re}\,S=\mathrm{Re}\,S(\rho_2)$ and the imaginary part $\mathrm{Im}\,S=\mathrm{Im}\,S(\rho_2)$ of

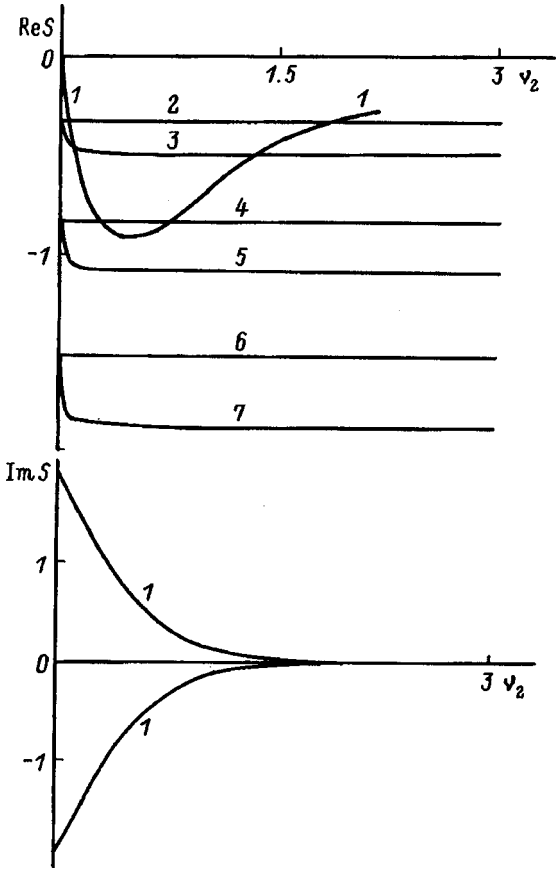

FIG. 2. $\mathrm{Re}\,S=\mathrm{Re}\,S(\nu_2)$ and $\mathrm{Im}\,S=\mathrm{Im}\,S(\nu_2)$ plotted as functions of ν_2 in the subcritical regime for $W=2$. $m=2$, $\nu_1=0.01$, $\rho_1=1$, $\rho_2=1.5$.

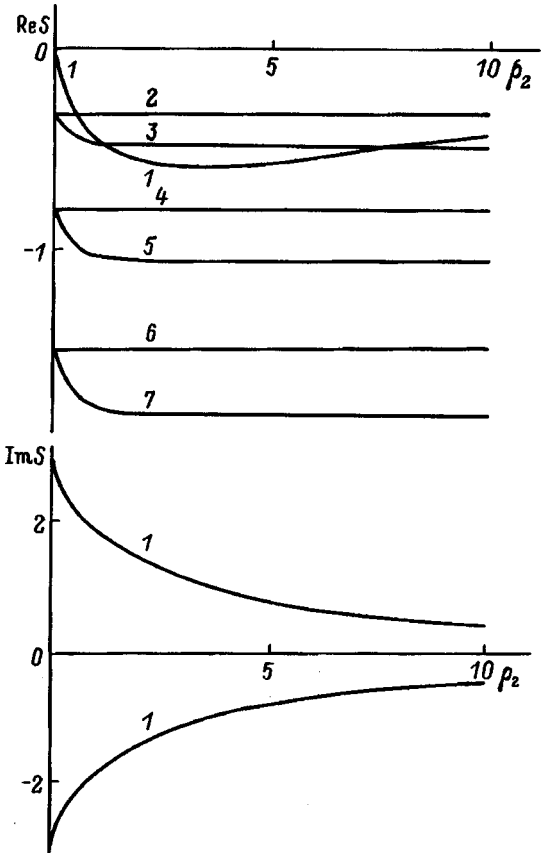

FIG. 4. $\mathrm{Re}\,S=\mathrm{Re}\,S(\rho_2)$ and $\mathrm{Im}\,S=\mathrm{Im}\,S(\rho_2)$ plotted as functions of ρ_2 in the subcritical regime for $W=0$. $m=2$, $\nu_1=0.01$, $\nu_2=0.1$, $\rho_1=1$.

the complex frequency of the capillary motions of the liquid in the drop and of the liquid surrounding it as functions of the dimensionless density of the medium ρ_2 in the subcritical regime in the absence of charge on the interface $W=0$ (Fig. 4) and in the supercritical regime for $W=2$ (Fig. 5).

In Figs. 2–5 the branches with numbers greater than *1* correspond to vortical poloidal motions, which exist both in the drop and in the surrounding medium. In the figures the poloidal motions corresponding to the drop are labelled by even numbers, and those pertaining to the medium are labelled by odd numbers. It can be seen that in the limit $\rho_2\to 0$ the curves corresponding to the vortical poloidal component of the velocities of the surrounding liquid coalesce with the curves corresponding to the vortical poloidal component of the velocities of the liquid in the drop. Note that in the calculations behind Figs. 1–5, as the third scaling parameter we took the density of the liquid in the drop, i.e., $\rho_1=1$.

Figure 6 plots the dependence of the real part of the frequency on the dimensionless viscosity of the liquid in the

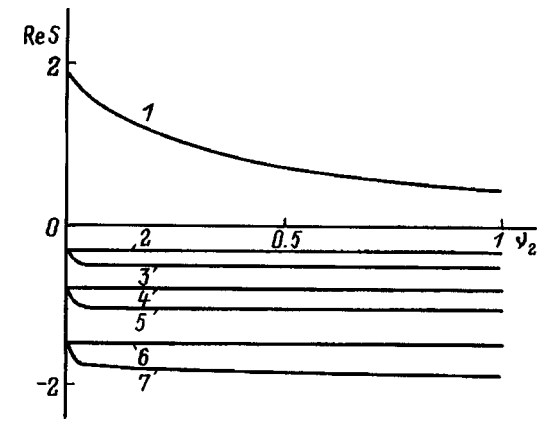

FIG. 3. $\mathrm{Re}\,S=\mathrm{Re}\,S(\nu_2)$ plotted as a function of ν_2 in the supercritical regime for $W=2$. $m=2$, $\nu_1=0.01$, $\rho_1=1$, $\rho_2=1.5$.

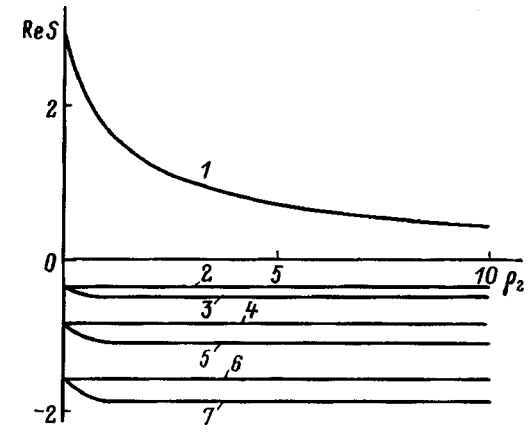

FIG. 5. $\mathrm{Re}\,S=\mathrm{Re}\,S(\rho_2)$ plotted as a function of ρ_2 for $W=2$. $m=2$, $\nu_1=0.01$, $\nu_2=0.1$, $\rho_1=1$.

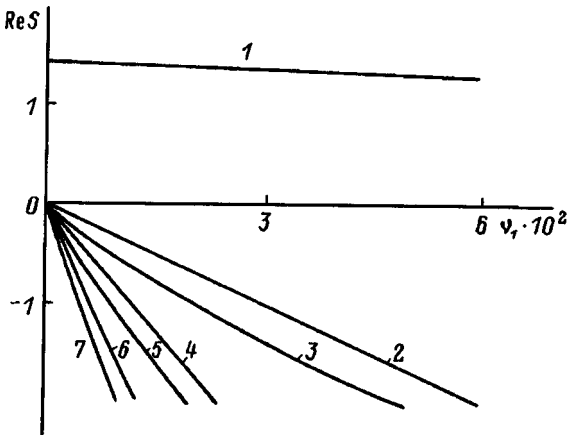

FIG. 6. Re S plotted as a function of ν_1 in the supercritical regime for $W=2$. $m=2$, $\nu_2=0.1$, $\rho_1=1.5$, $\rho_2=1$.

drop $\mathrm{Re}\,S=\mathrm{Re}\,S(\nu_1)$ in the supercritical regime ($W=2$) for all expressions scaled by ρ_2. It is easy to see that the instability growth rate falls off gently with ν_1 (curve *1*). The dependence of the growth rates of the vortical poloidal motions on ν_1, on the other hand, is quite noticeable (curves *2–7*).

Figure 7 plots the dependence of the real part of the frequency on the dimensionless density of the liquid in the drop $\mathrm{Re}\,S=\mathrm{Re}\,S(\rho_1)$ in the supercritical regime ($W=2$) for all expressions scaled by ρ_2. Curve *1* plots the falloff of the instability growth rate of the interface with increasing ρ_1. Curves *2–5*, etc., which plot the damping rates of the poloidal–vortical motions, depend on ρ_1 very weakly, falling with increasing ρ_1.

5. Let us turn now to the problem of finding the vortical toroidal component of the velocity field associated with the scalar function Ψ_2, which is determined by system of equations (35). Substituting expressions (36) into Eqs. (35), and employing recursion formulas (37), we find

$$b_2-c_2=0,$$

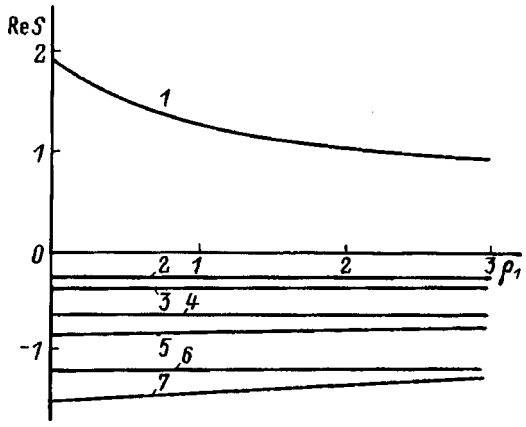

FIG. 7. Re S plotted as a function of ρ_1 in the supercritical regime for $W=2$. $m=2$, $\nu_1=0.01$, $\nu_2=0.1$, $\rho_2=1$.

$$\rho^{(1)}\nu^{(1)}\left[x_1\frac{i_{m+1}(x_1)}{i_m(x_1)}+(m-1)\right]b_2+\rho^{(2)}\nu^{(2)}\left[x_2\frac{k_{m-1}(x_2)}{k_m(x_2)}+(m+2)\right]c_2=0.$$

The above system of algebraic equations has a nontrivial solution if the determinant of the matrix of coefficients of b_2 and c_2 is equal to zero. This condition also determines the dispersion relation describing the spectrum of vortical toroidal motions in the drop and in the medium

$$\rho^{(1)}\nu^{(1)}\left[x_1\frac{i_{m+1}(x_1)}{i_m(x_1)}+(m-1)\right]+\rho^{(2)}\nu^{(2)}\left[x_2\frac{k_{m-1}(x_2)}{k_m(x_2)}+(m+2)\right]=0.$$

Numerical calculations based on the above dispersion relation show that an increase in the dimensionless viscosity of the liquid of the drop leads to a rapid increase in the damping rates of the toroidal motions. The dependence on the viscosity of the medium and densities of both liquids is quite insignificant.

CONCLUSION

In our theoretical study of the capillary vibrations of a charged, viscous, incompressible drop in a viscous, incompressible insulating medium we have found that the viscosity and density of the medium have a substantial effect both on the structure of the spectrum of capillary motions of the liquid in the drop and the liquid in the medium, and on the regularities of realizations of the instability of the charged interface: the instability growth rates fall off rapidly with growth of ν_2 and ρ_2, and the damping rates of the vortical poloidal motions undergo a considerable increase.

The decrease of the instability growth rates may mean an increase in the probability of breakup of a strongly charged drop into two parts of comparable size as was observed by Ryce and Wyman[7] and Ryce and Patriarghe[8], and a decrease in the probability of breakup via the Rayleigh channel described in Ref. 9.

APPENDIX

The electric field pressure at the interface of a conducting medium and an insulating medium is defined as follows:

$$p_E=\frac{\varepsilon}{8\pi}E^2\Big|_{r=R+\xi}.$$

Let Φ be the potential of the electric field in the insulator. We represent it in the form $\Phi=\Phi_0+\delta\Phi$, where Φ_0 is the potential in the absence of perturbations and $\delta\Phi$ is an added term due to a small perturbation of the surface of the drop. Thus

$$p_E=\frac{\varepsilon}{8\pi}(\nabla\Phi_0+\nabla(\delta\Phi))^2\Big|_{r=R+\xi}.$$

We expand this expression in a series out to terms of order ξ and $\delta\Phi$

$$p_E \approx \frac{\varepsilon}{8\pi}(\nabla\Phi_0)^2\Big|_{r=R+\xi} + \frac{\varepsilon}{8\pi}2\nabla\Phi_0\cdot\nabla(\delta\Phi)\Big|_{r=R+\xi}$$
$$= \frac{\varepsilon}{8\pi}(\nabla\Phi_0)^2\Big|_{r=R} + \frac{\varepsilon}{8\pi}\frac{\partial(\nabla\Phi_0)^2}{\partial r}\Big|_{r=R}\xi$$
$$+ \frac{\varepsilon}{4\pi}(\nabla\Phi_0)\Big|_{r=R}(\nabla\delta\Phi_0)\Big|_{r=R}.$$

Making use of the fact that the electric field on the surface of a conductor is perpendicular to the surface, we obtain

$$p_E = \frac{\varepsilon}{8\pi}\left(\frac{\partial\Phi_0}{\partial r}\right)^2\Big|_{r=R} + \frac{1}{8\pi}\left|\left[\frac{\partial}{\partial r}\left(\frac{\partial\Phi_0}{\partial r}\right)^2\right]\right|_{r=R}\xi$$
$$+ \left|\frac{1}{4\pi}\frac{\partial\Phi_0}{\partial r}\right|_{r=R}\frac{\partial(\delta\Phi)}{\partial r}\Big|_{r=R}.$$

The potential Φ should satisfy the following conditions: $\Delta\Phi=0$; $\Phi\to 0$ as $r\to\infty$; and $\Phi=\text{const}$ for $r=R+\xi$. Thus, for Φ_0 and $\delta\Phi$ we have either

$$\Delta\Phi_0=0, \quad \Delta\delta\Phi=0;$$

$$\Phi_0\to 0, \quad \delta\Phi\to 0 \ \text{ as } \ r\to\infty;$$

$$\Phi_0|_{r=R} + \xi\cdot\frac{\partial\Phi_0}{\partial r}\Big|_{r=R} + \delta\Phi|_{r=R} = \text{const} \ \text{ for } \ r=R$$

or, setting $\Phi_0|_{r=R}=\text{const}$, we obtain

$$\delta\Phi|_{r=R} = -\xi\frac{\partial\Phi_0}{\partial r}\Big|_{r=R}.$$

Thus, for Φ_0 we find $\Phi_0=Q/\varepsilon r$. We seek the solution for $\delta\Phi$ in the form

$$\delta\Phi = \sum_n F_n\left(\frac{R}{r}\right)^{n+1}P_n(\mu),$$

where $\mu\equiv\cos\theta$ and $P_n(\mu)$ are the Lengendre polynomials normalized to unity.

From the boundary condition for the potential on the surface of the drop we obtain

$$\sum_n F_n P_n(\mu) = \xi\frac{Q}{\varepsilon R_2}.$$

Taking into account that $\int_{-1}^{1}P_n(\mu)P_m(\mu)d\mu=\delta_{nm}$, we obtain

$$F_n = \frac{Q}{\varepsilon R^2}\int_{-1}^{1}\xi(\theta)P_n(\mu)d\mu$$

$$\to \delta\Phi = \sum_n \frac{Q}{\varepsilon R^2}\left(\frac{R}{r}\right)^{n+1}P_n(\mu)\int_{-1}^{1}\varepsilon P_m(\mu)d\mu$$

$$\to p_E = \frac{1}{8\pi}\frac{Q^2}{\varepsilon R^4} - \frac{1}{2\pi}\frac{Q^2}{\varepsilon R^4}\frac{\varepsilon}{R}$$
$$+ \frac{1}{4\pi}\frac{Q^2}{\varepsilon R^4}\sum_{n=0}^{\infty}(n+1)P_n(\mu)\int_{-1}^{1}\xi P_n(\mu)d\mu.$$

ACKNOWLEDGMENTS

We wish to express our gratitude to A. É. Lazaryants for bringing this problem to our attention.

[1] A. C. Bailey, SCOPE **61**, 555 (1974).
[2] V. I. Kozhenkov and N. A. Fuks, Usp. Khim. **45**, 2274 (1976).
[3] A. I. Grigor'ev, Yu. V. Syshchikov, and S. O. Shiryaeva, Zh. Prikl. Khim. **62**, 2020 (1989).
[4] A. I. Grigor'ev and S. O. Shiryaeva, Izv. Akad. Nauk SSSR, Mekh. Zhidk. Gaza No. **3**, pp. 3–22 (1994).
[5] S. O. Shiryaeva, A. É. Lazaryants, A. I. Grigor'ev *et al.*, Preprint IM RAN No. 27 [in Russian], Yaroslavl (1994), 126 pp.
[6] S. O. Shiryaeva, M. I. Munichev, and A. I. Grigor'ev, Zh. Tekh. Fiz. **66**, (7), 1 (1996) [Tech. Phys. **41**, 635 (1996)].
[7] S. A. Ryce and R. R. Wyman, Can. J. Phys. **42**, 2185 (1964).
[8] S. A. Ryce and D. A. Patriarghe, Can. J. Phys. **43**, 2192 (1965).
[9] A. I. Grigor'ev and S. O. Shiryaeva, Zh. Tekh. Fiz. **61**(3), 19 (1991) [Sov. Phys. Tech. Phys. **36**, 258 (1991)].

Translated by Paul F. Schippnick

Calculation of the critical conditions of instability in an electric field of a hemispherical droplet on a hard substrate

S. O. Shiryaeva

Yaroslavl State University, 150000 Yaroslavl, Russia
(Submitted June 16, 1997)
Zh. Tekh. Fiz. **68**, 9–12 (September 1998)

The critical conditions of instability of a hemispherical drop of a conducting liquid lying on a hard, electrically conducting substrate in an electric field parallel to the symmetry axis of the drop are found. These critical instability conditions are found to be higher than those of an insulating drop of the same size. © *1998 American Institute of Physics.* [S1063-7842(98)00209-8]

In various problems of technical physics and geophysics, one encounters the problem of the electrostatic instability of drops of a conducting liquid that have settled onto conductors in an external electrostatic field. In particular, this problem is associated with the problem of increased energy losses on transmission lines in rainy weather,[1] with studies of the relationships governing St. Elmo's fire, which is due to the ignition of a corona discharge in the atmospheric electric field in the vicinity of water droplets settled onto tall objects,[2–4] and with the problem of the danger of fire and explosions in the washing out of highly flammable liquids from large storage tanks.[5] The following discussion is based on a method described in detail in Ref. 6 and used in Ref. 7.

1. We consider a drop of an ideal, incompressible, perfectly conducting liquid with density ρ and coefficient of surface tension σ, lying on a hard, flat, electrically conducting substrate. Let the entire system be found in an external uniform electrostatic field $\mathbf{E}_0$, perpendicular to the plane of the substrate. The question of the equilibrium shape of such a drop is very complicated since it depends on the form of the adhesion forces between the drop and the substrate, which are difficult to take into account. Therefore we assume that the liquid wets the substrate and the contact angle is equal to $\pi/2$, the shape of the drop is hemispherical, and, ignoring the question of the state of equilibrium of this shape, we pose the problem of determining the critical conditions of the instability of such a surface relative to the electric and capillary forces. Despite the arbitrariness of the problem as posed, it allows us, to first order, to shed some light on the question of the various conditions of excitation of instability of a drop in the free state and a drop seated upon a hard substrate.

The equation of perturbed wave motion of the surface of a drop in spherical coordinates with origin at the center of the base of the hemisphere and z axis perpendicular to the plane of the substrate is written in the form

$$r(\Theta,t)=R+\xi(\Theta,t) \quad \left(0\leqslant\Theta\leqslant\frac{\pi}{2}\right), \tag{1}$$

where R is the radius of the unperturbed hemispherical surface, $\xi(\Theta,t)$ is the axisymmetric perturbation of the surface of the drop ($\max|\xi|\ll R$).

A treatment of just the axisymmetric perturbations is justified by the fact that the critical conditions of excitation of the axisymmetric modes of the capillary vibrations of the surface are lower than for the nonaxisymmetric modes. Therefore, for the stated problem such a simplification is entirely reasonable.

We will solve the problem in the approximation in which we keep only terms linear in $|\xi|/R$. Wave motion of an ideal, incompressible liquid due to a perturbation of the surface, ξ, is potential with velocity potential $\Psi(r,\Theta,t)$ having the same order of smallness as $|\xi|/R$ and being a harmonic function

$$\Delta\Psi=0, \tag{2}$$

where Δ denotes the Laplacian operator.

We write the boundary conditions on the free surface of the drop defined by Eq. (1). In the linear approximation where we linearize in the small quantities of the problem, these boundary conditions pertain, as is customary in the theory of waves of infinitesimally small amplitude,[8] to the unperturbed surface

$$r=R: \quad \frac{\partial\xi}{\partial t}=\frac{\partial\Psi}{\partial r}, \tag{3}$$

$$-\rho\frac{\partial\Psi}{\partial t}+\delta p_E-\delta p_\sigma=0, \tag{4}$$

where δp_E and δp_σ are perturbations in the pressure of the electric forces and the pressure of the surface tension forces, and have first-order of smallness.

The solution of Eq. (2), bounded at the center of the hemisphere, has the form

$$\Psi=\sum_{n=0}^{\infty} C_n(t)r^nP_n(\cos\Theta), \tag{5}$$

where $P_n(\cos\Theta)$ are the Legendre polynomials, which satisfy the following conditions on the hemispherical surface[9]:

$$\int_0^1 P_n(x)dx=\begin{cases}1 & \text{for } n=0,\\ 0 & \text{for } n=2k,\\ & (k=1,2,3,\dots),\\ \dfrac{L_n}{M_n}\equiv A_n & \text{for } n=2k,\\ & (k=0,1,2,3,\dots),\end{cases} \tag{6}$$

where

$$L_n=(-1)^{\frac{1}{2}(n-1)}(n-1)!,\quad M_n=2^n\left(\frac{n-1}{2}\right)!\left(\frac{n+1}{2}\right)!;$$

$$\int_0^1 P_n(x)P_m(x)dx$$

$$=\begin{cases}\dfrac{1}{2n+1} & \text{for } m=n,\\ 0 & \text{for } (n-m)=2k,\\ & (k=1,2,3,\dots),\\ \dfrac{F_{n,m}}{G_{n,m}}\equiv B_{n,m} & \text{for } n=2l,\quad m=2k+1,\\ & (l,k=0,1,2,\dots),\end{cases} \tag{7}$$

where $F_{n,m}=(-1)^{\frac{1}{2}(m+n+1)}n!m!$,

$$G_{n,m}=2^{(m+n-1)}(n-m)(m+n+1)\left[\left(\frac{n}{2}\right)!\left(\frac{m-1}{2}\right)!\right]^2.$$

We also represent the perturbation of the surface of the drop $\xi(\Theta,t)$ in the form of an expansion in Legendre polynomials

$$\xi(\Theta,t)=\sum_{n=0}^{\infty} Z_n(t)P_n(\cos\Theta). \tag{8}$$

It is obvious that as the surface of the drop vibrates, its volume should not vary, i.e.,

$$\int_0^{2\pi}\int_0^{\pi/2}\int_0^{R+\xi} r^2dr\sin\Theta d\Theta d\varphi=\frac{2}{3}\pi r^3.$$

In the approximation linear in ξ/R the condition of constant volume of the drop takes the form

$$\int_0^1 \xi(\Theta,t)d(\cos\Theta)=0.$$

Substituting expansion (8) into this condition and taking into account property (6) of the Legendre polynomials, we obtain $Z_0=0$ and $Z_{2k+1}=0$ $(k=0,1,2,\dots)$. Employing this result, we rewrite expansion (8) as

$$\xi(\Theta,t)=\sum_{k=1}^{\infty} Z_{2k}(t)P_{2k}(\cos\Theta). \tag{9}$$

We assume (as is customary in the theory of the stability of the solutions of differential equations) that the time dependence of the perturbation $\xi(\Theta,t)$ is exponential, i.e.,

$$Z_n(t)\sim\exp(St), \tag{10}$$

where S is the complex frequency.

Bearing ansatz (10) in mind, we substitute solutions (5) and (9) into boundary condition (3) and, using property (7) of the Legendre polynomials, we obtain a relation between the coefficients $C_n(t)$ and $Z_n(t)$

$$C_{2k+1}(t)=0,$$

$$C_{2k}(t)=\frac{SZ_{2k}(t)}{2kR^{2k-1}}\quad (k=1,2,3,\dots,0). \tag{11}$$

In order to apply boundary conditions (4), it is necessary to write out expressions for the perturbations of the pressure, δp_E and δp_σ. The pressure of the surface tension forces on a distorted spherical surface are known[8]

$$p_\sigma=p_\sigma^{(0)}+\delta p_\sigma=\sigma\left[\frac{2}{R}-\frac{1}{R^2}(2+\hat{L})\xi\right], \tag{12}$$

where $p_\sigma^{(0)}$ is the pressure on the surface of the sphere and $\hat{L}$ is the angular part of the Laplace operator in spherical coordinates

$$\hat{L}P_n(\cos\Theta)=-n(n+1)P_n(\cos\Theta).$$

2. In order to write out the pressure of the electrical forces, we mathematically formulate the problem of calculating the electric field on the surface of the drop. The potential φ of the electric field near the surface of a perfectly conducting drop lying on a perfectly conducting flat, unbounded substrate in the presence of an external, uniform electrostatic field perpendicular to the surface of the substrate should satisfy the following boundary-value problem:

$$\Delta\varphi=0,$$

$$r\to\infty:\quad \varphi\to -E_0z,$$

$$r=R+\xi;\quad z=0:\quad \varphi=\text{const}=0. \tag{13}$$

We represent the potential φ in the form

$$\varphi=\varphi_0+\delta\varphi, \tag{14}$$

where φ_0 is the potential on the surface of the conducting hemisphere lying on a conducting substrate,[10]

$$\varphi_0=-E_0z\left(1-\frac{R^3}{r^3}\right)$$

$$=-E_0r\cos\Theta\left(1-\frac{R^3}{r^3}\right)\left(0\leqslant\Theta\leqslant\frac{\pi}{2}\right), \tag{15}$$

$\delta\varphi$ is the perturbation of the potential caused by the perturbation of the surface $\xi(\Theta,t)$ and has first-order smallness.

Substituting expansion (14) into problem (13) and taking into account the well-known solution (15), we obtain a boundary-value problem for $\delta\varphi$

$$\Delta(\delta\varphi)=0, \tag{16}$$

$$r\to\infty:\quad \delta\varphi\to 0, \tag{17}$$

$$r=R,\quad \Theta=\frac{\pi}{2}:\quad \delta\varphi=-\xi\frac{\partial\varphi_0}{\partial r}. \tag{18}$$

The solution of Eq. (16), satisfying condition (17), has the form

$$\delta\varphi=\sum_{n=0}^{\infty} D_n(t)\left(\frac{R}{r}\right)^{n+1} P_n(\cos\Theta). \tag{19}$$

Substituting solutions (19) and (15) and expansion (9) into boundary condition (18) for for $\Theta=\pi/2$, we obtain

$$\sum_{n=0}^{\infty} D_n(t)\left(\frac{R}{r}\right)^{n+1} P_n(0)=0.$$

Noting that $P_{2k}(0)\neq 0$ and $P_{2k+1}(0)=0$ ($k=0,1,2,\ldots$), it follows that $D_{2k}=0$ and $D_{2k+1}\neq 0$, i.e., solution (19) can be rewritten in the form

$$\delta\varphi=\sum_{k=0}^{\infty} D_{2k+1}(t)\left(\frac{R}{r}\right)^{2k+2} P_{2k+1}(\cos\Theta). \tag{20}$$

3. Substituting solutions (20) and (15) and expansion (9) into boundary condition (18) for $r=R$, we obtain

$$\sum_{k=0}^{\infty} D_{2k+1}(t)P_{2k+1}(\cos\Theta) = 3E_0\sum_{k=1}^{\infty} Z_{2k}(t)\cos\Theta P_{2k}(\cos\Theta). \tag{21}$$

Expanding the product $\cos\Theta P_n(\cos\Theta)$ in Legendre polynomials

$$\cos\Theta P_n(\cos\Theta)=a_n P_{n+1}(\cos\Theta)+b_n P_{n-1}(\cos\Theta),$$

$$a_n\equiv\frac{n+1}{2n+1},\quad b_n\equiv\frac{n}{2n+1} \tag{22}$$

and adducing property (7) of the Legendre polynomials, condition (21) yields the following equation relating the coefficients $D_{2k+1}(t)$ and $Z_{2k}(t)$:

$$D_{2k+1}(t)=3E_0[Z_{2k}(t)a_{2k}+Z_{2k+2}(t)b_{2k+2}]. \tag{23}$$

Thus, the solution of boundary-value problem (13) for the potential of the electric field in the described system has the form (14), (15), (20), and (23).

The electric field vector is given by

$$\begin{aligned}\mathbf{E}|_{r=R+\xi}&=-\nabla\varphi\approx 3E_0\cos\Theta\mathbf{e}_r\\ &+\left\{\left[\sum_{k=0}^{\infty} D_{2k+1}(t)\frac{(2k+2)}{R}P_{2k+1}(\cos\Theta)\right.\right.\\ &\left.-6E_0\sum_{k=1}^{\infty}\frac{Z_{2k}(t)}{R}\cos\Theta P_{2k}(\cos\Theta)\right]\mathbf{e}_r\\ &-\left[\sum_{k=0}^{\infty} D_{2k+1}(t)\frac{1}{R}\frac{dP_{2k+1}(\cos\Theta)}{d\Theta}\right.\\ &\left.\left.+3E_0\sum_{k=1}^{\infty}\frac{Z_{2k}(t)}{R}\sin\Theta P_{2k}(\cos\Theta)\right]\mathbf{e}_\Theta\right\}\\ &\equiv\mathbf{E}_0+\delta\mathbf{E}.\end{aligned} \tag{24}$$

The pressure of the electric field on the surface of the perturbed hemisphere, after linearizing expression (24) in the small quantities of the problem, is written in the form

$$\begin{aligned}P_E\Big|_{r=R+\xi}&=\frac{1}{8\pi}(\mathbf{E})^2\Big|_{r=R+\xi}\approx\frac{1}{8\pi}[(\mathbf{E}_0)^2+2\mathbf{E}_0\delta\mathbf{E}]\\ &\equiv P_E^{(0)}+\delta P_E,\\ P_E^{(0)}&=\frac{9E_0^2}{8\pi}\cos^2\Theta,\\ \delta P_E&\approx\frac{1}{4\pi}18E_0^2\sum_{k=0}^{\infty}\left\{(k-1)a_{2k-2}a_{2k-1}\frac{Z_{2k-2}(t)}{R}\right.\\ &+[(k-1)a_{2k-1}b_{2k}+ka_{2k}b_{2k+1}]\frac{Z_{2k}(t)}{R}\\ &\left.+kb_{2k+1}b_{2k+2}\frac{Z_{2k+2}(t)}{R}\right\}P_{2k}(\cos\Theta).\end{aligned} \tag{25}$$

4. Substituting solution (5) into Eq. (4), and also expressions (12) and (25) allowing for relation (11) and ansatz (10), we obtain

$$\begin{aligned}&\left\{\frac{\rho R}{2k}S^2-\frac{18E_0^2}{4\pi R}[(k-1)a_{2k-1}b_{2k}+ka_{2k}b_{2k+1}]-\frac{2\sigma}{R^2}[1\right.\\ &\left.-k(2k+1)]\right\}Z_{2k}-\frac{18E_0^2}{4\pi R}[(k-1)a_{2k-2}a_{2k-1}Z_{2k-2}\\ &+kb_{2k+1}b_{2k+2}Z_{2k+2}]=0(k=1,2,3,\ldots).\end{aligned} \tag{26}$$

This is an infinite system of homogeneous coupled equations defining the amplitudes of the various modes of the capillary vibrations. It has a nontrivial solution when the determinant of the matrix of coefficients of the amplitudes of the modes vanishes. The condition that the determinant of system (26) equals zero gives the dispersion relation of the problem, which has infinite order:

$$\begin{vmatrix} 4^{-1}\Theta+2-ya_2b_3 & -yb_3b_4 & 0 & \cdots\\ -ya_2a_3 & 8^{-1}\Theta+9-y(a_3b_4+2a_4b_5) & -2yb_5b_6 & \cdots\\ 0 & -2ya_4a_5 & 12^{-1}\Theta+20-y(2a_5b_6-3a_6b_7) & \cdots\\ \cdots & \cdots & \cdots & \cdots\\ \cdots & \cdots & \cdots & \cdots \end{vmatrix}=0,$$

where

$$y\equiv\frac{9}{4\pi}w,\quad w\equiv\frac{E_0^2R}{\sigma},\quad \Theta\equiv\frac{\rho R^3}{\sigma}S^2,$$

and a_n and b_n are defined by Eqs. (22).

In the zeroth approximation and neglecting the interaction of modes described by the nondiagonal terms of the

above determinant (dispersion relation), we obtain the frequencies of the capillary vibrations of the kth mode in the form

$$S^2=-\frac{2\sigma}{\rho R^3}k\left[k(k+1)-2-w\frac{9k[(2k+1)(2k^2-1)-4k]}{4\pi(4k^2-1)(2k+3)}\right]$$

$(k=2,4,6,\ldots)$.

The surface of the drop becomes unstable when the square of the frequency passes through zero $(S^2=0)$ and becomes positive. Thus, the critical conditions of instability of a hemispherical drop follow from the dispersion relation for $S^2=0$

$$\begin{vmatrix} 2-ya_2b_3 & -yb_3b_4 & 0 & \ldots \\ -ya_2a_3 & 9-y(a_3b_4+2a_4b_5) & -2yb_5b_6 & \ldots \\ 0 & -2ya_4a_5 & 20-y(2a_5b_6+3a_6b_7) & \ldots \\ \ldots & \ldots & \ldots & \ldots \\ \ldots & \ldots & \ldots & \ldots \end{vmatrix}=0. \tag{27}$$

Solving this equation by the method of successive approximations, one can obtain the critical conditions of excitation of the various modes of the capillary vibrations. Thus evaluation of a third-order determinant allows one to determine the critical conditions for the second, fourth, and sixth modes: $w_2\approx 7.79$, $w_4\approx 30.87$, $w_6\approx 57.75$. From these values it is clear that as the external field is increased $n=2$, the first mode to lose stability is the second one. This value of the parameter w defines the threshold of stability of the surface of a hemispherical drop, $w=7.79$. For comparison, note that a free drop with equal volume loses stability at $w=2.62$ (Ref. 11). For the critical value of the field strength of the external uniform electrostatic field in which a hemispherical drop becomes unstable, the above result implies an increase by a factor of roughly one-and-a-half in comparison with the critical value of the field for a free drop of equal volume.

In the zeroth approximation and neglecting the interaction of modes, it is not hard to obtain analytical expressions from Eqs. (26) for the critical dependence of the parameter w_k on the mode number in the form

$$w_k=\frac{4\pi[k(k+1)-2](4k^2-1)(2k+3)}{9[(2k+1)(2k^2-1)-4k]k}$$

$(k=2,4,6,\ldots)$.

CONCLUSION

By way of the above analysis we have shown that a drop of conducting liquid that has settled onto a conducting substrate is more stable in an external uniform electrostatic field than is a free drop of equal volume.

[1] É. M. Bazelyan, B. N. Gorin, and V. I. Levitov, *Physical and Engineering Fundamentals of Lightning Protection* [in Russian], Gidrometeoizdat (1978), 224 pp.
[2] A. I. Grigor'ev, I. D. Grigor'eva, and S. O. Shiryaeva, J. Sci. Expl. **5**, 163 (1991).
[3] I. D. Grigor'eva and S. O. Shiryaeva, Zh. Tekh. Fiz. **64**(9), 203 (1994) [Tech. Phys. **39**, 973 (1994)].
[4] O. A. Grigor'ev and S. O. Shiryaeva, Zh. Tekh. Fiz. **66**(2), 23 (1996) [Tech. Phys. **41**, 124 (1996)].
[5] E. Barreto, Aerosol Sci. **2**, 219 (1971).
[6] S. O. Shiryaeva and A. I. Grigor'ev, *Methods of Calculating Critical Conditions of Electrohydrodynamic Instabilities* [in Russian], Yaroslavl State Univ. Press, Yaroslavl (1996), 60 pp.
[7] S. O. Shiryaeva, A. I. Grigor'ev, and I. D. Grigor'eva, Zh. Tekh. Fiz. **65**(2), 1 (1995) [Tech. Phys. **40**, 117 (1995)].
[8] L. D. Landau and E. M. Lifshitz, *Fluid Mechanics*, 2nd ed. [Pergamon Press, Oxford, 1987; Mir, Moscow, 1986, 730 pp.].
[9] I. S. Gradshteyn and I. M. Ryzhik, *Tables of Integrals, Series, and Products* [Academic Press, New York, 1980; Nauka, Moscow, 1962, 1100 pp.].
[10] L. D. Landau and E. M. Lifshitz, *Electrodynamics of Continuous Media*, 2nd ed., edited by E. M. Lifshitz and L. P. Pitaevskii [Pergamon Press, Oxford, 1960; Nauka, Moscow, 1982, 620 pp.].
[11] G. Taylor, Proc. R. Soc. A **280**, 383 (1964).

Translated by Paul F. Schippnick

Instability of a charged interface of two immiscible viscous liquids with charge relaxation taken into account

D. F. Belonozhko, A. I. Grigor'ev, and S. O. Shiryaeva

Yaroslavl State University, 150000 Yaroslavl, Russia
(Submitted June 16, 1997)
Zh. Tekh. Fiz. **68**, 13–19 (September 1998)

On the basis of an analysis of a derived dispersion relation, it is demonstrated that there can be two different types of instability relative to the free charge of a charged, planar interface between two viscous immiscible liquids with finite electrical conductivity in a gravitational field. For large values of the surface charge density, depending on the viscosities and ratio of conductivities of the media, one can observe either an aperiodic (of the Tonks–Frenkel type) or oscillatory instability of the interface. Increasing the viscosity of the lower liquid leads to a substantial drop in the increments of the mentioned instability types and alters the critical conditions for manifestation of the oscillatory instability, whereas varying the viscosity of the upper surface has only a very weak effect on these characteristics. © *1998 American Institute of Physics.* [S1063-7842(98)00309-2]

The phenomenon of instability of the interface of two immiscible liquids, differing in their physical-chemical properties, has been investigated in various limiting situations more than a few times in connection with numerous physical, geophysical, and technical problems (see, for example, Refs. 1–4 and the literature cited therein). Nevertheless, many questions associated with this phenomenon have been only sparsely studied because of the cumbersomeness of the dispersion relations which obtain even in idealized models and admit an analytical analysis only in asymptotic situations. The present paper investigates the influence of the viscosities and electrical conductivities of two liquids in contact on the stability of a flat, charged interface between them and on the spectrum of the capillary motions that arise.

1. Let two immiscible, viscous, electrically conducting liquids fill all of space in the gravitational field. Let the unperturbed interface between them coincide with the XY plane of a Cartesian coordinate system whose z axis point up, in the direction opposite the force of gravity. We take the upper liquid with kinematic viscosity ν_1 and density ρ_1 filling the half-space $z>0$ to be conducting with conductivity σ_1 and dielectric constant ε_1. The lower liquid fills the half-space $z<0$ and has kinematic viscosity ν_2, density $\rho_2>\rho_1$, dielectric constant ε_2, and conductivity σ_2. We also assume that the unperturbed interface is uniformly charged with surface charge density $\varkappa$ and possesses surface tension with coefficient γ, and that the charge carriers on the interface have mobility b. We describe the electrostatic fields $\mathbf{E}_1$ and $\mathbf{E}_2$ in the upper and lower regions with the help of the electrostatic potentials Φ_1 and Φ_2, respectively. Armed with the above tools, we write the following linearized system of equations to help us identify the conditions under which the instability in the described system is manifested:

$$\frac{\partial \mathbf{U}_j}{\partial t} = -\frac{1}{\rho_j}\operatorname{grad} P_j + \nu_j \Delta \mathbf{U}_j + \mathbf{g}, \quad j=1,2, \tag{1}$$

$$\operatorname{div} \mathbf{U}_j = 0, \quad \Delta \Phi_j = 0, \quad \mathbf{E}_j = -\operatorname{grad} \Phi_j, \tag{2),(3}$$

$$z \to -\infty: \quad \mathbf{U}_1 = 0, \tag{4}$$

$$\mathbf{E}_1 = E_{10}\mathbf{n}_z, \tag{5}$$

$$z \to \infty: \quad \mathbf{U}_2 = 0, \tag{6}$$

$$\mathbf{E}_2 = E_{20}\mathbf{n}_z. \tag{7}$$

In these expressions $P_j = P_j(\mathbf{r},t)$ is the pressure and $\mathbf{U}_j = \mathbf{U}_j(\mathbf{r},t)$ is the velocity field inside the jth liquid; $\mathbf{g}$ is the acceleration due to gravity, and $\mathbf{n}_z$ is the z basis vector, and Δ denotes the Laplacian operator. On the interface of the two media, perturbed by capillary wave motion, described by the equation $z=\zeta(x,y,t)$, the following boundary conditions should be satisfied:

$$4\pi\varkappa = \varepsilon_1(\mathbf{n}_1,\mathbf{E}_1) + \varepsilon_2(\mathbf{n}_2,\mathbf{E}_2), \tag{8}$$

$$\frac{\partial \varkappa}{\partial t} + \operatorname{div}_s(\varkappa U_\tau + \varkappa b E_\tau) + \sigma_1(\mathbf{n}_1,\mathbf{E}_1) + \sigma_2(\mathbf{n}_2,\mathbf{E}_2) = 0, \tag{9}$$

$$\operatorname{div}_s \equiv \frac{\partial}{\partial x} + \frac{\partial}{\partial y}, \quad \Phi_1 = \Phi_2, \tag{10}$$

$$\mathbf{U}_1(\mathbf{r},t) = \mathbf{U}_2(\mathbf{r},t), \tag{11}$$

$$U_{jz} \approx \frac{\partial \zeta}{\partial t}, \quad j=1,2, \tag{12}$$

$$\frac{\nu_1}{\rho_1}[(\boldsymbol{\tau}_1(\mathbf{n}_1,\nabla),\mathbf{U}_1) + (\mathbf{n}_1(\boldsymbol{\tau}_1,\nabla),\mathbf{U}_1)] - \frac{\nu_2}{\rho_2}[(\boldsymbol{\tau}_2(\mathbf{n}_2,\nabla),\mathbf{U}_2) + (\mathbf{n}_2(\boldsymbol{\tau}_2,\nabla),\mathbf{U}_2)] = \Pi_\varkappa, \tag{13}$$

$$P_1 - P_2 + 2\nu\rho_2 \frac{\partial U_{2z}}{\partial z} - 2\nu\rho_1 \frac{\partial U_{1z}}{\partial z} = P_\varkappa + P_\gamma. \qquad (14)$$

In these relations

$$P_\gamma = -\gamma \frac{\partial^2 \zeta}{\partial x^2}$$

is the pressure of the surface tension forces under the perturbed liquid surface;[5]

$$P_\varkappa = P_{\varkappa 1} - P_{\varkappa 2},$$

$$P_{\varkappa j} = \frac{\varepsilon_j}{8\pi}[(\mathbf{n}_j, \mathbf{E}_j)^2 - (\boldsymbol{\tau}_j, \mathbf{E}_j)^2] \quad (j = 1,2) \qquad (15)$$

is the electrostatic pressure on it due to the presence of surface charge distributed with surface density $\varkappa$;[6]

$$\Pi_\varkappa = \Pi_{\varkappa 1} - \Pi_{\varkappa 2},$$

$$\Pi_{\varkappa j} = \frac{\varepsilon_j}{4\pi}(\mathbf{n}_j, \mathbf{E}_j)(\boldsymbol{\tau}_j, \mathbf{E}_j) \quad (j = 1,2) \qquad (16)$$

is the electrical part of the tangential components of the stress tensor; $\boldsymbol{\tau}_j$ and $\mathbf{n}_j$ are unit vectors tangent and normal to the surface of the jth liquid, respectively, and the notation $(\ldots, \ldots)$ is used for the scalar (dot) product.

2. We will solve problem (1)–(16) using the classical methods[5,6] of hydrodynamics, dividing the velocity field $\mathbf{U}_j = \mathbf{U}_j(\mathbf{r},t)$ into two components: a potential component [with velocity potential $\varphi_j(\mathbf{r},t)$] and a vortical component [describing the current function $\psi_j(\mathbf{r},t)$]

$$U_{xj} = \frac{\partial \varphi_j}{\partial x} - \frac{\partial \psi_j}{\partial z},$$

$$U_{zj} = \frac{\partial \varphi_j}{\partial z} + \frac{\partial \psi_j}{\partial x} \quad (j = 1,2). \qquad (17)$$

The pressures $P_1(\mathbf{r},t)$ and $P_2(\mathbf{r},t)$ in the upper and lower liquids can be written in the form

$$P_j = -\rho_j \frac{\partial \varphi_j}{\partial t} + \rho_j g \zeta \quad (j = 1,2). \qquad (18)$$

We seek the scalar functions φ_j and ψ_j in the form[5,6]

$$\varphi_1(x,z,t) = A_1 \exp(-kz)\exp(st - ikx),$$

$$\psi_1(x,z,t) = B_1 \exp(-q_1 z)\exp(st - ikx),$$

$$\varphi_2(x,z,t) = A_2 \exp(kz)\exp(st - ikx),$$

$$\psi_2(x,z,t) = B_2 \exp(q_2 z)\exp(st - ikx),$$

$$q_j^2 = k^2 + s/\nu_j. \qquad (19)$$

The electric field in the upper and lower medium is defined by the potentials

$$\Phi_1 = E_{01} z + D_1 \exp(-kz)\exp(st - ikz),$$

$$\Phi_2 = E_{02} z + D_2 \exp(kz)\exp(st - ikz), \qquad (20)$$

where s is the complex frequency, k is the wave number, and A_j, B_j, and D_j are constants.

Substituting expressions (17)–(20) into Eqs. (1)–(16) allows us to obtain a homogeneous system of six linear equations in the six unknown constants A_j, B_j, D_j. Setting the determinant of the matrix of coefficients of the unknown amplitudes A_j, B_j, and D_j equal to zero is a necessary and sufficient condition for the existence of a nontrivial solution of the problem. This condition gives the dispersion relation for the spectrum of capillary motions of the liquid in the analyzed system. In dimensionless variables, in which $g = \rho_2 = \gamma = 1$, and the characteristic scales of the dimensioned quantities have the form

$$s_* = \left(\frac{\rho_2 g^3}{\gamma}\right)^{1/4}, \quad k_* = \left(\frac{\rho_2 g}{\gamma}\right)^{1/2}, \quad \rho_* = \rho_2, \quad B_* = \sqrt{\rho_2},$$

$$\nu_{1*} = \left(\frac{\gamma^3}{\rho_2^3 g}\right)^{1/4}, \quad \nu_{2*} = \left(\frac{\gamma^3}{\rho_2^3 g}\right)^{1/4},$$

$$\beta_* = \left(\frac{\gamma}{\rho_2 g^3}\right)^{1/4}, \quad W_* = \sqrt{\rho g \gamma},$$

the dispersion relation can be written in the form

$$-\alpha^2(s^2 Z_1 Z_3 + sk\Theta d) - sk^3 H\Lambda + Z_1^2(s^4(\rho+1) \times Z_1 - 4s^2 k^3 \nu^2 (\rho-1)^2 d + 4s^3 k^2 \nu(\rho-1) \times Z_2 + 4\rho s^4 k) + Z_3(s^3 k^2 \Theta Z_1 + s^3 k\Theta(\rho+1)d + k^2(H + \Lambda s)(s^2 Z_2 - 2sk\Theta\nu(\rho-1)d) = 0,$$

where

$$Z_1 = \rho(\sqrt{k^2 + s/\nu_2} - k) + (\sqrt{k^2 + s/\nu_1} - k),$$

$$Z_2 = \rho(\sqrt{k^2 + s/\nu_2} - k) - (\sqrt{k^2 + s/\nu_1} - k),$$

$$Z_3 = 1 + s\beta + \beta kB\sqrt{\frac{\varepsilon}{1+\varepsilon} 4\pi W},$$

$$d = (\sqrt{k^2 + s/\nu_1} - k)(\sqrt{k^2 + s/\nu_1} - k),$$

$$\sigma = \frac{\sigma_1}{\sigma_2}, \quad \varepsilon = \frac{\varepsilon_1}{\varepsilon_2}, \quad \beta = \frac{\varepsilon_1 + \varepsilon_2}{4\pi(\sigma_1 + \sigma_2)},$$

$$B = \frac{b}{\sqrt{\varepsilon_1 + \varepsilon_2}}, \quad \rho = \rho_1/\rho_2, \quad W = \frac{\varepsilon_1 E_{10}^2}{4\pi},$$

$$\alpha^2 = Z_3(k(\rho-1) - k^3) + k^2 F, \quad F = F_1 + F_2,$$

$$F_1 = W(1-\sigma)\left(s\beta\frac{1-\sigma}{1+\varepsilon} + \frac{1+\varepsilon\sigma^2}{1+\sigma}\right),$$

$$F_2 = W\left(1 + \frac{\sigma}{\varepsilon}\right)\left(1 + \frac{\sigma^2}{\varepsilon}\right)\beta kB\sqrt{\frac{\varepsilon}{1+\varepsilon} 4\pi W},$$

$$H = W\left(1 + \frac{\sigma}{\varepsilon}\right)\left(s\beta\left[1 - \frac{1-\sigma}{1+\varepsilon}\right] + \frac{2\sigma}{1+\sigma}\right),$$

$$\Lambda = W\beta\left(1 + \frac{\sigma}{\varepsilon}\right)\left(1 - \frac{1-\sigma}{1+\varepsilon}\right),$$

$$\Theta = W(1 - \varepsilon\sigma)\beta\left(1 - \frac{1+\sigma}{1+\varepsilon}\right).$$

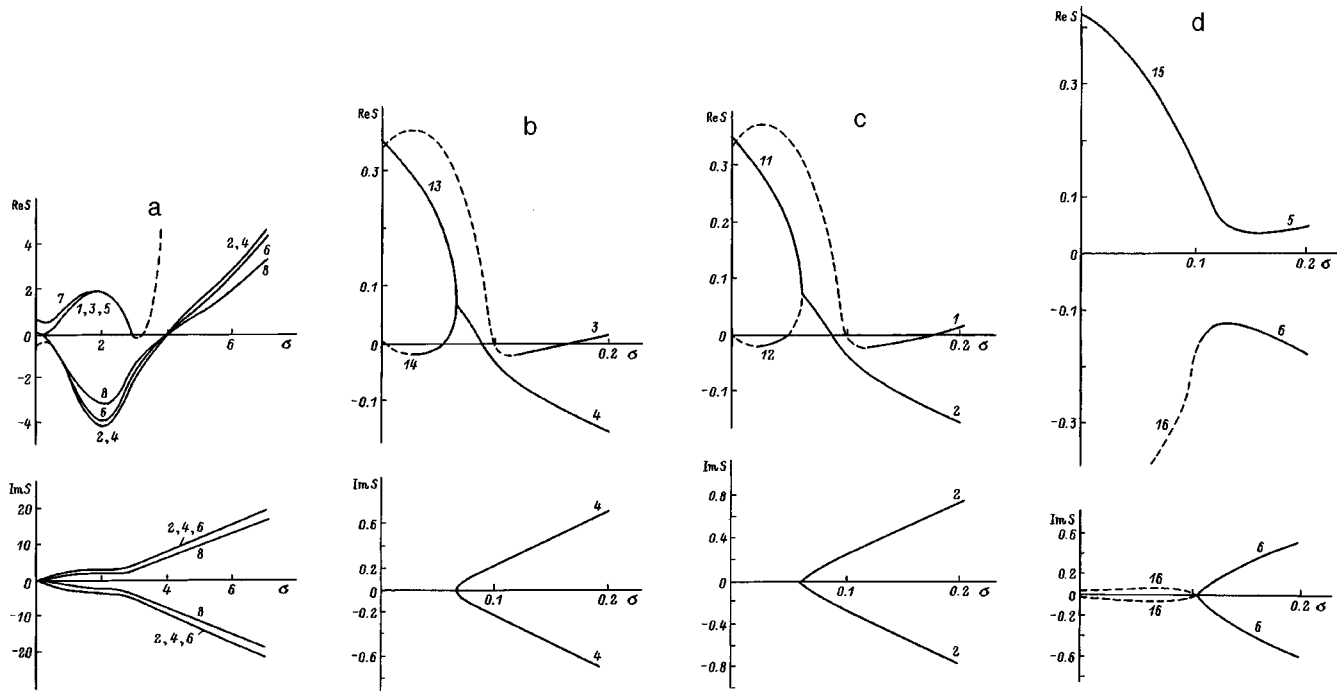

FIG. 1. The real Re $s(\sigma)$ and imaginary Im $s(\sigma)$ parts of the complex frequency, plotted as functions of the ratio of conductivities of the upper and lower liquid for $k=1$, $\nu_1=\nu_2=0.02$, $\varepsilon=10$, $\beta=0.01$, $W=2.15$, $b=0.01$ and the following values of ρ: *1, 2* — 0.001; *3, 4* — 0.01; *5, 6* — 0.1; *7, 8* — 0.5; a — coarser scale; b, c, d — left side of a plotted on a finer scale for $\rho=0.001$, 0.01, and 0.1, respectively. The branches with the even numbers for the branch *6–16* (the dashed curves are the branches lying on the lower sheet of the Riemann surface — the unobservable solution).

3. Figure 1 presents results of a numerical analysis of the dispersion relation (21) in the form of curves plotting the dimensionless complex frequency s as a function of σ, the ratio of conductivities of the upper and lower liquids ($\sigma\equiv\sigma_1/\sigma_2$) for different values of the parameter ρ, $k=1$, and $W=2.15>W_*$ (using the indicated scaling $W_*=k+1/k=2$ is the critical value of the parameter W for realization of the Tonks–Frenkel instability for $\sigma_1=0$, Refs. 7 and 8). On the scale shown in Fig. 1a some details important for an understanding of the physical essence of the problem are invisible and are replotted in Figs. 1b and 1c on a finer scale [the numbering of the branches in Fig. 1d was chosen with the configurations of Figs. 1b and 1c in mind]. It can be seen from the figures that in the larger part of the region of variation of the parameter σ ($0.5\lesssim\sigma<7$) the nature of the solutions depends only weakly on the ratio of densities of the two liquids ρ [branches *1, 3, 5* and *2, 4* merge on the scale of Fig. 1a]. In all of the cases under consideration the region $0.5<\sigma<3$ stands out. This is the region in which aperiodic instability is realized (the branches with odd numbers less than *10*). The increment of this instability reaches its maximum at $\sigma\simeq2$, and as σ increases to 3 the real part of branches *1, 3, 5, 7* passes through zero and becomes negative, describing aperiodically damped motion of the liquid. With further increase of σ these branches pass into the lower sheets of the four-sheet Riemann surface on which the dispersion relation (21) is defined.

Besides the aperiodic instability, wave motion is also observed associated with charge relaxation on the free surface of the liquid (the branches with even numbers). Branches *2, 4, 6, 8* for $0.5\lesssim\sigma\lesssim4$ correspond to waves whose damping decrement is maximum for $\sigma\simeq2$. For $\sigma>4$ the real part of the branches of the wave motions becomes positive, which implies the onset of exponential growth of the wave amplitudes. The frequencies of the unstable waves and their increments grow with increase of σ. The influence of the parameter ρ on the character of the solutions in the region $0.5\lesssim\sigma<\infty$ becomes noticeable only for $\rho\gtrsim0.1$ and reduces to a lowering of the decrements (for $0.5\lesssim\sigma<4$) and increments (for $\sigma>4$) of the wave motions. The physical meaning of the appearance of an oscillatory instability in a electrostatic field normal to the interface is connected with driving of thermal capillary waves by waves of electric charge redistributing itself over the interface (electric-field pressure waves). If, on the other hand, the density of the upper liquid is less than the density of the lower liquid (as is the case here), then the oscillatory instability of the interface is realized. In all probability, it is just this instability that was observed in the experiments of M. D. Gabovich *et al.*[9]. It is clear that the oscillatory instability of capillary waves on the interface of two viscous liquids should substantially depend on the viscosities of both liquids.

It follows from Figs. 1b–1d that for $\rho\leqslant0.01$ the branches of the oscillatory motions *2* and *4* begin at the branch point (at $\sigma\simeq0.05$) formed by the branch of the aperiodic instability identified at $\sigma=0$ with the Tonks–Frenkel instability [the odd branches with numbers greater than *10* in Figs. 1b–1d] and the charge-relaxation branch [the even branches with numbers greater than *10* in Figs. 1b–1d]. The charge-relaxation motion is aperiodically damped for $\rho\leqslant0.01$ [Figs. 1b and 1c] and can show up in the form of an aperiodic instability for $\rho=0.01$ [Fig. 1c]. Near $\sigma=0$ the

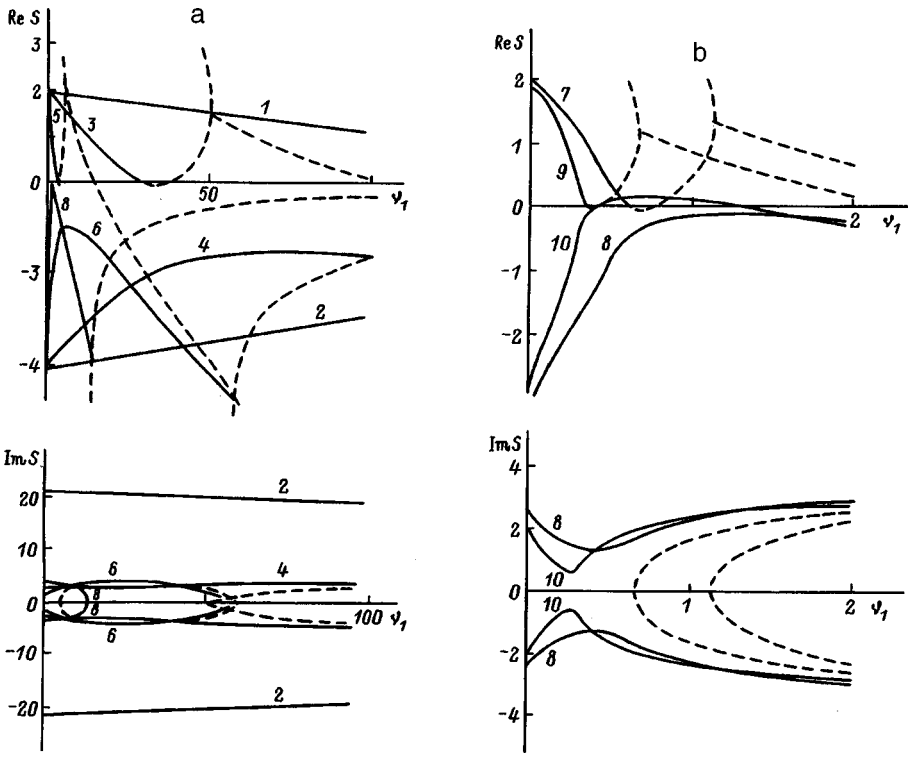

FIG. 2. Curves of the dependence of the same quantities as in Fig. 1 on the kinematic viscosity of the upper liquid for $\sigma=2$ and $\nu_2=0.02$; the values of the parameters $k,\varepsilon,\beta,W,b,\rho$ are the same as for Fig. 1 (*9, 10* — $\rho=0.9$).

corresponding branch passes into the lower sheets of the Riemann surface. In the real plane the branch point [the intersection point of branches *2, 11, 12* in Fig. 1b and points *4, 13, 14* in Fig. 1c] is positive and the apparent branch of oscillatory motion should define the onset of the oscillatory instability with increment much less than the increment of the Tonks–Frenkel instability. This increment decreases rapidly with increase of σ and already for $\sigma<0.01$ the curves turn out to be branches *2* and *4* of the damped oscillatory motion seen in Fig. 1a. According to Fig. 1a, as $\rho\to1$ ($\rho<1$) the decrements of the oscillatory motion decrease and the increments of the oscillatory instability (this is noticeable only for $\rho\simeq0.9$ on the scale of Fig. 1).

We analyzed the effect of the viscosities of the upper and lower liquids on the development of the observed forms of instability separately. The most interesting results of our numerical analysis of Eq. (17) are presented in the form of the dependence of the complex frequency s on the kinematic viscosity of the upper liquid ν_1 [Figs. 2a and 2b] and the lower liquid ν_2 [Figs. 3a and 3b] for different values of ρ. The results presented in Fig. 2a have a model character and show that for $\rho\ll1$ the increments of the aperiodic instability (the odd branches in the figures) noticeably decrease, but vanish only at an anomalously high value of $\nu_{1*}\gg1$ (the kinematic viscosity of the upper liquid). For $\nu_1>\nu_{1*}$ these branches describe aperiodically damped motion and pass into the lower sheets of the Riemann surface. With increase of ν_2 the increments decrease much faster and depend much more weakly on ρ [branches *1, 3, 5, 7* in Figs. 3a and 3b merge on the scale of this figure in the region of the aperiodic instability]. The minimum value of ν_2, above which the aperiodic instability does not exist, is less than unity in all the situations considered and the phenomenon can be identified with a real physical situation.

An asymmetry of variation of the investigated dependences with variation of ν_1 is observed *vis-à-vis* the dependences on ν_2. First of all, the effects associated with the variation of ν_1 are much weaker than those associated with variation of ν_2 and depend on the parameter ρ in the instability regions. Second, with increase of ν_1 to values $\nu_1>\nu_{1*}$ the branches of the aperiodic instability pass into the lower sheets of the Riemann surface [the odd branches in Figs. 2a and 2b] whereas continuation of the branches of the aperiodic motion into the region $\nu_2>\nu_{2*}$ (ν_{2*} is defined in analogy with ν_{1*}) leads to the appearance of periodically damped motion with a damping decrement noticeably increasing with growth of ρ [the odd branches in Fig. 3a].

The indicated asymmetry manifests itself in the most interesting way *vis-à-vis* oscillatory motion. The damping decrements pass through a minimum: up to the disappearance of the aperiodic instability with growth of ν_2 [the branches with even numbers in the region $\nu_2<\nu_{2*}$ in Figs. 2a and 2b] and after its disappearance with growth of ν_1 [the branches with even numbers for $\nu_1<\nu_{1*}$ in Figs. 3a and 3b]. The minimum decrement decreases with growth of ρ. For the dependences of the dimensionless complex frequency on ν_1 an increase of ρ to 0.9 [branch *10* in Fig. 2b] leads to the result that the extremum of the real part of the branch of the oscillatory motion turns out to be positive, i.e., it characterizes an increment of the oscillatory instability. Further increase of ν_1 stabilizes the motion of the liquid, and branch *10* for $\nu_1>1.5$ corresponds to periodically damped motion. Such an effect is not observed in the dependences on ν_2. The above analysis showns that the oscillatory instability and the

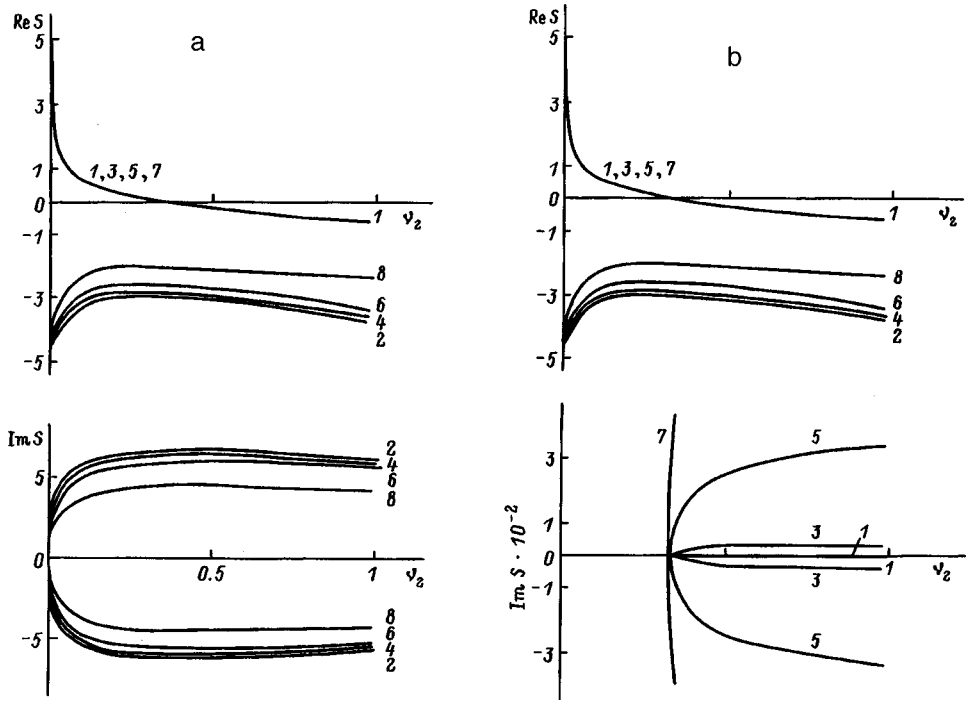

FIG. 3. Same as Fig. 2 for the lower liquid: $\sigma=2$, $\nu_1=0.02$; the values of the remaining parameters are the same as in Fig. 2.

aperiodic instability are mutually exclusive since they cannot exist simultanously. This explains why the oscillatory instability is not seen in Figs. 2a and 2b).

We also performed a numerical analysis of the behavior of the branches of the oscillatory instability as a function of the behavior of the kinematic viscosity of the media for $\sigma=7$ and 0.08 and for values of ρ for which the given instability exists. We found that, as in the above analysis, only when the viscosity of the upper liquid ν_1 is increased to anomalously high values do the increments of the oscillatory instability decrease noticeably and even disappear, and this effect is that much stronger, the larger is ρ. The phenomena associated with variation of ν_2 are analogous but more noticeable (the oscillatory motion becomes aperiodically damped already at a value of $\nu_2=\nu_{2*}$, where $0<\nu_{2*}\lesssim 1$, and further growth of ν_2 is accompanied by an increase in the increment of this motion) and depends weakly on ρ.

CONCLUSION

On a flat interface of two viscous incompressible immiscible conducting liquids (when the density of the upper liquid is much less than that of thge lower one) located in an electrostatic field perpendicular to the interface, instabilities of both aperiodic and oscillatory type can be realized. The oscillatory instability takes place when the external electrostatic field exceeds a critical value for appearance of an aperiodic instability of Tonks–Frenkel type. Which type of instability will occur in a given case (aperiodic or oscillatory) is governed by the ratio of conductivities of the upper and lower liquids, and for its value close to unity $\rho\lesssim 1$, by the kinematic viscosity of the upper liquid. The increments of the instabilities of either kind and the critical conditions for the appearance of an oscillatory instability fall much faster with increase of the kinematic viscosity of the lower medium than with growth of the kinematic viscosity of the upper medium.

[1] O. A. Grigor'ev and S. O. Shiryaeva, Zh. Tekh. Fiz. **66**(2), 23 (1996) [Tech. Phys. **41**, 124 (1996)].
[2] O. A. Grigor'ev and S. O. Shiryaeva, Izv. Ross. Akad. Nauk Mekh. Zhidk. Gaza, No. 1, 98 (1996).
[3] S. O. Shiryaeva, O. A. Grigor'ev, and A. I. Grigor'ev, Zh. Tekh. Fiz. **66**(9), 74 (1996) [Tech. Phys. **41**, 869 (1996)].
[4] D. F. Belonozhko, A. I. Grigor'ev, and S. O. Shiryaeva, Pis'ma Zh. Tekh. Fiz. **23**(6), 74 (1996) [Tech. Phys. Lett. **23**(3), 242 (1996)].
[5] V. G. Levin, in *Physical-Chemical Hydrodynamics* [in Russian], Fizmatgiz, Moscow (1959), 699 pp.
[6] J. R. Melcher and W. J. Schwarz, Phys. Fluids **11**, 2604 (1968).
[7] L. Tonks, Phys. Rev. **48**, 562 (1935).
[8] Ya. I. Frenkel', Zh. Eksp. Teor. Fiz. **6**, 348 (1936).
[9] M. D. Gabovich and V. Ya. Poritskiĭ, JETP Lett. **33**, 304 (1981).

Translated by Paul F. Schippnick

Generation of currents in gases by fast, highly charged ions

A. B. Voĭtkiv and B. G. Krakov

U. A. Arifov Institute of Electronics, Academy of Sciences of Uzbekistan, 700143 Tashkent, Uzbekistan
(Submitted April 23, 1997)
Zh. Tekh. Fiz. **68**, 20–23 (September 1998)

It is shown that an exit asymmetry of the electrons and recoil ions formed during ionization of atoms in elementary collision events with fast, highly charged ions can give rise to macroscopic electron and recoil ion currents during the bombardment of a gaseous target by a beam of fast, highly charged ions. © *1998 American Institute of Physics.*
[S1063-7842(98)00409-7]

It is well known[1] that the differential cross section for photoionization of an atom is not symmetric with respect to the substitution $\vartheta \to \pi - \vartheta$, where ϑ is the exit angle of the photoelectron relative to the direction of the momentum of the incident photon. This asymmetry in the exit angle of the photoelectron is a consequence of the fact that the photon has momentum. Although this asymmetry is very small for small photon energies ($h\nu < 1$ a.u.), it can, nevertheless, lead to macroscopic effects such as an electron drag current during electromagnetic irradiation of semiconductors[2] and gases.[3]

In recent years considerable attention has been devoted to studies of the ionization of atoms during collisions with fast, highly charged ions (see, e.g., Refs. 4–10 and the literature cited therein). A substantial asymmetry of the exiting electrons has been observed during ionization of atoms: a large fraction of these electrons have a positive projection of their velocity in the direction of motion of the fast, highly charged ion, and this effect occurs during single, as well as double, triple, or higher ionization of atoms. It has also been found[4,6–9] that the recoil ions formed during ionization of atoms in collisions with fast, highly charged ions have predominantly negative projections of their velocity along the direction of motion of the highly charged ions.

In this paper we shall show that the asymmetry, i.e., the predominant directions of the velocities of the electrons and recoil ions, observed in an elementary act of ionization of an atom in the course of a collision with a fast, highly charged ion can lead to the generation of macroscopic electron and recoil ion currents during bombardment of a gaseous target by a beam of fast, highly charged ions.

Consider a gas, initially consisting of neutral atoms with a density n_a, which is bombarded by a beam of fast particles with density n_i and velocity v ($v \gg v_0 = 2 \times 10^8$ cm/s). Let $d^2\sigma_e/(d\varepsilon d\Omega)$ be the differential cross section for the ''formation'' of a free electron with energy[1)] ε and a definite direction of escape from the atom in the collision of an incident particle with a target atom. Then,

$$\Delta n_e = n_i n_a v \frac{d^2\sigma_e}{d\varepsilon d\Omega} \Delta\varepsilon \Delta\Omega \tag{1}$$

is the number of electrons ''produced'' within a unit volume of the target per unit time in collisions with a beam of fast bombarding ions and which have energies lying within a narrow interval from ε to $\varepsilon + \Delta\varepsilon$ and escape directions within a small element of solid angle $\Delta\Omega$. Let $\tau_e(\varepsilon)$ be the average momentum relaxation time of electrons with energy ε. Then, we can write

$$\frac{d}{dt}\Delta N_e = -\frac{\Delta N_e}{\tau_e(\varepsilon)} + n_i n_a v \frac{d^2\sigma_e}{d\varepsilon d\Omega} \Delta\varepsilon \Delta\Omega, \tag{2}$$

where ΔN_e is the concentration of free electrons participating in the current that have energies within the interval from ε to $\varepsilon + \Delta\varepsilon$ and velocities directed within $\Delta\Omega$.

Assuming that the fast particle beam was injected into the target at time $t = 0$, we obtain

$$\frac{d^2 N_e}{d\varepsilon d\Omega} = n_i n_a v \tau_e \frac{d^2\sigma_e}{d\varepsilon d\Omega} (1 - \exp(-t/\tau_e(\varepsilon))). \tag{3}$$

The electron current density is given by

$$j_{el} = -|e| \int d\Omega \int d\varepsilon v_e \cos\vartheta \frac{d^2 N_e}{d\varepsilon d\Omega}, \tag{4}$$

where e is the electronic charge, $v_e = (2\varepsilon/m_e)^{1/2}$ and m_e are the electron velocity and mass, and ϑ ($0 \leqslant \vartheta \leqslant \pi$) is the exit angle of the electron relative to the direction of the velocity of the fast, highly charged ion.

For purposes of an estimate, we shall assume that, on the average, the first collision of an electron with an atom already eliminates the electron from the current.[3,11] Assuming that the gaseous target is dense enough that the mean free path of the electrons and, accordingly, the time $\tau_e(\varepsilon)$ is determined by collisions with target atoms rather than with the vessel walls (at the ordinary densities of highly charged ions in a beam, the concentration of the resulting recoil ions is much lower than the neutral gas atom concentration, so collisions of the electrons with recoil ions can be neglected), we have $\tau_e(\varepsilon) = (n_a v_e \sigma_{ea})^{-1}$, where $\sigma_{ea}(\varepsilon)$ is the total cross section for interaction of an electron of energy ε with an atom.

In the steady state ($t \gg \tau_e$), we find

$$j_{el} = -A_{el}|e| n_i v, \tag{5}$$

where

$$A_{el}=2\pi\int_0^{\infty}\frac{d\varepsilon}{\sigma_{ea}(\varepsilon)}\int_0^{\pi}d\vartheta\sin\vartheta\cos\vartheta\frac{d^2\sigma_e}{d\varepsilon d\Omega}. \qquad (6)$$

The number of free electrons produced by a beam of fast, highly charged ions in a gas is proportional to the density of gas atoms, and their ''lifetime'' in the current is inversely proportional to this density. Thus the final expression (5) for the electron current density is independent of the density of atoms. The cross sections for ionization of atoms in collisions with fast, highly charged ions fall off quite rapidly with the degree of ionization.[8,9] Therefore, for estimating the electron current we can set in Eq. (6)

$$\frac{d^2\sigma_e}{d\varepsilon d\Omega}\simeq\frac{d^2\sigma_e^{(1+)}}{d\varepsilon d\Omega},$$

where the doubly differential cross section for single ionization of an atom stands on the right.

The most detailed studies, so far, have been made of collisions of fast, highly charged ions with helium atoms, and values of the doubly differential cross section for single ionization of helium at several values of the parameters (charge, velocity) of the fast, highly charged ions have been tabulated.[5,12–14] As an example, we shall estimate the electron current density produced by bombarding a gas of helium atoms with beams of Mo^{40+} (25 MeV/amu) and Ne^{10+} ions (5 MeV/amu). In order to obtain values for the total interaction cross section $\sigma_{ae}(\varepsilon)$ of the electrons with helium atoms (mainly determined by elastic collisions and ionization), we have used published[11,15–17] data on the elastic collision and ionization cross sections. A numerical calculation yields $A_{el}\simeq 2.1$ and 1 for bombardment with Mo^{40+} (25 MeV/amu) and Ne^{10+} ions (5 MeV/amu), respectively. For ion densities in the beam $n_i\simeq 1-100\,\mathrm{cm}^{-3}$ and velocities $v_{\mathrm{Mo}}\simeq 7\times10^9$ cm/s and $v_{\mathrm{Ne}}\simeq 3\times10^9$ cm/s (corresponding to the indicated collision energies), we have $j_{el}^{\mathrm{He}}\simeq 2\times10^{-9}-10^{-7}$ and $0.4\times10^{-9}-10^{-7}$ A/cm^2, respectively, for bombardment by beams of Mo^{40+} (25 MeV/amu) and Ne^{10+} (5 MeV/amu).

It has been shown[4,6–9] that the (total) momentum of the electrons which escape during ionization of an atom and the momentum of the resulting recoil ions have projections on the direction of the velocity of the fast, highly charged ions which are roughly equal in magnitude and opposite in sign. Therefore, during bombardment of a gas target by a beam of fast, highly charged ions, besides an electron current there should also be a recoil ion current j_i. At first glance it appears that, because of the very large mass difference between the electrons and atoms, the recoil ion current should be negligible compared to the electron current. We note, however, that Eq. (5) for the electron current density does not contain the carrier masses. Thus, we might expect that this large mass difference does not have a critical effect on the magnitude of the ion current.

As opposed to the situation with the electron current, in finding the recoil ion current it is necessary, in general, to take the initial thermal motion of the gas atoms into account, and for the total velocity $\mathbf{u}$ of the recoil ions we have $\mathbf{u}=\mathbf{u}_T+\mathbf{u}_R$, where $\mathbf{u}_T$ is the thermal velocity of the atoms and $\mathbf{u}_R$ is the additional velocity of the recoil ions acquired during ionization of an atom in a collision with a fast, highly charged ion. An analysis of published data[4,7,8] shows that the average energies of singly charged helium recoil ions formed in collisions with fast, highly charged ions are of the order of a few thousandths of an electron volt, and that the energy of singly charged argon recoil ions formed in such collisions[8] are of a similar order of magnitude. (We note that the energy of the recoil ions depends quite weakly on the charge and velocity of the highly charged ions,[18] so that the recoil energy will be of this order over a rather wide range of variation in the charges and velocities of the fast, highly charged ions.) For sufficiently low (of the order of 10 K or below) gas target temperatures, the total energy and velocity of even singly charged recoil ions will be determined mainly by the energy E_R and velocity $\mathbf{u}_R$ which they acquire during the ionization of an atom. In this case let us estimate the contribution $j_i^{(1)}$ to the ion current from those singly charged recoil ions which are formed directly in collisions with fast, highly charged ions. The quantity $j_i^{(1)}$ can serve as an estimated lower bound on the total recoil ion current. Repeating the calculations done above to find the electron current, for $j_i^{(1)}$ we can obtain

$$j_i^{(1)}=A_{\mathrm{ion}}|e|n_i v, \qquad (7)$$

where

$$A_{\mathrm{ion}}=2\pi\int_0^{\infty}\frac{dE_R}{\sigma_{ia}^{(1)}(E_R)}\int_0^{\pi}d\vartheta_i\sin\vartheta_i\cos\vartheta_i\frac{d^2\sigma_1}{dE_R d\Omega_i}, \qquad (8)$$

$(d^2\sigma_1)/(dE_R d\Omega_i)$ is the doubly differential cross section for formation of singly charged recoil ions, ϑ_i is the escape angle of the ion relative to the direction of motion of the fast, highly charged ion, and $\sigma_{ia}^{(1)}(E_R)$ is the total cross section for collisions of an ion with atoms leading to its loss from the current.

As Eqs. (7) and (8) imply, the expression for the ion current density at low target temperatures does not contain the masses of the recoil ions explicitly, and so the difference in the magnitudes of the electron and ion currents in this case is attributable only to the differences in the corresponding cross sections. For this reason, the electrons, which move at very much higher velocities, undergo collisions more often and, therefore, are more rapidly removed from the current. Thus, the predominance of the electrons in the velocities can be compensated (partially) by very much higher steady-state densities of the ion current carriers.

We now estimate $j_i^{(1)}$ for bombardment of a helium target. As far as we know, no direct data on $(d^2\sigma_1)/(dE_R d\Omega_i)$ have been published. However, it has been shown[7] that for single ionization of helium by fast, highly charged ions, the approximation $\mathbf{P}_e\simeq-\mathbf{P}_R$ holds (see also Ref. 10), where $\mathbf{P}_e$ and $\mathbf{P}_R$ are the momenta of the escaping electron and recoil ion, respectively. Therefore, as an estimate, we can assume

$$\frac{d^2\sigma_1}{dE_R d\Omega_i}\simeq\frac{M_a}{m_e}\frac{d^2\sigma_e^{(1+)}}{d\varepsilon d\Omega}$$

for comparing these cross sections in the corresponding ranges of the energies E_R and ε ($E_R\simeq(m_e/M_a)\varepsilon$, where M_a

is the mass of the atom) and angles $\vartheta_i \simeq \pi - \vartheta$. At low collision energies, singly charged recoil ions moving in a gas of their own species of atoms will be removed from the current mainly through resonant charge exchange.[11,14] Thus, as an estimate we shall assume that

$$\sigma_{ia}^{(1)}(E_R) \simeq \sigma_{ex}(E_R),$$

where the resonance charge exchange cross section stands on the right.

Using published data for the cross section $\sigma_{ex}(E_R)$ for charge exchange of singly ionized helium ions on helium atoms,[11,15,19] we find the ion current density induced in a helium target by a beam of Mo^{40+} ions (25 MeV/amu) to be

$$j_i^{(1)} = -0.05|e|n_i v \simeq 0.025 j_{el}^{\mathrm{He}}.$$

Let us consider the opposite limit, in which the magnitude of the total energy and velocity of singly charged recoil ions are essentially determined just by their thermal motion with $u_T \gg u_R$. In this case we get for the contribution $j_i^{(1)}$ to the current from the recoil ions

$$j_i^{(1)} = |e|n_i v \sigma_{\mathrm{ion}}^{(1)} \langle u_R \rangle \int du_T \frac{F(u_T)}{\sqrt{2} u_T \sigma_{ia}^{(1)}(u_T)}, \tag{9}$$

where

$$\langle u_R \rangle = \left(\int \frac{2\pi}{\sigma_{\mathrm{ion}}^{(1)}} \int dE_R u_R \int_0^{\pi} d\vartheta_i \sin\vartheta_i \cos\vartheta_i \frac{d^2\sigma_1}{dE_R d\Omega_i} \right) \tag{10}$$

is the drift velocity of the singly charged recoil ions, $\sigma_{\mathrm{ion}}^{(1)}$ is the (total) cross section for single ionization of an atom in collisions with fast, highly charged ions, and $F(u_T)$ is the Maxwellian velocity distribution function of the gas atoms.

Given that the cross section $\sigma_{ia}^{(1)}$ changes very slowly with the collision velocity for $kT > 10^{-2}$ eV (where k is Boltzmann's constant and T is the absolute temperature), we can write

$$j_i^{(1)} = A_{\mathrm{ion}}^T |e| n_i v, \tag{11}$$

$$A_{\mathrm{ion}}^T = \frac{\sigma_{\mathrm{ion}}^{(1)}}{\sqrt{2}\sigma_{ia}^{(1)}(u_T^0)} \langle u_R \rangle \langle u_T^{-1} \rangle, \tag{12}$$

where $\langle u_T^{-1} \rangle = (2M_a/kT)^{1/2}$ is the average value of the reciprocal of the thermal speed of the atoms and $u_T^0 \simeq (kT/M_a)^{1/2}$.

Equations (9)–(12) imply that at temperatures such that $kT \gg P_R^2/2M_a$ we have $j_i^{(1)} \propto A_{\mathrm{ion}}^T \propto T^{-1/2}$.

Using data from Ref. 8, we shall estimate the magnitude of $j_i^{(1)}$ for bombardment of a gas of helium atoms at $T = 300$ K by a beam of Xe^{44+} ions (6.7 MeV/amu). These data imply that $\langle u_R \rangle \simeq -2 \times 10^4$ cm/s and $\sigma_{\mathrm{ion}}^{(i)} \simeq 5 \times 10^{-15}$ cm^2. (A calculation using the formula obtained in Ref. 19 yields a similar value for this cross section.) In addition, for $T = 300$ K, we have $\langle u_T^{-1} \rangle \simeq 10^{-5}$ s/cm, $\sigma_{ia}^{(i)} \simeq 10^{-14}$ cm^2, and, therefore, $j_i^{(1)} \simeq -0.1|e|n_i v$. Although A_{ion}^T should decrease with rising temperature according to Eq. (12), its value for bombardment with a beam of Xe^{44+} (6.7 MeV/amu) at $T = 300$ K turned out to be somewhat higher than the above estimate of A_{ion} for bombardment with a beam of Mo^{44+} (25 MeV/amu) at $T < 10$ K. This is related to three factors: first, because of the smaller (almost a factor of two for roughly equal charges) collision velocity of the highly charged ions with the atoms, the cross section for ionization during bombardment with Xe^{44+} (6.7 MeV/amu) is considerably higher than for collisions with Mo^{40+} (25 MeV/amu); second, for the same reason the asymmetry in the directions of the momenta of the recoil ions is greater;[10] and, third, as the velocity of the atoms increases, the cross section $\sigma_{ia}^{(1)}$ decreases, and, while for collision energies $E > 10^{-2}$ eV this cross section depends very weakly on the collision rate, when $E < 10^{-3}$ eV this cross section increases quite rapidly ($\sigma_{ia}^{(1)} \propto E^{-1/2} \propto u^{-1}$) with decreasing velocity.[19,20]

In conclusion, we note that these estimates of the current densities are such as to permit fully an experimental observation of this effect, and the ion component of the current forms a significant fraction of the total current and would itself be experimentally observable.

[1)] We assume that the energy with which an electron leaves an atom is much greater than the average thermal energy of the atoms. Since the typical energies are $\varepsilon \sim 5$–10 eV, even for single ionization, this condition is satisfied for any gas temperature at which it is still possible to assume that the gas initially consists of neutral atoms.

[1] A. Sommerfeld, *Atomic Structure and Spectral Lines* [Methuen, London, 1934; GITTL, Moscow, 1956].
[2] A. A. Grinberg and L. L. Makovskiĭ, Fiz. Tekh. Poluprovodn. **4**, 1162 (1970) [Sov. Phys. Semicond. **4**, 822 (1970)].
[3] M. Ya. Amus'ya, A. S. Baltenkov, A. A. Grinberg, and G. S. Shapiro, Zh. Éksp. Teor. Fiz. **68**, 28 (1975) [Sov. Phys. JETP **41**, 14 (1975)].
[4] R. Moshammer, J. Ullrich, M. Unverzagt *et al.*, Phys. Rev. Lett. **73**, 3371 (1994).
[5] N. Stolterfoht, H. Platten, G. Schiwietz *et al.*, Phys. Rev. A **52**, 3796 (1995).
[6] R. Moshammer, M. Unverzagt, W. Schmitt *et al.*, Nucl. Instrum. Methods Phys. Res. B **108**, 425 (1996).
[7] R. Moshammer, J. Ullrich, M. Unverzagt *et al.*, Nucl. Instrum. Methods Phys. Res. B **107**, 62 (1996).
[8] P. Jardin, A. Cassimi, J. P. Grandin *et al.*, Nucl. Instrum. Methods Phys. Res. B **107**, 41 (1996).
[9] M. Unverzagt, R. Moshammer, W. Schmitt *et al.*, Phys. Rev. Lett. **76**, 1043 (1996).
[10] A. B. Voitkiv, J. Phys. B **29**, 5433 (1996).
[11] D. R. Bates, *Atomic and Molecular Processes* [Academic Press, New York, 1962; Mir, Moscow (1964), 777 pp.].
[12] N. Stolterfoht, D. Schneider, J. Tanis *et al.*, Europhys. Lett. **4**(8), 899 (1987).
[13] N. Stolterfoht, D. Schneider, J. Tanis *et al.*, ''Tabulated double differential cross sections for electron emission in 25-Mev/u Mo^{40+} + He collisions,'' Hahn-Meitner Institute, Berlin (1995).
[14] N. Stolterfoht, D. Schneider, J. Tanis *et al.*, ''Tabulated double differential cross sections for electron emission in 5-Mev/u C^{6+}, O^{8+}, Ne^{10+} + He collisions,'' Hahn-Meitner Institute, Berlin (1995).
[15] N. Mott and H. Massey, *The Theory of Atomic Collisions*, 3rd ed. [Clarendon Press, Oxford (1965); Mir, Moscow (1969), 765 pp.].
[16] G. F. Drukarev, *Collisions of Electrons with Atoms and Molecules* [Plenum Press, New York (1987); Nauka, Moscow (1978), 256 pp.].
[17] M. B. Shan, D. S. Elliot, P. McCallion, and H. B. Gilbody, J. Phys. B **21**, 2751 (1988).
[18] C. L. Cocke and R. E. Olson, Phys. Rep. **205**, 153 (1991).
[19] B. M. Smirnov, *Atomic Collisions and Elementary Processes in Plasmas* [in Russian], Atomizdat, Moscow (1968), 363 pp.
[20] A. B. Voĭtkiv and A. V. Koval', Izv. Vyssh. Uchebn. Zaved. Fiz. **38**(2), 23 (1995).

Translated by D. H. McNeill

Effect of residual gas on the ion charge distribution in vacuum arc discharge plasmas

A. G. Nikolaev, E. M. Oks, and G. Yu. Yushkov

Tomsk State University for Control Systems and Radio Electronic, 634050 Tomsk, Russia
(Submitted June 24, 1997)
Zh. Tekh. Fiz. **68**, 24–28 (September 1998)

A magnetic mass analyzer and time-of-flight mass spectrometer are used to study the effect of the pressure and type of residual gas on the ion charge distribution in the plasma of an arc discharge with a cathode spot. The possibility of ionizing a substantial fraction of the gas atoms in this type of discharge is pointed out. © *1998 American Institute of Physics.* [S1063-7842(98)00509-1]

Vacuum arc discharges with a cathode spot that provides the plasma forming medium for a self-sustained discharge by evaporating the cathode material have been the object of intense basic and applied research for many years.[1–6] Information on the charge distribution of the ions generated in a vacuum arc discharge plasma and on the factors affecting this distribution is important, both for understanding the plasma formation and current carrying processes in this type of discharge and for attaining the optimum parameters of the vacuum arc in switches, ion sources, ion-plasma sputterers, and other devices based on these discharges. In a vacuum arc discharge the average charge of metal ions is, to a great extent, determined by the cathode material and can vary between 1 and 3 on going from light materials to heavier materials.[7] The fraction of highly charged ions also increases in a strong magnetic field,[8,9] when the arc current is increased,[10] or the duration of the arc burn is shortened.[11]

Although it has been reliably established experimentally that the ionization processes in a vacuum arc discharge take place within a quite localized region immediately adjacent to the cathode spot, where the density of atoms of the evaporated cathode material is much greater than the residual gas density, a small change in the density of this gas does have a major effect on the charge distribution of the metal ions.[12–16]

In this paper we present the results of some measurements of the charge distribution of the ions in a vacuum arc discharge plasma for different pressures of gas injected into the discharge gap.

EXPERIMENTAL TECHNIQUE

Studies of the ion charge distribution were made on test stands at GSI (Gesellschaft für Schwerionenforschung mbH, Darmstadt, Germany) and LBNL (Lawrence Berkeley National Laboratory, Berkeley, USA) in the framework of joint research projects with these scientific organizations. Vacuum arc discharges were ignited in the electrode system of the high-current, wide-aperture ion beam sources MEVVA-4 (GSI)[17] and MEVVA-5 (LBNL).[18] Identical in their operating principles, these devices differ only slightly in design.

A sketch of the MEVVA-5 source is shown in Fig. 1. A vacuum arc discharge (100–500 A, 250 μs, 1–5 pulses/s) was ignited between one of 18 cathodes, mounted in a ''revolver'' arrangement, and a hollow anode, one part of which was the inner surface of a solenoid which created a pulsed magnetic field of up to 10 kGs in the cathode region of the discharge. The vacuum arc was initiated in the traditional way, based on using an auxiliary discharge plasma along the surface of a ceramic,[19] but in a number of the experiments the initial plasma required to excite the cathode spot was created by a version of a gas discharge in crossed $E \times H$ fields.[20] The pumping systems of the test stands ensured a base pressure of below 10^{-6} Torr. The working gas (H_2, He, Ne, N_2, O_2, Ar, Xe) was injected directly into the cathode region of the discharge. It was also possible to inject gas into the beam transport region, avoiding the discharge chamber. The pressure control system made it possible to vary the pressure smoothly from the base pressure to 10^{-3} Torr. Here the pressure was measured in the beam transport region immediately behind the ion accelerator gap. Because of a pressure drop as gas flows through the aperture in the anode and the grid of the accelerating system, the actual gas pressure, as shown by estimates and indicated by the experiments, was higher than the measured value by roughly an order of magnitude for 10^{-6}–10^{-5} Torr and by a factor of 3–5 for pressures in the 10^{-4} Torr range.

The ion charge distribution was measured with the aid of a magnetic mass charge separator (GSI)[21] and a time-of-flight spectrometer (LBNL).[22] In both cases, the ions extracted from the plasma were accelerated by a voltage of 30–60 kV using a three-electrode multiaperture extraction system.[23] In order to eliminate the effect of the arc pulse duration, all measurements of the ion charge distribution were made 100 μs after discharge ignition.

EXPERIMENTAL RESULTS

Although changing the working gas species led to a number of distinctive effects for each gas, for all the gases used in the experiment a rise in the gas pressure caused a drop in the total ion current extracted from the plasma and a reduction in the fraction of multiply charged ions and led to the appearance of gas ions in the mass–charge spectrum of the ion beam.

Figures 2 and 3 show plots of the pressure dependences of the total ion current and of the charge components of this

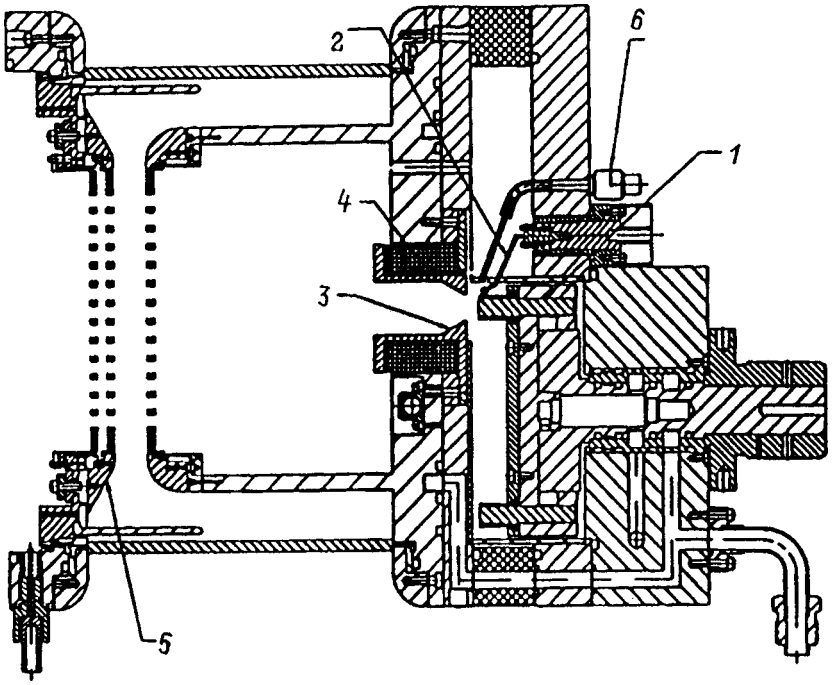

FIG. 1. The MEVVA-5 ion source with a gas feed system: *1* — cathode, *2* — trigger electrode, *3* — anode, *4* — accelerator system, *5* — magnetic field winding, *6* — gas inlet.

current separated by the magnetic mass separator corresponding to the cases of hydrogen feed into a system with a molybdenum cathode and argon feed into a system with a steel cathode. It is noteworthy that a redistribution of the currents in the different charge states occurs both when the total ion current is fixed and when it is reduced. The effect of the residual gas pressure on the ion charge distribution begins to be felt even at the lowest gas pressures. The multiply charged ions are most sensitive to the residual gas pressure. As can be seen from these curves, the currents of triply and quadruply charged ions fall off most rapidly as the pressure is raised. In other experiments, a residual gas pressure in excess of about 5×10^{-6} Torr caused quadruply charged uranium ions to disappear almost completely from the measured spectrum, although in a strong magnetic field these ions formed 30% of the total ion current at pressures an order of magnitude lower.

A typical plot of the ion charge distribution as a function of gas pressure for the example of an aluminum cathode, oxygen gas material pair is shown in Fig. 4. The ion charge distribution evidently differs substantially between the base pressure and higher pressures: the fraction of multiply charged ions decreases sharply, and the fraction of singly charged ions increases accordingly. While it is generally true that the fraction of singly charged ions in the distribution increases with increasing pressure, and the current of multiply charged ions always falls, in the case of doubly and, in some experiments, triply charged ions the pressure dependence of the fraction constituted by these components is nonmonotonic and has a distinct maximum. The existence of an optimum pressure for obtaining a maximum density of dou-

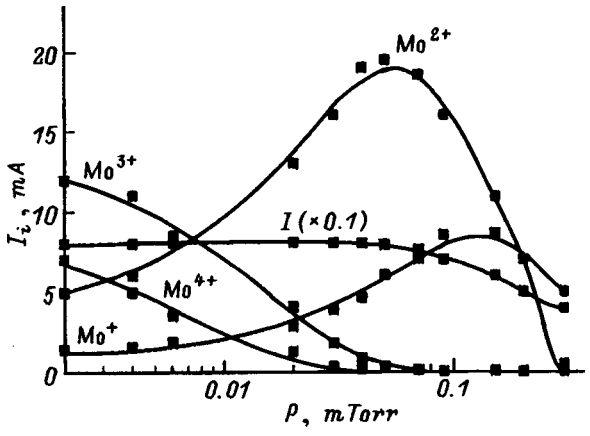

FIG. 2. Total ion current extracted from the plasma, together with its charge components, as functions of gas pressure in the discharge vessel. Molybdenum cathode, hydrogen gas feed, discharge current $I=260$ A, magnetic field $B=6$ mT.

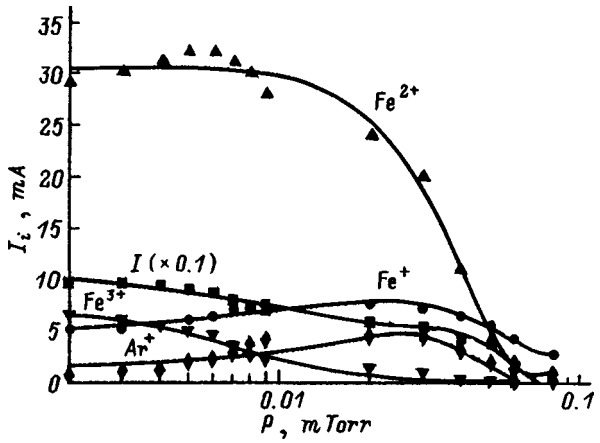

FIG. 3. Total ion current extracted from the plasma, together with its charge components, as functions of gas pressure in the discharge vessel. Steel cathode, argon gas feed, discharge current $I=250$ A, magnetic field $B=5$ mT.

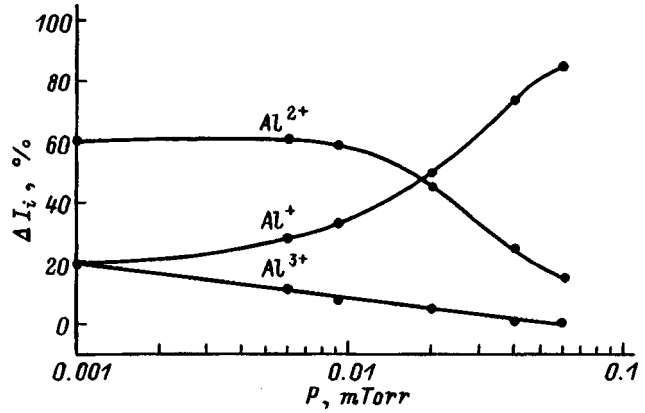

FIG. 4. Effect of oxygen pressure on the charge distribution of aluminum ions for a discharge current of 250 A.

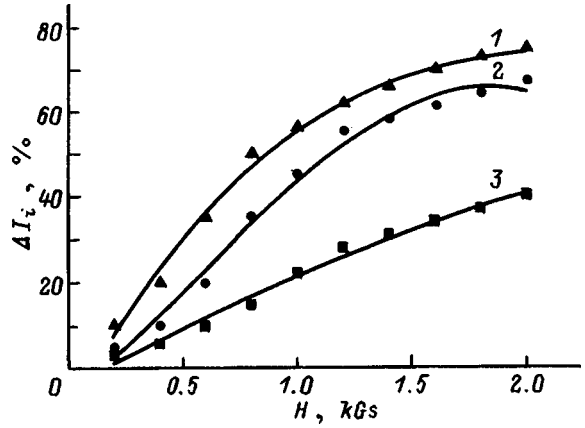

FIG. 6. Fraction of gas ions in the extracted beam as a function of the magnetic field in the discharge system. Titanium cathode, nitrogen gas feed (pressure 0.3 mTorr), discharge current (A): *1* — 120, *2* — 180, *3* — 280.

bly or triply charged ions is revealed most clearly when helium is used as a working gas (Fig. 5).

The experiments showed that in this discharge system, efficient generation of feed gas ions and the appearance of a significant fraction of them in the ion spectrum is possible only when the discharge system is placed in a magnetic field. In addition to choosing the right pressure and using a gas with a large ionization cross section, one can also increase the fraction of gas atoms ionized by raising the magnetic field and reducing the arc current (Fig. 6). When molecular diatomic gases (N_2 and O_2) are used, the fraction of atomic ions increases as the magnetic field is raised (Fig. 7). It should be noted that the choice of cathode material has no noticeable effect on the generation of gas ions in this type of discharge.

These results make it possible to generate mixed (gas–metal) ion beams and use them to treat the surface of construction materials. Gas–metal compounds produced in this way (nitrides, oxides, etc.) can greatly improve the operating properties of a surface. Table I lists the results of some tests of the wear resistance of stainless steel samples treated with gas–metal ion beams. It is seen that the greatest enhancement in wear resistance (by more than a factor of 40) is observed for a beam containing nitrogen and titanium.

Another interesting application might be the use of a gas to control the charge distribution of the metal ions in a vacuum arc plasma. Thus, for an arc with a magnesium cathode under ordinary burning conditions, more than 80% of the ions are doubly ionized. In some experiments using an ion source based on a vacuum arc as an injector for heavy ion accelerators, a high current beam of singly ionized magnesium ions has been needed. This problem was solved by feeding a small amount of nitrogen into the discharge gap of the ion source, which raised the fraction of singly charged magnesium ions in the ion beam from 20 to 70%.

CONCLUSION

At least two important practical conclusions follow from the results presented here: multiply charged ions can exist in a vacuum arc discharge plasma only for very low residual gas pressures. For example, in order to obtain a significant fraction of quadruply and quintuply ionized metal ions, it is necessary to reduce the pressure to 10^{-6} Torr. At elevated residual gas pressures (on the order of 10^{-4} Torr), in an arc

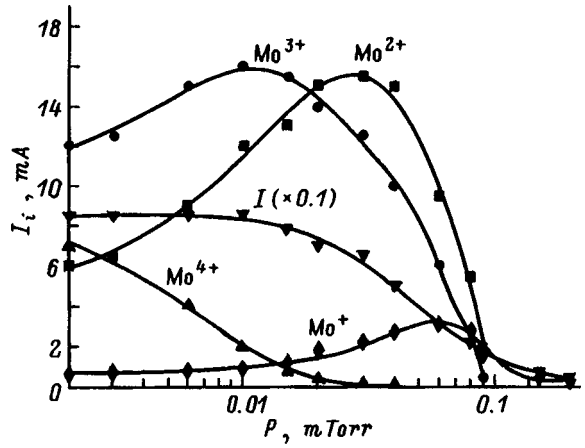

FIG. 5. Total ion current extracted from the plasma, together with its charge components, as functions of gas pressure in the discharge vessel. Molybdenum cathode, helium gas feed, discharge current $I=280$ A, magnetic field $B=8$ mT.

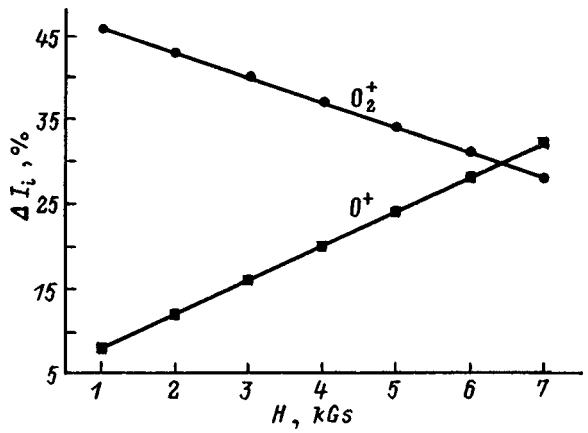

FIG. 7. The gas component of the ion current as a function of magnetic field. Aluminum cathode, oxygen gas feed (pressure 0.2 mTorr), ratio of discharge current to magnetic induction $I/B=0.1$.

TABLE I.

Sample No.	Ion composition	Wear (arb. units)		Enhancement factor
		implanted region	initial surface	
1	Ti (100%)	15.94	24.82	1.6
2	Ti (60%) + N (40%)	1.05	44.04	42.0
3	Al (50%) + O (50%)	2.92	27.96	9.6
4	C (50%) + N (50%)	31.71	60.91	1.9
5	Cr (50%) + O (50%)	2.83	27.37	9.7

discharge with a cathode spot in a magnetic field it is possible to generate gas ions and extract them from the plasma and the fraction of gas ions may be comparable to or even exceed the amount of metal ions in the overall ion flux.

These data make it possible to approach the choice of working parameters for ion-plasma devices based on vacuum arc discharges in a more systematic way.

The authors thank the leader of the plasma applications group at the Lawrence Berkeley National Laboratory (Berkeley, California, USA), Dr. Ian Brown, and the leaders of the ion injector laboratory at the GSI (Darmstadt, Germany), Drs. Bernhard Wolf and Peter Spaedtke, for providing the opportunity to measure the ion charge distribution in the vacuum arc discharge plasmas, as well as Dr. Peter Evans of the National Nuclear and Technology Research Center (Sydney, Australia) for conducting tests of the wear resistance of the irradiated samples.

This work was supported by Grant No. 96-02-16669 of the Russian Fund for Fundamental Research.

[1] G. Lafferty (Ed.), *Vacuum Arcs* [Wiley, New York (1980); Mir, Moscow (1982), 428 pp.].
[2] G. A. Mesyats, *Ectons* [in Russian], Parts 1–3, Nauka, Ekaterinburg (1993), 690 pp.
[3] V. I. Rakhovskiĭ, *Physical Principles of Electrical Current Switching in Vacuum* [in Russian], Nauka, Moscow (1970), 536 pp.
[4] *Proceedings of the 17th International Symposium on Discharge and Electrical Insulation in Vacuum*, Berkeley, California, USA (1996), Vol. 1–2, p. 1093.
[5] *Abstracts of Talks at the IVth All-Russia Conference on the Modification of the Properties of Construction Materials by Charged Particle Beams* [in Russian], Scientific Research Institute for Nuclear Physics, Tomsk University, Tomsk (1996), 551 pp.
[6] R. L. Boxman, P. Martin, and D. Sanders (Eds.), *Vacuum Arc Science and Technology*, Noyes, New York (1995).
[7] W. D. Davis and H. C. Miller, J. Appl. Phys. **40**, 2212 (1969).
[8] E. M. Oks, I. G. Brown, M. R. Dickinson *et al.*, Appl. Phys. Lett. **67**, 200 (1995).
[9] E. Oks, A. Anders, I. Brown *et al.*, IEEE Trans. Plasma Sci. **PS-24**, 1174 (1996).
[10] A. Anders, S. Anders, B. Juttner, and I. Brown, IEEE Trans. Plasma Sci. **PS-21**, 305 (1993).
[11] A. Anders, S. Anders, A. Forster, and I. Brown, Plasma Sources Sci. Technol. **1**, 263 (1992).
[12] I. I. Aksenov, I. I. Konovalov, V. G. Padalka *et al.*, Fiz. Plazmy **11**, 1373 (1985) [Sov. J. Plasma Phys. **11**, 787 (1985)].
[13] Lipin Yu, Vacuum **41**, 2217 (1990).
[14] A. Ben-Shalom, R. L. Boxman, and X. Goldsmidt, IEEE Trans. Plasma Sci. **PS-21**, 435 (1993).
[15] P. Spaedtke, H. Emig, B. H. Wolf, and E. Oks, Rev. Sci. Instrum. **65**, 3113 (1994).
[16] B. H. Wolf, H. Emig, D. M. Ruck *et al.*, Nucl. Instrum. Methods Phys. Res. B **106**, 651 (1995).
[17] B. H. Wolf, H. Emig, P. Spaedtke, and D. Ruck, Rev. Sci. Instrum. **65**, 3091 (1994).
[18] I. G. Brown, Rev. Sci. Instrum. **65**, 3061 (1994).
[19] I. Brown, IEEE Trans. Plasma Sci. **PS-21**, 537 (1993).
[20] A. G. Nikolaev, E. M. Oks, G. Yu. Yushkov *et al.*, Rev. Sci. Instrum. **67**, 3095 (1996).
[21] I. G. Brown, P. Spaedtke, H. Emig *et al.*, Nucl. Instrum. Methods Phys. Res. A **295**, 12 (1990).
[22] I. G. Brown, B. Feinberg, and J. E. Galvin, J. Appl. Phys. **63**, 4889 (1988).
[23] E. Oks, P. Spaedtke, H. Emig, and B. H. Wolf, Rev. Sci. Instrum. **65**, 3109 (1994).

Translated by D. H. McNeill

Mechanism for the influence of the geometric parameters on the electrical characteristics of Penning ion sources

R. P. Babertsyan, É. S. Badalyan, G. A. Egiazaryan, and É. I. Ter-Gevorkyan

Erevan State University, Erevan, Armenia
(Submitted July 15, 1997)
Zh. Tekh. Fiz. **68**, 29–32 (September 1998)

A steady-state Penning ion source is studied experimentally. Depending on the geometric parameter l_a (the anode length to diameter ratio) and pressure, maxima are observed in the discharge current and in the ion beam current extracted from an aperture at the center of the cathode. It is shown that at pressures of the order of 10^{-4} Torr, two maxima appear in these currents: one, for short discharge gaps with $l_a=1-1.5$, corresponds to a diverging ion beam, and the other, for longer anodes with $l_a=4-5$, to a collimated ion beam. At pressures of the order of 10^{-5} Torr, only one maximum appears in these currents, for short anodes $l_a=2-3$ with a diverging ion beam. A physical explanation is proposed for these findings.
 [S1063-7842(98)00609-6]

In most papers on Penning discharges, the geometric parameters of the electrode system have been chosen without adequate justification. In the meantime, it has recently been shown[1–3] that the geometric parameter l_a of the discharge gap does affect the discharge characteristics, both quantitatively and qualitatively. In Ref. 1 the ignition potential of the discharge was found to depend significantly on the discharge gap length. The optimum length, at which the ignition potential is lowest, was established. In Ref. 2 primary attention was devoted to clarifying the effect of the discharge gap length on the instability of the discharge and on the generation of high-frequency oscillations.

In this paper some new experimental data are presented on the main discharge characteristics as functions of the physical and geometric parameters. From a wide range of pressures that were used, here we present data for two pressures, 5×10^{-5} and 4.5×10^{-4} Torr.

The experimental technique is discussed in an earlier paper.[3] The length of the discharge gap was varied smoothly using a special device described there.[3] The parameters were the anode voltage U_A, the magnetic induction B, and the residual air pressure P. The currents to the cathode were measured using a collector mounted 2 cm behind the central aperture of the fixed cathode. The results of these measurements are shown in Figs. 1 and 2. As can be seen from these figures, the curves are rather complicated. As l_a is varied, there is a significant change in the discharge current I_d and in the total beam ion current I_i and axial beam current I_{ax}. At $P=4.5\times10^{-4}$ Torr these currents each have two maxima, while at $P=5\times10^{-5}$ Torr only one clearly distinct maximum is observed, i.e., l_a plays an important role in the discharge ionization processes and determines the location and boundaries of the intense ionization regions.

A hollow-cathode Penning discharge is maintained by high secondary ion-electron emission γ and volume ionization α, where γ and α are the Townsend coefficients.[4] To first order, these coefficients are determined by the relations between the electric and magnetic fields. For fixed values of the magnetic induction and anode voltage, a change in the geometric parameter has a significant effect on the distribution of the nonuniform electric field, which, in turn, is reflected in the space charge distribution.[2]

Penning discharges burn in different regimes, ranging from a uniform to a nonuniform distribution of the space charge in the discharge gap, and can also exist in a plasma regime, depending on the physical and geometric parameters.[4,5]

At low pressures and for certain magnetic fields inside short anodes, the space charge distribution becomes nonuniform.[6] In the anode region, the azimuthally drifting electron sheath enters an unstable state for a certain charge density (a diocotron-type instability) and generates high-frequency oscillations which can be detected by a spectrum analyzer.[2] Curve *3* of Fig. 1a shows the frequency ν of the oscillations in the ac part of the discharge current as a function of l_a for $P=5\times10^{-5}$ Torr. It can be seen that the oscillations appear only within a small range of l_a for a certain magnetic field strength in the region of the first maximum; the frequency of these oscillations falls linearly with increasing l_a. Comparing these data with the known formula for the frequency of the diocotron oscillations, $\nu\approx E_r/B$ (Refs. 5 and 6), we find that the radial component E_r of the electric field in the azimuthally drifting electron sheath decreases as l_a is raised. At the same time, the potential at the center of the discharge cell, U_0, increases,[7] and there is an increase in the longitudinal potential fall responsible for γ processes and initial ionization near the axis. Despite some reduction in E_r, it is still sufficient for intense avalanche formation, since for these high radial electric fields and low pressures, the energy acquired by the electrons lies within an interval corresponding to the peak of the ionization function. (Calculations show that this energy lies within 100–300 eV.) The generation of high-frequency oscillations with increasing l_a in this interval is evidence that E_r is still high, and the rise in

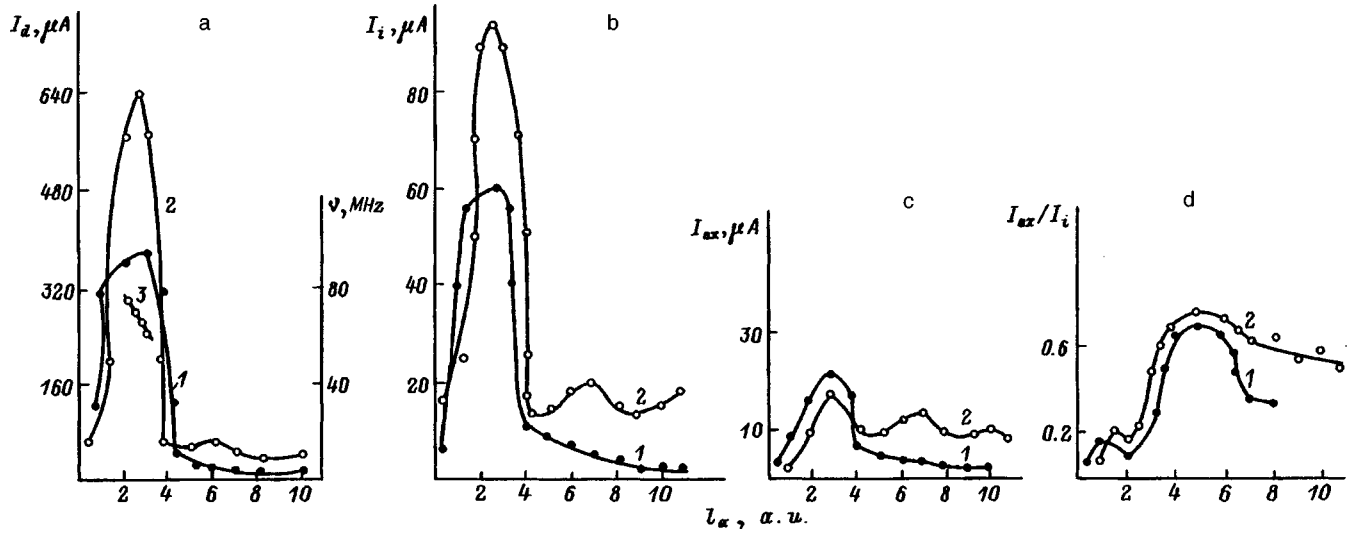

FIG. 1. The discharge current and frequency of diocotron oscillations (a), beam ion current (b), and its axial component (c), as well as their ratio (d), as functions of the geometric parameter for an anode voltage $U_A=2$ kV and magnetic induction $B=600$ G (*1*), 900 G (*2*). The pressure is 5×10^{-5} Torr.

the longitudinal potential fall is reflected mainly in an increase in the on-axis ionization. In fact, as can be seen from Fig. 1d, there is a rapid rise in the ratio I_{ax}/I_i when l_a is increased within the range of 2–4.

Thus in short discharge gaps with $l_a=2-3$ the radial potential drop is large, and the relationship of the radial and axial electric field distributions is such as to ensure a maximum radial ionization (all the currents reach their maxima). Here the longitudinal ionization reaches its maximum, but it only serves as a supplier of initial electrons. The most intense ionization processes take place near the anode.

As l_a is increased, the continuing rise in the longitudinal potential fall and the improvement in the ionization conditions on axis (right-hand branches of all the curves in Figs. 1a–1c) do not fully make up for the reduction in ionization owing to the drop in the average radial electric field due to the decrease in the radial potential drop. The absence of high-frequency oscillations for $l_a>3$ is confirmed by a noticeable reduction in the radial electric field near the anode and a reduction in the electron density in the sheath. Thus, radial ionization deteriorates and there is a reduction in the number of ions incident on the cathode, there is a reduction of the γ processes, and the ionization on axis decreases. As a result, a drop in all the currents is observed for $l_a>3$ (Figs. 1a–1c). As can be seen from Fig. 1d, the ratio I_{ax}/I_i changes little for $l_a=4-6$, i.e., within this range of variation of l_a the radial and axial ionization decrease in almost the same way.

Subsequently, all the electrical characteristics show a weak dependence on l_a, and their absolute magnitudes are small (Figs. 1a–1c). At pressures exceeding 5×10^{-5} Torr the plots of all the currents as functions of l_a change shape, and by $P=4.5\times10^{-4}$ Torr they differ greatly from the curves obtained for 5×10^{-5} Torr. Thus, for short anodes with $l_a=1-2$, the axial current beyond the cathode aperture

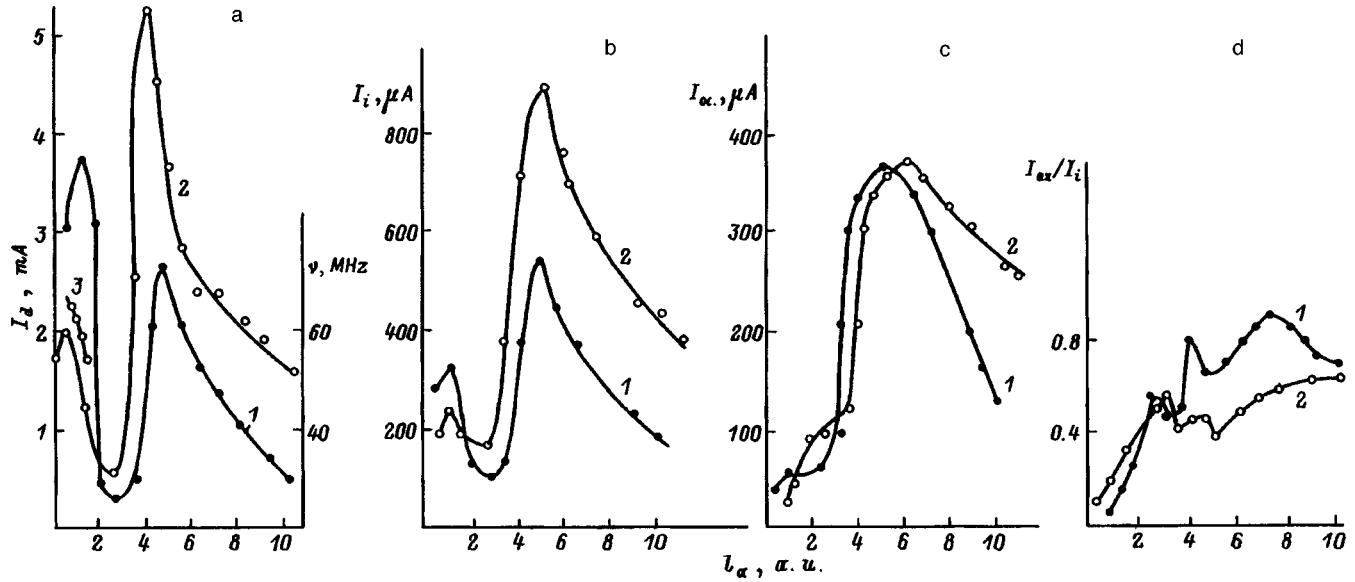

FIG. 2. As in Fig. 1, but for $P=4.5\times10^{-4}$ Torr.

becomes negative (the axial ion current is less than the electron current). This is associated with the onset of the diocotron instability in the anode sheath; it also occurred at a pressure of 5×10^{-5} Torr,[8] but at higher pressures the electron current is substantially higher than the ion current and reaches $I_{ax}\approx350$ μA. Further on, at 4.5×10^{-4} Torr, two distinct maxima are formed: one at short lengths with $l_a=1-1.5$ and the other in the interval $l_a=4-5$ (Figs. 2a–2c).

The mechanism for formation of the first maximum is analogous to that pointed out above for a pressure of $P=5\times10^{-5}$ Torr. Now, how can we explain the appearance of the second maximum at $P=4.5\times10^{-4}$ Torr in the range of long discharge gaps, when the discharge seems to acquire a new impulse and the currents I_d, I_i, and I_{ax} again begin to rise? We have shown previously[1–3,7] that within the range $l_a=0.5-5$ the potential U_0 of the center of the discharge cell increases, then its growth slows down and somehow approaches ''saturation.'' The radial distribution of the electric potential changes accordingly. For $l_a>3$ the radial electric field is considerably lower than the field for the first maximum. Thus, for low pressures $P<5\times10^{-5}$ Torr and $l_a>4$, the radial ionization, which plays a decisive role in a Penning discharge, is much weaker, despite the large longitudinal potential drop, and all the currents are small and have no second maximum. However, as the pressure is raised, the electron–neutral collision frequency increases, and the fractional contribution of axial ionization changes (it increases) owing to the large longitudinal potential fall. The effective ion–electron emission coefficient γ^* increases: $\gamma^*=P\gamma l_a/\lambda_e(1-\delta)$, where γ is the secondary ion-electron emission coefficient, P is the gas pressure, λ_e is the electron mean free path for $P=1$ Torr, δ is the secondary electron emission coefficient under electron bombardment, and l_a is the anode length.[9] Here there is an increase in the longitudinal component of the velocity of the ions heading toward the cathodes and of the electrons emitted from the cathodes. (The initial velocities of these electrons obey a cosine distribution.) For $l_a>3$ and pressures raised to $P>5\times10^{-5}$ Torr, an ever larger number of secondary electrons participates in ionization processes within the axial region. Despite the weakened radial field, the overall ionization also begins to rise because of the substantial increase in the longitudinal ionization: all the currents I_d, I_i, and I_{ax} again increase (the left branches of the second maximum curves in Figs. 2a–2c).

Thus for $l_a=4-5$ and $P=4.5\times10^{-4}$ Torr the radial potential drop is low, but the axial potential drop is substantial and ensures a maximum total level of ionization. The region of intense ionization expands toward the discharge axis.

The ratio I_{ax}/I_i reaches a maximum at $l_a=7-8$ and exceeds 0.8, while the same ratio is of the order of 0.2 for short gaps (Figs. 1d and 2d). Thus, optimal conditions for ionization near the axis are created for lengths $l_a=7-8$. The most favorable conditions for total ionization (for I_d and I_i), however, correspond to $l_a=4-5$ (Figs. 2a and 2b).

In the second drop in the currents I_d, I_i, I_{ax} as functions of l_a ($l_a>5$) the average electric field strength along the radius is very small, and radial ionization is greatly weakened. And, despite the possibility of enhanced ionization owing to the large longitudinal potential drop, the overall ionization decreases with increasing l_a (Figs. 2a–2c). Under these conditions, a region where the electric field is negligible develops inside the anode. In fact, measurements in an electric bath[3] showed that for $l_a<4$ the axial potential distribution $U(0,z)$ is parabolic, while for $l_a>4$ the distribution on the axis has a region with zero gradient ($E_z=0$) whose extent increases as the anode is lengthened. A zero-gradient region which expands with l_a also develops in the radial potential distribution near the plane of symmetry of the discharge. The actual distribution $U(r,z)$ in a hot discharge is determined by the cell geometry, but also by the effect of space charge,[7] which, in turn, depends on the physical parameters of the discharge (on P, U_A, B). The zero-gradient regions $U(0,z)$ and $U(r,0)$ form a region which becomes a ''trap'' for the particles created in it, i.e., a compensated space charge develops in this part. As l_a increases ($l_a>5$), the zero-gradient region expands both along the axis and radially, and the ''active zone'' in which the charged particles gain energy for ionization shrinks back toward the anode and cathodes. As a result, all the currents decrease (Figs. 2a–2c).

As the pressure increases to $P>5\times10^{-5}$, these processes are enhanced, the effect of the ions held in the ''trap'' becomes important, and the compensated space charge becomes a rarefied plasma which occupies an ever larger part of the discharge gap.

The displacement of the maxima to one side or the other is determined by the magnitudes of the other parameters. In particular, the effect of the magnetic field shows up in the number of trapped electrons and in the height $h_i=m/e\cdot E_r/B^2$ of the cycloid along which an electron gains energy for ionization. Thus, depending on the discharge burning conditions, a change in the magnetic field can either increase or decrease the rate of ionization and affect the discharge characteristics.

CONCLUSIONS

1. Depending on the geometric parameter and pressure, maxima appear in both the beam ion current and the discharge current, whose levels are determined by the anode voltage and magnetic induction.

2. At pressures of the order of 10^{-4} Torr, two maxima show up in all the currents: one corresponding to a diverging ion beam, in the region $l_a=1-1.5$, and the second, corresponding to a collimated ion beam, for $l_a=4-5$. For $l_a=7-8$ the degree of collimation exceeded 80% at an ion current of the order of 300 μA.

3. At pressures of the order of 10^{-5} Torr, only one clearly distinct maximum appears in these currents for short discharge gaps ($l_a=2-3$), while no second maximum is observed in long discharge gaps.

4. These observations are explained by the combined action of the electric field components and the differential effect of the pressure on the ionization processes along the axis and along the radius of the discharge.

[1] R. P. Babertsyan, É. S. Badalyan, G. A. Egiazaryan, and É. I. Ter-Gevorkian, Zh. Tekh. Fiz. **57**, 1992 (1987) [Sov. Phys. Tech. Phys. **32**, 1198 (1987)].
[2] R. P. Babertsyan, É. S. Badalyan, G. A. Egiazaryan, and É. I. Ter-Gevorkian, Zh. Tekh. Fiz. **59**(10), 43 (1989) [Sov. Phys. Tech. Phys. **34**, 1117 (1989)].
[3] R. P. Babertsyan, É. S. Badalyan, G. A. Egiazaryan, and É. I. Ter-Gevorkian, Zh. Tekh. Fiz. **66**(6), 77 (1996) [Tech. Phys. **41**, 563 (1996)].
[4] Nguyen Khieu Thi, Dissertation [in Russian], Moscow State University (1968).
[5] É. M. Reĭkhrudel', G. V. Smirnitskaya, and G. A. Egiazaryan, Zh. Tekh. Fiz. **43**, 130 (1973) [Sov. Phys. Tech. Phys. **18**, 83 (1973)].
[6] W. Khauer, J. Appl. Phys. **37**, 602 (1996).
[7] R. P. Babertsyan, É. S. Badalyan, G. A. Egiazaryan, and É. I. Ter-Gevorkian, in *Physics. An Intercollegiate Collection of Scientific Papers* [in Russian], Erevan (1985), pp. 34–42.
[8] R. P. Babertsyan, G. A. Egiazaryan, and É. I. Ter-Gevorkian, Zh. Tekh. Fiz. **64**(10), 202 (1994) [Tech. Phys. **39**, 1069 (1994)].
[9] É. M. Reĭkhrudel' and É. Kh. Isakaev, Zh. Tekh. Fiz. **36**, 653 (1966) [Sov. Phys. Tech. Phys. **11**, 486 (1966)].

Translated by D. H. McNeill

Ranges of low-energy heavy ions in beryllium, boron, carbon, and silicon

E. G. Sheĭkin

A.O. Scientific-Research Enterprise for Hypersonic Systems, 196066 St. Petersburg, Russia
(Submitted January 21, 1997; resubmitted June 17, 1997)
Zh. Tekh. Fiz. **68**, 33–36 (September 1998)

Based on a theory of the passage of low-energy, heavy ions through matter, simple analytical expressions are obtained for calculating the average projected ranges of the ions and the rms deviations of the projected ranges. The theoretical and experimental ranges of heavy ions with atomic numbers $29 \leqslant Z_1 \leqslant 83$ in targets of Be, B, C, and Si are compared. The theory is found to be in good agreement with experiment. © *1998 American Institute of Physics.* [S1063-7842(98)00709-0]

A theory has been developed[1] for the propagation of low-energy, heavy ions in an amorphous medium in the case where the main process determining the ion transport is their elastic scattering on target atoms. The elastic scattering process is described in the approximation of a modified hard sphere model.[2] The elastic scattering cross section is determined in terms of the stopping power s_n for the interaction potential in a Thomas–Fermi model. It is assumed that an ion is stopped in the material when its energy falls below some threshold value E_{th}. Analytical expressions have been obtained[1] in these approximations for calculating the average projected range of the ions $\overline{R_p}$ and the rms deviation ΔR_p of the projected ranges. In this paper the theoretical results of obtained in Ref. 1 are compared with experiment,[3–6] and some simple expressions are proposed for calculating $\overline{R_p}$ and ΔR_p. The formulas for calculating $\overline{R_p}$ and ΔR_p from Ref. 1 are:

$$\overline{R_p}=\sum_{k=1}^{\infty} q_k \overline{x_k}, \quad \overline{R_p^2}=\sum_{k=1}^{\infty} q_k \overline{x_k^2},$$

$$\Delta R_p=\sqrt{(\overline{R_p^2}-\overline{R_p}^2)}, \tag{1}$$

where x_k is the distance from the surface of the solid to the point at which the ion undergoes its kth collision, q_k is the probability that an ion is stopped after the kth collision, which is given by

$$q_k=\xi_k-\xi_{k-1},$$

$$\xi_k=1-Q^k\sum_{i=0}^{N}(-1)^i c_k^i\left[\alpha^i-\frac{E_{\text{th}}}{E}\sum_{j=0}^{k-1}\frac{1}{j!}\ln^j(\alpha^i E/E_{\text{th}})\right],$$

$$k>N, \quad \xi_k=0, \quad k\leqslant N, \tag{2}$$

where E is the initial ion energy, N is the integer part of $\ln(E/E_{\text{th}})/\ln(\alpha)$, $\alpha=((m_1-m_2)/(m_1+m_2))^2$, m_1 is the ion mass, m_2 is the target atom mass, and

$$c_k^i=\frac{k!}{i!(k-i)!}, \quad Q=1/(1-\alpha).$$

The mean values $\overline{x_k}$ and $\overline{x_k^2}$ in Eq. (1) are defined by

$$\overline{x_k}=\sum_{j=0}^{k-1}\overline{\lambda_j\mu_j}, \quad \overline{x_k^2}=\overline{x_k}^2+\sum_{j=0}^{k-1}(\overline{\lambda_j^2\mu_j^2}-\overline{\lambda_j}^2\overline{\mu_j}^2). \tag{3}$$

Here λ_j is the mean free path of the ion between the jth and $(j+1)$th collisions, and μ_j is the cosine of the angle between the direction of motion of the ion after the jth collision and the normal to the target surface. The average values $\overline{\mu_j}$ and $\overline{\mu_j^2}$ are defined by

$$\overline{\mu_j}=\mu_0(\overline{\cos\Theta})^j,$$

$$\overline{\mu_j^2}=\frac{1}{3}+\left(\mu_0^2-\frac{1}{3}\right)\left(\frac{3\overline{\cos^2\Theta}-1}{2}\right)^j,$$

where θ is the scattering angle of an ion in collisions with target atoms in the laboratory coordinate system and μ_0 is the initial value of μ. In the following we shall set $\mu_0=1$.

In the modified hard sphere model the averages $\overline{\cos\Theta}$ and $\overline{\cos^2\Theta}$ are given by

$$\overline{\cos\Theta}=\begin{pmatrix} 1-\frac{1}{3}(m_2/m_1)^2, & m_1>m_2, \\ \frac{2}{3}(m_1/m_2), & m_1\leqslant m_2, \end{pmatrix}$$

$$\overline{\cos^2\Theta}=1-\frac{1}{4}(1+(m_2/m_1)^2)+\frac{1}{16}(m_1/m_2)\times(1-(m_2/m_1)^2)^2\ln(1/\alpha). \tag{4}$$

For $m_1>m_2$, in calculating $\overline{\cos^2\Theta}$ it is convenient to use the Taylor series expansion of this expression. In particular, when $m_1/m_2\geqslant 2$, for calculating $\overline{\cos^2\Theta}$ with a relative error of less than 0.1% we obtain the following expression:

$$\overline{\cos^2\Theta}\approx 1-\frac{2}{3}(m_2/m_1)^2+\frac{2}{15}(m_2/m_1)^4.$$

Expressions for the average values $\overline{\lambda_j}$ and $\overline{\lambda_j^2}$ in Eq. (3) have been obtained[1] using the following approximation[7] for s_n:

$$s_n=\frac{g\sqrt{\varepsilon}}{b+\varepsilon} \quad \text{for } g=0.45, \quad b=0.3. \tag{5}$$

The reduced energy is defined by

$$\varepsilon = E\frac{m_2 a}{Z_1 Z_2 e^2 (m_1+m_2)},$$

where Z_1 and Z_2 are the nuclear charges of the ion and target atom, respectively, a is the screening parameter, and e is the electron charge.

We use the Lindhard approximation, in which $a=0.8853a_0/(Z_1^{2/3}+Z_2^{2/3})^{1/2}$ and a_0 is the Bohr radius. In this case[1]

$$\overline{\lambda_j} = \lambda_0[b+\gamma^j(1/2)+\varepsilon\gamma^j(3/2)],$$

$$\overline{\lambda_j^2} = 2\lambda_0^2[b^2\gamma^j(1)+2b\varepsilon\gamma^j(2)+\varepsilon^2\gamma^j(3)], \qquad (6)$$

where $\gamma(w)=(1-\alpha^{1+w})/((1-\alpha)(1+w))$, $\lambda_0=\sqrt{\varepsilon}/(2gn\pi a^2)$, and n is the density of the target atoms.

The set of equations (1)–(6) can be used to calculate the dependence of the range of the ions on their energy for a given value of E_{th}. We determine E_{th} as in Ref. 1, using the equation $E_{\text{th}}=E_d/(1-\alpha)$ obtained by equating the maximum energy transferred to a target atom in a collision to the displacement energy E_d. The displacement energy E_d for different target materials ranges between 10 and 35 eV.[8]

Let us examine how important it is to include E_{th} in calculating the ranges of heavy ions with energies $\varepsilon \leqslant 0.1$. We consider the limit $E_{\text{th}}=0$. We introduce special notation for the limiting ion ranges when $E_{\text{th}}=0$: L_p is the limiting value of the average projected range and ΔL_p is the limiting value of the rms deviation of the projected range. According to Eq. (2), for $E_{\text{th}}=0$, $q_k=0$ for any finite number k. Thus, according to Eqs. (1)–(3), we have

$$L_p=\sum_{j=0}^{\infty}\overline{\lambda_j\mu_j}, \quad (\Delta L_p)^2=\sum_{j=0}^{\infty}(\overline{\lambda_j^2\mu_j^2}-\overline{\lambda_j^2}\,\overline{\mu_j^2}). \qquad (7)$$

After some simple transformations, Eqs. (3)–(7) yield

$$L_p=\lambda_0\left[\frac{b}{1-\gamma(1/2)\overline{\cos\Theta}}+\frac{\varepsilon}{1-\gamma(3/2)\overline{\cos\Theta}}\right],$$

$$(\Delta L_p)^2=\lambda_0^2\left\{\frac{2}{3}\left[\frac{b^2}{1-\gamma(1)}+\frac{2b\varepsilon}{1-\gamma(2)}+\frac{\varepsilon^2}{1-\gamma(3)}\right]+\frac{4}{3}\left[\frac{b^2}{1-\tau\gamma(1)}+\frac{2b\varepsilon}{1-\tau\gamma(2)}+\frac{\varepsilon^2}{1-\tau\gamma(3)}\right]-\left[\frac{b^2}{1-(\gamma(1/2)\overline{\cos\Theta})^2}+\frac{2b\varepsilon}{1-\gamma(1/2)\gamma(3/2)(\overline{\cos\Theta})^2}+\frac{\varepsilon^2}{1-(\gamma(3/2)\overline{\cos\Theta})^2}\right]\right\}, \qquad (8)$$

where $\tau=(3\overline{\cos^2\Theta})/2$.

Figure 1 shows plots of $\overline{R_p}/L_p$ as functions of the ion energy for different ion–target pairs. In calculating $\overline{R_p}$ for all the targets it has been assumed that $E_d=25$ eV. Clearly, for large ε the ratio $\overline{R_p}/L_p$ is close to unity and falls off as the ion energy is reduced. For fixed ε the ratio $\overline{R_p}/L_p$ falls off as both Z_1 and Z_2 decrease. For $\varepsilon<0.05$ the difference between $\overline{R_p}$ and L_p becomes significant. In this energy range, it is necessary to account correctly for the threshold energy ε_{th} when calculating the projected range of ions in a material. Comparative calculations of the functions $\overline{R_p}(\varepsilon)$ and $L_p(\varepsilon)$, as well as of $\Delta R_p(\varepsilon)$ and $\Delta L_p(\varepsilon)$, were done for a large set of ion–target combinations that satisfy the condition $m_1/m_2 \geqslant 2$. On the basis of these calculations we obtained the following approximate expressions for the projected range of an ion in matter:

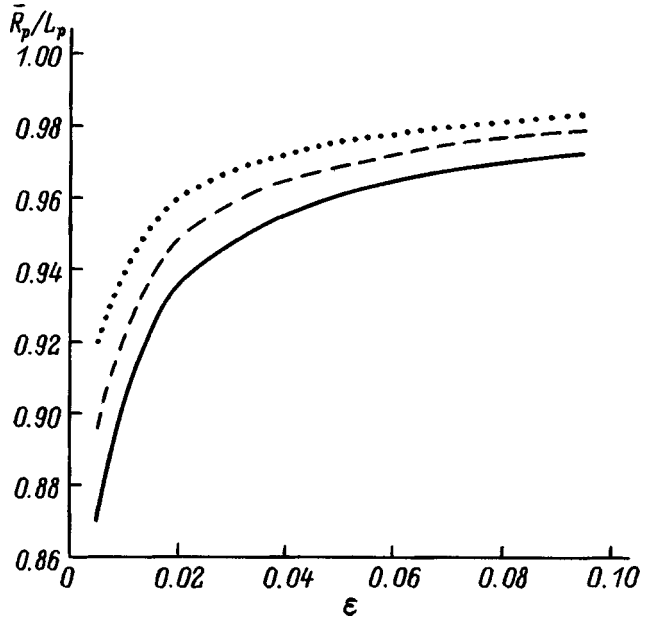

FIG. 1. The ratio $\overline{R_p}/L_p$ as a function of ion energy for $E_d=25$ eV; the solid curve is for Pb–C, the dashed curve for Cs–Si, and the dotted curve for Pb–Si.

$$\overline{R_p}(\varepsilon)\approx L_p(\varepsilon)-\left(\frac{m_1}{m_1+m_2}\right)^{0.8}L_p(\varepsilon_{\text{th}}),$$

$$\Delta R_p(\varepsilon)\approx\Delta L_p(\varepsilon). \qquad (9)$$

The relative error in formulas (9) at energies $0.005\leqslant\varepsilon\leqslant 0.1$ was less than 0.3% for $\overline{R_p}$ and 1% for ΔR_p. Thus, the projected rangess of ions in matter can be calculated simply and with high accuracy using Eqs. (8)–(10).

For small m_2/m_1 the expressions for calculating the limiting ion range L_p and ΔL_p in Eq. (9) can be greatly simplified. Using Taylor series expansions of the functions L_p and ΔL_p defined by Eqs. (8) and keeping only the first terms of the expansions, we obtain approximate expressions for the limiting ion range:

$$\tilde{L}_p=\lambda_0\left(1+\frac{m_1}{m_2}\right)\left(b+\varepsilon\left(\frac{1}{3}+0.52\frac{m_2}{m_1}\right)\right),$$

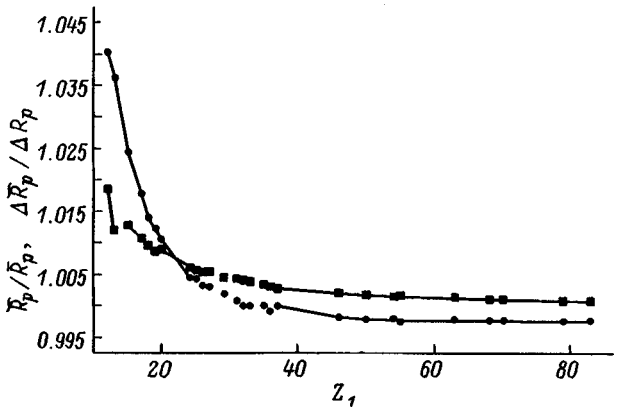

FIG. 2. The ratio of the approximate values of the ion ranges to the exact values as a function of ion atomic number Z_1: $\varepsilon=0.01$; ■ — $\tilde{R}_p/\bar{R}_p$; ● — $\Delta\tilde{R}_p/\Delta R_p$.

$$(\Delta\tilde{L}_p)^2=0.5\frac{m_1}{m_2}\left(1+\frac{m_2}{m_1}\right)^2\left[b^2\left(1-\frac{1}{6}\frac{m_2}{m_1}\right)+b\varepsilon\times\left(1+\frac{5}{4}\frac{m_2}{m_1}\right)+\varepsilon^2\left(\frac{1}{3}-\frac{1}{2}\frac{m_2}{m_1}\right)\right]. \quad (10)$$

As a statement of the approximate character of these equations, a tilde is placed over the symbols for the corresponding quantities. For $m_1/m_2\geqslant 2$ and $\varepsilon\leqslant 0.1$, the relative discrepancy of the approximations $\tilde{L}_p$ from the exact L_p is less than 2% and that of $\Delta\tilde{L}_p$ from ΔL_p is less than 3.5%. These discrepancies are less than the usual errors in an experimental determination of ion ranges in matter. Thus, it is appropriate to introduce the following approximations for calculating ion ranges based on Eqs. (9) and (10):

$$\tilde{R}_p(\varepsilon)=\tilde{L}_p(\varepsilon)-\left(\frac{m_1}{m_1+m_2}\right)^{0.8}\tilde{L}_p(\varepsilon_{\text{th}}),$$

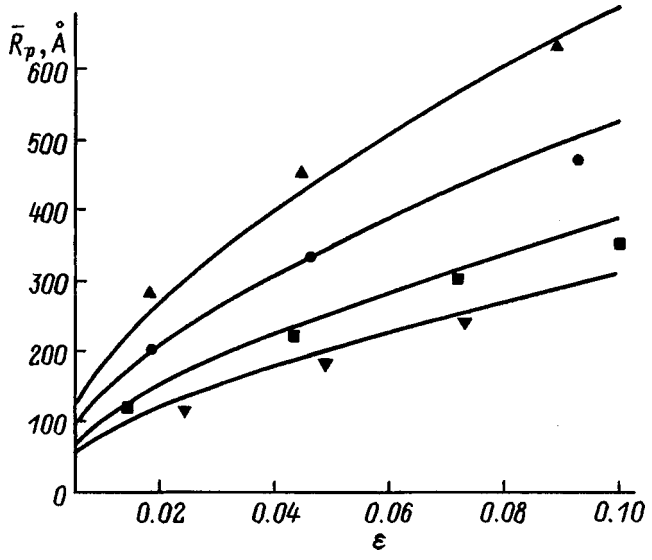

FIG. 3. Ion range $\bar{R}_p$ as a function of energy. The curves show the results of a calculation according to Eqs. (1)–(6), ▲ — Pb–Be, ● — Au–B, ■ — Eu–C, ▼ — Pd–Si.

TABLE I. Parameters of experimental and theoretical ranges of ions.

				Experiment		Theory	
Ion	Target	E, keV	ε	$\bar{R}_p$, Å	ΔR_p, Å	$\bar{R}_p$, Å	ΔR_p, Å
Bi	Be	20	0.0174	280	–	251	41
		50	0.0436	450	–	424	67
		100	0.0872	650	–	640	102
	B	20	0.0165	180	30	202	35
		50	0.0411	285	60	339	59
		100	0.0823	440	90	511	89
	Si	20	0.0133	160	50	230	62
		50	0.0333	270	75	379	101
		100	0.0666	425	115	562	152
Pb	Be	20	0.0179	280	–	251	41
		50	0.0446	450	–	423	67
		100	0.0893	630	–	640	102
	B	20	0.0169	175	30	202	36
		50	0.0421	310	70	339	59
		100	0.0843	450	100	510	89
	C	20	0.0154	205	44	203	38
		50	0.0384	315	60	340	62
		100	0.0769	495	91	510	93
Au	B	20	0.0186	200	50	198	36
		50	0.0464	330	70	334	59
		100	0.0928	470	90	504	91
	C	20	0.0169	197	25	200	38
		50	0.0423	315	47	335	62
		100	0.0846	460	80	504	95
	Si	20	0.0149	250	54	226	62
		50	0.0373	375	84	373	103
		100	0.0746	484	130	557	156
Yb	B	20	0.0245	180	40	190	37
		50	0.0612	310	60	323	62
	C	20	0.0223	176	35	192	39
		50	0.0558	295	59	324	65
	Si	20	0.0194	200	43	219	64
		50	0.0486	310	84	365	108
		100	0.0972	468	126	552	167
Eu	Be	20	0.0337	220	–	227	43
		50	0.0842	365	–	392	74
	C	50	0.0720	302	64	315	68
	Si	20	0.0247	194	29	212	67
		50	0.0618	318	68	357	113
Cs	Be	20	0.0455	200	–	220	44
	B	20	0.0427	165	45	177	39
	C	20	0.0387	170	43	179	41
		50	0.0968	290	69	310	72
	Si	20	0.0327	137	50	207	70
	Si	50	0.0819	270	84	354	121

$$\Delta\tilde{R}_p(\varepsilon)=\Delta\tilde{L}_p(\varepsilon). \quad (11)$$

Figure 2 shows a comparison of the exact ion ranges in carbon calculated using Eqs. (1)–(6) with the approximate values calculated using Eqs. (10) and (11). The comparison is over a wide range of variation in Z_1 from 12 (magnesium) to 83 (bismuth). It is clear from Fig. 2 that the error in the approximate calculation of the ion ranges using Eq. (11) is small and falls off rapidly with increasing Z_1. For $Z_1>20$, corresponding to $m_2/m_1<0.3$, the discrepancies of the approximate ranges $\tilde{R}_p$ and $\Delta\tilde{R}_p$ from the exact values are less than 1%. This means that a reliable estimate of the ratio $\Delta R_p/\bar{R}_p$ can be obtained from Eqs. (10) and (11). Assuming that the parameters m_2/m_1 and ε are small (with the restric-

tion that $\varepsilon_{th} \ll \varepsilon \leqslant 0.1$), we expand the ratio of the functions $\Delta\tilde{R}_p$ and $\tilde{R}_p$ in a Taylor series. Restricting consideration to terms of first order in smallness, we obtain

$$\Delta R_p/\overline{R}_p \approx \frac{(1+(\varepsilon/b-m_2/m_1)/6)}{1-\sqrt{\varepsilon_{th}/\varepsilon}}\sqrt{\frac{m_2}{2m_1}}. \qquad (12)$$

For $m_2/m_1 < 0.3$, Eq. (12) gives the ratio $\Delta R_p/\overline{R}_p$ to high accuracy. In particular, when $\varepsilon = 0.1$ the exact calculation using Eqs. (1)–(6) gives $\Delta R_p/\overline{R}_p = 0.427$ for the pair Ca–C, while the approximation (12) gives $\Delta R_p/\overline{R}_p = 0.424$. For the pair Pb–C, the results of the exact and approximate calculations coincide to the third decimal place, with $\Delta R_p/\overline{R}_p = 0.184$.

Let us compare some experimental data[3–6] with the calculations. In order not to introduce an additional element of uncertainty, for comparison we use the exact calculations according to Eqs. (1)–(6). Figure 3 shows the ion ranges as functions of energy for three different ion–target combinations. As can be seen from the figure, the experimental data are in good agreement with the theory. A sample comparison of experimental and theoretical results for 19 ion–target combinations at different ion energies is shown in Table I. An analysis of these data shows that for targets of Be, B, and C there is, on the whole, good agreement between the experimental and theoretical values of $\overline{R}_p$ and ΔR_p. For the Si targets, the theoretical values of $\overline{R}_p$ and ΔR_p are generally higher than the experimental.

Let us make a statistical analysis of a comparison of the theoretical ion ranges in these targets with the experimental values given in Refs. 3–6 for ions with atomic numbers from $Z_1 = 29$ to 83 and energies $\varepsilon \leqslant 0.1$. We consider the dimensionless quantities δ_1 and δ_2, which are introduced as follows: $\delta_1(\varepsilon_i)$ is the ratio of the experimental value of $\overline{R}_p$ to the theoretical, and $\delta_2(\varepsilon_i)$ is the ratio of the experimental value of ΔR_p to the theoretical, where ε_i is are the corresponding ion energies.

Table II lists the results of a statistical analysis of the values obtained for $\delta_1(\varepsilon_i)$ and $\delta_2(\varepsilon_i)$ for the different targets. The mathematical expectations $\overline{\delta_1}$ and $\overline{\delta_2}$ are the values of the corresponding sets of $\delta_1(\varepsilon_i)$ and $\delta_2(\varepsilon_i)$ averaged over ε_i and Z_1, and σ_1 and σ_2 are the rms deviations of the corresponding values of δ_1 and δ_2. Table II shows that the experimental and theoretical results are, on average, in good agreement. The insignificant deviations of $\overline{\delta_1}$ and $\overline{\delta_2}$ from unity for B and C and the only slightly greater deviation for Si may be caused by errors in the experimental range measurements, as well as by the approximate nature of the theoretical approach developed here. The systematic discrepancy between the theoretical and experimental values of the ranges for Si may be caused by the influence of an inelastic stopping process that has not been taken into account here. The values of $\overline{\delta_1}$ and $\overline{\delta_2}$ given in Table II can be used for correcting theoretical values of ion ranges in Be, B, C, and Si targets.

TABLE II. Results of a statistical analysis of a comparison of experimental and theoretical ranges of ions in matter.

Target	$\overline{\delta_1}$	σ_1	$\overline{\delta_2}$	σ_2
Be	1.02	0.075	–	–
B	0.92	0.053	1.07	0.16
C	0.93	0.066	0.93	0.18
Si	0.88	0.12	0.72	0.12

[1] E. G. Sheĭkin, Zh. Tekh. Fiz. **67** (10), 16 (1997) [Tech. Phys. **42**, 1128 (1997)].
[2] E. G. Sheĭkin, Zh. Tekh. Fiz. **66** (10), 63 (1996) [Tech. Phys. **41**, 1005 (1996)].
[3] M. Behar, P. F. Fichtner, C. A. Oliveri *et al.*, Nucl. Instrum. Methods Phys. Res. B **6**, 453 (1985).
[4] P. F. Fichtner, M. Behar, C. A. Oliveri *et al.*, Nucl. Instrum. Methods Phys. Res. B **28**, 481 (1987).
[5] M. Grande, M. Behar, J. P. Biersack, and F. C. Zawislak, Nucl. Instrum. Methods Phys. Res. B **45**, 689 (1990).
[6] M. Grande, F. C. Zawislak, D. Fink, and M. Behar, Nucl. Instrum. Methods Phys. Res. B **61**, 282 (1990).
[7] V. V. Yudin, Dokl. Akad. Nauk **207**, 325 (1972) [Sov. Phys. Dokl. **17**, 1076 (1972)].
[8] W. Eckstein, *Computer Simulation of Ion–Solid Interactions* [Springer-Verlag, Berlin–New York (1991); Mir, Moscow (1995), 320 pp.].

Translated by D. H. McNeill

Emission of single gamma rays by electrons with energies of hundreds of GeV in oriented crystals

A. Kh. Khokonov and M. Kh. Khokonov

Kabardino-Balkar State University, 360004 Nalchik, Russia
(Submitted October 28, 1996; resubmitted June 17, 1997)
Zh. Tekh. Fiz. **68**, 37–41 (September 1998)

Cross sections are calculated for the emission of single hard photons by electrons with energies of 150–1000 GeV as they pass through oriented crystals at small angles to the crystallographic axes. The contribution of incoherent emission at isolated atoms of the crystal is taken into account in the calculations, along with the emission in the continuum potential. The calculations are compared with the customary Bethe–Heitler spectrum for a thick amorphous target with allowance for photon absorption due to electron–positron pair production. It is shown that, in this range of energies, an oriented crystal can be more efficient than a thick amorphous target for creating a larger number of hard gamma rays with energies comparable to the energies of the emitting electrons. © *1998 American Institute of Physics.* [S1063-7842(98)00809-5]

Experimental measurements[1,2] of the spectra of gamma rays emitted by electrons with energies of 150–240 GeV show that, as the electrons move through crystals at small angles to the principal crystallographic axes, there is a sudden rise in the radiation yield compared to the ordinary Bethe–Heitler bremsstrahlung emission in an amorphous medium. The intensity of the radiation in the spectral peak is then two orders of magnitude higher, and the electrons lose almost all their energy to radiation over thicknesses that are more than an order of magnitude less than the radiation length in the amorphous material. Theoretical calculations based on the use of the synchrotron approximation for the radiation cross sections including quantum mechanical effects[3–6] provide a qualitative description of the properties of the spectrum at these energies.

The quantity measured in the experiments is $\omega W_\omega(E,z)$, where $W_\omega(E,z)$ is the probability that the total energy of all the photons emitted by electrons with initial energy E is equal to ω, and z is the crystal thickness. In practice, however, one is interested in knowing the number $N_\omega(z)$ of single hard photons emitted over the entire time of passage through the crystal, where ω now represents the energy of a single photon. This quantity has not yet been measured experimentally because of technical difficulties, but the problem has been examined theoretically to some extent.[6,7]

In this paper we present the results of some Monte Carlo calculations of $N_\omega(z)$. The computational technique has been described in detail elsewhere,[4,8] and we have used the following assumptions: (a) it was assumed that the electrons uniformly fill the entire region available to them in the transverse plane and (b) the cross sections for emission of individual photons were calculated using the quantum mechanical synchrotron formulas.[9,10] In the calculations multiple scattering of electrons on the atoms of the crystal lattice was taken into account, along with the reduction in transverse energy owing to radiation. As opposed to our earlier papers,[4,5] in these calculations we have calculated the transverse coordinates of the emission point, whereas in Refs. 4 and 5 cross sections averaged over a transverse uniform distribution were used.

In order to estimate the efficiency of oriented crystals compared to amorphous media it is necessary to compare the characteristics of the radiation for both cases, not for targets of the same thickness, as done previously,[1–4] but for targets with thicknesses which can be regarded as optimal for both cases. In the case of amorphous media, this thickness is of the order of the radiation length $L_{\rm rad}$ and for crystals, this thickness is several hundred microns for incidence angles of the order of the Lindhard critical angle.

It is known that the Bethe–Heitler spectrum for high-energy electrons can be described by a universal function, i.e., the shape of the photon spectrum for a target of given thickness (measured in units of the radiation length $L_{\rm rad}$) is essentially independent of the atomic number of the target material and initial electron energy. (Here we are speaking, not of a differential cross section for emission per unit path length, but of a cross section for emission in a target with a finite thickness, taking the multiplicity of the radiation into account.) This is confirmed by Fig. 1, which shows the results of our numerical simulation of the spectra $N_\omega(z)$ of single photons emitted by electrons with different energies as they pass through different amorphous targets. In these calculations we have taken into account the multiphoton character of the emission and also the absorption of photons due to electron–positron pair production. The elementary cross sections for emission and e^+e^- pair production have been calculated using the conventional Bethe–Heitler formulas. The suppression of radiation in the soft region of the spectrum on account of the Landau–Pomeranchuk effect has been neglected. The low frequency threshold for bremsstrahlung was assumed to be $\omega_{\min}=0.005E$ in the numerical simulations.

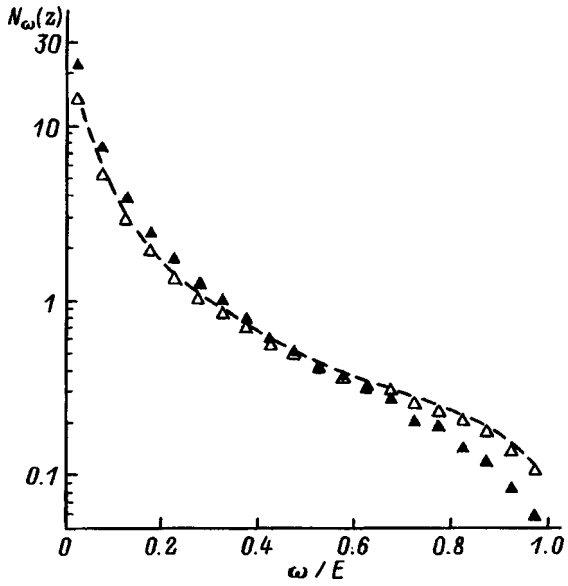

FIG. 1. The number N_ω of photons emitted in an amorphous medium. The dashed curve is for 150 GeV electrons in silicon of thickness $z=L_{\rm rad}/2$; ▲ — for 150 GeV electrons in silicon of thickness $z=L_{\rm rad}$; △ — for 240 GeV electrons in germanium of thickness $z=L_{\rm rad}/2$.

Figure 1 shows that the photon spectrum in an amorphous target can be described by a universal function if the target thickness is taken in units of the radiation length $L_{\rm rad}$,

$$1/L_{\rm rad}=4\alpha Z^2 r_e^2 N \ln(183Z^{-1/3}),$$

where $\alpha=1/137$, Z is the atomic number of the target, r_e is the classical radius of the electron, and N is the number of atoms per unit volume of the target.

As Fig. 1 implies, the optimum thicknesses of amorphous targets for obtaining the highest number of hard gamma rays with energies $\omega>0.8E$ are of the order of $z\sim 0.5L_{\rm rad}$. In thicker crystals the number of high energy photons at the exit decreases owing to electron–positron pair production. In the following discussion we shall compare the results for an oriented crystal with amorphous targets of thickness $z=L_{\rm rad}/2$.

If a relativistic electron moves in a crystal near the crystallographic axes, then the high-power coherent electromagnetic emission in the continuum potential of these axes (channelling radiation) is accompanied by incoherent bremsstrahlung on the individual atoms of the crystal. In an amorphous medium the number of collisions of a passing particle with atoms obeys a Poisson distribution, with the average number of collisions being $\langle n_{\rm am}\rangle=N\sigma z$, where σ is the total scattering cross section. In our calculations the scattering cross section was computed using the Molière atomic potential including the Debye–Waller factor.[8] According to these calculations, the mean free path $1/\sigma N$ in different amorphous targets was 2.8 μm in diamond ($Z=6$), 1.0 μm in silicon ($Z=14$), 0.25 μm in germanium ($Z=32$), and 0.04 μm in gold ($Z=79$). In the following we shall refer to irregular collisions with individual atoms as close collisions, as opposed to the distant collisions that lead to a regular deflection of the electron trajectory as a result of the continuum potential.

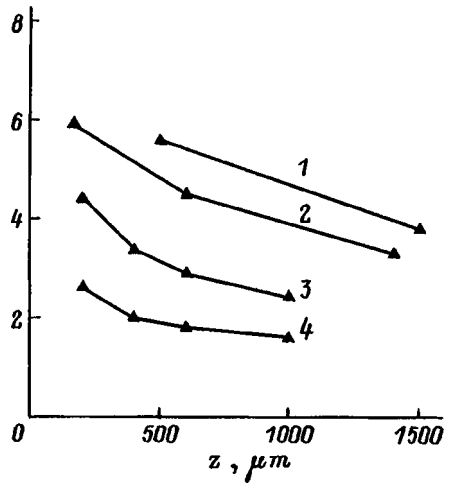

FIG. 2. Ratio of the number of close incoherent collisions in oriented crystals to the number of collisions in amorphous targets as a function of the crystal thickness for 150 GeV electrons. *1* — ⟨110⟩ diamond, *2* — ⟨110⟩ silicon, *3* — ⟨110⟩ germanium, and *4* — ⟨100⟩ gold.

For axially channeled electrons with a transverse energy ε, the number of incoherent close collisions with individual atoms exceeds the same number for an amorphous medium by a factor of $S_0/S(\varepsilon)$,[8] where $S(\varepsilon)$ is the area accessible to an electron in the transverse plane and S_0 is the transverse area per atomic string. This increase in the contribution from incoherent scattering is a consequence of the redistribution of the flux of negatively charged particles in the transverse phase space (the flux peaking effect).[11] As a result, the statistical distribution of the number of close collisions with individual atoms in an oriented crystal differs substantially from a Poisson distribution, and the contribution of this factor becomes greater with increasing electron energy owing to reduced dechannelling.

Figure 2 illustrates the increase in the number of irregular close collisions in oriented crystals as compared to the corresponding amorphous media for 150 GeV electrons in different materials. The ordinate in Fig. 2 is the ratio of the number of collisions of electrons with atoms in a crystal to the number of collisions in an amorphous medium. For light materials (C, Si) the number of close collisions in oriented crystals can be 5–6 times the number in amorphous media. In heavy crystals this ratio drops to ~2 because of strong multiple scattering. The calculations shown in Figs. 2–7 were done for electron beams with a divergence of $0.2\Theta_L$ (where Θ_L is the Lindhard critical angle).

The differences in the statistics of close collisions in the amorphous material and in an oriented crystal lead to differences in the incoherent bremsstrahlung yield. Figure 3 shows spectra of the incoherent radiation at individual atoms in a 600 μm-thick oriented germanium crystal for different electron energies. The dashed curves in Figs. 3–7 represent the Bethe–Heitler spectrum in an amorphous target. It is clear from Fig. 3 that the redistribution of the electrons in the transverse plane leads to a large enhancement in the contribution from incoherent bremsstrahlung in an oriented crystal compared to the amorphous material, as well as to a dependence of the shape of the emission spectrum on the energy.

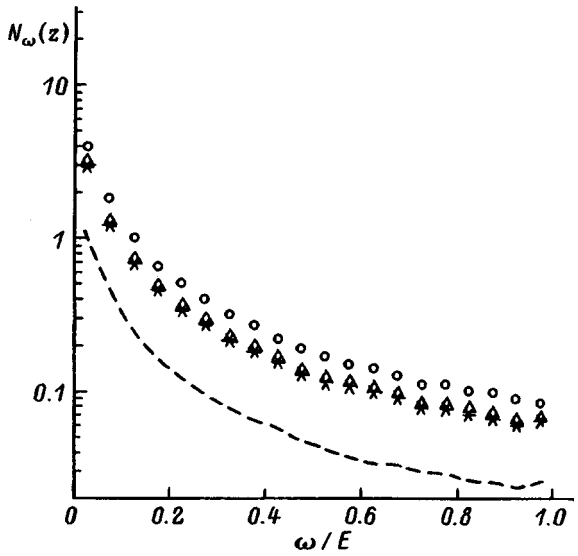

FIG. 3. Spectrum of single photons due to incoherent bremsstrahlung in an oriented ⟨110⟩ germanium crystal: $z=600$ μm; electron energy (GeV): * — 150, △ — 240, ○ — 1000. Amorphous germanium of the same thickness.

Combined spectra of the photons emitted owing to coherent emission in the continuum potential of the atomic strings and to incoherent emission at individual atoms are shown in Figs. 4 and 5 for 150 GeV electrons in ⟨110⟩ crystalline silicon and for 150 and 240 GeV electrons in ⟨110⟩ germanium. The angular divergence of the electron beam as it enters the crystal is $0.2\Theta_L$, where Θ_L is the Lindhard critical angle. The dashed curves in Figs. 4–7 correspond to the emission spectra in amorphous targets with optimal thicknesses $z=L_{\text{rad}}/2$. Figures 4 and 5 show that up to electron energies $\leqslant 300$ GeV, the number of emitted photons in an amorphous material of thickness $z=L_{\text{rad}}/2$ exceeds the corresponding number emitted in oriented crystals with thicknesses of 600 and 1400 μm in the hard part of the

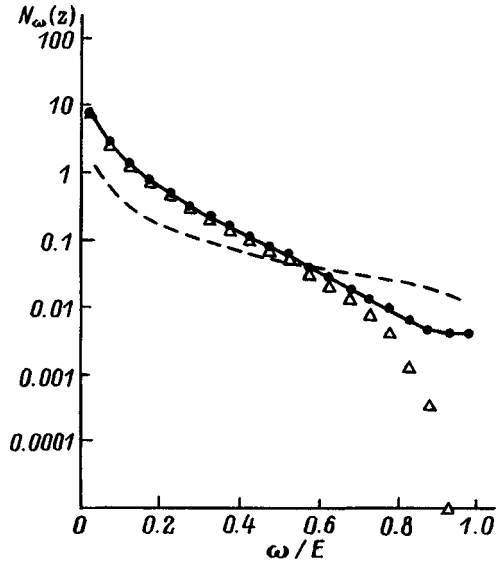

FIG. 4. Single photon spectrum for 150 GeV electrons in ⟨110⟩ silicon; $z=1400$ μm (solid curve); contribution of the synchrotron-like coherent part (△).

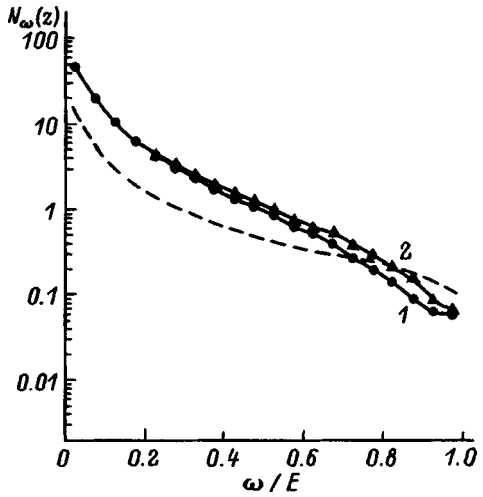

FIG. 5. Single photon spectrum for 150 (*1*) and 240 GeV (*2*) electrons in ⟨110⟩ germanium; $z=600$ μm.

spectrum $\omega \geqslant (0.6-0.80)E$, while in the soft part of the spectrum the oriented crystal is more efficient. In addition, the emission in the hard part of the spectrum for an oriented crystal is mainly from the incoherent contribution (cf. Fig. 4, where the contribution of the synchrotron-like emission is indicated by the hollow triangles). The coherent part, on the other hand, is the sum of contributions from channelled and quasichannelled electrons. Here the synchrotron character of the emission spectrum means that the cross sections for emission by quasichannelled electrons, averaged over the transverse plane, are independent of their transverse energy, while for the channelled particles, with finite transverse trajectories, the emission cross sections depend strongly on the transverse energy. The total photon emission cross section per unit length in the synchrotron approximation depends weakly on the total energy of the electrons. For synchrotron-like emission, the mean free path averaged over the transverse coordinate for 150 GeV quasichannelled electrons is 85 μm in diamond, 135 μm in silicon, 104 μm in germanium,

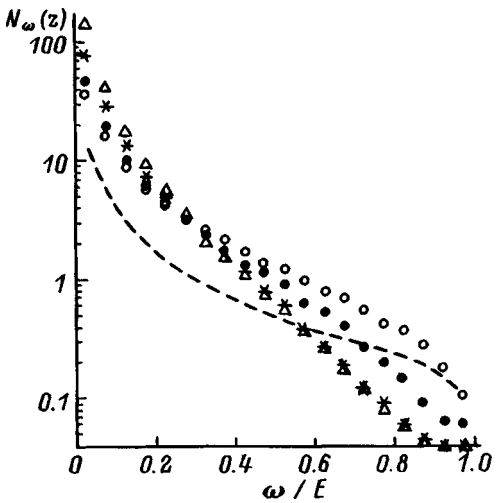

FIG. 6. Single photon spectrum for 150 GeV electrons in various oriented crystals: * — 2000 μm, ⟨110⟩ diamond; △ — 1400 μm, ⟨110⟩ silicon; ● — 600 μm, ⟨110⟩ germanium; ○ — 200 μm, ⟨100⟩ gold.

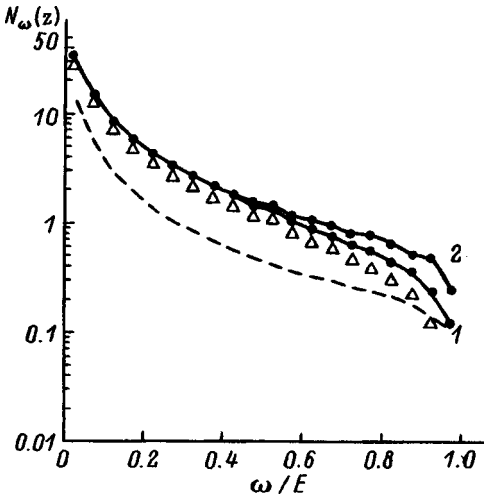

FIG. 7. The same type of spectrum as in Fig. 6 for 200 μm-thick $\langle 100\rangle$ gold: *1* — 240, *2* — 1000 GeV.

and 50 μm in gold. When the electron energy is raised to 1000 GeV, the mean free path in germanium increases to 140 μm. For channelled electrons (the transverse energy of these electrons is negative), the mean free path increases sharply as the absolute value of the transverse energy is raised; thus, for transverse energies $\varepsilon \sim -U_0/2$, the mean free path decreases by an order of magnitude (here U_0 is the depth of the potential barrier in the atomic string) compared to the quasichannelled electrons. In our calculations, the thicknesses of the oriented crystals were chosen to be close to optimal. In thicker crystals, the contribution from the absorption of hard gamma rays increases owing to the coherent production of electron–positron pairs in the transverse electrostatic field of the atomic strings.

The number N_ω of emitted gamma rays is plotted in Fig. 6 as a function of their energy ω for 150 GeV electrons in different crystals. It is clear that the heavy crystals are more efficient than light crystals for purposes of obtaining a large number of hard gamma rays. As opposed to the amorphous materials, the photon spectra in oriented crystals cannot be represented in terms of any universal curve. The efficiency of oriented crystals increases with the electron energy. This is confirmed by the data shown in Fig. 7, which illustrates the calculations for 240 and 1000 GeV electrons in a 200-μm-thick $\langle 100\rangle$ gold crystal. In this case, the number of emitted photons for the oriented crystal exceeds the number for an amorphous target of thickness $z = L_{\rm rad}/2$ over the entire range of emitted photon energies.

There is some practical interest in knowing the number of photons emitted per electron within a given frequency interval. These data are shown in Table I. The results for the amorphous medium correspond to 150 GeV electrons in silicon with a thickness of $L_{\rm rad}/2$.

In experiments at electron energies of 150–300 GeV, oriented crystals with thicknesses of several hundred microns are usually used. In order to estimate the efficiency of these crystals for obtaining the maximum number of hard gamma rays, it is necessary to compare them with unoriented (amorphous) substances having thicknesses of the order of $L_{\rm rad}/2$.

The spectrum of the photons emitted by electrons moving near the atomic axes in an oriented crystal is the sum of two contributions: coherent emission in the field of the continuum potential of the atomic strings and incoherent emission on individual atoms in the crystal lattice. For electron energies above $\sim$100 GeV, the coherent contribution is given to a sufficient degree of accuracy by the standard quantum mechanical synchrotron formulas, while the incoherent contribution is given by the Bethe–Heitler formulas for an amorphous medium, but including the effect of the spatial redistribution of the charged particle flux in the transverse phase space (flux peaking effect). This last effect leads to a substantial enhancement in the contribution of the incoherent part compared to that for an amorphous target of the same thickness.

For relatively soft photons (with $\omega/E \sim 0.1$–0.3) emitted by 150–300 GeV electrons in oriented silicon and germanium crystals, the synchrotron-like coherent part exceeds the incoherent part by an order of magnitude. Because of the more rapid decrease in the synchrotron emission cross section with increasing photon energy as compared to the Bethe–Heitler formulas, the emission of hard photons with energies $\omega \geqslant (0.6$–$0.8)E$ in these crystals is caused mainly by the incoherent part at electron energies of 150–300 GeV. Here an amorphous target of thickness $\sim L_{\rm rad}/2$ turns out to be more efficient for generating photons with energies $\omega \geqslant (0.6$–$0.8)E$.

In heavy oriented crystals (e.g., gold or tungsten), on the other hand, even when they are relatively thin ($\sim$200 μm), the number of radiated photons at the same energies may

TABLE I. The number of single photons with energies ω lying in different intervals (here $u = \omega/E$).

	E, GeV	z, μm	$0.1<u<0.2$	$0.2<u<0.5$	$0.5<u<0.8$	$0.8<u<0.9$	$u>0.9$
C $\langle 110\rangle$	150	2000	1.38	0.756	0.075	0.005	0.004
Si $\langle 110\rangle$	150	1400	1.04	0.675	0.078	0.0052	0.004
Ge $\langle 110\rangle$	150	600	0.81	0.635	0.144	0.011	0.0064
	240		0.86	0.78	0.183	0.018	0.0078
	1000		0.88	0.89	0.280	0.045	0.0210
Au $\langle 100\rangle$	150	200	0.735	0.741	0.231	0.0325	0.0143
	240		0.738	0.782	0.260	0.040	0.0180
	1000		0.710	0.790	0.310	0.060	0.0360
Amorph.		$L_{\rm rad}/2$	0.26	0.27	0.10	0.021	0.014

Note: The initial angular divergence of the electron beam is $0.2\theta_L$, where θ_L is the Lindhard critical angle.

exceed the number emitted from thick amorphous targets over the entire spectrum. Unlike with amorphous targets, the efficiency of oriented crystals as sources of hard photons increases as the energy of the incident electrons is raised.

We thank Prof. Erik Uggerhoj for helpful discussions of the problems examined in this paper, as well as of the problems involved in setting up experiments to measure single photon spectra at these energies.

[1] A. Belkacem *et al.*, Phys. Lett. B **213**, 211 (1986).
[2] R. Medenwaldt *et al.*, Phys. Lett. B **242**, 517 (1990).
[3] Yu. V. Kononets, J. Moscow Phys. Soc. **2**, 71 (1992).
[4] M. Kh. Khokonov, Nucl. Instrum. Methods Phys. Res. B **74**, 375 (1993).
[5] V. V. Beloshitsky, M. A. Kumakhov, and A. Kh. Khokonov, Nucl. Instrum. Methods Phys. Res. B **62**, 207 (1991).
[6] A. Kh. Khokonov and M. Kh. Khokonov, Pis'ma Zh. Tekh. Fiz. **22**(5), 14 (1996) [Tech. Phys. Lett. **22**, 183 (1996)].
[7] M. Kh. Khokonov, Proc. RREPS-93, Tomsk (1993), p. 231.
[8] M. Kh. Khokonov and F. K. Tuguz, Nucl. Instrum. Methods Phys. Res. B **82**, 46 (1993).
[9] V. N. Baĭer, V. M. Katkov, and V. M. Strakhovenko, *Electromagnetic Processes at High Energies in Oriented Single Crystals* [in Russian], Nauka, Moscow (1989).
[10] J. C. Kimball and N. Cue, Phys. Rep. **125**, 68 (1985).
[11] M. A. Kumakhov, Usp. Fiz. Nauk **15**, 427 (1975).

Translated by D. H. McNeill

Fluctuation mechanism for formation of discontinuous tracks by fast ions in crystals

V. A. Belyĭ and F. F. Komarov

Belarus State University, 220064 Minsk, Belarus
(Submitted March 26, 1997; resubmitted August 18, 1997)
Zh. Tekh. Fiz. **68**, 42–45 (September 1998)

The effect of multiple loss and trapping of electrons on the formation of discontinuous tracks by high-energy ions in crystals is examined. A proposed model of charge fluctuations makes it possible to estimate quantitatively the longitudinal size of the defects in a discontinuous track, while an extended thermal spike model, which includes Coulomb repulsion, yields reasonable values for the transverse dimensions of the defects. © *1998 American Institute of Physics.* [S1063-7842(98)00909-X]

INTRODUCTION

At present the most widely accepted model for the formation of latent tracks in crystals is the thermal spike model. According to this model, the energy lost by a high-energy ion excites the electronic subsystem of the crystal, while the energy of the excited electrons is subsequently transferred to the lattice atoms through an electron–phonon interaction and leads to local melting of the target. Because of the high rate of cooling, the melted region cannot crystallize epitaxially and solidifies in an amorphous or fine-grained crystalline state, forming a latent track.

The purpose of this paper is to generalize the thermal spike model for explaining the formation of discontinuous tracks. In the proposed model the critical parameter for formation of an amorphous region is considered to be the magnitude of the inelastic energy losses by an ion along a unit path in the crystal. If these losses exceed a certain threshold value, then disordering or even melting of a local region of the target takes place, and, as a consequence, a track is formed. Thus the formation of a discontinuous track can be related to fluctuations in the inelastic energy losses by an ion, which, in turn, are closely associated with fluctuations in the effective charge of the ion.[1]

For comparing the proposed model with experimental data, we have used the results of a recent experiment by Gaiduk *et al.*[2] According to their data, when an indium phosphide (InP) crystal is bombarded by 250 MeV xenon (Xe) ions at a fluence of 7×10^{12} cm^{-2}, at a depth on the order of 6–10 μm the continuous track from the Xe becomes discontinuous, with defects of about 35 nm in length and with this same distance between defects. The overall length of the discontinuous tracks is about 5 μm. The proposed model has also been compared with experimental data on the formation of discontinuous tracks in germanium.[3]

CROSS SECTIONS FOR CAPTURE AND LOSS OF ELECTRONS BY IONS

The basis of the model for formation of discontinuous tracks can be taken to be oscillations in the effective charge of the ion about some average value as it moves in the target. For determining the average charge we can use a semiempirical formula proposed by Dmitriev and Nikolaev[4] for ions with energies above 100 MeV:

$$q_0 = Z_i\left[1+\left(\frac{1}{Z_i^{\alpha}}\frac{v}{v'}\right)^{-1/k}\right]^{-k}, \tag{1}$$

where Z_i is the nuclear charge of the ion, v is its velocity, $k=0.6$, $v'=3.6\times10^6$ m/s, and $\alpha=0.48$.

As an ion moves through the target it loses its energy through elastic and inelastic collisions. Making use of the fact that elastic collisions can be neglected in the case of high-energy ions, we obtain the variation in the energy loss by a 250 MeV Xe ion in indium phosphide shown in Fig. 1. It is clear from this figure that the energy losses at the depth for formation of a discontinuous track (about 10 μm) are 12 keV/nm. At this depth the energy of the ion is 100 MeV and its velocity is 1.2×10^9 m/s. This implies that the average charge of the Xe during formation of a discontinuous track is $q_0\approx24.7$.

To determine the average distance over which a fluctuation in the ionic charge occurs, we use the effective cross sections for capture/loss of an electron by an ion moving in the solid. Several theoretical models have been proposed for determining this cross section for ions that are in the equilibrium (average) charge state. In the following we shall use the Bohr formula for heavy ions in heavy targets[4]

$$\sigma_0 \approx \pi a_0^2 (Z_i^{1/3}+Z_T^{1/3})\left(\frac{v_0}{v}\right)^2, \tag{2}$$

where σ_0 is the capture/loss cross section for an electron by an ion, Z_i is the nuclear charge of the ion, Z_T is the nuclear charge of the target atoms, v is the ion velocity, and $v_0=2.19\times10^6$ m/s.

For the Xe ion in the region of formation of a discontinuous track, this formula yields $\sigma_0=1.8\times10^{-17}$ cm^2.

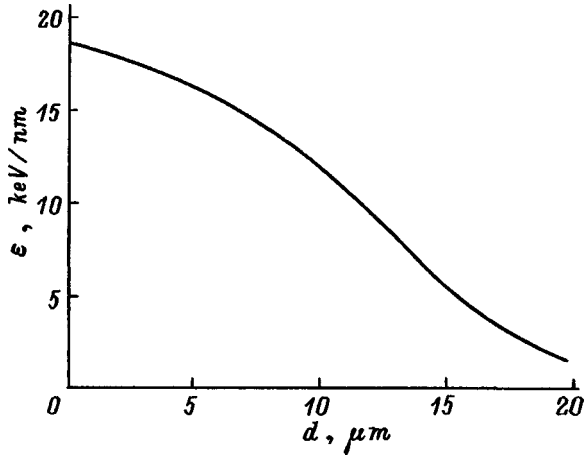

FIG. 1. The energy loss ε by 250 MeV Xe ions in InP as a function of depth d.

FLUCTUATIONS IN THE CHARGE STATE OF THE ION AND THE FORMATION OF DISCONTINUOUS TRACKS

Given that the probability of a change in the charge state of the ion over a path length x is given by $P=N\sigma x$, where N is the atomic density of the target, for the statistical mean free path for charge exchange we can write

$$\lambda=\frac{1}{N\sigma}. \tag{3}$$

Using the above values for σ, we obtain a mean free path for charge exchange of Xe ions in InP of $\lambda=14$ nm. This value is somewhat shorter than the experimentally measured $\lambda\approx 35$ nm.[2] This difference can be explained by a need for stronger fluctuations in the energy losses by the ion, i.e., it is necessary to include processes involving the capture/loss of several electrons. Thus the relative probabilities for processes involving a multiple change in the charge is roughly 60% for capture/loss of two electrons, 40% for three electrons, and 20% for four electrons.[4] Processes with larger changes in the charge are improbable and we shall neglect them below. In view of what we have said, for the length of the defects in the region of a discontinuous track we obtain a value, $\lambda\approx 30-35$ nm, which is 2–3 times greater than that calculated using Eq. (3) and which is thus in good agreement with the experimental value.[2] Given that for such fluctuations in the charge of the ion, its energy losses may vary by up to 50% of their magnitude (owing to the quadratic dependence on the ionic charge), the length of a discontinuous track from an Xe ion in indium phosphide ends up being roughly equal to 4-5 μm (Fig. 1), which has been observed experimentally.[2]

If the proposed model is applied to data on the bombardment of germanium by 150 MeV iodine ions,[3] then Eq. (3) gives $\lambda\approx 21$ nm, which is in fairly good agreement with experiment (15 nm), from which we may assume that processes involving the loss/capture of single electrons are sufficient for the formation of discontinuous tracks by iodine ions in germanium.

COMBINATION MODEL OF TRACK FORMATION

At present the most widely used model of track formation is the thermal spike model. In this model it is assumed that the energy lost as the ion moves causes local melting of the target near the ion trajectory, and if the melted region that is formed cools rapidly it cannot crystallize, and a region of amorphous or finely dispersed material, i.e., a track, develops around the ion trajectory. Despite its qualitative agreement with experiment, the thermal spike model has a number of shortcomings. In particular, this model does not take into account the formation of a nonequilibrium charge as a result of the escape of the electrons excited out of the ion trajectory. At the same time, the loss of even one electron per ten atoms leads to an additional Coulomb repulsion energy of ~ 0.3 eV per atom, which is comparable to the energy required for melting (≈ 1 eV in indium phosphide).

Another shortcoming of the proposed calculations based on the thermal spike model is the neglect of the energy required to melt the target material (although this energy can be several times the energy required to heat it to the melting point). It is most convenient to introduce this energy at once into the effective melting temperature, referring to it as the total melting temperature. Thus for indium phosphide, the total melting temperature will be about 2500 K (as opposed to 1335 K for the customary melting temperature).

To determine the heating of the target we shall use a model analogous to that proposed by Izui.[5] Thus, assuming that the ionization potentials of the atoms are the same as the classical energy levels in the Bohr model and that the cross section for excitation of the target electrons obeys the Rutherford formula,[6] we obtain an average of 300 detached electrons per nanometer of ion path with an average energy of 27 eV (for losses of 10 keV/nm) or 38 eV (for losses of 14 keV/nm). In escaping from the excitation center, the electrons interact with the longitudinal acoustic phonons and transfer their energy to the lattice at a rate of[7]

$$\left|\frac{d\varepsilon}{dt}\right|=\frac{2^{3/2}}{\pi}\frac{C^2}{\hbar^4}\frac{m^{5/2}}{NM}\varepsilon^{3/2}, \tag{4}$$

where ε is the electron energy, C is the deformation potential constant (assumed equal to 7.3 eV), m is the electron mass, M is the average mass of the target atoms, and N is the atomic density of the target.

Integrating this expression for the density n of energy loss by the excited electrons, we obtain

$$Q(t)=n\left|\frac{d\varepsilon}{dt}\right|=nA\left(\frac{A}{2}t+\varepsilon_0^{-1/2}\right)^{-3}, \tag{5}$$

$$A=\frac{2\sqrt{2}}{\pi}\frac{C^2}{\hbar^4}\frac{m^{5/2}}{NM}. \tag{6}$$

For calculating the heating of the target in cylindrical coordinates we use the expression[6]

$$T(r,t)=\frac{1}{4\pi K}\int_0^t\frac{Q(t')}{t-t'}\exp\left\{-\frac{r^2}{4D(t-t')}\right\}, \tag{7}$$

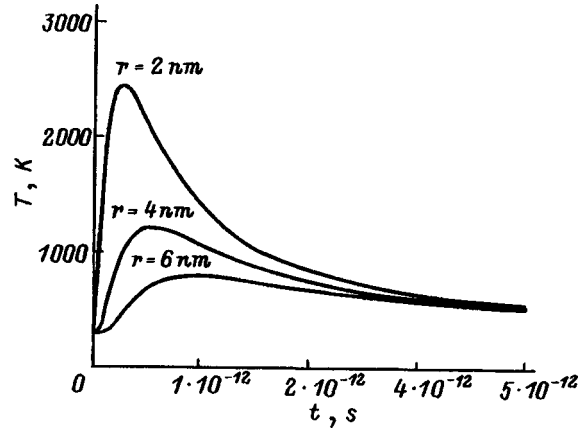

FIG. 2. The temperature (T) distribution around the trajectory of a xenon ion in indium phosphide for energy losses ε of 10 keV/nm.

where K and D are the thermal conductivity and thermal diffusivity, respectively, of the target, n is the number of excited electrons contributing to local heating of the target (roughly half of the overall number of excited electrons), and ε_0 is the average energy of these electrons.

These calculations yield the curves shown in Figs. 2 and 3. It is clear from these figures that if we neglect the nonequilibrium charge (in which case the total melting temperature is 2500 K), then even for the maximum energy losses by the ion, the radius of the melted region is less than two nanometers (Fig. 3) and apparently cannot cause the formation of an amorphous region. At the same time, even a qualitative allowance for the Coulomb repulsion of the target atoms, as done above, leads to a 0.3 eV enhancement in the energy of the atoms, which is equivalent to a reduction in the total melting temperature by 30% (i.e., to 1700 K). Such a reduction in the total melting temperature means that in the regions of the ion trajectory where the ion energy losses are 10 keV/nm, the radius of the melted region is 2 nm, i.e., a track is not formed, while in the regions where the losses are 14 keV/nm, the melted region is about 4 nm, i.e., a track is formed. Thus the proposed thermal spike model can explain the formation of a discontinuous track and yields reasonable values for the radius of the deformed region.[2]

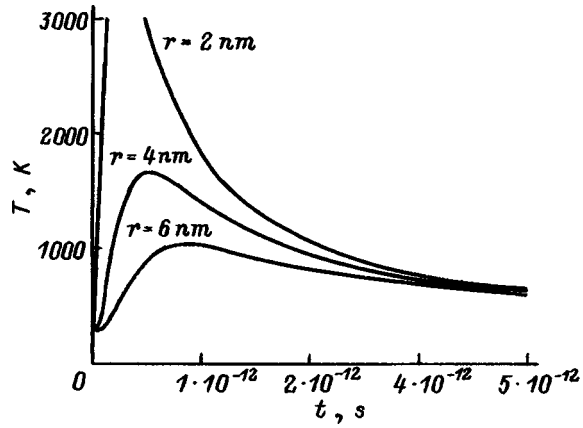

FIG. 3. The temperature (T) distribution around the trajectory of a xenon ion in indium phosphide for energy losses ε of 14 keV/nm.

CONCLUSION

The model proposed here for fluctuations in the ionic charge state makes it possible to explain, qualitatively and quantitatively, the formation of discontinuous tracks as high-energy ions move in crystals. The calculations presented here show that in some crystals it is sufficient for an ion to lose/capture one electron in order to form discontinuous tracks (e.g., the iodine ion in germanium), while in other crystals processes involving several electrons are required (e.g., for the xenon ion in indium phosphide).

An analysis of the thermal spike model has shown that nonequilibrium charge created by the passing ion plays a major role in track formation. Semiquantitative allowance for this charge has made it possible to determine the transverse dimensions of the defects in a discontinuous track and to obtain numerical values consistent with experimental data.[2]

This paper was partially supported by the International Soros Science Education Program (ISSEP).

[1] F. F. Komarov, A. P. Novikov, and A. F. Burenkov, *Ion Implantation* [in Russian], Izd-vo Universiteta, Minsk (1994), 303 pp.
[2] P. I. Gaiduk, F. F. Komarov, W. Wesch *et al.*, Phys. Rev. Lett., in press.
[3] S. Furino *et al.*, Nucl. Instrum. Methods Phys. Res. B **107**, 223 (1996).
[4] H. D. Betz, Rev. Mod. Phys. **44**, 465 (1972).
[5] K. Izui, J. Phys. Soc. Jpn. **20**, 915 (1965).
[6] L. D. Landau and E. M. Lifshitz, *Quantum Mechanics: Non-Relativistic Theory*, 3rd ed. [Pergamon Press, Oxford (1977); [Nauka, Moscow (1974)].
[7] E. M. Conwell, in *Solid State Physics*, Suppl. 9, Academic Press, New York (1967) [*Kinetic Properties of Semiconductors in High Electric Fields*, Mir, Moscow (1970), 384 pp.].

Translated by D. H. McNeill

Iron garnet films with enhanced thermal stability of their magnetic parameters

S. I. Yushchuk, P. S. Kostyuk, and I. E. Lopatinskiĭ

Lvov Polytechnic State University, 290646 Lvov, Ukraine
(Submitted May 23, 1997)
Zh. Tekh. Fiz. **68**, 46–50 (September 1998)

The ferromagnetic resonance in $Y_3Fe_{5-x}Ga_xO_{12}$ $(0 \leqslant x \leqslant 0.63)$, iron garnet films obtained by liquid phase epitaxy on substrates of gadolinium gallium garnet is studied at temperatures of 213–353 K. It is found that in the case of liquid phase epitaxy the distribution coefficient of the gallium in the films varies from 2.2 to 4.0, depending on the composition and growth conditions. It is found that the resonance magnetic fields can be temperature stabilized through temperature-induced changes in the saturation magnetization and anisotropy field. © *1998 American Institute of Physics.* [S1063-7842(98)01009-5]

In recent years there has been increasing interest in the use of single crystal films of the iron garnets in microwave devices employing magnetostatic waves (MSWs).[1,2] The basic requirements for these devices are minimal magnetic losses during propagation of the MSWs and high-frequency stability in the operating temperature range. The magnetic losses are determined by the width ΔH of the ferromagnetic resonance line. For films of yttrium iron garnet (YIG), one can obtain a minimum of $\Delta H \leqslant 0.5$ Oe. One of the ways of improving the operating stability of these MSW devices may be to use iron garnet films with enhanced thermal stability of their magnetic parameters. The YIG films used in MSW devices, with their minimal magnetic losses, however, do not have satisfactory thermal stability.

This paper is devoted to a search for iron garnet films with minimal ferromagnetic resonance line widths and enhanced thermal stability. For this purpose, we have examined the possibility of raising the thermal stability of the parameters of $Y_3Fe_{5-x}Ga_xO_{12}$ $(0 \leqslant x \leqslant 0.6)$ iron garnet films through different temperature variations in the saturation magnetization $4\pi M_s$ and the anisotropy field H_a.

The films were grown by the liquid phase epitaxy method using isothermal loading of a horizontal substrate of (111) gadolinium gallium garnet (GGG) in a supercooled fluxed melt of the garnet-forming oxides Fe_2O_3, Y_2O_3, and Ga_2O_3 and a $PbO–B_2O_3$ flux with a total mass of 6 kg. The composition of the melting stock was calculated from the molar proportions of $R_1–R_4$ (Ref. 3). These proportions were chosen on the basis of considerations of the stability of the garnet phase for compositions containing different amounts of gallium ions. As the parameter x in the chemical formula of the iron garnet films was changed from 0.03 to 0.6, the proportions $R_1–R_4$ had the following values or ranges of values: $R_1 = 28.35–29.96$, $R_2 = 17.2–685.0$, $R_3 = 15.6$, and $R_4 = 0.149$. The ratio $R_2 = Fe_2O_3/Ga_2O_3$ characterizes the amount of gallium oxide introduced into the stock for substitution for the iron oxide. High saturation temperatures of the melt, 1220–1235 K, were chosen based on the requirement of minimal entry of Pb^{2+} ions into the epitaxial layers.[4]

The grown Ga:YIG films with $x \leqslant 0.3$ and a thickness of 1–10 μm had a smooth, shiny surface without bumps or microcracks. However, as the film thickness and gallium content were increased, the surface quality deteriorated. It was not possible to grow high-quality films with $x \geqslant 0.6$ and thicknesses greater than 5 μm because of the large difference in the crystal lattice parameters of the film and substrate, $\Delta a \geqslant 0.015$ Å. The gallium ion content in the Ga:YIG films according to local x-ray microanalysis differed slightly from the calculated values (see Table I). This discrepancy can be explained by the fact that in calculating the compositions of the stock we neglected the variation in the distribution coefficient[5] K_{Ga} with the gallium content and the growth temperature regime. In the calculations for the stock we used $K_{Ga} = 2.2$. The distribution coefficient of the gallium in the films was determined according to the formula

$$K_{Ga} = \frac{\left(\frac{x_{Ga}}{x_{Ga}+x_{Fe}}\right)_f}{\left(\frac{x_{Ga}}{x_{Ga}+x_{Fe}}\right)_m}, \tag{1}$$

where x_{Ga} and x_{Fe} are the gallium contents of the film (f) and fluxed melt (m).

It can be seen from the Table I that the values of K_{Ga} for the Ga:YIG films with $x \leqslant 0.1$ differ substantially the published value, $K_{Ga} = 2.2$.[5]

The composition of the Ga:YIG substituted films depends, not only on the composition of the fluxed melt, but also on the rate of growth, which, in turn, depends on the degree of supercooling of the melt, ΔT. Changing the concentrations of Ga^{3+} and Pb^{2+} in the Ga:YIG films leads to changes in the parameters $4\pi M_s$ and ΔH. Figure 1 shows plots of the film growth rate f, $4\pi M_s$, and ΔH as functions of the degree of supercooling ΔT for a fluxed melt with $x = 0.1$. The ferromagnetic resonance parameters were measured using a waveguide technique[6] on samples with diameters of 0.1 mm prepared by chemical etching.[7]

It is clear from Fig. 1 that, with increasing supercooling, the rate of film growth increases linearly. The saturation magnetization also increases. When the degree of supercooling is varied from 5 to 40 K, the distribution coefficient K_{Ga}

TABLE I. Compositions of the Ga:YIG films, crystal lattice parameters, and gallium distribution coefficients.

Calculated composition* x	Composition of ferrite film x	Lattice parameter of GGG substrate, Å	Lattice parameter of film, Å	Distribution parameter of Ga^{3+}, relative units
0.03	0.028	12.3821	12.3723	4.0
0.05	0.053	12.3826	12.3718	3.1
0.1	0.140	12.3822	12.3735	2.8
0.3	0.380	12.3826	12.3708	2.4
0.5	0.560	12.3821	12.3691	2.4
0.6	0.630	–	–	2.2

*From the gallium oxide content in the melting stock.

falls from 3.39 to 2.23, which indicates a reduction in the Ga^{3+} ion content of the films. Since the gallium ions replace Fe^{3+} ions mainly at tetrahedral sites, this should lead to a rise in the saturation magnetization, as is observed.

As for the parameter ΔH, in Fig. 1 it passes through a minimum at $\Delta T = 18$ K and then rises again. The rise in ΔH is most likely caused by an increase in the amount of Pb^{2+} ions entering the film from the melt, at a rate proportional to the rate of growth of the ferrite film.[8] The existence of a minimum in the ΔH curve can be explained by mutual charge compensation of Pb^{2+} and Pt^{4+} ions, the latter being always present in a small amount in the stock owing to the platinum crucible.[3]

Figure 2 shows the width of the ferromagnetic resonance line and the anisotropy field as functions of the gallium ion content in Ga:YIG substituted films grown at a fixed supercooling temperature $\Delta T = 10$ K. It is clear that, with increasing amounts of gallium in the films, ΔH initially decreases, reaching a minimum of 0.2 Oe at $x = 0.18$. This figure also shows a plot of the anisotropy field H_a as a function of the concentration, a curve which has a sharp minimum that is shifted somewhat relative to the minimum in the ΔH curve. It may be concluded that these curves are correlated, i.e., the width of the ferromagnetic resonance line of Ga:YIG films depends on the magnitude of the anisotropy field. ΔH for single crystal Ga:YIG films increases even when $x \geqslant 0.3$, unlike for bulk single crystal Ga:YIG, in which the width of the ferromagnetic resonance line hardly changes up to $x = 0.8$.[6]

The difference in the behavior of ΔH in films and single crystals is caused by the fact that the anisotropy field in the bulk single crystals is crystallographic in nature, while in the films it consists of three components: magnetocrystalline, induced by stresses, and induced during the growth process. The stress and growth induced components of the anisotropy field result from the peculiarities of the techniques used to fabricate the films.

The increase in the anisotropy field in Ga:YIG films as the gallium content is raised (Fig. 2) is related to the growth of elastic stresses which arise in the film–substrate system owing to mismatch of their crystal lattice parameters. According to our measurements, as x is increased from 0.1 to 1.0, the difference in the lattice parameters of the film and substrate increases from 0.0087 to 0.0206 Å; with the large mismatches, this leads to the appearance of cracks in the films with $x = 1.0$.

We have measured the temperature variations in the saturation magnetization, anisotropy field, and resonance fields for Ga:YIG films with different x. The temperature range 213–353 K corresponds to the most realistic operating temperatures for microwave devices in which ferrite films may be used. The resonance fields $H_r^{\perp}$ and $H_r^{\parallel}$ were measured for directions of the constant magnetic field normal (perpendicular resonance) and tangential (parallel resonance) to the plane of the film. The measured temperature variations in the resonance fields $H_r^{\perp}$ and $H_r^{\parallel}$ for Ga:YIG films with different compositions are plotted in Fig. 3. As can be seen from Fig. 3, for a given temperature the resonance field $H_r^{\perp}$ decreases by roughly 100–150 Oe when the amount of gal-

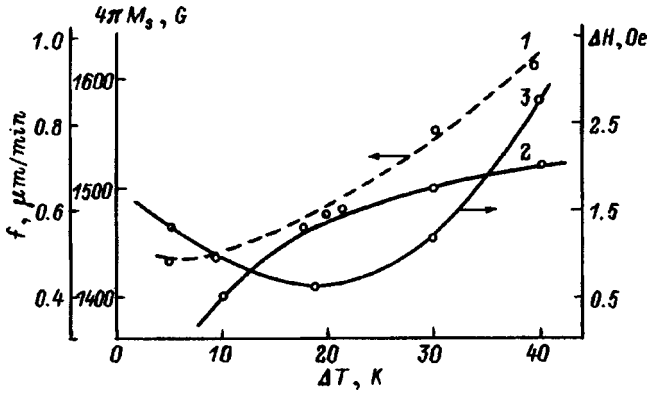

FIG. 1. The growth rate f_p (*1*), saturation magnetization $4\pi M_s$ (*2*), and ferromagnetic resonance line width ΔH (*3*) at $T = 295$ K as functions of the degree of supercooling ΔT.

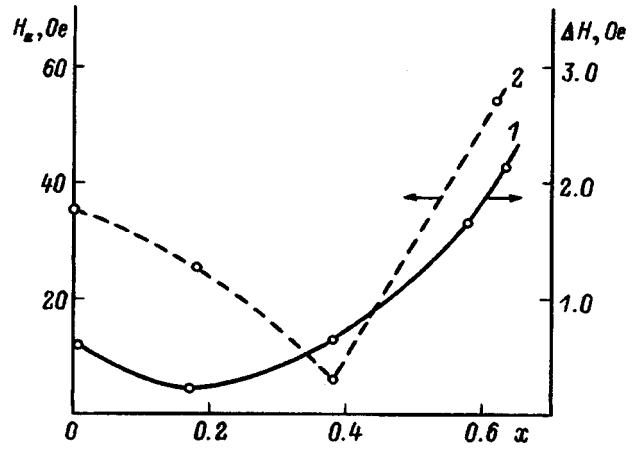

FIG. 2. The ferromagnetic resonance line width ΔH (*1*) at $T = 295$ K and the anisotropy field H_a (*2*) as functions of gallium ion content (x) in $Y_3Fe_{5-x}Ga_xO_{12}$ films.

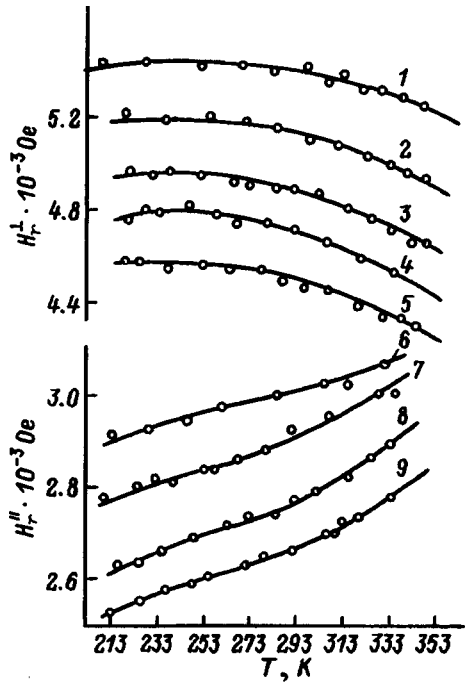

FIG. 3. Temperature variations in the resonance fields $H_r^{\perp}$ and $H_r^{\parallel}$ for $Y_3Fe_{5-x}Ga_xO_{12}$ films: $x=0$ (*1, 9*), 0.14 (*2, 8*), 0.38 (*3, 7*), 0.56 (*4*), and 0.63 (*5, 6*).

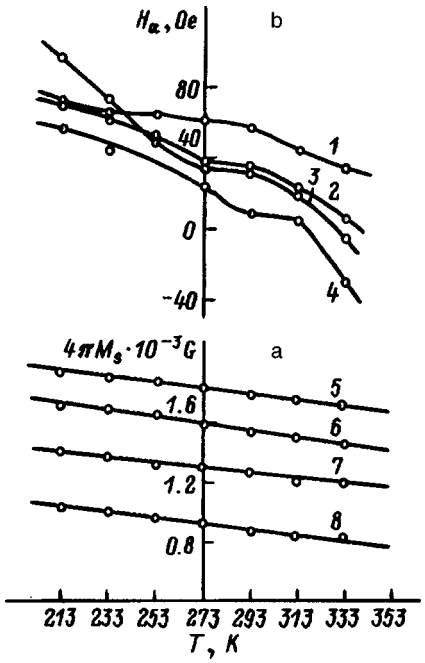

FIG. 4. Temperature variations in the saturation magnetization (a) and anisotropy field (b) of $Y_3Fe_{5-x}Ga_xO_{12}$ ferrite films: $x=0.63$ (*1*), 0.14 (*2, 6*), 0 (*3, 5*), 0.38 (*4, 8*), and 0.23 (*7*).

lium in the ferrite film is increased by 0.1 atom per formula unit (curves *1–5*). For the parallel resonance, $H_r^{\parallel}$ increases by 50–100 Oe when x is increased by 0.1 (curves *6–9*). For the perpendicular resonance[9]

$$\frac{\omega_{\perp}}{\gamma} = H_r^{\perp} - 4\pi M_s + H_a, \tag{2}$$

where $\omega_{\perp}$ is the resonance frequency and γ is the gyromagnetic ratio, equal to 2.8 MHz/Oe. The value of the resonance field $H_r^{\perp}$ is determined by the microwave frequency, the saturation magnetization $4\pi M_s$, and the anisotropy field H_a.

For the longitudinal resonance, at which

$$\frac{\omega_{\parallel}}{\gamma} = \sqrt{(H_r^{\parallel} + H_a)(H_r^{\parallel} + 4\pi M_s + H_a)}, \tag{3}$$

when the frequency is constant, the resonance field should increase as the saturation magnetization is lowered. Thus, at a constant frequency, for ferrite films with different gallium contents, the values and temperature variations of $H_r^{\perp}$ and $H_r^{\parallel}$ are determined by the parameters $4\pi M_s$, H_a, and their temperature variations (Fig. 4). Figure 4a implies that as the Ga^{3+} ion content of the film is increased, in addition to a decrease in the saturation magnetization (curves *5–8*) there is also a change in its temperature dependence. When the temperature is raised from 213 to 353 K, for pure YIG (curve *5*)the slope of the curve is 2.9 G/K, while for films with $x=0.38$ (curve *8*) it is 2.0 G/K.

It can be seen from Fig. 4b that within the temperature range studied here, the anisotropy field of Ga:YIG films changes little compared to pure YIG for small substitutions ($x=0.14$), while for $x=0.38$ it decreases significantly, and for large substitutions ($x=0.63$), it increases significantly. It is evident from Fig. 4b that the temperature variations in the anisotropy field are smallest for a composition with a large substitution, $x=0.63$ (curve *1*).

According to Eqs. (2) and (3), in order to maintain a constant operating frequency in microwave devices, i.e., to enhance their thermal stability, it is necessary that the magnitude of the temperature variations in the resonance field be compensated by the combined magnitude of the temperature changes in $4\pi M_s$ and H_a. In practice, thermal drift of the resonance frequency away from a fixed frequency is determined by the change in the resonance field with temperature relative to its value at room temperature T_k.

The temperature drifts of the resonance field for parallel $\Delta H_r^{\parallel} = H_{rT}^{\parallel} - H_{rk}^{\parallel}$ and perpendicular $\Delta H_r^{\perp} = H_{rT}^{\perp} - H_{rk}^{\perp}$ resonances are plotted in Fig. 5 for Ga:YIG ferrite films with $x=0$–0.63. Here $H_{rT}^{\parallel}$ and $H_{rT}^{\perp}$ are the resonance fields at temperature T and $H_{rk}^{\parallel}$ and $H_{rk}^{\perp}$ are the resonance fields at T_k. It clear from Fig. 5 that as the amount of Ga^{3+} in the films is increased, the slopes of the $\Delta H_r^{\parallel}(T)$ and $\Delta H_r^{\perp}(T)$ curves are significantly reduced. Thus, for a film with $x=0.63$, the slope of the $\Delta H_r^{\perp}(T)$ curve is more than a factor of 2 smaller than for a pure YIG film: $\alpha_7=1.4$ Oe/K and $\alpha_{11}=3.2$ Oe/K, respectively. For comparison, for the two resonances dashed lines with slopes $\alpha_5=\alpha_6=1.0$ Oe/K are shown in Fig. 5.

A comparison of the temperature dependences $\Delta H_r^{\perp}(T)$ and $\Delta H_r^{\parallel}(T)$ shows that for films with the same composition, a plot of the drift of the resonance field is more gradual for the parallel resonance than for the perpendicular resonance. For example, for a film with $x=0.63$, within the same temperature interval, at the perpendicular resonance one has $\alpha_7=1.4$ Oe/K, while at the parallel resonance $\alpha_4=1.0$ Oe/K.

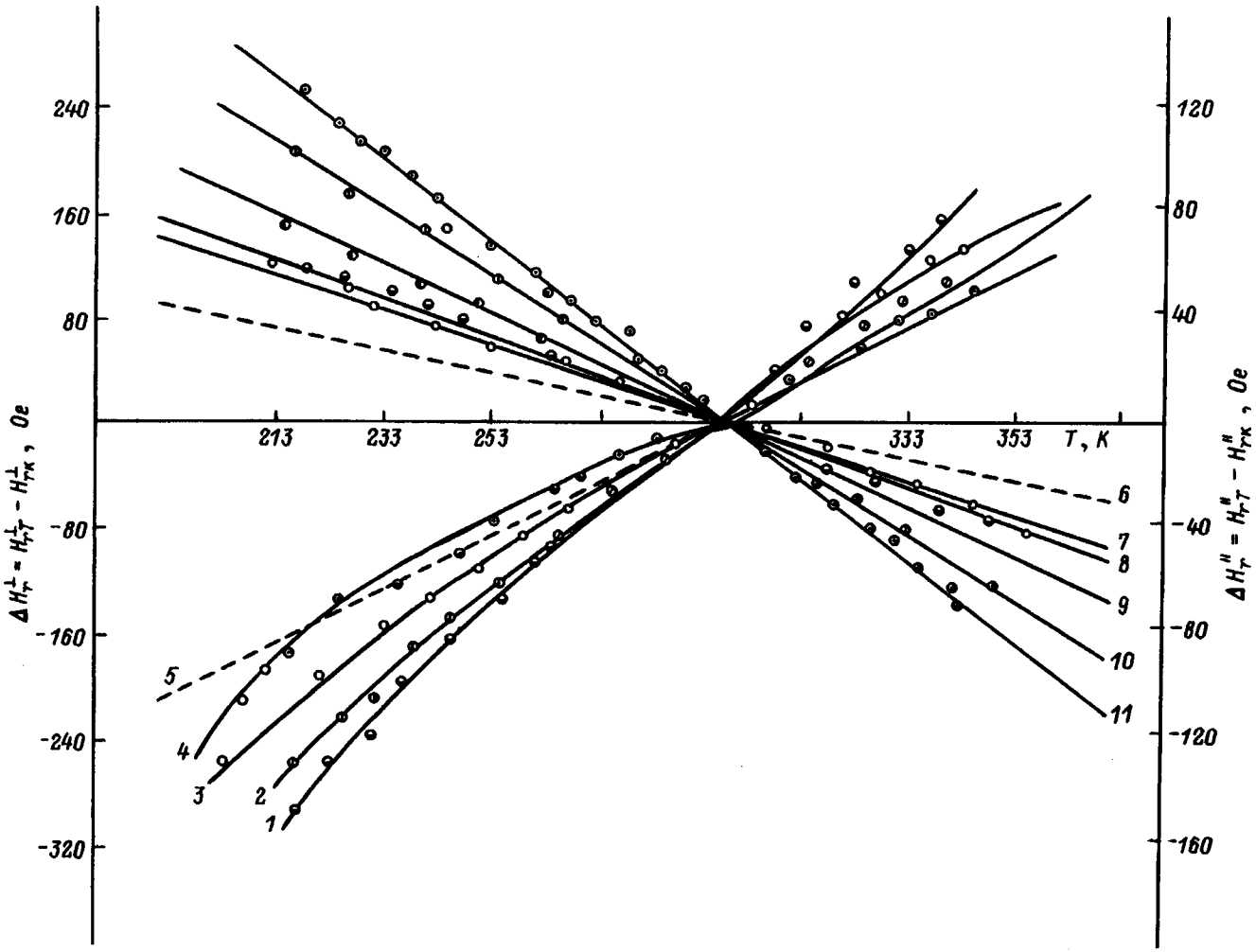

FIG. 5. Temperature variations in the drift of the resonance field for the parallel $\Delta H_r^{\parallel}$ and perpendicular $\Delta H_r^{\perp}$ resonances: $x=0$ (*1*, *11*), 0.14 (*2*, *10*), 0.38 (*3*, *9*), 0.63 (*4*, *7*), 0.56 (*8*); (*5*, *6*) curves with slope $\alpha_5=\alpha_6=1.0$ Oe/K.

Replacing the Fe^{3+} ions in YIG films by nonmagnetic Ga^{3+} ions, therefore, makes it possible to enhance the temperature stability of the resonance field, but this increases the width of the ferromagnetic resonance line. In addition, it is not possible to grow thick films with a high gallium content ($x \geqslant 0.63$) because of the mechanical stresses resulting from the increasing difference between the crystal lattice parameters of the film and substrate.

[1] M. R. Adam and D. K. Shroder, Élektronika **53** (11), 74-84 (1980).
[2] V. A. Nikitov and S. A. Nikitov, Zarubezhnaya Élektronika, No. 12, pp. 11–23 (1981).
[3] A. M. Balbashov and A. Ya. Chervonenkis, in *Magnetic Materials for Microelectronics* [in Russian], Énergiya, Moscow (1979), p. 159.
[4] H. L. Glass and M. T. Elliot, J. Cryst. Growth **27**, 253 (1974).
[5] A. Eschenfelder, in *Magnetic Bubble Technology*, Springer, Berlin (1980), p. 334.
[6] Yu. M. Yakovlev and S. Sh. Gendelev, in *Single-Crystal Ferrites in Radio Electronics* [in Russian], Sov. Radio, Moscow (1975), p. 269.
[7] S. I. Yushchuk and P. S. Kostyuk, Prib. Tekh. Éksper. **39**(6), 79 (1996).
[8] H. L. Glass, J. Cryst. Growth **33**, 183 (1977).
[9] H. L. Glass, H. W. Liaw, and M. T. Elliott, Mater. Res. Bull. **12**, 735 (1977).

Translated by D. H. McNeill

Photon scanning tunneling microscope with a nonresonance atomic-force regime

D. A. Lapshin

Institute of Spectroscopy, Russian Academy of Sciences, 142092 Troitsk, Moscow District, Russia
(Submitted November 29, 1996; resubmitted July 8, 1997)
Zh. Tekh. Fiz. **68**, 51–58 (September 1998)

A design of a photon scanning tunneling microscope is presented. The shear-force regime and the advantages of nonresonance excitation of the probe are discussed in detail. It is suggested that the replica method be used to estimate the size of the active part of the probe.
 [S1063-7842(98)01109-X]

INTRODUCTION

Near-field microscopy makes it possible to overcome the diffraction limit, which limits the resolution of classical optical microscopy.[1] The possibilities of realizing spectroscopy with submicron spatial resolution are generating great enthusiasm. The appreciable achievements made in this field include the visualization of individual fluorescence molecules,[2,3] measurement of the fluorescence times of individual molecules,[4,5] and low-temperature luminescence spectroscopy of semiconductor materials.[6] Possible applications in the field of control of local chemical reactions[7] and recording information[8] are also quite interesting.

To obtain maximum resolution the probe must be positioned near the surface at a distance of the order of several nanometers. For this reason, practical work requires a method for monitoring the probe–surface distance that is independent of the optical channel of the microscope. The so-called shear-force method is most widely used.[9,10] This method makes it possible to obtain a topographic image of the surface simultaneously with an optical image. To implement the method, oscillations of the probe must be excited at the resonance frequency in a plane perpendicular to the plane of the surface under study. It has been observed experimentally that near the surface the oscillation amplitude decreases as a result of interaction with the surface (Fig. 1). The distance dependence of the amplitude is smooth and makes it possible to monitor the probe–surface distance in the nanometer range. However, until very recently the character of the probe–surface interaction remained a subject of discussion. As follows from the name of the method, it was assumed that the probe is undergoes something like viscous damping on account of capillary or van der Waals forces.[9] To monitor the oscillation amplitude the probe is illuminated on one side by a laser beam, while a two-section photodiode, which detects light redistribution between its two sections, is placed on the other side. Since the signal from the photodiode is weak, a photosensitive method of synchronous detection is used to analyze it. In this scheme the signal at the detector output depends on both the amplitude and phase of the signal and can assume both positive and negative values. In our experiments we sometimes observed a jump-like change in the amplitude of the detector signal with a change in sign, which agrees with reports of contrast inversion in topographic images.[11] In this case protuberances in the image look like depressions and vice versa. Such effects are difficult to explain on the basis of a viscous model of damping.

A completely different model of the probe–surface interaction was proposed in Ref. 12. We note first that for the probe tip to move parallel to the surface during the oscillations special forces must be applied. For this reason, during measurements in the shear force regime the trajectory of the probe tip virtually always makes an acute angle with the surface. This means that for a sufficiently small probe–surface distance the probe tip will touch the surface, which should disturb the amplitude and frequency characteristics of the oscillations. In Ref. 12 an experimental investigation was performed of the resonance curve in vacuum at liquid-helium temperature, which made it possible to remove immediately the question of capillary forces. It was shown that the observed amplitude and frequency dependences of the resonance curve agree well with a mathematical model constructed on the basis of a model where the probe touches the surface even at the lower part of its trajectory. A very important observation is that because the elastic constant of the free part of the probe is different from that of the conical part the resonance frequency increases on contact with the surface. It is impossible to explain the increase in resonance frequency on the basis of a viscous damping model.

Thus the shear force regime is, in the main, analogous to the tapping mode regime or the touching regime, which is well known in atomic-force microscopy.[13,14] For this reason, in what follows we shall call it the atomic-force regime. The decrease in the amplitude of the signal in the atomic-force channel as the surface is approached is due to the limitation of the oscillation amplitude of the probe by the rigid wall as a result of mechanical contact.

Hence follows an important conclusion: The resolution of the microscope in the atomic-force regime is determined by the contact zone, i.e., it depends on the radius of curvature of the tip and does not depend, in the general case, on the oscillation amplitude. Of course, for large amplitudes distortions of the image of the surface are possible in the form of parasitic ''shadows,'' and so on, on account of excess touchings, for example, if the height of the protuberances is much greater than the rounding diameter of the probe, while the distance between the protuberances is less than the amplitude of the probe oscillations. For this reason, from the standpoint

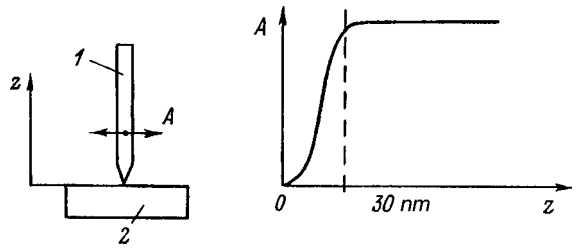

FIG. 1. Shear force effect: Decrease in the amplitude A of forced oscillations of a microscope probe as a result of interactions with the surface (*1* — probe, *2* — sample).

of resolution the regime where the amplitude of the probe oscillations equals the radius of curvature of the probe is optimal: For smaller amplitudes the signal/noise ratio decreases in the detection channel and for larger amplitudes the probability of parasitic effects increases.

It is now possible to understand the mechanism leading to inversion of contrast which is sometimes observed in topographic images. To a first approximation, the oscillating probe can be treated as a classical oscillator excited by an external force. The response function χ of a harmonic oscillator can be described as the sum of the real χ' and imaginary χ'' parts.[15–17] The form of these components is well known and is shown in Fig. 2. The interaction of the probe with the surface, on the one hand, increases the resonance frequency[12] and, on the other, changes the phase of the oscillations, since terms reflecting the interaction with the surface must be added in the equation of motion of the oscillator. The magnitude of the phase shift will depend on the duration of the interaction with the surface as well as on local mechanical properties of the surface. A change in the phase of the signal can be interpreted just as a change in the ratio of the real and imaginary parts of the response function. The change in phase of oscillations even with a constant amplitude will give rise to a change in the signal amplitude at the output of the synchronous detector. Therefore the magnitude of the detector signal can depend on the local elastic properties of the surface.

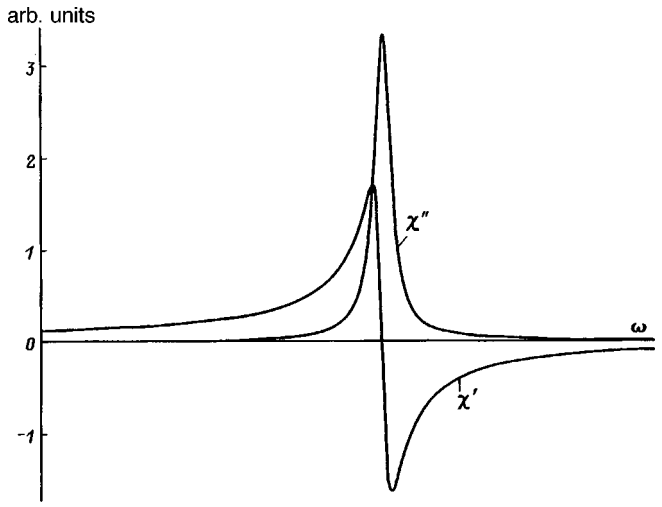

FIG. 2. Response function χ of a harmonic oscillator to an external exciting force: χ' — real part, χ'' — imaginary part.

Another possibility is illustrated in Fig. 2: If χ' makes the larger contribution to the output signal, then an increase in the resonance frequency will result in a shift of the χ' curve rightward and depending on the position of the working point, which is fixed during the measurements and is determined by the frequency of the sound generator, both an increase and a decrease in signal amplitude, right down to a change in sign, can be observed. For this reason, an increase in the resonance frequency as a result of the interaction with the surface could also be responsible for the contrast inversion sometimes observed in top topographic images.

In summary, it can be concluded that the root of the problem lies in the superposition of phase and amplitude effects during operation near the resonance frequency. Therefore it is more convenient to work in the nonresonance regime. In this case the amplitude function will be determined by the cutoff of the probe displacement on contact with the surface, while phase effects will be absent. We shall present a design of a near-field microscope with a nonresonance atomic-force regime and we shall present some results obtained using this microscope.

PHOTON SCANNING TUNNELING MICROSCOPE

The layout of the microscope is displayed in Fig. 3. A He–Ne laser beam passes through a prism at the total internal reflection angle.[18] The sharpened tip of an optical fiber, functioning as a probe, is placed at the bottom in the region of the surface light wave. Part of the surface light wave is scattered by the probe and trapped by the optical fiber. The photomultiplier signal at the other end of the optical fiber is proportional to the intensity of the light wave. In current terminology, this type of microscope is called a photon scanning tunneling microscope.[19,20]

We employed a multimode quartz fiber, sharpened by etching in a 40% aqueous solution of hydrofluoric acid.[21] In our experiments, a unmetallized probe without an aperture was used: On account of the exponential dependence of the intensity of the surface wave on the distance to the surface, the field component makes the main contribution to the signal near the probe tip, making it possible to obtain a resolution of less than 200 nm.[20] A metallized tip with an aperture makes it possible to obtain a resolution down to 20 nm,[22] but it is more difficult to analyze the data and the mechanism of the interaction of the surface wave with the probe cannot be described by a simple model of the type scattering by a dielectric sphere.

In our design the scanning apparatus moves the grating while the tip is stationary. For this, the prism is rigidly secured to a table in the form of a glass disk, which is at rest on three metal balls, glued to 32 mm long, 10 mm in diameter, and 0.75 mm thick piezoelectric tubes (only two balls are shown in Fig. 2). The inner and outer surface of each tube is metallized and divided into four electrodes, which are connected in a manner so that application of voltage to a group of electrodes produces bending of the tube in the corresponding direction.[23] The electrodes of the three tubes are con-

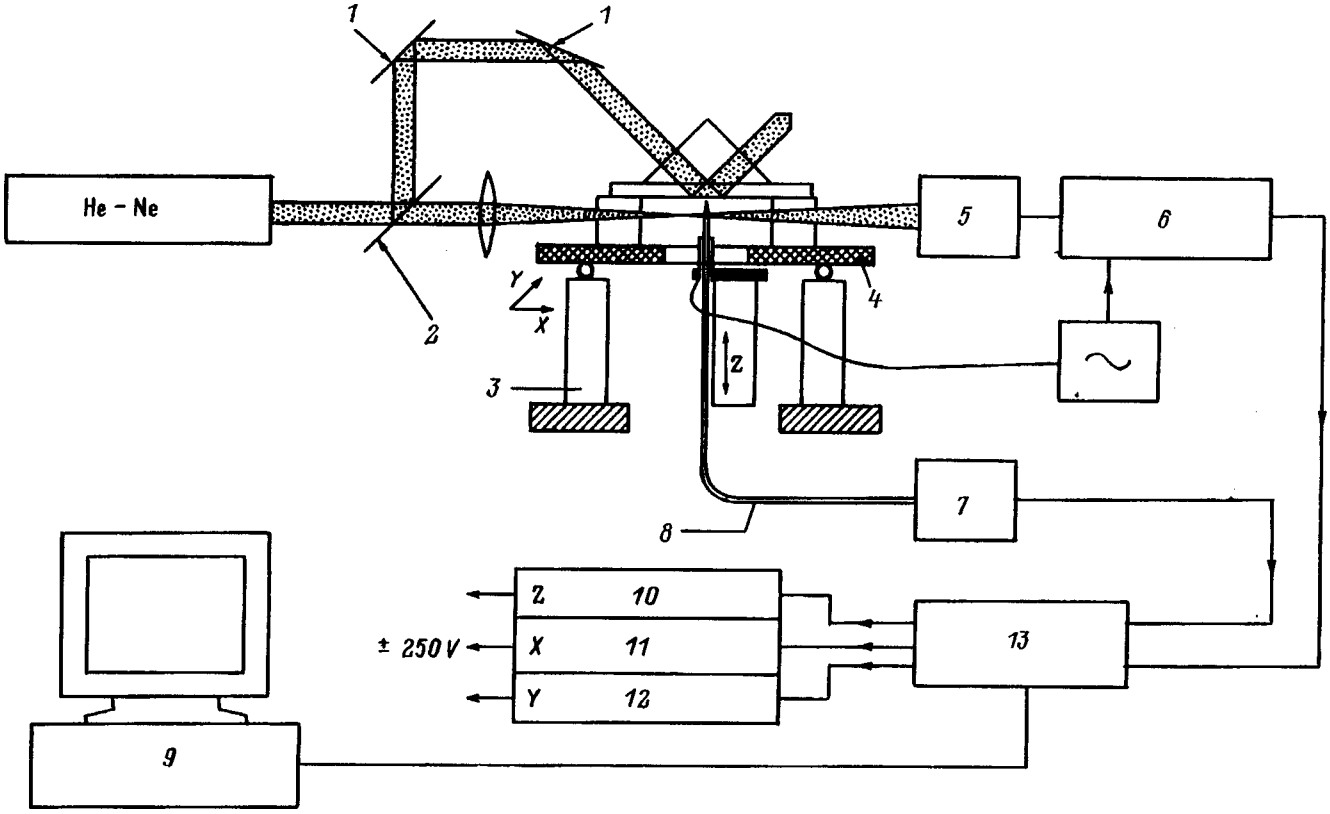

FIG. 3. Schematic diagram of a photon scanning tunneling microscope: 1 — Mirror, *2* — beam splitter, *3* — piezoelectric tube, *4* — table, 5 — photodiode, *6* — synchronous amplifier, *7* — photomultiplier, *8* — optical fiber, *9* — computer, *10–12* — high-voltage amplifiers, *13* — controller.

nected in parallel, so that the tubes move synchronously and set the table in motion with its orientation remaining constant. Moreover, this design makes it possible to move the table discretely with a step of less than 1 μm. For this, a sawtooth voltage must be applied to the scanner electrodes.[24] The large piezoelectric tube at the center of Fig. 3 provides fine regulation of the distance between the surface of the sample and the probe. The micrometer screw for coarse regulation is not shown in the figure. For controlling voltages of $+/-$ 250 V, the scanning field equals 14.5 μm, while the regulation range in the vertical direction is 5 μm.

To implement the atomic-force regime an additional tubular piezoelectric element (outer diameter 1.3 mm, inner diameter 0.8 mm, length 8 mm) is placed in the top part of the central piezoelectric tube in order to excite oscillations of the free end of the optical fiber in a plane perpendicular to the plane of the figure. The oscillating part of the optical fiber is illuminated from the side by a laser beam, and the scattered light is detected with a two-section photodiode on the opposite side. Using a feedback loop, the amplitude can be maintained at a prescribed level by moving the tip in the vertical direction, and in so doing the tip–surface distance remains constant during scanning.

In our work we employed nonresonance excitation of the tip oscillations, in contrast to all works of which we know, where a resonance method was used. According to our observations, the nonresonance method is distinguished by greater stability, and we employed a frequency below the first resonance frequency for flexural oscillations of the probe, ordinarily in the range 5–10 kHz.

In the standard regime the detected signal from the photodiode was used in a feedback loop, terminating on the fine-adjustment piezoelectric tube. This made it possible to maintain the probe–surface distance constant during scanning. In this case the trajectory of the probe tip repeats the topographic profile of the surface, while at each scan point the microscope controller records the optical signal and the topographic signal in the atomic-force channel. The microscope controller is a separate unit and is coupled with a PC through an ISA bus by means of a special interface card.

MEASUREMENTS

As a first example we present an image of a simple model structure in the form of a standing surface wave.[25] The arrangement of the experiment is displayed in Fig. 4. The laser beam undergoes total internal reflection at the glass–air interface. A flat metal mirror is placed in the path of the beam, so that the light propagating in the forward and backward directions forms on the surface a standing light wave with period $d=\lambda/2n\sin\Theta$. For $n=1.5$ and $\Theta=45°$ the distance between the maxima of the light wave for $\lambda=633$ nm equals 3000 nm.

Figure 5 shows an image of the intensity of the light field obtained in the optical channel. In addition, the distance between the probe and the glass was maintained constant (50

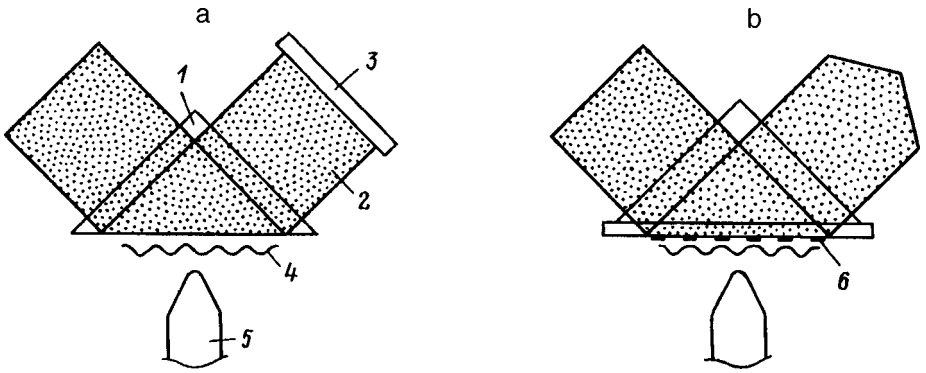

FIG. 4. Schematic diagram of an experiment measuring the intensity of a surface standing light wave (a) and intensity of a light wave above the surface of a diffraction grating (b): *1* — Prism, *2* — mirror, *3* — light, *4* — near-field, *5* — probe, *6* — grating.

nm) by feedback in the atomic-force channel. As expected, the signal profile is sinusoidal. The local nonuniformities in the image are due to external mechanical perturbations during recording. The increase in the period of the structure from left to right is due to the nonlinearity of the piezoelectric scanning apparatus.

A trace of the optical signal with the probe moving in a direction perpendicular to the surface is displayed in Fig. 6. The plot illustrates the well-known exponential dependence of the field of the surface light wave.[18] When this dependence was measured, the mirror was removed (Fig. 4b). The damping depth of the field equals 130 nm.

As another example illustrating the possibilities of the microscope, we present an image of a flat diffraction grating consisting of Ni stripes on a glass surface prepared by photolithography. The lines are 40 nm high, the period of the grating is 10 μm, and the width of a metal line is 3 μm. Figure 7 shows a three-dimensional topographic image obtained of the grating in the atomic-force channel in the nonresonance regime, while Fig. 8 displays an image of the section of the grating (top view) in the topographic and optical channels. The height of a line is 40 nm, which agrees well with the grating fabrication data. Crests of height $\sim$40 nm are observed along the edges of the metal lines. We believe that this is a result of mass transfer, due to the details of the technological process, during etching.

Here we emphasize that the microscope controller which we have developed rules out possible image distortions due to underregulation or overregulation in the feedback circuit in the presence of sharp changes in the surface profile. For this, before each point is recorded the microscope controller checks for the absence of an error signal in the feedback loop. In addition, each scan is recorded in both the forward and backward directions. Comparing these profiles likewise makes it possible to avoid errors which could be due, for example, to creep of the piezoelectric ceramic in the vertical direction. The first scan lines of the image (at the bottom of the figure) are shifted rightward as a result of creep of the piezoceramic in the horizontal direction. The large ''hump'' in the upper left corner is, we believe, a dust particle settling from the air on the surface of the grating.

The optical image corresponds, with good accuracy, to the details of the topographic image, i.e., the fringes of the minimum of the optical signal correspond to the metal lines of the diffraction grating. The fine details in the form of small spots in the topographic image, which evidently corre-

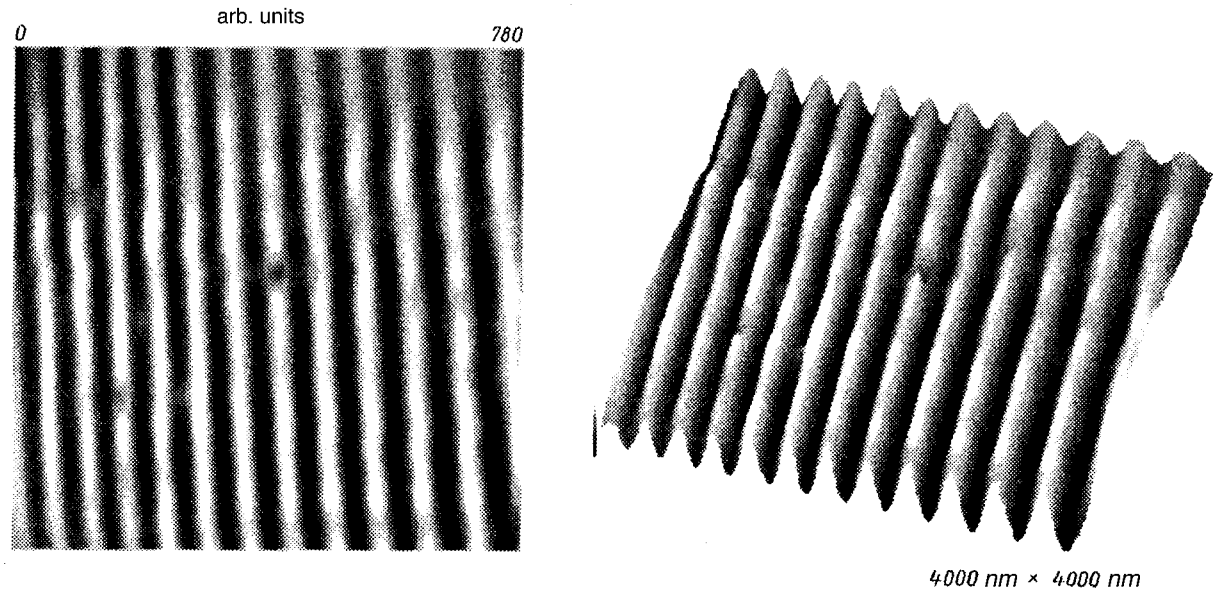

FIG. 5. Image of a surface standing light wave on the surface of a glass prism. The distance between maxima $\sim$300 nm (I is the intensity in arbitrary units).

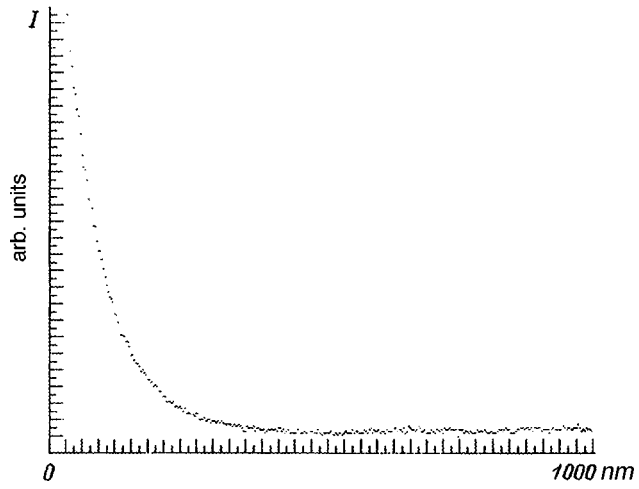

FIG. 6. Intensity of a surface wave versus the probe–surface distance.

spond to residues of the metal which have not been removed, correspond to dips in the form of dark spots in the optical signal. The resolution of the microscope can be estimated, on the basis of the image obtained, to be 0.1 μm in both channels.

REPLICA METHOD

The most important parameter of the microscope, determining its resolution, is the radius of curvature of the probe. Most authors use an electron microscope to estimate this parameter. We propose using for this purpose the method of replicas, by which we mean producing artificially an impression of the probe tip in a soft material. The process leading to the formation of submicron-size impressions of this kind has been investigated in detail in a number of works.[16,17,26] By investigating the time dependence of the displacement of an indenter under the action of an external force it has been shown that in the general case elastic relaxation of the material is observed after the load is removed. As a result of this relaxation, the depth of the impression is less than the depth of indentation, while the angle of the impression cone is larger than that of the indenter. In soft materials, specifically in Al, this type of relaxation is small, so that the impression repeats the shape of the indenter to a high degree of accuracy.

In our design the high stiffness of the needle in the vertical direction permits indentation to a depth of several microns. We used Al and fused rosin as the indentation materials. Practice showed good reproducibility of the impressions in these materials as well as the absence of tip deformation during the indentation process, making it possible to estimate the shape of the probe from the shape of the impression.

To visualize the shape of the impression, we use the microscope in the atomic-force regime with the same probe as the one used for making the impression. Figure 9 shows an image of the impression of a tip which was used in this work (a surface defect, existing prior to indentation, is present in the bottom right-hand corner). The section on the right-hand side of the figure makes it possible to estimate the

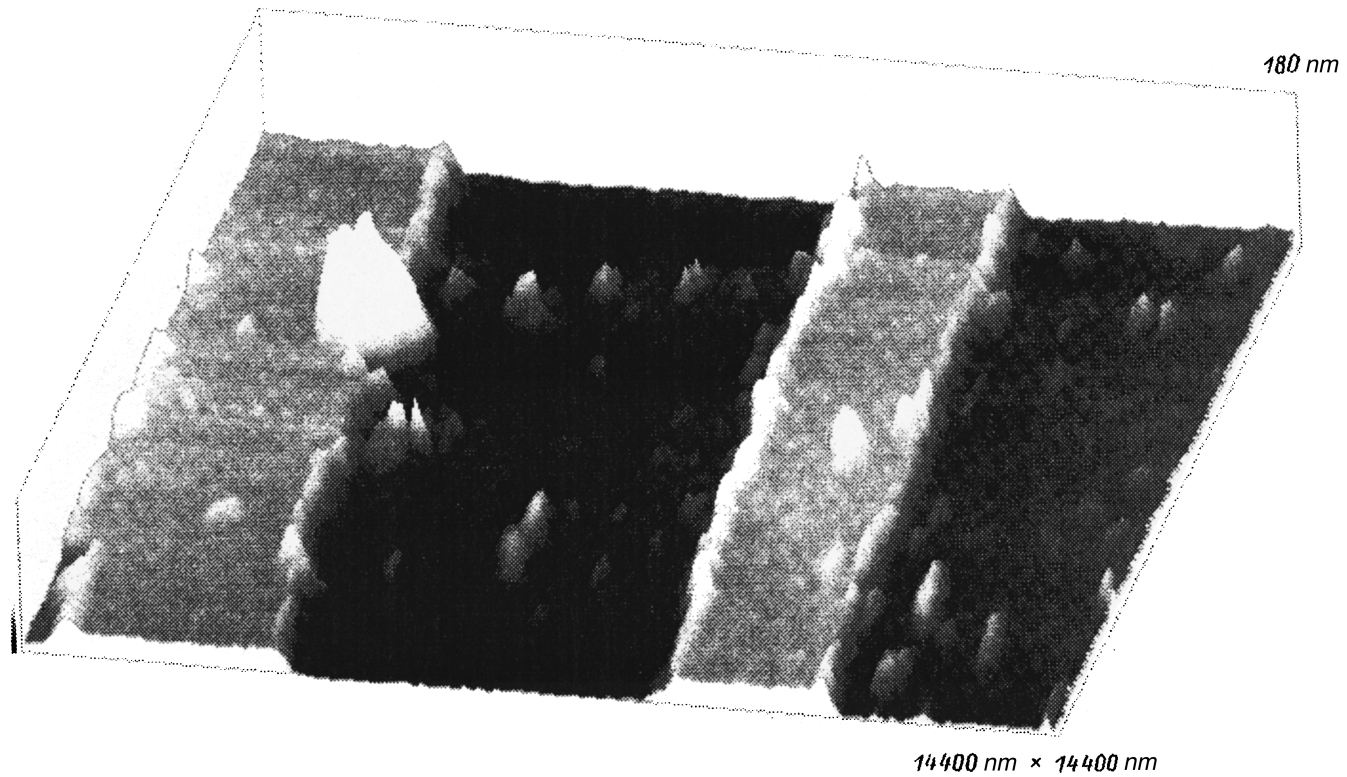

FIG. 7. Three-dimensional image of a section of a diffraction grating on a glass surface. The image was obtained in the atomic-force channel of the microscope. Period of grating 10 μm.

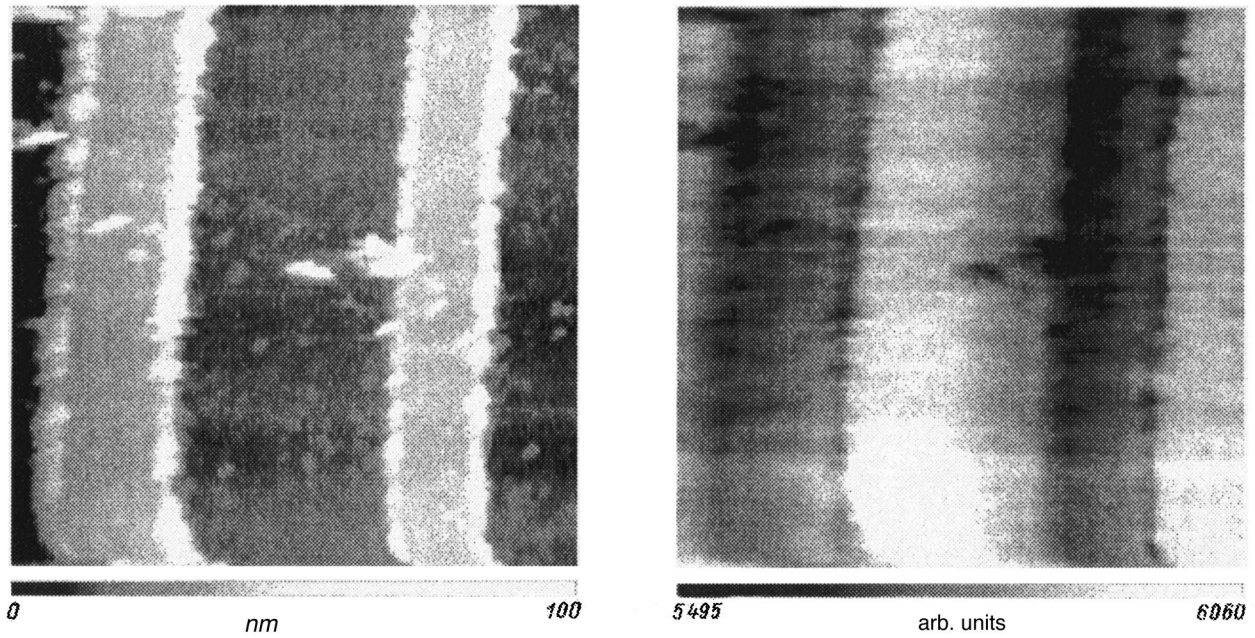

FIG. 8. Atomic-force (left) and optical (right) images of a section of a diffraction grating. The vector k of the surface wave is directed along the lines of the grating.

radius of curvature of the probe as 0.1 μm and the cone angle as 150°, which agrees with the estimate, presented above, of the resolution of the microscope. The possibility of visualizing the impression of a probe using the same probe can seem unlikely. Here it is necessary to underscore once again that the shape of the impression is somewhat different from that of the probe because the material undergoes relaxation, while the amplitude of the probe oscillations does not exceed the radius of curvature of the probe and in the present measurements was equal to ~100 nm. This makes it possible to attribute the impression to the probe right down to the very bottom. The proposed method does not make it possible to reproduce the exact shape of the probe from the image of the impression, but rather it is only a method for estimating the upper limit of the size of the probe.

The proposed method has a number of considerable advantages over the standard method of electron microscopy: possibility of obtaining a three-dimensional image and not a

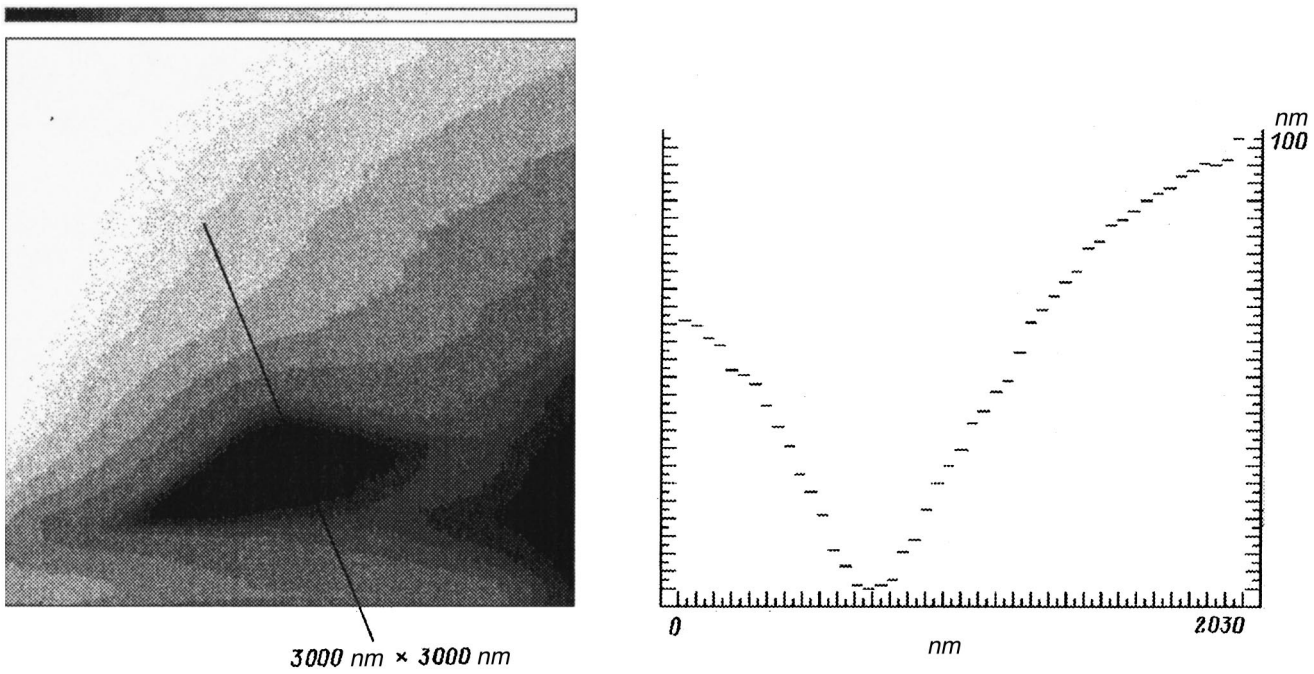

FIG. 9. Image of an impression of a needle tip in fused rosin. Right side — section along a line.

projection on a plane, as in an electron microscope; possibility of studying dielectric tips without premetallization; relative simplicity and low cost, since the impression is monitored in the same microscope in which investigations are conducted, so that less time is spent and the probability of damaging the tip as a result of transporting the probe from one microscope to another is decreased.

CONCLUSIONS

1. It was demonstrated that the atomic-force channel of the microscope can operate in the nonresonance regime. This regime is distinguished by greater stability as compared with the resonance method of excitation. The resolution of the microscope is determined by the radius of curvature of the probe and, in the general case, does not depend on the amplitude of the oscillations of the probe.

2. It was shown that an impression of the probe can be produced in soft materials (aluminum and fused rosin). Visualization of the impression in the atomic-force regime using the same probe makes it possible to estimate the size of the active part of the probe.

[1] D. W. Pohl, W. Denk, and M. Lanz, Appl. Phys. Lett. **44**, 651 (1984).
[2] E. Betzig and J. Chichester, Science **262**, 1422 (1993).
[3] A. J. Meixner, Opt. Eng. (Bellingham) **34**, 2324 (1995).
[4] X. S. Xie and R. C. Dunn, Science **265**, 361 (1994).
[5] W. P. Ambrose, Science **264**, 364 (1994).
[6] H. F. Hess, Science **264**, 1740 (1994).
[7] G. Krausch, Opt. Commun. **119**, 283 (1995).
[8] E. Betzig, Appl. Phys. Lett. **61**, 142 (1992).
[9] R. Toledo-Crow, Appl. Phys. Lett. **60**, 2957 (1992).
[10] E. Betzig, P. L. Finn, and S. J. Weiner, Appl. Phys. Lett. **60**, 2484 (1992).
[11] H. Heinzelmann, Opt. Eng. (Bellingham) **34**, 2441 (1995).
[12] M. J. Gregor, Appl. Phys. Lett. **68**, 307 (1996).
[13] Q. Zong, Surf. Sci. Lett. **290**, L688, (1993).
[14] H. G. Hansma, Scanning **15**, 296, (1993).
[15] A. B. Pippard, *The Physics of Oscillations*, Cambridge University Press, N. Y. , 1989, Vol. 1; 1983, Vol. 2; Vysshaya Shkola, Moscow, 1985, 456 pp.].
[16] M. F. Doerner and W. D. Nix, J. Mater. Res. **1**, 601 (1986).
[17] J. Mencik and M. V. Swain, J. Mater. Res. **10**, 1491 (1995).
[18] E. I. Butikov, *Optics* [in Russian], Vysshaya Shkola, Moscow, 1986.
[19] D. Courjon, K. Sarayeddine, and M. Spajer, Opt. Commun. **71**, 23 (1989).
[20] R. C. Reddick, R. J. Warmack, and T. L. Ferrell, Phys. Rev. B **39**, 767 (1989).
[21] D. W. Pohl and D. Courjon, *Near Field Optics*, NATO ASI Series E, Kluwer, Dordrecht, 1993, Vol. 242, pp. 131–139.
[22] M. Naya, Opt. Commun. **124**, 9 (1996).
[23] G. Binning and D. P. E. Smith, Rev. Sci. Instrum. **57**, 1688 (1986).
[24] D. W. Pohl, Rev. Sci. Instrum. **58**, 54 (1987).
[25] A. J. Meixner, M. A. Bopp, and G. Tarrach, Appl. Opt. **33**, 7995, (1994).
[26] B. Bhushan and V. N. Koinkar, Appl. Phys. Lett. **64**, 1653 (1994).

Translated by M. E. Alferieff

Interaction of intense IR laser radiation with *a*-C:H protective coatings

E. A. Konshina

S. I. Vavilov State Optical Institute All-Russia Science Center, 199034 St. Petersburg, Russia
(Submitted April 16, 1997)
Zh. Tekh. Fiz. **68**, 59–66 (September 1998)

The results of a determination of the optical breakdown thresholds of air near the surface of copper laser mirrors with *a*-C:H protective coating by intense pulsed 10.6 μm radiation are analyzed and systematized. It is shown that there is no correlation between the breakdown threshold of a coated mirror, the reflectance of the coating, and the breakdown threshold of the initial copper surface. Experimental dependences of the threshold of optical breakdown of coated mirrors on the *a*-C:H thickness and deposition rate as well as the storage time of the mirrors are given. Estimates are made of the rise in the surface temperature in the irradiation zone for the case of an ideal adhesive contact and calculations are made of the damage threshold of the coating in the case that the adhesive contact between the mirror and the coating is impaired. The effect of the *a*-C:H coating properties and the conditions at the polished metal surface–protective coating interface on the optical breakdown threshold is discussed. [S1063-7842(98)01209-4]

INTRODUCTION

An important question in producing optical components for lasers is the interaction of laser radiation with matter. Passive elements (windows, mirrors) used in the gas media of pulsed CO_2 lasers are exposed to intense laser light fluxes. Optical breakdown and plasma formation at the surface of optical components change the lasing regime and destroy the functioning of the laser system. For this reason, the radiation hardness of an optical component is determined by the power density level of the radiation corresponding to the plasma formation threshold. This threshold depends not only on the parameters of the laser radiation (form, duration, pulse repetition frequency, and size of the irradiation spot) but also on the surrounding medium, the state of the surface, and the material of the optical component.[1] Copper mirrors, which have high reflectances and optical breakdown thresholds, are widely used in laser technology. However, their use is limited by low corrosion resistance and mechanical strength. The service life of the mirrors can be prolonged by using protective coatings. The good prospects for using solid, chemically inert, and IR transparent diamond-like coatings consisting of amorphous hydrogenated carbon (*a*-C:H) as coatings providing protection from intense 10.6 μm radiation for laser copper mirrors was first demonstrated in Ref. 2. Mirrors with a protective *a*-C:H coating had a high breakdown threshold. Such a coating did not change the shape of the optical surface or the reflectance of the copper mirror, it decreased the roughness of the initial surface, and substantially increased its mechanical strength and corrosion resistance. Further investigations showed that the conditions of plasma formation at the surface of *a*-C:H coated mirrors depend on the thickness of the coating and can decrease with time.[3] However, the nature of the observed phenomena is not completely understood.

In the present paper a systematic analysis is given of the effect of different factors on the optical breakdown threshold of copper mirrors with a *a*-C:H protective coating. Approximate calculations of the surface temperature in an irradiation spot and the breakdown thresholds of a coating as a function of its thickness, taking account of adhesive contact at the mirror–coating boundary, are performed. The effect of the properties of *a*-C:H and conditions at the polished metal surface–protective coating interface on the threshold of optical breakdown near the surface are discussed.

EXPERIMENTAL METHODS AND RESULTS

A protective *a*-C:H coating was obtained by chemical deposition of hydrocarbon vapors in a dc glow discharge plasma.[4] The coating was deposited on the surface of polished copper mirrors, ranging in size from 40 to 60 mm, at the temperature of the surrounding medium. One-quarter or one-half of the mirror surface was left uncoated in order to perform comparative tests. The mirror surface prior to deposition of the coating was worked with a glow discharge plasma of an inert gas to clean the surface. To optimize the conditions under which the *a*-C:H coating is obtained, the parameters of the deposition process were varied: pressure in the vacuum chamber from 1×10^{-2} to 1×10^{-1} Pa, the interelectrode voltage from 600 to 1400 V, and the acetylene content in the mixture with inert gas. Krypton and argon were used as the inert gas. The coating thickness was varied in the range 0.03–0.7 μm. The thickness was monitored with a MII-4M microinterferometer with a relative measurement error of less than 10%.

To determine the stability of the *a*-C:H coated mirrors with respect to the action of laser radiation, the power density corresponding to the optical breakdown threshold near their surface was determined. The breakdown threshold was taken as the minimum laser power density corresponding to the appearance of a flame and obtained in a series of tests on

FIG. 1. Histogram of the pulsed IR laser radiation power densities corresponding to the optical breakdown threshold.

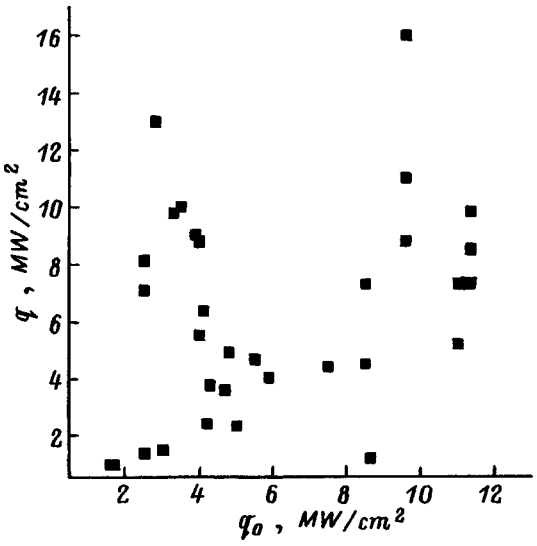

FIG. 2. Distribution of the pulsed IR laser radiation power density q corresponding to the optical breakdown threshold as a function of the breakdown threshold q_0 of an uncoated copper surface.

different sections of the mirror surface. The tests were performed at 10.6 μm in atmospheric-pressure air using an electric discharge CO_2 laser[5] with a pulse duration of 15 μs at the base and 10 μs according to the width. The irradiation spot was 0.3 cm in diameter. Some of the radiation energy was diverted to an IMO-2 laser pulse energy meter.

A histogram of the values of the power density q of pulsed IR laser radiation, which correspond to the optical breakdown threshold at the surface of a copper *a*-C:H coated mirror for $N=32$ samples is presented in Fig. 1. The average, maximum, and minimum values of the power density were equal to 6.2, 16, and 1 MW/cm^2, respectively.

The threshold radiation power densities of the coated mirrors versus the breakdown thresholds q_0 of the initial uncoated surface of the mirrors are shown in Fig. 2. One can see that these values are random and there is no regularity in the distribution of the points in Fig. 2. A coating could both increase the optical breakdown threshold of the mirror surface severalfold and decrease it in individual cases. A numerical analysis of the values of the breakdown thresholds presented in Fig. 2 gave a correlation coefficient ~ 0.3 with 32 samples.

The measurements of the reflectance R of an *a*-C:H coated copper mirror at 10.6 μm were performed using a multipass refractometer with an error of $\pm 0.3\%$. The measurements showed that $R=98.4-99.0\%$ and its deviation from the reflectance of the initial surface of the copper mirror fell within the limits of the measurement error. The threshold values of the power density q of the *a*-C:H coated mirrors as a function of the surface reflectance R of the component are presented in Fig. 3. One can see that there is no correlation between these values. The protective *a*-C:H coating protects the surface of the copper mirror from oxidation and makes it possible to maintain a constant surface reflectance during storage for several years.

The threshold power densities of *a*-C:H coated copper mirrors as a function of the coating thickness d are shown in Fig. 4. Despite the large variance of the points, one can see that in a narrow interval of coating thicknesses from 0.1 to 0.2 μm the breakdown threshold tends to increase, and as the thickness increases further, the breakdown threshold decreases. The maximum in the experimental curve shows that at least two competing processes influence the development of optical breakdown at the surface of an *a*-C:H coated mirror, one process promoting an increase and the other a decrease in the threshold.

Attempts to determine the dependence of the optical breakdown threshold of *a*-C:H coated mirrors on the technological parameters of the deposition process (gas pressure p in the vacuum chamber, interelectrode voltage u, and ion

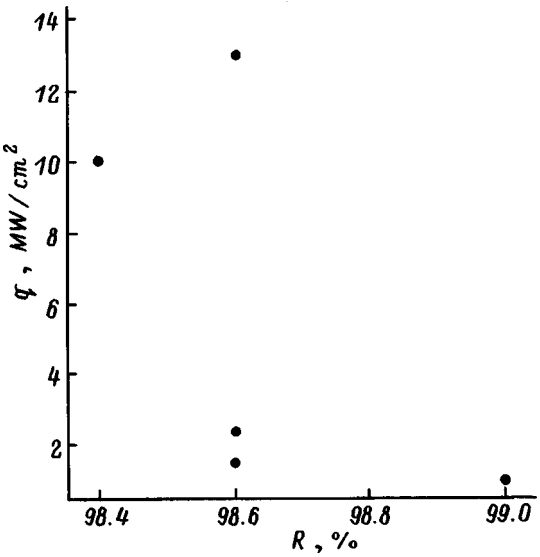

FIG. 3. Optical breakdown threshold of *a*-C:H coated mirrors as a function of their reflectance.

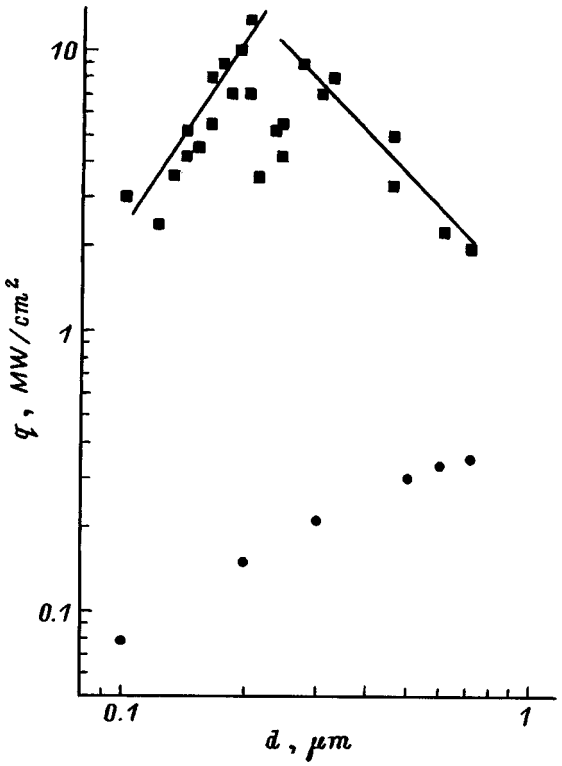

FIG. 4. Threshold pulsed IR radiation power densities versus the protective coating thickness: ■ — for experimental near-surface breakdown thresholds of *a*-C:H coated copper mirrors, ● — for the computed values of the laser damage thresholds of an *a*-C:H coating in the case of impaired adhesive contact between the coating and the mirror.

current i on the substrate) were unsuccessful. The breakdown thresholds of 0.13 ± 0.01 μm thick *a*-C:H coatings as a function of the deposition rate v are presented in Fig. 5. The breakdown threshold q varied from 2 to 5.2 MW/cm^2 with v

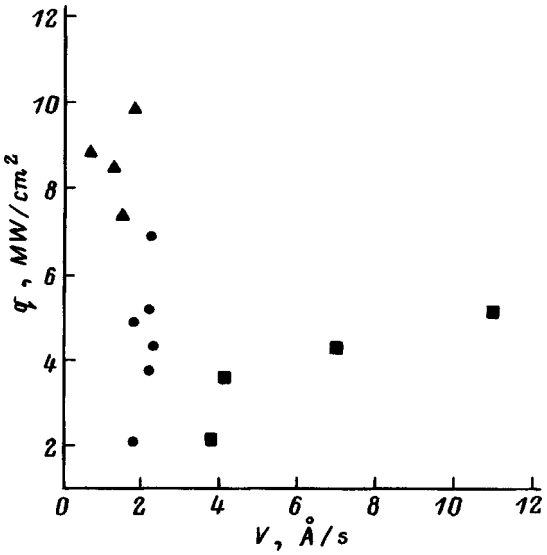

FIG. 5. Threshold breakdown power densities as a function of the deposition rate: ■ — from acetylene with $u=800$–900 V, $i=2$–11 mA, and $p=1$–7×10^{-2} Pa; ● — from a mixture of acetylene with argon (50%) with $u=900$–1000 V, $i=4$–8 mA, and $p=1.3$–2.6×10^{-2} Pa; ▲ — from a mixture of acetylene with krypton (66%) with $u=1200$–1400 V, $i=20$ mA, and $p=5\times10^{-2}$ Pa.

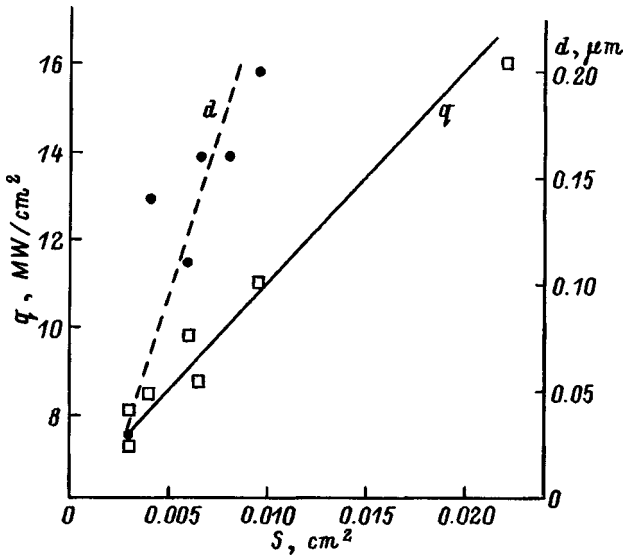

FIG. 6. Damage area on a mirror surface due to optical breakdown as a function of the power density at the breakdown threshold and as a function of the coating thickness.

increasing from 4 to 12 Å/s for coatings obtained from acetylene with $u=800$–900 V in the interval $i=2$–11 mA and $p=1$–7×10^{-2} Pa. Decreasing the deposition rate to $v=2.0\pm0.2$ Å/s by diluting the acetylene with argon (50%) and using $u=900$–1000 V, $i=4$–8 mA, and $p=5\times10^{-2}$ Pa increased q up to 7 MW/cm^2. For deposition rates $v<2$ Å/s and coatings obtained from a mixture of acetylene with krypton (66%) with $u=1200-1400$ V, $i=20$ mA, and $p=5\times10^{-2}$ Pa the value of u increased up to 11 MW/cm^2. The dependence $q(v)$ obtained shows that the decrease in the *a*-C:H deposition rate as a result of a decrease in the acetylene concentration in the plasma increases the breakdown threshold of a mirror with a protective coating.

The area s damaged on the surface of a *a*-C:H coated mirror as a result of optical breakdown could vary from $\sim0.2\times10^{-2}$ to $\sim4\times10^{-1}$ cm^2. The change in s as a function of the coating thickness d and radiation power density q for coatings obtained from a mixture of acetylene with krypton (66%) in the interval of deposition rates $v=0.7$–1.8 Å/s is shown in Fig. 6. One can see that for $d<0.2$ μm the value of s increases in proportion to the increase in q. For coatings which have a structured absorption spectrum with several maxima, lying above the energy ~1.5 eV (Fig. 7, curve *1*), irreversible changes in the color in the irradiation spot occurred at the locations exposed to intense laser radiation. We observed similar changes in color by heating the experimental coatings in vacuum up to $T=420$ °C. As follows from the results of IR and Raman scattering spectroscopy, the appearance of shift of the maximum in the electronic absorption spectrum in the direction of lower energies is caused by structural changes associated with a transition of carbon atoms from the sp into the sp^2 valence state and enlargement of the polycyclic aromatic groups in the *a*-C:H structure.[6] Thermographic investigations of the carbon condensates obtained in a gas discharge showed that an exothermic effect not accompanied by a change in mass and associated with structural changes is observed in the temperature interval

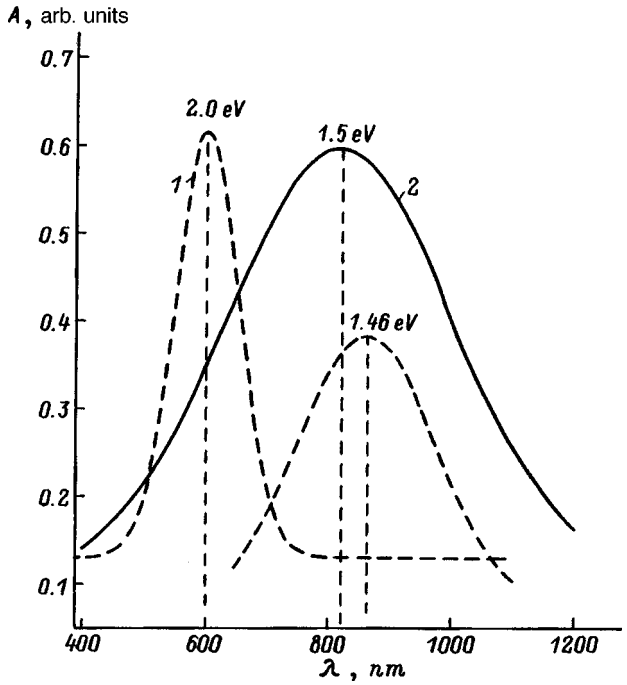

FIG. 7. Spectral dependences of the absorption of the mirrors.

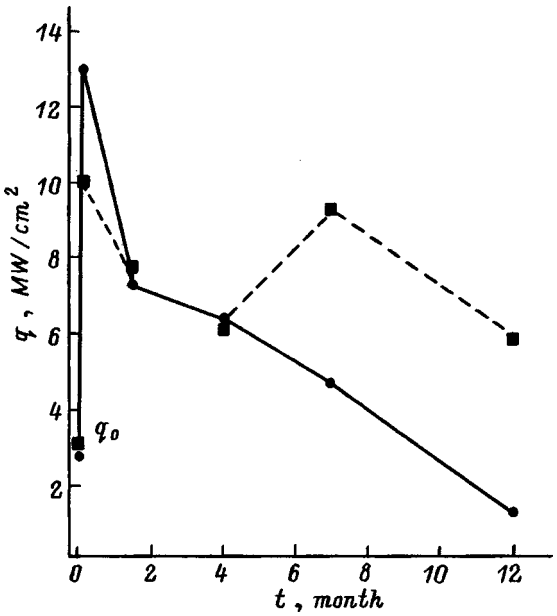

FIG. 8. Variation of the optical breakdown threshold q of copper mirrors with a protective a-C:H coating as a function of the storage time t of the mirrors under room conditions.

250–400 °C, while at temperatures above 450 °C the conventional oxidative reaction characteristic for carbon-containing materials occurs.[7] For gray-black a-C:H coatings, which possess a structureless absorption spectrum with a maximum at $\sim$1.5 eV (Fig. 7, curve *2*), the above-described thermochromic changes are uncharacteristic. As a rule, at the center of damage the coating burned up and erosion of the copper surface was observed. The edges of the damage to the coating had small local foci of damage. Complete destruction of the coating is possible at 1000 °C as a result of thermal destruction of a-C:H followed by oxidation of the hydrocarbon products which are released. Therefore it can be concluded, on the basis of the character of the damage observed in the coating as a result of optical breakdown, that the surface temperature in the irradiation spot can vary from 420 to 1000 °C.

The results of numerous tests on two mirrors with a gray-black coating during the course of a year are shown in Fig. 8. The samples were stored in the room atmosphere. The initial values $q=10$ and 13 MW/cm^2 of the optical breakdown threshold at the surface of a coated mirror were several times higher than the breakdown thresholds q_0 of the initial surface of the copper mirror and during the course of the year decreased to values close to the initial values 1.2 and 5.9 MW/cm^2, respectively, for the mirrors. A similar decrease of the breakdown threshold during storage of coated mirrors was also observed for other samples. Considering the stability of the properties of a-C:H, the decrease in the breakdown thresholds with time could be due to a change in the conditions at the mirror–coating interface. This is supported by the increase in the damaged area accompanied by simultaneous decrease of the breakdown threshold, observed as a result of the tests.

COMPUTATIONAL RESULTS

To determine the effect of the mirror–a-C:H coating interface on the breakdown threshold, calculations were performed of the temperature increase in the spot irradiated with pulsed IR radiation and of the breakdown threshold of a coating as a function of the adhesive contact. van der Waals forces act at the boundary between the mirror and the a-C:H coating.[8] In the absence of an adhesive contact between them, the coating should be heated by the radiation under conditions of thermal insulation, in which case the thermal resistance $r\to\infty$. Conversely, in the case of strong coupling $r\to 0$ and ideal thermal contact can be assumed.[9]

Let us consider the case of ideal thermal contact of the coating with the copper surface. The penetration depth of the IR radiation is $\delta=1/\alpha$, where α is the linear absorption coefficient. For the a-C:H coating investigated, the extinction coefficient $k=2.5–1.6\times10^{-2}$ at 10.6 μm with $n=2.0–2.4$ variable acetylene content in the mixture with inert gas.[10] In this case $\alpha=300–190$ cm^{-1}, and δ does not exceed 44 μm, which is much larger than the thickness of the coating. Therefore the temperature on the surface of the coating will correspond to the temperature of the surface layer of the copper, where $r=0$. The surface temperature T of copper mirrors with $\alpha=10^5–10^6$ cm^{-1} was estimated using a formula obtained by solving a differential equation describing the propagation of heat in a semi-infinite layer of matter bounded by the plane $Z=0$ on which radiation is incident:

$$T(0,\tau)=\frac{2q(1-R)\sqrt{\chi R}}{K\sqrt{\pi}}, \tag{1}$$

where q is the intensity of the radiation incident on the surface of the mirror, K is the thermal diffusivity, and χ is the thermal conductivity.

The calculations employed the experimental values, presented in Fig. 3, of the threshold power densities and reflection coefficients of coated mirrors. The values $K=0.913$ cal/sm·s·deg and $\chi=1.1$ cm^2/s for copper were taken from Ref. 11. The computed value of the temperature of the surface layer of an *a*-C:H coated mirror for the case of ideal adhesive contact between them does not exceed 200 °C for a mirror with $R=98.6\%$ and $q=13$ MW/cm^2.

In the case that there is no adhesive contact and $r\to\infty$, the radiation flux incident on the surface should be completely absorbed by a coating of thickness d in the time of the laser pulse τ. The power density for which the coating is heated up to the damage temperature can be determined as

$$q=q^*/A(d), \tag{2}$$

where q^* is the radiation power flux density absorbed by the coating and $A(d)$ is the absorption coefficient of the coating.

Neglecting heat removal into the copper mirror

$$q^*=\frac{TC\rho d}{M\tau}, \tag{3}$$

where C is the specific heat, ρ is the density, and M is the molecular weight of the carbon coating.

In the case of a transparent film, as the coating thickness increases, oscillations due to the interference of light in the layer are superposed on the weak monotonic growth of $A(d)$. In the simplest theoretical description of the absorbing power of a *a*-C:H coated copper mirror, the well-known solution of the classical problem of electrodynamics of the reflection of light from the surface of a uniform layer with sharp interfaces with bounding media, characterized, just as the layer, by frequency-dependent optical constants n and k, can be used.[12] For thin films ($d\ll\lambda/n$, $d\ll k^{-1}$) it follows from the solution, specifically, that

$$A(d)\approx A_0+\beta_1 d+\beta_2 d^2, \tag{4}$$

where

$$A_0=4n_2/[(n_2+1)^2+k_2^2]. \tag{5}$$

For the case that the extinction coefficient of the film $k_1\ll n_1$,

$$\beta_1\approx\pi A_0^2/\lambda\cdot k_2/n_2(n_1^2-1), \tag{6}$$

$$\beta_2\approx(\pi A_0/\lambda)^2(n_1^2-1)/n_2(n_2^2+k_2^2-n_1^2). \tag{7}$$

Substituting the optical constants for an *a*-C:H coating $n_1=2$ and $k_1=2.5\times10^{-2}$ at 10.6 μm (Ref. 10) and a copper mirror $n_2=11$ and $k_2=60.6$ (Ref. 13) into Eqs. (5), (6), and (7) we obtained

$$A(d)=0.012=7.05d+1.3\times10^6 d^2. \tag{8}$$

Formulas (3) and (8) were used to calculate the incident IR radiation flux densities q that heat the *a*-C:H coating up to the temperature of evaporation of the coating in the absence of adhesion and thermal contact in the interval of d from 0.1 to 0.7 μm. The following values were used for the calculations: $C=0.17$ cal/mole·deg,[7] $\rho=2.4$ g/cm^3, $M=12$ g/mole, and $\tau=15$ μs. The temperature $T=1000$ °C at which complete destruction of the coating and a transition into a gaseous state occur was taken as the temperature at which the coating is destroyed. The computed curve of the destruction threshold of an *a*-C:H coating is presented in Fig. 4. According to the calculation, the power density required to destroy an *a*-C:H coating with impaired adhesive contact increases monotonically as the coating thickness. For coating thickness equal to 0.7 μm, the power density required for complete destruction of the coating reached 0.35 mW/cm^2 and was an order of magnitude lower than the optical breakdown thresholds obtained experimentally.

DISCUSSION

The mechanism of near-surface optical breakdown accompanying the irradiation of metal mirrors is closely linked with the state of the polished surface: the presence of adsorbed impurities, embedded particles, and imperfection of the base itself. Being in poor thermal contact with the metal, such defects can be rapidly heated in a radiation field and serve as a source of ionized vapors and emission particle fluxes. As a result of the appearance of initial electrons and easily ionized matter, the conditions for the development of an electron avalanche — onset of optical breakdown — are eased in the surrounding medium.[14] The deposition of a protective *a*-C:H coating on the metallic surface can change the mechanism of the interaction of pulsed IR radiation with the mirror. The absence of a correlation between the breakdown thresholds of a coated mirror and a polished copper surface (Fig. 2) as well as between the breakdown thresholds and the reflectance (Fig. 3) shows that the conditions of plasma formation at the surface of the metal and the protective *a*-C:H coating are different. The effect of the properties of the coating on the interaction with intense IR radiation is manifested in the dependence of the optical breakdown threshold on the thickness (Fig. 4) and the deposition rate of the coating (Fig. 5).

An investigation using the adsorption-ellipsometric method showed that *a*-C:H coatings with $n>2.0$ are distinguished by low porosity.[15] Their optical properties do not change and they protect the mirror surface from oxidation by the surrounding medium. Such a coating should block the surface of the metal, impeding emission fluxes from leaving the surface of the coating under the action of pulsed laser radiation. This can explain the increase in the breakdown threshold of a mirror as the thickness of the *a*-C:H coating increases to 0.2 μm (Fig. 4). The decrease in the breakdown threshold with a further increase in the coating thickness (Fig. 4) and during storage of coated mirrors (Fig. 8) could be due to a change in the conditions at the mirror–coating interface.

A polished copper surface is a defective layer of a material that forms as a result of the destruction of the faces of polycrystals and that can contain pores and cavities. As was shown earlier, preliminary cleaning of the mirror surface in a glow discharge in an inert gas opens up the pores and can be accompanied by trapping of inert gas by the copper surface,[8] Diffusion of impurities and gases onto the mirror-coating interface should cause a local decrease of the adhesive contact. This process degrades the protective properties of the

coating and can decrease the breakdown thresholds of *a*-C:H coated mirrors during storage (Fig. 8). The lower computed values obtained for the breakdown thresholds of coatings exposed to IR radiation pulses for the case of impaired adhesive contact (Fig. 4) confirm this conjecture.

As the coating thickness increases, relaxation of the internal compressive stresses, which are characteristic for solid *a*-C:H coatings, becomes more likely. It has been established experimentally that for a coating thickness of 0.35 μm the internal compressive stresses can cause spontaneous separation of the coating from the surface of the copper mirror with the mirror when it heats up to 200 °C.[8] Local destruction of the adhesive and thermal contact at the mirror–coating interface can occur under heat and shock action of the laser radiation. Keeping this in mind, the decrease of the threshold radiation power densities in the experimental dependence $q(d)$ (Fig. 4) for $d>0.2$ μm can be explained by a degradation of the adhesive contact by the internal compressive stresses, which increase with increasing coating thickness. For substantial thicknesses of the protective coating $d\geqslant 0.7$ μm, the experimental values of the breakdown threshold approach the computed values for the case of impaired adhesive and thermal contact.

The character of the damage to *a*-C:H coatings attests to the fact that the temperature in the irradiation spot exceeds the maximum computed temperature (200 °C), obtained for the case of an ideal adhesive contact. Thermochromic changes in the coating, which are observable as a result of optical breakdown, show that the surface in the spot heats up to 420 °C. Complete destruction of an *a*-C:H coating can occur at 1000 °C, by-passing the melting stage. Heating up to such a temperature is possible as a result of the interaction of the coating with the plasma formed as a result of optical breakdown. The size of the damage to a 0.1–0.2 μm thick coating as a result of near-surface optical breakdown increased together with the radiation power density, but it did not exceed the area of the irradiation spot (Fig. 6). At the same time, the observed increase in the size of the region of damage in time can be explained by the decrease in the adhesive and thermal contact of the coating.

The increase in the breakdown threshold of *a*-C:H coated mirrors accompanying a decrease in the coating deposition rate in Fig. 5 shows that the *a*-C:H properties influence the plasma formation process at the surface of coated mirrors during optical breakdown. *a*-C:H condensation kinetics strongly influences the average order of the structure, determined by the sizes of the π-bonded clusters.[16] π-clusters consist of polycyclic aromatic groups, polyene and polyyne chains with a single system of conjugation of multiple bonds.[17] A decrease of the deposition rate of *a*-C:H coatings obtained from acetylene promotes an increase in the sizes of such clusters, a decrease in the content of bound hydrogen, and a decrease in the optical gap width.[18] At the same time, the optical absorption in the visible region of the spectrum and the refractive index increase.[16] *a*-C:H coatings with a structureless electronic spectrum (Fig. 7, curve *2*), which were obtained with deposition rates of less than 2 Å/s, had the highest optical breakdown thresholds. Such coatings are distinguished by low resistivity 10^7-10^8 $\Omega\cdot$cm from coatings with a structured electronic spectrum (Fig. 7, curve *1*), the resistivity equals $10^{11}-10^{12}$ $\Omega\cdot$cm. It can therefore be concluded that the electronic structure of *a*-C:H plays a large role in plasma formation at the surface of a mirror during optical breakdown.

The absorption of a 0.1 eV photon during the action of IR radiation on an *a*-C:H coating is sufficient to generate charge carriers inside the region of conjugation of π electrons, i.e., on an individual π cluster. Exciton formation is possible in an *a*-C:H coating whose electronic spectrum has maxima with energy above the optical band gap. The subsequent motion of the exciton depends on the degree of localization of the π electrons, and for an amorphous structure it can have a hopping character. The dissipation of energy on optical phonons should give rise to heating of the protective *a*-C:H coating under the action of IR radiation and to thermal emission of electrons. The higher the conductivity of the coating, the lower that likelihood that the coating will be heated during the action of the laser pulse and the higher the optical breakdown threshold are.

The possibility of local heating of the coating due to absorption of 10.6 μm radiation by defects and different inclusions at the mirror–coating boundary cannot be ruled out. The worse the adhesive and thermal contact at the metal–coating interface, the more likely the coating will be heated up to temperatures of thermal destruction and optical breakdown in the vapors of matter as a result of absorption of the IR radiation. The thermal model of near-surface optical breakdown is considered to be best substantiated.[1] It consists in stagewise development of breakdown: heating and vaporization of the barrier material, avalanche-like absorption in the vapors, and formation of a plasma focus with a transition into air plasma. According to the thermal mechanism, optical breakdown near the surface of an *a*-C:H coated mirror can develop as a result of local heating in separate sections of the laser irradiation zone up to temperatures above 450 °C, thermal destruction of the coating, and oxidation of hydrocarbon products of decomposition. Such a mechanism is most likely for a metallic coated mirror in the case $0<r<\infty$. At the same time, the possibility of tribo- and mechanoemission of electrons during crack formation as a result of the relaxation of internal compressive stresses in the coating as $r\rightarrow\infty$ cannot be excluded.

CONCLUSIONS

A systematic analysis of the effect of different factors on the breakdown threshold of copper mirrors with a protective *a*-C:H coating was performed. The investigations showed that the conditions of plasma formation under the action of intense 10.6 μm laser radiation at the surface of a metal are different from the conditions in the case of a protective *a*-C:H coating. For coating thickness less than 0.2 μm the near-surface optical breakdown threshold of mirrors is determined by the properties of *a*-C:H. The increase in the breakdown threshold of a mirror after an *a*-C:H coating is deposited on its surface is achieved as a result of a blocking effect due to the mechanical strength and chemical resistance of the amorphous coating as well as its optical and electrical prop-

erties. Higher breakdown thresholds were observed on *a*-C:H coatings obtained with deposition rates less than 2 Å/s. Such coatings are distinguished by a structureless electronic spectrum with the depths of trap levels not exceeding ~ 1.5 eV and by resistivities of 10^7–10^8 $\Omega \cdot$cm. For *a*-C:H protective coating thicknesses greater than 0.2 μm, the breakdown threshold of mirrors is determined by the conditions at the metal–*a*-C:H interface. A decrease in the bonding force between them as a result of relaxation of compressive stresses in the coating causes the breakdown threshold to decrease as the *a*-C:H thickness increases. The local impairment of adhesive contact due to diffusion of impurities and gases from a near-surface layer of the copper mirror onto the interface causes the thermal resistance to increase and the optical breakdown threshold to decrease during storage of the mirrors.

The results obtained will assist in understanding how the operation of passive CO_2-laser components protected by *a*-C:H coatings is affected by their interaction with intense laser radiation fluxes.

We thank E. M. Yudintsev for performing the tests of the optical breakdown threshold of mirrors and T. A. Zhevlakova for measuring the reflectances of the mirrors as well as N. A. Novoselov for technical assistance.

[1] A. M. Bonch-Bruevich, I. A. Didenko, and L. N. Kaporskiĭ, in *Low-Threshold Optical Breakdown of Gases Near a Surface (Review of Experimental and Theoretical Works)* [in Russian], Belorussian Academy of Science, Minsk (1985), p. 60.

[2] A. V. Balakov, E. A. Konshina, O. G. Peskov, and O. A. Shorokhov, in *Abstracts of the 3rd All-Union Conference on Laser Optics* [in Russian], Leningrad (1981), p. 365.

[3] A. V. Balakov, E. A. Konshina, and E. M. Yudentsev, in *Abstracts of the 4th All-Union Conference on Laser Optics* [in Russian], Leningrad (1983), p. 337.

[4] A. V. Balakov and E. A. Konshina, Zh. Tekh. Fiz. **52**, 810 (1982) [Sov. Phys. Tech. Phys. **27**, 521 (1982)].

[5] A. S. Zakharovm, A. A. Zelenov, E. P. Semenov, and E. M. Yudintsev, Opt. Mekh. Prom. No. **6**, 29 (1977).

[6] E. A. Konshina and A. V. Baranov, Poverkhnost', No. 4, 53 (1989).

[7] V. A. Semenovich, L. A. Sheguorskiĭ, B. V. Ogorodnikov, and É. A. Pugach, Sverkhtverdye Mater., No. 6, 17 (1984).

[8] A. V. Balakov, E. A. Konshina, and T. I. Kalugina, Opt. Mekh. Prom. No. **12**, 37 (1986).

[9] I. M. Karpman, M. N. Libenson, and E. B. Yakovlev, in *Laser Thermolithography in the Production of Integrated Circuits* [in Russian], Leningrad (1981), pp. 4–12.

[10] V. B. Yakovlev, L. K. Vasil'eva, V. V. Veremeĭ, and E. A. Konshina, Zh. Prikl. Spektrosk. **53**, No. 5, 863 (1990).

[11] J. F. Ready, in *Effects of High Power Laser Radiation* [Academic Pres, New York, 1971; Mir, Moscow, 1974, pp. 89–92.].

[12] A. M. Bonch-Bruevich and M. I. Libenson, Izv. Vyssh. Uchebn. Zaved. Fiz. **46**, 1104 (1982).

[13] *Thin Film Physics* (Mir, Moscow, 1967), Vol. 2, p. 294.

[14] V. I. Konov, A. M. Prokhorov, and N. I. Chapliev, Izv. Akad. Nauk SSSR **48**, 1591 (1984).

[15] V. A. Tolmchev and E. A. Konshina, Diamond Relat. Mater. **5**, 1397 (1996).

[16] E. A. Konshina and V. A. Tolmachev, Zh. Tekh. Fiz. **65**, 175 (1995) [Tech. Phys. **40**, 97 (1995)].

[17] A. V. Baranov and E. A. Konshina, Opt. Spektrosk. **65**, 856 (1988) [Opt. Spectrosc. **65**, 506 (1988)].

[18] E. A. Konshina, Fiz. Tverd. Tela (St. Petersburg) **37**, 1120 (1995) [Phys. Solid State **37**, 610 (1995)].

Translated by M. E. Alferieff

Nonelectrical method of pumping solid-state lasers

V. M. Shmelev, A. D. Margolin, N. Ya. Vasilik, and V. G. Krupkin

Institute of Chemical Physics, Russian Academy of Sciences, 117977 Moscow, Russia

V. T. Volov and D. B. Volov

Samara Institute of Rail Transportation Engineers, 443066 Samara, Russia
(Submitted April 28, 1997)
Zh. Tekh. Fiz. **68**, 67–70 (September 1998)

An alternative, nonelectrical method for obtaining a dense radiating plasma and the possibilities of using this method to pump solid-state lasers are investigated. The plasma was obtained experimentally by heating the working gas in a two-stage ballistic plasmatron. A new device — a vortex chamber — is proposed for transferring energy into the plasmatron–laser system.
 [S1063-7842(98)01309-9]

INTRODUCTION

Powerful sources of visible and UV radiation are required in order to accomplish diverse photochemical transformations and to solve a number of technological problems,[1,2] for optical pumping of lasers,[3–5] and so on. At the present time, pulsed gas-discharge tubes have found wide application for these purposes.[6] The source of radiation is an electric-discharge plasma with a temperature of 10 to 12 thousand degrees.

An alternative, nonelectrical method for obtaining a radiating plasma could be heating the working gas up to temperatures 6 to 12 thousand degrees with adiabatic compression of the gas in a special apparatus — a ballistic plasmatron. However, experiments[7–9] on single adiabatic compression of a gas by a freely flying piston showed the ballistic plasmatron to have a low energy efficiency as a source of optical radiation as compared with pulsed gas tubes.

An effective method for increasing the specific energy of a plasmatron is preheating the working gas.[10–12] This can be achieved by using several stages of compression and expansion using intermediate membranes, valves, and pistons in the system.

In the present paper we propose a nonelectrical method for obtaining plasma with temperature up to 15 000 K, using nonisentropic heating of the working gas in a ballistic apparatus with two-stage compression.

MULTISTAGE COMPRESSION

As is well known,[2] in a ballistic setup with volume V_0 and single compression of the gas up to pressure P_m and temperature T_m, plasma energy

$$E=\frac{P_m V_0}{1-\gamma}\left(\frac{T_0}{T_m}\right)^a\left(1-\frac{T_m}{T_0}\right), \quad a=\frac{\gamma}{\gamma-1},$$

where T_0 is the initial temperature of the working gas and γ is the ratio of specific heats, can be attained.

If the gas is heated in several successive stages (compression — expansion into an evacuated volume — compression and so on), then for an infinite number of such cycles the limiting energy of the plasma can be brought up to a value E_∞ given by[10,11]

$$E_\infty=\frac{P_m V_0}{\gamma-(T_0/T_m)}.$$

For example, for a monatomic gas ($\gamma=1.67$) with $T_0=300$ K heated up to temperature 6000 K the limiting efficiency E_∞/E_1 of multistage compression is 39 times higher than that of single-stage compression. In contrast to the multistage heating, where the intermediate steps of heating the gas are separated in space, there also exists another possibility of increasing the specific energy of a plasma by gradually accumulating energy in the system.[11] In this case the intermediate stages of heating the gas are separated in time and the system reaches a quasicontinuous radiation regime after a certain number of compression–expansion cycles.

TWO-STAGE HEATING OF A GAS

A large increase in the efficiency of heating the working gas can be achieved in relatively simple, two-stage adiabatic compression setups — ballistic plasmatrons with two freely moving pistons (Fig. 1). One piston with mass m_1 is placed at the start of the shaft of the setup, and another piston with mass $m_2<m_1$ is placed at certain distance X_0 from the first piston. The second piston contains a blow-off valve (in the simplest case, a through opening). To extract optical radiation, a bulb with transparent walls is attached to the end of the plasmatron shaft. The plasma produced under adiabatic compression flows into the bulb through a supersonic nozzle. A rupturing diaphragm can be placed in front of the nozzle, and the bulb itself is preevacuated.

The working cycle of gas compression and plasma generation proceeds as follows. Under the action of the pushing gas the heavy piston compresses gas in the region between the two pistons, and the second piston, having adequate inertia, plays the role of a wall. Next, the preheated working gas flows through the valve (or opening) in the second piston into the space in front of the pistons. At the second stage of

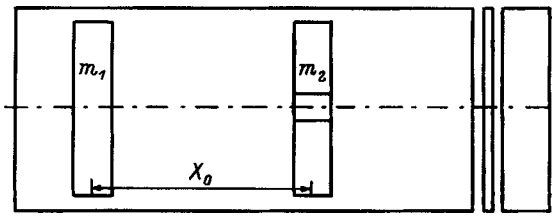

FIG. 1.

adiabatic heating of the gas, the gas is simultaneously compressed by the two pistons, moving approximately with the same speed. The plasma formed during the final compression flows through the nozzle into the transparent flask, where rapid deexcitation of the plasma occurs at low pressure.

The nonisentropic nature of the gas heating is due to the gas flow through the valve in the second piston. Calculations show that the degree of growth of the specific entropy $\varkappa$, determined in terms of the increase Δs of the specific entropy of the gas at the end of compression and the specific heat C_v, is

$$\varkappa=\exp(\Delta s/c_v)=(\rho/\rho_0)^{\gamma(\gamma-1)}\gamma^{\gamma-1}/(\gamma+1)^{\gamma}, \tag{1}$$

where ρ_0 and ρ are the gas density before and after compression.

The entropy increase (1) depends on the degree of gas compression and can reach a large magnitude ($\varkappa\gg 1$).

Let us estimate the maximum attainable specific energy E_2 of the plasma at a fixed finite temperature T_m and pressure P_m, optimizing the output parameters of the system. If the entire working gas of mass M_2 is initially confined in the volume V_1 between the pistons, then at the first stage of compression up to some pressure P_3 the gas is heated up to an intermediate temperature T_3

$$\frac{T_3}{T_0\gamma}=\left(\frac{P_3}{P_0}\right)^{c}, \quad c=\frac{\gamma-1}{\gamma}.$$

From the condition that the final values of the temperature T_m and pressure P_m are reached at the second stage of compression of the already heated gas we obtain a relation determining the required mass of the working gas

$$M_2=\frac{\mu V_0}{RT_0}(T_0/T_m)^{\gamma^2/(\gamma^2-1)}P_3^{1/(\gamma+1)} \times P_m^{\gamma/(\gamma+1)}\beta^{1/(1+\gamma)}(1-\beta)^{\gamma/(1+\gamma)}, \tag{2}$$

where $\beta=V_1/V_0$, μ is the molecular weight of the gas, and R is the gas constant.

The highest energy E_2 of the plasma is reached with the maximum mass of the working gas, which is a function of the position of the second piston $M_2=f(\beta)$.[11] It is easy to see that the extremum of the function (2) is reached for $\beta=1/(1+\gamma)$. If we set $P_3=P_m$ (i.e., the choice of the maximum pressure of compression is determined only by the strength characteristics of the apparatus), then in this case the expression for the optimal gas mass will be

$$M_2=\frac{\mu V_0 P_m}{RT_0}(T_0/T_m)^{\gamma^2/(\gamma^2-1)}\gamma^{\gamma/(\gamma+1)}/(\gamma+1). \tag{3}$$

The required gas mass M_1 for a single-compression setup is

$$M_1=\frac{\mu V_0 P_m}{RT_0}\left(\frac{T_0}{T_m}\right)^{\gamma/(\gamma-1)}. \tag{4}$$

Comparing expressions (3) and (4), we obtain that for the optimal value of β the specific energy characteristics of a two-stage compression plasmatron are higher by a factor $\eta=M_2/M_1$ given by

$$\eta=(T_m/T_0)^{\gamma/(\gamma^2-1)}\gamma^{\gamma/(\gamma+1)}/(\gamma+1). \tag{5}$$

The increase in the temperature of the working gas at the first stage of compression equals

$$T_3/T_0=(T_m/T_0)^{\gamma/(\gamma+1)}(1+\gamma)^{(\gamma-1)/\gamma}\gamma^{(1-\gamma)/(\gamma+1)}. \tag{6}$$

One can see from Eqs. (5) and (6) that the values of η and T_3 increase with T_m, and for $T_m/T_0=$ const η is all the higher, the smaller γ is. For example, for a monatomic gas heated from room temperature up to $T_m=8000$ K the efficiency of a two-stage compression plasmatron will be more than an order of magnitude higher, while preliminary heating of the gas does not exceed 1500 K.

Let us now consider the case where the working gas initially occupies the entire volume V_0 of the plasmatron shaft. After the first stage of heating of a portion of the working gas compressed between the pistons and expansion of the gas, the temperature of the gas drops by approximately a factor of $1/\beta$ as a result of mixing with the remaining portion of the gas which has the initial temperature.

Performing similar calculations we obtain optimal values of the parameters $\beta=1/\gamma$, as well as the corresponding expression for the required gas mass and factor η by which the efficiency of the apparatus increases:

$$M_2=\frac{\mu V_0 P_m}{RT_0}(T_0/\gamma T_m)^{\gamma^2/(\gamma^2-1)}(\gamma-1)^{\gamma/(\gamma+1)},$$

$$\eta=(\gamma T_m/T_0)^{\gamma/(\gamma^2-1)}(\gamma-1)^{\gamma/(1+\gamma)}\gamma^{\gamma/(1-\gamma)}. \tag{7}$$

The amount of preheated gas at the first stage of compression equals

$$(T_3/T_0)=(\gamma-1)^{(1-\gamma)/(1+\gamma)}(\gamma T_m/T_0)^{\gamma/(\gamma+1)}.$$

If the initial volume V_0 of the setup and final volume V_k up to which the gas is compressed are taken as the input parameters of the problem, then the plasma temperature will be determined by the degree of compression and in the optimal regime equals

$$T_m/T_0=(\gamma-1)^{\gamma(\gamma-1)}\gamma^{-\gamma^2}(V_0/V_k)^{(\gamma^2-1)}. \tag{8}$$

It follows from Eq. (8) that for $\gamma\sim 1.4$ the plasma temperature is a linear function of the degree of compression of the gas. For $\gamma<1.4$ the production of high plasma temperatures by increasing the degree of compression of the working gas becomes inefficient.

The energy efficiency (7) of the nonisentropic two-stage compression with the working gas heated up to a temperature of the order of 10 000 K is approximately 10 times higher than the efficiency of single-stage adiabatic compression.

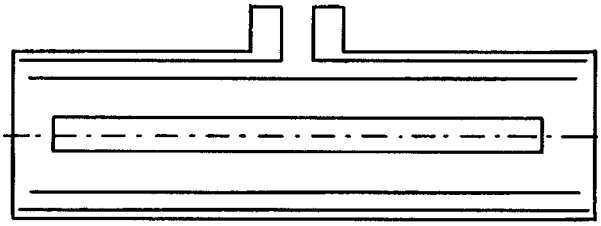

FIG. 2.

PUMPING A LASER WITH PLASMA RADIATION

The radiation from a xenon plasma heated by the thermal method up to temperatures 10 000–15 000 K can be used with adequate efficiency to pump a solid-state laser.[3–5]

Experimental setups in which xenon and argon plasma with temperature above 10 000 K and compression pressure of about 1000 atm with specific plasma energy above 10 kJ per liter of internal volume of the apparatus and efficiency of conversion of the energy of the pushing gas into the internal plasma energy of up to 80% have been developed at the Institute of Chemical Physics of the Russian Academy of Sciences. In a number of experiments, where a neodymium rod was irradiated with plasma radiation, lasing with energy up to $E=10$ J per pulse has been obtained. The lasing time was about 1 ms. The dimensions of the ballistic plasmatron are several times smaller than the dimensions of a setup with similar power but pumped by an electric tube.

Diverse schemes for extracting the plasma radiation from a ballistic plasmatron are possible for pumping a laser rod. For example, radiation can be extracted directly through a transparent window placed at the end of the setup[3–5] or using an intermediate chamber into which plasma flows through a supersonic nozzle.

Let us consider the case where the heated gas, after rupturing a membrane, passes through the entrance channel into an optical chamber. A shock wave is formed and moves with supersonic velocity toward the opposite end of the chamber. Energy is radiated at this time. The radiation reaches the active medium and lasing occurs, just as in an ordinary solid-state laser.

In such a pumping scheme radiation losses can occur directly at the entrance into the optical chamber and in the circumflow channel. Theoretical analysis shows that for such gas dynamics of the flow a system of oblique/straight shocks, where most of the radiation energy is radiated, arises. The energy is dissipated on the large surface of the channels, while strongly cooled gas enters the chamber. Illumination of the active medium by the direct wave of radiation moving along the rod is not optimal: At each moment in time only a section of the active medium is pumped.

To eliminate these drawbacks and to increase operational reliability a fundamentally new design of the optical chamber is proposed. In this design, gas is blown in not from the end but rather tangentially from the side surface. After flowing through the shortened entrance channel the gas, acquiring a swirling motion, moves in both directions (Fig. 2).

In this optical chamber there are no losses in an axial chamber due to entrance shocks. The dissipation of radiation on the walls of the entrance channel is decreased by approximately a factor of 2 as a result of the decrease in the interaction surface, and losses are decreased by another factor of 2 because of a decrease in the length of the input section. Moreover, here more uniform illumination of the active medium is achieved, and a two-mirror cavity can be used. But the gas motion in such a chamber is extremely complicated. It is necessary to solve a three-dimensional gas-dynamic problem.

Computer calculations performed with the program developed in Ref. 13 showed that a head wave is formed after the membrane is ruptured. On detaching from a sharp edge the wave is diffracted at an angle of the order of 40° in the direction of the central shaft, as a result of which there occurs an impact against the quartz tube of one or another intensity. The magnitude of the impact depends mainly on the length of the entrance channel: the longer the channel, the weaker the impact. On the other hand, as the length of the entrance channel increases, radiation losses increase. Calculations show that the optimal channel length here is $L/d=1$.[14] Even the first experiments with a vortex chamber showed that quartz tubes with a wall thickness approximately half that of an ordinary chamber operates successfully in the computed regimes of the plasmatron. Theoretical calculations of the gas motion have been performed for the proposed design of the optical chamber, and it is expected that the efficiency of the apparatus will increase on the whole by at least an order of magnitude.

[1] L. T. Bugaenko, M. G. Kuz'min, and L. S. Polak, *High-Energy Chemistry* [in Russian], Khimiya, Moscow (1988), 366 pp.
[2] Yu. A. Kolbanovskiĭ, V. S. Shchipachev, N. Ya. Chernyak *et al.*, *Chemical-Impulsive Compression of Gasses in Chemistry and Technology* [in Russian], Nauka, Moscow (1982), 240 pp.
[3] C. L. Smith, E. Homentowski, and C. S. Stokes, Appl. Opt. **6**, 1130 (1967).
[4] G. K. Grosòy and R. C. Honey, Appl. Opt. **6**, 1339 (1963).
[5] A. J. Landerman, S. R. Byron, and W. W. Lawrece, Appl. Opt. **6**, 1743 (1969).
[6] G. N. Rokhlin, *Discharge Light Sources* [in Russian], Énergoatomizdat, Moscow (1991), 720 pp.
[7] J. A. Dowling, J. Shumsky, J. Echerman, and R. E. Schelier, Appl. Phys. Lett. **12**, 184 (1968).
[8] J. A. Dowing, Appl. Opt. **12**, 1867 (1969).
[9] Yu. N. Ryabinin, *Gases at High Densities and Temperatures* [in Russian], Fizmatgiz, Moscow, 1959.
[10] N. A. Zlatin *et al.*, *Ballistic Setups and Their Application in Experimental Investigations* [in Russian], Nauka, Moscow, 1974.
[11] A. D. Margolin, N. Ya. Vasilik, V. M. Shmelev *et al.*, in *Abstracts of the 1st All-Union Symposium on Radiation Plasma Dynamics* [in Russian], Énergoatomizdat, Moscow (1989), p. 33.
[12] A. D. Margolin, N. Ya. Vasilik, V. M. Shmelev *et al.*, in *Abstracts of the 15th Interdisciplinary Seminar ''Atomic-Hydrogen Energetics and Technology* [in Russian], Moscow, 1990.
[13] D. B. Volov, *Promising Information Technologies in Scientific Investigations, Design, and Teaching* [in Russian], Samara, 1995, p. 96.
[14] D. B. Volov, *Promising Information Technologies in Scientific Investigations, Design, and Teaching* [in Russian], Samara (1995), p. 97.

Translated by M. E. Alferieff

Spectral and scintillation characteristics of compound x-ray detectors based on calcium iodide crystals

S. S. Novosad

I. Franko L'vov State University, 290005 L'vov, Ukraine
(Submitted May 5, 1997; resubmitted August 26, 1997)
Zh. Tekh. Fiz. **68**, 71–73 (September 1998)

The results of an investigation of the spectral and scintillation properties of pure and Tl^+, Eu^{2+}, Fe^{2+}, Co^{2+}, and Ni^{2+} activated calcium iodide crystals as well as the results of measurements of the scintillation characteristics of compound x-ray detectors based on calcium iodide crystals are reported. It is shown that paired CaI_2 and CaI_2:Tl crystals can be used to fabricate compound detectors with different fluorescence times. On account of their high light output and good energy resolution CaI_2 and CaI_2:Eu crystals are suitable for compound detectors with different technical light output. CaI_2 or CaI_2:Eu scintillators together with scintillators based on calcium iodide with iron-group luminescence quenching impurity (Fe^{2+}, Co^{2+}, and Ni^{2+}) can be used to obtain compound detectors with different physical light output. © *1998 American Institute of Physics.* [S1063-7842(98)01409-3]

Fast elemental analysis of raw materials, intermediate materials at different stages of a technological process, and finished products is becoming increasingly important in modern industry. It is especially important in performing mass analyses during geological and geophysical investigations.[1–3]

In probe-type x-ray radiometric apparatus employed for x-ray fluorescence analysis of complex ores for elements with close atomic numbers, compound x-ray detectors consisting of two scintillators with different fluorescence times or different light output are used.[3,4]

It is known[5–7] that calcium iodide crystals possess better scintillation properties than NaI_2:Tl, CsI:Na, and CsI:Tl crystals. In this connection, it is of practical interest to investigate the possibility of using calcium iodide crystals for compound x-ray detectors.

In Ref. 5 it is shown that at room temperature the scintillation crystals CaI_2 and CaI_2:Tl excited by ^{137}Cs γ rays luminesce in a close spectral region. The fluorescence times of the crystals differ substantially and equal 550 and 1100 ns, respectively.

In the course of investigations of the x-ray luminescence of CaI_2:TlI crystals, which we grew by the Stockbarger method from specially purified raw material, it was established that the luminescence in the temperature interval 90–400 K consists of a nonelementary band with a maximum at 400–450 nm and the spectral composition is close to that of CaI_2 radiation.[7–10] The room-temperature light output (scintillation amplitude) of the CaI_2 and CaI_2:TlI crystals obtained is approximately 1.75 and 1.5 times greater than that of the scintillator NaI:Tl. These calcium iodide crystals are also characterized by a high energy resolution.

The results of our investigations together with the data of Ref. 5 show that CaI_2 and CaI_2:TlI crystals can be used in pairs to fabricate compound detectors with different fluorescence times, since they meet the requirements for scintillators in this case[3,4] and they are distinguished advantageously from known scintillators by the fact that both scintillators can be prepared from the same material.

In fabricating compound detectors with different technical light output, to increase the luminosity of the setup and decrease requirements for the active source of primary γ-radiation we packaged both CaI_2 or CaI_2:Eu based scintillators with high identical light output and close spectrometric properties in the same container (see Fig. 1) with a Duralumin case *1*. Optical contact between the single-crystal scintillator wafers *5* and *5′* and the output window *2* was accomplished with silicone glue *3*. Finely dispersed magnesium oxide powder *7* was used as a reflector. The single-crystal wafers were separated by a Duralumin barrier *6* or reflector powder. A 0.1–0.2 mm thick beryllium disk, secured in the container case by an elastic ring *9*, was used as the entrance window *8*. The entire structure of the container was sealed with epoxy glue *10*. To obtain different technical light output from individual single-crystal scintillator wafers, a $\sim$10–15 nm thick metallic palladium film *4* was deposited, as a neutral light filter with fixed transmission, on the output window of one of the scintillators by the vacuum evaporation method.

The scintillation characteristics of the best samples of compound detectors with different light output, which were fabricated from CaI_2 and CaI_2:Eu, are presented in Table I. The scintillation characteristics of a compound detector fabricated from NaI:Tl are also presented in this table for comparison. It follows from the data presented in Table I that detectors based on calcium iodide possess better spectrometric characteristics than detectors based on NaI:Tl. The energy resolutions δ_1 and δ_2 of scintillators with and with, respectively, a light filter equal 26–27 and 68–70%, respectively.

However, this method of obtaining compound detectors is still laborious and expensive. Moreover, when such containers are prepared for packaging or in the process of pack-

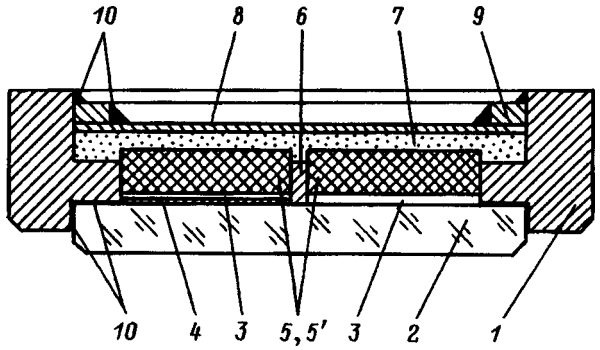

FIG. 1.

aging, additional inconveniences arise because of the possibility of damaging the deposited film used as a neutral light filter. The compound-detector technology simplifies considerably if the detector is fabricated on the basis of two scintillators possessing different physical light output, since then the neutral light filter can be eliminated from the container design.

To study the possibility of obtaining the spectrometric scintillators with low light output, which could be used for fabricating compound x-ray detectors with different light output, we grew, from highly pure CaI_2 salt by the Stockbarger method, calcium iodide crystals with luminescence-quenching iron-group impurities and investigated the optical-luminescence properties of the crystals in the temperature interval 90–295 K.

Wide activator bands with maxima in the region 260–340 nm, which are associated with charge transfer,[11] and narrow activator bands, due to $d-d$ transitions in Fe^{2+}, Co^{2+}, and Ni^{2+} ions present in the octahedral environment of the halide ions and observed on the long-wavelength shoulder of the charge transfer bands, were observed in the absorption spectra of the $CaI_2:FeCl_2$, $CaI_2:CoCl_2$, and $CaI_2:NiI_2$ crystals obtained. When these crystals are excited by light from the region of activator absorption, luminescence of activator centers is not observed and the intensity of the nonactivator luminescence, excited by light from the region of the excitonic absorption edge (230–240 nm), decreases considerably as the impurity content increases. Fe^{2+}, Co^{2+}, and Ni^{2+} ions likewise do not form in calcium iodide luminescence centers emitting in the visible region of the spectrum under x-ray excitation, but rather they are quenchers of the x-ray luminescence of the base of the crystals. The changes occurring in the spectral composition of the luminescence of $CaI_2:Co^{2+}$ and $CaI_2:Ni^{2+}$ crystals as the impurity content increases are caused by reabsorption.

Calcium iodide crystals with low concentrations of iron, cobalt, and nickel ions are characterized under x-ray excitation by weak thermal luminescence, while it is essentially not observed in heavily doped crystals.

In the process of measuring the scintillation characteristics of x-ray detectors fabricated on the basis of Fe^{2+}, Co^{2+}, and Ni^{2+} activated calcium iodide crystals it was established that as the concentration of the luminescence-quenching impurity in CaI_2 increases, the light output of the scintillators can be decreased within wide limits while preserving the spectrometric properties of the crystals.

The results of measurements of the luminescence and scintillation properties of calcium iodide crystals activated with iron, cobalt, and nickel ions are presented in Table II. The table also presents average data on the light output and energy resolution which were obtained in measurements on at least three x-ray detectors fabricated from the same single crystal. It follows from the data in Table II that to fabricate compound x-ray detectors with paired highly efficient CaI_2 and $CaI_2:Eu$ scintillators, calcium iodide crystals activated with luminescence-quenching impurities can be used as scintillators with low light output.

Measurements of the scintillation properties of the experimental samples of detectors fabricated on the basis of CaI_2 and $CaI_2:Fe$ established that for a coefficient of amplitude separation of the signal equal to 4 obtained with the MoK_α line the best detectors had an energy resolution of 72 and 27%, respectively, for crystals with and without a quenching impurity, i.e., these compound detectors are very competitive with compound detectors fabricated on the basis of two CaI_2 or $CaI_2:Eu$ crystals using neutral light filters.

We also observed that the intensity of the x-ray luminescence of the scintillator is observed to decrease with additional activation of NaI:TlI from melt by $FeCl_2$ or $CoCl_2$ impurities. Here the quenching impurities Fe^{2+} and Co^{2+} have virtually no effect on the spectral composition of the luminescence. Compound detectors fabricated on the basis of NaI:Tl and NaI:Tl, Fe with different light output and a coefficient of amplitude separation of the signal of 2.1 had an energy resolution of 60 and 34%, respectively, for crystals with and without a quenching impurity.

In summary, it follows from the results obtained in this work that CaI_2 and $CaI_2:Tl$ crystals can be used in pairs to fabricate compound x-ray detectors with different fluorescence times. On account of their high light yield and good

TABLE I. Spectrometric and luminescence characteristics of compound detectors with different technical light output.

Crystal No.	Crystal	Coefficient of amplitude separation of the signal	Energy resolution with Mo K_α ($E_{ex}=17.4$ keV)		Luminescence band maximum, nm
			δ_1	δ_2	
1	NaI : Tl, NaI : Tl	4.0	36	74	415
2	CaI_2, CaI_2	4.0	27	72	410−415
3	CaI_2: Eu, CaI_2: Eu	3.8	26	68	465−470

TABLE II. Luminescence and scintillation characteristics of calcium iodide crystals activated with iron group ions (E_{ex}=17.4 keV, MgO reflector, FÉU-35A).

Crystals	Luminescence band maximum, nm	Light output, arb. units	Energy resolution, %
CaI_2 (reference)	410−415	100	27
CaI_2: 0.01 mole % $FeCl_2$	410−425	73	43
CaI_2: 0.10 mole % $FeCl_2$	415−425	45	47
CaI_2: 1.00 mole % $FeCl_2$	415−425	21	80
CaI_2: 0.03 mole % $CoCl_2$	420−430	50	45
CaI_2: 1.50 mole % $CoCl_2$	430−460	14	90
CaI_2: 0.01 mole % NiI_2	420−440	47	48
CaI_2: 0.10 mole % NiI_2	420−440	20	95

energy resolution CaI_2 CaI_2:Eu crystals are suitable for compound detectors with different technical light output. CaI_2 or CaI_2:Ei scintillators together with scintillators based on calcium iodide with a luminescence-quenching iron-group impurity (Fe^{2+}, Co^{2+}, and Ni^{2+}) can be used to fabricate compound detectors with different physical light output.

[1] R. I. Plotnikov and G. A. Pshenichnyĭ, in *X-Ray Fluorescence Analysis* [in Russian], Atomizdat, Moscow (1973), 264 pp.
[2] L. V. Viktorov, V. M. Skorikov, V. M. Zhukov, and B. V. Shul'gin, Izv. Akad. Nauk SSSR, Neorg. Mater. **27**, 2005 (1991).
[3] V. A. Meĭer and M. M. Filippov, Vest. LGU, No. 18, 133 (1974).
[4] M. M. Filippov, *Author's Abstract of Candidate's Dissertation*, Leningrad (1977).
[5] R. Hofstadter, E. W. O'Dell, and S. T. Schmidt, IEEE Trans. Nucl. Sci. **NS-11**, 12 (1964).
[6] A. B. Lyskovich, O. O. Novosad, and M. R. Panasyuk, in *Abstracts of the 6th All-Union Conference on the Synthesis, Production, and Application of Scintillators* [in Russian], All-Union Scientific-Research Institute of Single Crystals, Kharkov (1971), pp. 19–21.
[7] S. S. Novosad, Vest. L'vovskogo Univ. Ser. Fiz. Éksp. Teor. Fiz. (Vyshcha Shkola, L'vov), No. 11, pp. 44–47 (1976).
[8] S. S. Novosad and N. K. Gloskovskaya, in *Abstracts of the 4th All-Union Conference on Radiation Physics and Chemistry of Ionic Crystals*, Salaspils (1978), Part 1, pp. 143–144.
[9] N. K. Gloskovskaya and S. S. Novosad, in *Abstracts of the 5th Ural Spectroscopy Conference*, Sverdlovsk (1980), p. 83.
[10] T. I. Triska and Z. L. Shevkis, in *Single Crystals, Scintillators, and Organic Luminophores* [in Russian], All-Union Scientific-Research Institute of Single Crystals, Cherkassy (1972), pp. 44-46.
[11] A. S. Marfunin, *Introduction to the Physics of Minerals* [in Russian], Nedra, Moscow, (1974), 324 pp.

Translated by M. E. Alferieff

Chaotization and decay instability of a diffraction-catastrophe field in the presence of focusing of high-power laser radiation in a nonlinear medium

V. Yu. Osipov

A. F. Ioffe Physicotechnical Institute, Russian Academy of Sciences, 194021 St. Petersburg, Russia
(Submitted May 12, 1997)
Zh. Tekh. Fiz. **68**, 74–83 (September 1998)

Focusing of a high-power laser beam, whose initial wave front is deformed by spherical aberration and astigmatism, in a medium with refractive-index nonlinearity is investigated by the computer experiment method. It was found that the extended formations which arise near the focus are no longer diffraction catastrophes, since they are structurally unstable. It is shown that weak disturbances of the shape of the initial wave front produce extremely strong distortions of the optical field in the focusing region. As the wave propagates in the z direction, spatial chaos in the distribution of the optical field develops in the region of focusing (from 137 to 142 mm). Optical turbulence arises in the focusing region as a result of self-diffraction of light by self-induced nonuniformities of the refractive index of the medium. After the region with the smallest cross section of the formation near the focus, the three-dimensional optical field has the form of chaotically dispersing ''splashes'' and extended ''filamentary ejecta.'' © *1998 American Institute of Physics.* [S1063-7842(98)01509-8]

INTRODUCTION

Caustic formations arising in the region of focusing of complicated wave fronts are the subject of study of a new avenue, which arose at the beginning of the 1980s, in optics — the optics of catastrophes.[1,2] Optical or diffraction catastrophes are caustic wave formations in the region of focusing that are structurally stable with respect to weak disturbances of the primary wave front that is subjected to focusing. In the theory of catastrophes, wave fields the can be transformed into one another by means of a diffeomorphism transformation are structurally stable. Closed classes of such three-dimensional fields comprise different types of diffraction catastrophes. There are no more than seven of such different classes of fields.[1,2]

As an example, we note that in the process of the evolution of an ideal spherical wave front or of a spherical wave front deformed by a spherical aberration in the focusing region there arise caustic formations which are not diffraction catastrophes, since the wave fields that are formed in the process are structurally unstable with respect to small disturbances of the shape of the primary wave front. Thus an ideal focus is a structure of infinite codimension and in the presence of small disturbances of an ideal spherical wave front it ''disintegrates'' into a collection of speckle elements that cannot be transformed into the wave field of an ideal focus by diffeomorphism transformation.

For a number of practical problems of laser physics it is of interest to employ for pumping of the working media a primary wave front for which the caustic formation in the focusing region is structurally stable. Pumping of the working medium with focusing is employed in the following situations: for pumping a small amount of matter, for realizing superhigh pump intensities, to produce a population-inverted region in the form of an extended focal filament, and so on. The plasma-spark channel realized in gases in a region of extended focusing[3–5] can serve as an active amplifying medium of a short-wavelength laser with $\lambda < 1000$ Å. Moreover, the focusing of high-power radiation into a liquid medium is used in devices for passive phase conjugation by means of stimulated Mandel'shtam–Brillouin scattering (SMBS).[6,7] In the latter case, conversely, it would be interesting if the region of generation of SMBS of the radiation in a liquid localized in the region of the caustic focus were structurally unstable for very weak fluctuations of the shape of the wave front which is to undergo phase conjugation. For the phase conjugation method this effect apparently gives a high selectivity with respect to a parameter such as the shape of the wave front, and it effects phase conjugation with a high degree of accuracy.

It is interesting[8] that a structurally stable three-dimensional distribution of the optical field in the focusing region is obtained during evolution of a spherical wave front deformed by strong spherical aberration and weak astigmatism. Such a caustic formation is a diffraction catastrophe.[1] When a working medium is pumped by high-power laser radiation, nonlinear effects due to the quadratic dependence of the refractive index on the amplitude of the light wave will arise.[9] The pumping light will be diffracted by three-dimensional index modulation gratings self-induced in the focusing region. It is of interest to investigate how the nonlinear effects which in the standard situation lead to self-focusing will change a structurally stable diffraction catastrophe in the focusing region and whether or not the resulting formation near the focus will once again be structurally stable.

INITIAL DATA

We shall study in the half-space $z>0$ the propagation of a scalar wave for which the distribution of the complex amplitude in the (x,y) plane at $z=0$ has the form

$$A(x,y,0)=A_0 \exp(i\cdot\varphi(x,y)), \tag{1}$$

where

$$\varphi(x,y)=\frac{2\pi}{\lambda}[(\tilde{F}-\sqrt{\tilde{F}^2-x^2-y^2}) + a(x^2+y^2)^2+c(y^2-x^2)]. \tag{2}$$

Here the phase function $\varphi(x,y)$ determines the shape of the wave front near the plane $z=0$; λ is the wavelength of the radiation in vacuum; a is the third-order spherical aberration constant; c is an effective coefficient characterizing astigmatism; A_0 is the amplitude of the field on the wave front surface near the $z=0$ plane. The intensity distribution of the wave ($I\sim A_0^2$) over the effectively open aperture of the wave front is constant $A_0^2(x,y)=$ const. The first term in brackets in Eq. (2) corresponds to an ideal sphere with radius $\tilde{F}$, while the second and third terms in Eq. (2) characterize the deformation of an ideal spherical wave front by spherical aberration and astigmatism, respectively.

To compare our results with Ref. 8, we shall perform the calculations with the following parameters: $a=1.2\times10^{-6}$ mm^{-3}, $c=9.96\times10^{-16}$ mm^{-1}, $\tilde{F}=141.699$ mm, and $\lambda=0.6328$ μm. We assume the aperture of the initial wave front at $z=0$ to be 20 mm in diameter. The longitudinal focusing error, corresponding to rays from the edge of such an aperture, equals approximately $\delta s\cong-10$ mm. We shall assume that the region $0<z<135.5$ mm is free space, while the half-space $z\geqslant135.5$ mm is filled with a nonlinear liquid medium. The liquid can be carbon disulfide, nitrobenzene, toluene, and silicon tetrachloride. Since $\tilde{F}>135.5$ mm, a converging beam definitely focuses in the liquid medium at some distance from the free space–nonlinear liquid interface. For the nonlinear medium, the index of refraction depends as follows on the amplitude $|A(x,y,z)|$ of the intensity vector of the electric field:[9,10]

$$n=n_0+n_2''|A(x,y,z)|^2, \tag{3}$$

where the coefficient n_2'' gives rise to the nonlinearity of the medium, n_0 is the constant part of the refractive index, the quantity $(1/2)|A(x,y,z)|^2 n_0(\varepsilon_0/\mu_0)^{1/2}$ in the SI system of units corresponds to the local intensity of the electromagnetic field at the point (x,y,z) and $(\mu_0/\varepsilon_0)^{1/2}=120\pi$ Ω is the characteristic impedance of free space.

In a medium with refractive index n_0 the wavelength of the radiation and hence the characteristic size of the diffraction structures in a caustic are n_0 times smaller than in a vacuum. For this reason, to compare the caustic field in a nonlinear medium with a caustic in free space (for example, air or vacuum) we shall assume that for $z\geqslant135.5$ mm the electromagnetic wave propagates in a medium with an effective refractive index

$$\tilde{n}=1+\frac{n_2''}{n_0}|A(x,y,z)|^2. \tag{4}$$

We choose the ratio of the parameters n_2''/n_0 and A_0 so that the dimensionless quantity $(n_2''/n_0)|A_{\max}|^2$ would equal 0.0049. Here $|A_{\max}|$ is the maximum amplitude of the field realized in the plane $z=140.55$ mm with the initial wave focused in free space. Propagating in free space $0<z<135.5$ mm, the wave arrives at the plane $z=135.5$ mm with a maximum amplitude such that $(n_2''/n_0)|A_{\max}|^2=0.0011$.

In what follows, we shall call the medium linear if its effective refractive index always equals 1 and nonlinear if Eq. (4) holds.

PROCEDURE OF THE COMPUTER EXPERIMENT

A computer program operating under the following approximations was devised for the investigations. As the light propagated in the region of focusing in the z direction, the radiation from the jth layer was transferred to the $j+1$ layer by means of the Fresnel–Kirchhoff integral. We shall explain this. Each successive layer j modulated the refractive index of the medium in the (x,y) plane in accordance with the light intensity distribution in the jth layer. Next, the self-induced diffraction of light by the section between the jth and $(j+1)$th layers, caused by modulation of the refractive medium of the index in the (x,y) plane from the jth layer, was calculated. Here the complex transmission function $\exp(i\cdot\Delta\phi(x,y))$, where $\Delta\phi(x,y)$ is the distribution of the phase delay in the (x,y) plane, acquired from the induced part of the refractive index of the medium in the distance Δz between the $j+1$th and jth layers, played the role of a phase screen (''obstacle''). This phase screen was imagined to be in the jth layer. The result of the diffraction of light by the phase screen was calculated, by means of the Fresnel–Kirchhoff integral extended to the case of nonuniform waves, for a plane displaced from the screen by a distance Δz.[11] The product of the complex transmission function of the phase screen and the distribution of the complex amplitude of the field for the jth layer, obtained in the preceding iteration, was substituted into the integrand as the new distribution of the complex amplitude of the field in the (x,y) plane. The result of these calculations was the distribution of the complex amplitude of the wave in the (x,y) plane for the $(j+1)$th layer.

This process was repeated with step $\Delta z=50$ μm over the extent of the region of focusing of the wave front located 135.5–142 mm from the exit window of the focusing system. The caustic formation under investigation was 6.5 mm long and possessed transverse dimensions not exceeding 550×550 μm. Thus the passage of light through the focusing region was calculated in the next higher order approximation after the Born approximation, taking account of the secondary scattering of light by nonuniformities of the medium.[12] It is important to underscore here that the nonuniformities of the medium are self-induced in the high-power radiation field on account of the Kerr dependence of the refractive index on the light intensity. Only the secondary small-angle forward scattering in the interval of angles relative to the z

axis from $-16.5°$ to $+16.5°$ was taken into consideration in the calculations. The absorption of the medium and backscattering as well as scattering by larger angles in the forward direction were also neglected. The latter was due to the limitations of the computer. The calculation was performed in the scalar approximation neglecting the rotation of the polarization plane of the radiation in the process of diffraction by self-induced nonuniformities. It was assumed that the nonlinear correction to the refractive index develops instantaneously. The fluctuations of the initial wave front subject to focusing were prescribed by the method of spatial randomization of the positions of the reference nodes in the aperture plane of the wave front. The number of nodes where the wave front was prescribed was equal to 512×512 points. These points formed a quasiregular grid of nodes. The position of an arbitrary node was prescribed randomly within the region of discretization.

The main idea employed, making it possible to model numerically the self-diffraction of light by self-induced index nonuniformities of the medium in the focusing region, was that on a small spatial section of thickness Δz the induction of index nonuniformities in the transverse plane (x,y) and the diffraction propagation of a wave on this section can be separated and they can be calculated separately in succession. The accuracy of the method increases as the step size Δz decreases.

ANALYSIS OF THE RESULTS

Two realizations of the wave field in the nonlinear medium were calculated. They correspond to two random realizations of the wave front in front of the entrance into the nonlinear medium.

The realizations of the three-dimensional near-focus fields, obtained by sectioning the latter by the longitudinal plane yOz, are shown in Figs. 1a and 1b. Only the intensity distribution of the wave field was recorded in the figure. It is clearly seen that the fine details of the interior structure of the two realizations of the field are different. The realizations of the field have features in common which are absent for a diffraction catastrophe in a linear medium (Fig. 1c).

Figure 2 shows for the case of a nonlinear medium the z dependence of the energy flux $\approx\int\int I(x,y,z)dxdy$ through a transverse area S_A of size 547×547 μm (curve *1*). Here $I(x,y,z)$ is the three-dimensional distribution of the field intensity. The corresponding z dependences of $\int\int I(x,y,z)dxdy$ are virtually identical for both realizations of the field in the nonlinear medium. The decrease in the energy flux with increasing z is due to the fact that some radiation escapes from the fixed transverse area S_A, i.e., it is due to defocusing of the light beam. Figure 2 also shows the analogous dependence for the field in a linear medium (curve *2*). Comparing the curves *1* and *2* in Fig. 2 shows that beam defocusing in the nonlinear medium for $z>137.5$ mm occurs more rapidly than in the case of a linear medium. This is due to scattering of radiation by self-induced refractive-index nonuniformities. The same figure shows for a nonlinear medium the z dependence of the parameter

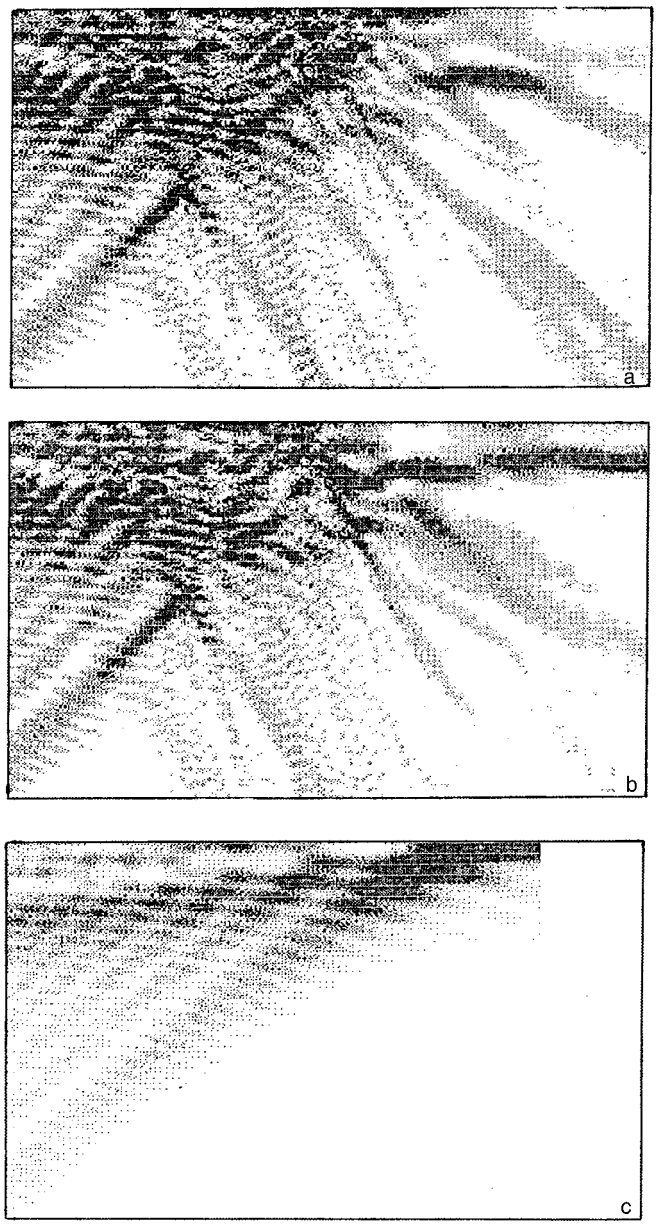

FIG. 1. Distribution of the intensity of the wave field near the focus in nonlinear and linear media: a — nonlinear medium, realization 1; b — nonlinear medium, realization 2; c — linear medium. The extent in the horizontal direction is 7 mm and the extent in the vertical direction is 153 μm.

$$\delta\Phi=\left\{\int\int_{S_A}(I_1(x,y,z)-I_2(x,y,z))^2dxdy\right\}^{1/2},$$

characterizing the integral rms deviation of two realizations of the field from one another in an arbitrary section (x,y) with $z=$ const (curve *3*). One can see that in the interval $z=135.5$–137.0 mm $\delta\Phi$ increases very little with increasing z, but for $z>137.0$ mm a sharp increase of $\delta\Phi$ is observed. The parameter $\delta\Phi$ reaches its maximum value at $z=138.6$ mm, where it is approximately 20 times larger than its initial value, occurring at the entrance into the nonlinear medium. The maximum value of the parameter $\delta\Phi$ occurs in the region of greatest bunching of the wave field, and then for $z=138.6\ldots142.5$ mm, as the beam defocuses, the parameter

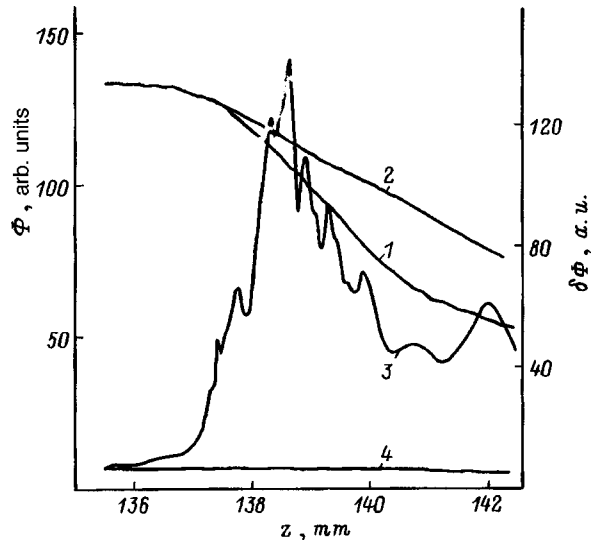

FIG. 2. Energy flux Φ through a transverse area and the parameter $\delta\Phi$.

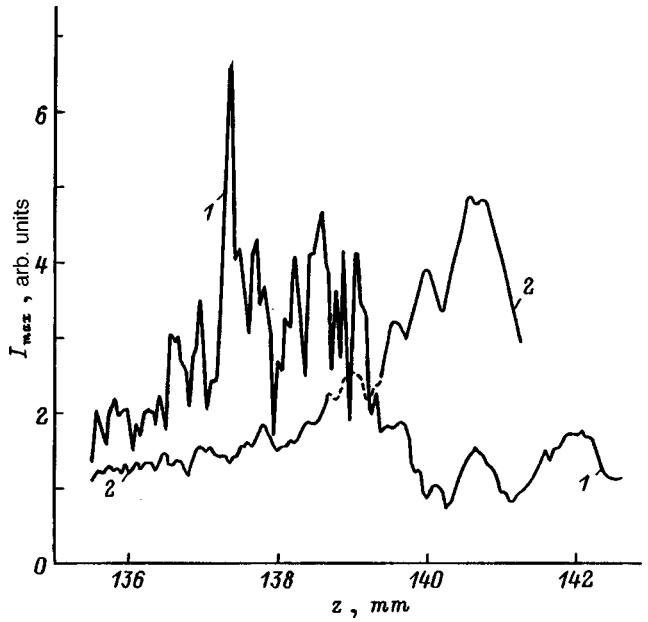

FIG. 3. Maximum intensity in the (x,y) section: *1* — nonlinear medium, realization 1; *2* — linear medium.

$\delta\Phi$ decreases, but remains, once again, greater than its initial value at the entrance of the radiation into the nonlinear medium.

The z dependence of the parameter $\delta\Phi$ constructed for two realizations of a wave field in a linear medium is displayed for comparison in Fig. 2 (curve *4*). The constancy of the curve *4* and its low level signify that in the latter case we are dealing with two realizations of structurally stable diffraction catastrophes. Therefore it is obvious that the increase in the parameter $\delta\Phi$ in the medium with a nonlinearity is due to the fact that the wave field in such a medium becomes structurally unstable as it bunches up, and a spatial chaotization of the optical field develops in the system as z increases. The maximum chaotization develops after the region where the concentration of the field is greatest.

This is seen from Fig. 3, where the z dependence of the maximum intensity of the field in the section (x,y) is shown for the case of focusing of a field in a nonlinear medium. The maximum field intensity occurs in the section $z=137.35$ mm. In the case of focusing of radiation in a linear medium the maximum concentration of the field occurs in the section $z=140.55$ mm; in this case, the intensity of the field reaches a value 1.36 times lower than in the case of focusing in a nonlinear medium.

As was noted in Ref. 8, the diffraction catastrophe formed in the course of the evolution of a wave front with spherical aberration and astigmatism has a structure which in the presence of nonlinearity in the medium and with increasing laser power forms a tapered waveguide. Part of the focused radiation will be trapped in such a self-induced waveguide and channeled in it. This is why higher values of the field intensity will be achieved in the focusing region in a medium with nonlinearity during evolution of a wave front of a special form, as noted above, than in the linear medium, and this will happen at smaller values of z.

The curves of the maximum values of the intensity in one of the 45° sectors of the section (x,y) as a function of the parameter z for two realizations of the wave field in a nonlinear medium are shown in Fig. 4. One can see from Fig. 4 that in the interval 135.5–137.35 mm the z dependences of $I_{\max}$ are identical for the two realizations of the field to a high degree of accuracy. However, after the maximum intensity is reached in the section $z=137.35$ mm the plots of the functions $I^1_{\max}(z)$ and $I^2_{\max}(z)$ differ very strongly and behave differently. For $z<137.35$ mm the coordinates $(x^i,\ y^i)$ of the maxima in the transverse section with $z=\text{const}$ are identical for two realizations of the field, while for $z>137.35$ mm the coordinates of these maxima are no longer the same. This confirms the fact that after the wave passes the section where the intensity of the field reaches its maximum value, as the wave continues to advance the struc-

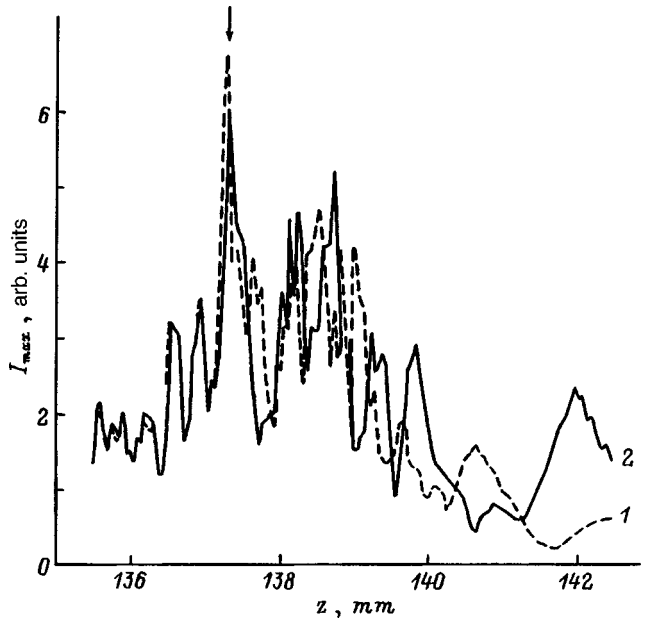

FIG. 4. Maximum intensity in one of the 45° sectors of the section (x,y); *1* — $I^1_{\max}(z)$ for field realization 1, *2* — $I^2_{\max}(z)$ for field realization 2.

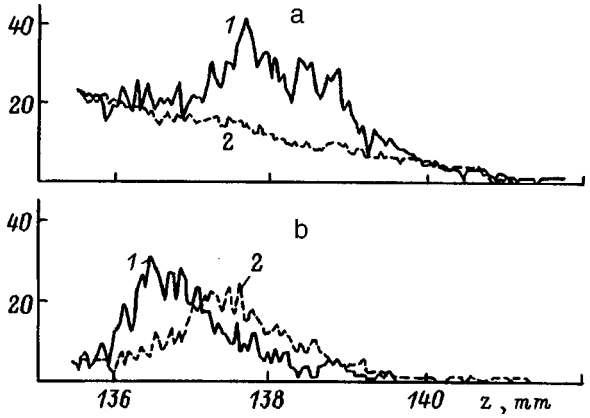

FIG. 5. Number of local field maxima in a quadrant of the transverse section (x,y): a — for local maxima of the first type, b — for local maxima of the second type; *1* — nonlinear medium, realization 1; *2* — linear medium. Quadrant size 153×153 μm.

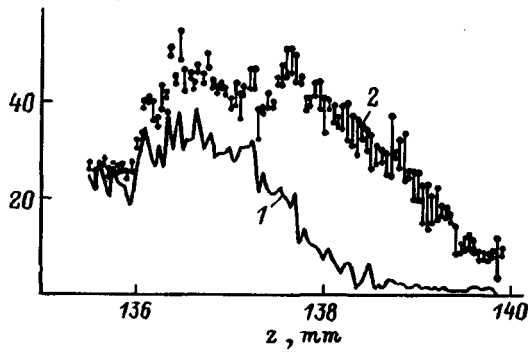

FIG. 6. Number of coinciding speckle elements and the total number of speckle elements in a quadrant of the transverse section for two realizations of the field in a nonlinear medium: *1* — number of coinciding speckle elements, *2* — total number of speckle elements. The quadrant size is the same as in Fig. 5.

tural instability increases and chaotization of the wave field develops. Indeed, by observing the position of a cardinal point of the wave field such as the point of the maximum intensity of the field in one of the 45° sectors of the section (x,y), it can be concluded that structural instability of the field occurs for $z>137.35$ mm.

As the wave advances in the nonlinear medium the number of local maxima of the field evolves according to a different law than for a structurally stable field in a linear medium. Figure 5 shows the dependence of the number of local maxima in the transverse section (x,y) (number of speckle elements) as a function of the coordinate z for fields in nonlinear and linear media for two types of maxima: maxima where the curvature of the intensity distribution in mutually orthogonal directions differs by not more than a factor of 4 (Fig. 5a) and maxima where the difference is greater than a factor of 4 (Fig. 5b). For maxima of the first type, which correspond to compactly localized speckle elements, their total number decreases from 21 to 1 as z increases from 135.5 to 142 mm in the case of a linear medium. For a nonlinear medium, in the interval from 136 to 139.5 mm the total number of compactly localized maxima is greater than the corresponding number of maxima of the field for a linear medium. The largest total number of maxima of the first type equals 40 for $z=137.95$ mm for one realization of the field and 41 for $z=137.65$ mm for the other realization of the field. The excess, as compared with the case of a linear medium, number of maxima of the field reflects the development of spatial disorder in the transverse structure of the beam and strong mixing of excess speckle elements.[6] Speckle elements of the first type, randomly distributed in the transverse plane, trace out along the z axis curvilinear tubes which interweave with one another in a complicated manner. It is obvious that such tubes are narrow microwaveguide channels with high light intensity. Since the medium is nonlinear, a field configuration of the specklon type,[6,13] where the nonuniformities of the field intensity coincide with the index nonuniformities of the medium, is realized automatically. The limited extent of such tubes along z determines the length of the speckle field elements of the first type.

For field maxima of the second type, which correspond to speckle elements with a pronounced sickle shape in the transverse plane, the analogous dependences for the cases of linear and nonlinear media are shown in Fig. 5b.

As z increases, for $z>135.5$ mm, the specific number of speckle elements in the transverse plane, the coordinates of the elements being the same for the two realizations of the field in the nonlinear medium (curve *1* in Fig. 6), gradually decreases. Thus, for $z=135.5$ mm for both field realizations the coordinates (x^i,y^i) of virtually all speckle elements are identical. In turn, for $z=139$ mm the coordinates (x^i,y^i) of only 6% of the total number of speckle elements in the transverse plane are the same. Curve *2* in Fig. 6 shows for two realizations of the nonlinear field the z dependence of the total number of speckle elements in the transverse plane.

The typical pattern of the field in a nonlinear medium is shown in Fig. 7 for a different set of transverse sections (x,y).

The following results also attest to the structural instability of near-focus formations in a nonlinear medium provided that the prototypes of these formations in a linear medium were structurally stable. For each realization of the field the entropy of the field intensity distribution $I(x,y)$ in a transverse section of the focusing beam at $z=$ const was analyzed. Following Ref. 14, the entropy of the intensity distribution $I(x,y)$ on an aperture of area S_A was determined as $S(z)=-\Sigma_{k,l}P_{kl}(z)\ln P_{kl}(z)$, where $P_{kl}(z)=\Delta x\cdot\Delta y\cdot\mathfrak{B}_{kl}(z)$, with

$$\mathfrak{B}(x,y,z)=I(x,y,z)/\int\int_{S_A}I(x,y,z)dxdy.$$

Here part of the formulas are written in a discrete representation for a regular two-dimensional grid of nodes $k,\overline{l}$ on an area S_A of size 547×547 μm. $\mathfrak{B}_{kl}(z)$ are the discrete readings of the probability density $\mathfrak{B}(x,y,z)$ at the nodes k,l; $\Delta x\cdot\Delta y$ is the size of a unit cell in the grid of nodes. The quantity $\Delta x\cdot\Delta y\cdot\mathfrak{B}_{kl}(z)$ is physically meaningful only for low light intensity levels corresponding to detection of indi-

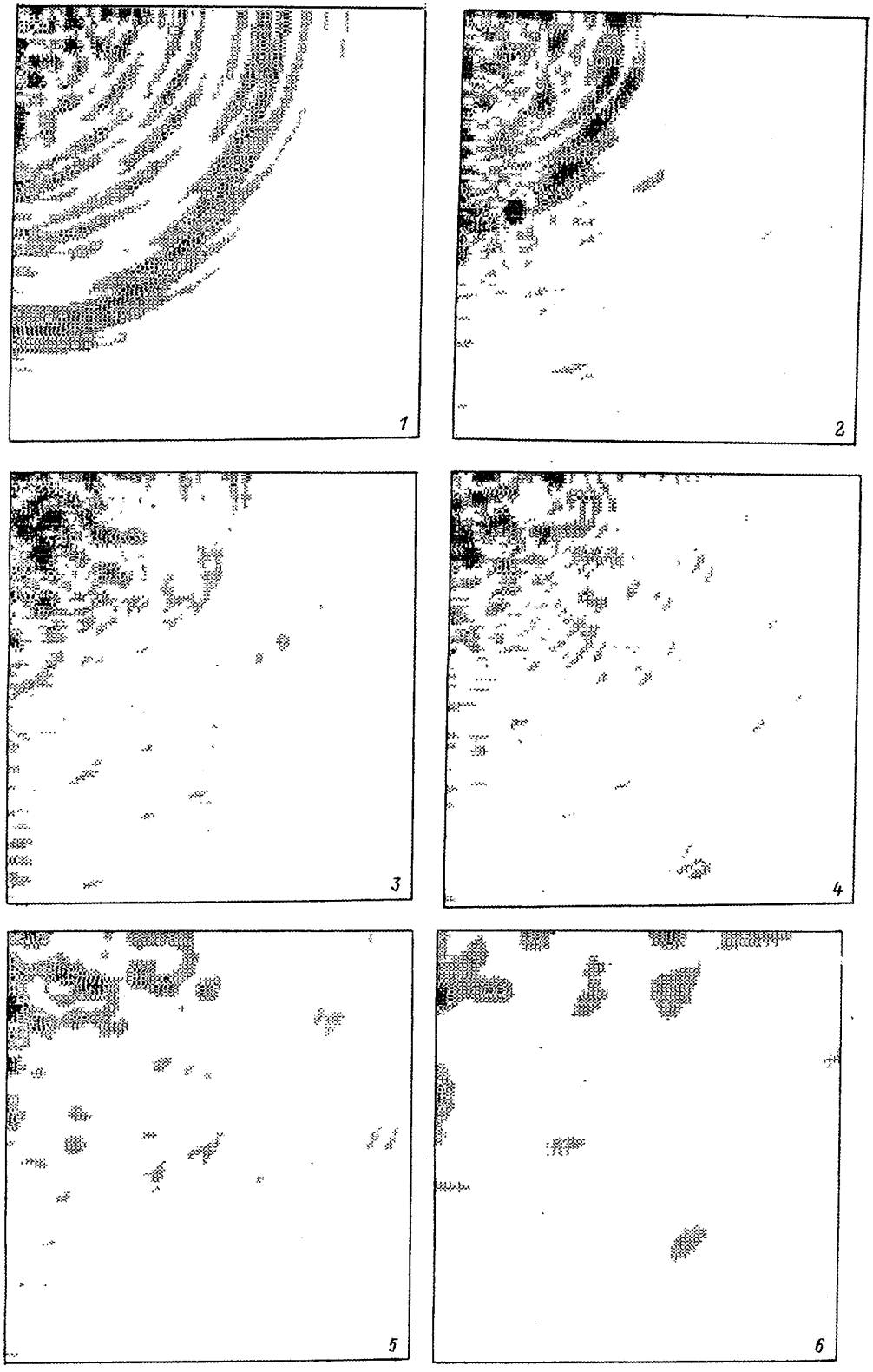

FIG. 7. Intensity distribution of the wave field near the focus in a nonlinear medium. Coordinate z, mm: *1* — 136.5, *2* — 137.5, *3* — 138.5, *4* — 139, *5* — 139.5, *6* — 140.5. The quadrant size is the same as in Fig. 5.

vidual photons. Thus, for two realizations of the wave field in a nonlinear medium the z dependence of the modulus $|S_2-S_1|$ of the entropy difference was constructed (curve *1* in Fig. 8). The initial randomly perturbed wave fronts in the case of a linear medium give two other realizations of the wave field, for which an analogous z dependence of $|S_2-S_1|$ was constructed (curve *2* in Fig. 8). Comparing curves *1* and *2* in Fig. 8 shows that in the case of a linear medium the structurally stable focal formations give small values of $|S_2-S_1|$ with weak random perturbation of the wave front,

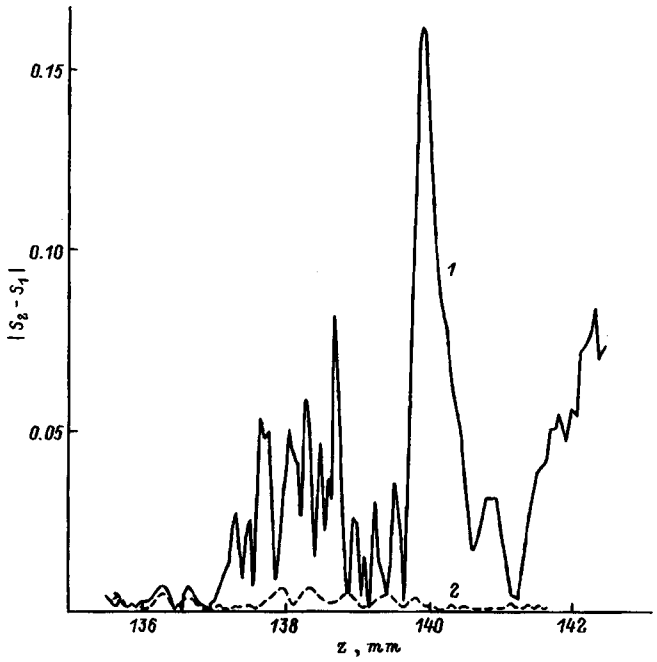

FIG. 8. Difference of the entropies which correspond to two realizations of the field distribution in the transverse section (x,y).

deformed by spherical aberration and astigmatism. These small quantities occur for all z in the interval from 135.5 to 142 mm. In a nonlinear medium, in turn, weak random perturbations of the initial wave front lead to a rapid growth of $|S_2-S_1|$ for $z>137$ mm.

In principle, it can be asserted that the structural instability starts to develop in a nonlinear medium at $z>137$ mm, i.e., well before the plane with the highest field intensity is reached, when the main cardinal points of the wave realizations are still the same. Curve *3* in Fig. 2 also attests to such an onset of spatial turbulence in a nonlinear medium.[1)] One can see from the this curve that the dependence $\delta\Phi(z)$ first changes character at $z=137$ mm: The plateau for $z<137$ mm is replaced by a sharp rise at $z>137$ mm.

If the shape of the wave front at the entrance into the system fluctuates very little in time, being subject to random processes, then temporal turbulence will also be present in the focusing region in the nonlinear medium, i.e., in definite time intervals a three-dimensional formation near the focus will have a structure that is different from the structure existing at a preceding moment in time, and the turbulences will not transform into one another by means of a diffeomorphism transformation. The appearance of strong chaotic pulsations of the amplitude of the wave field that accompany temporal turbulence is also obvious considering the finite polarizability time of a nonlinear medium.

Comparing the images of the wave formations presented in Fig. 1 for the cases of nonlinear and linear media in a longitudinal plane yOz, one can see that the self-diffraction in the nonlinear medium is equivalent to diffraction of the ''outgoing'' radiation at the edge of a tapered waveguide. The ''splashes'' and ''filamentary ejecta'' observed after the region of greatest squeezing of the beam and dispersing in the forward direction in a wide interval of angles comprise the diffraction field of the edge of the self-induced tapered waveguide in a nonlinear medium.

A result of practical importance obtained in this investigation is that in a medium with refractive-index nonlinearity higher values of the local intensity than in the case of a linear medium can be obtained by using a wave front deformed by spherical aberration and astigmatism for focusing.

In summary, when a specially shaped wave front is focused in a uniform nonlinear medium, the nonlinear interactions of the partial waves lead to the appearance of complicated spots (speckle elements) arranged chaotically in the transverse plane. This is due to the appearance of chaos in nonlinear wave fields as the wave propagates in the z direction.[16,17] As z increases, for $z>137$ mm, the decay instability of wave formation, which is due to the chaotic behavior of the phases of the interacting partial waves, occurs. As a result, a transition to weak turbulence occurs.

INTERPRETATION OF THE APPEARANCE OF CHAOS

The wave beam formed during focusing can be conceptually divided into many (about 10^5) partial plane waves, emanating from regions uniformly distributed over the initial aperture of the wave front as $z=0$. Then appearance of spatial chaos can be easily understood by geometric-optics analysis of the nonlinear interaction of many partial waves in a medium with refractive-index nonlinearity.

It is well known that several partial waves can arrive at each point of the caustic zone arising during the evolution of a complicated wave front. In our case, at least five partial beams interfere at each point of the central part of the focusing region. In turn, at least three partial beams interfere at each point located in a narrow layer outside the central part of the focusing region.[8] Let us examine the first layer of thickness Δz in a nonlinear medium. The incident partial beams are scattered by weak refractive-index nonuniformities ($\Delta n\leqslant 0.01$) induced by the interference field of the same partial waves. To a first approximation this scattering can be treated as a perturbation acting only on the phase of each partial wave but not on its amplitude.[18] Each partial beam in such scattering undergoes a small lateral displacement. As a result, scattered partial beams arrive in the next layer of the medium and are once again scattered by the weak nonuniformity induced by the interference field of the preceding partial waves, and so on. In the presence of a nonlinear interaction with a large number of partial waves, the phase of each individual wave varies in an irregular manner as the wave propagates. Ultimately, the directions of the energy fluxes in an extended focal region have a complicated, irregular, entangled form. This is an illustration of the well-known thesis that a weak turbulence arises in a wave process in the presence of a large number of weakly interacting waves .[19–21] As a result, a complicated specklon structure with a characteristic scale in the transverse section of the order of one cell of the field pattern arises in the focusing region. Turbulence appears as a result of vanishingly small random disturbances, which are always present, of the wave front initially subjected to focusing. The external perturbations of the wave front produce the turbulence. They can be regarded as some

chaotic noise. In the presence of high light intensities in the focusing region the nonlinear medium acts as an amplifier of noise arriving from outside. On account of the enormous gain of such an ''amplifier,'' even a very small disturbance of the initial wave front radically changes the beam and wave pattern of the field being analyzed.

We note that in Ref. 22 it was proved that chaos appears when two waves interfere in a nonlinear medium. It was also indicated there that chaos can appear in experiments on light-induced self-diffraction.

The conclusion is that nonlinear effects destroy the structurally stable diffraction catastrophe in the focusing region and the formation arising near the focus in the new situation has a spatially and temporally turbulent distribution of the field amplitude. Spatial turbulence (in the present situation this is simply structural instability) follows directly from computer experiments. Temporal turbulence will occur in the case that the small fluctuations of the shape of the initial wave front are different at each moment in time or when the finite polarization time of the medium is taken into account.

Part of this work was performed as part of a Project of the Institute of Supercomputing and Databases of the Ministry of Science of the Russian Federation with the support of the Russian program ''Fullerenes and Atomic Clusters.''

[1)]The term ''optical turbulence'' for waves in nonlinear media, where stochastization and decay of wave structures occur, was used in, for example, Ref. 15. In Ref. 15, however, wave structures in a ring-shaped nonlinear resonator with two-dimensional feedback were studied. Instability in this case was due to large-scale transverse interactions in a coherent laser beam.

[1] J. N. Hannay, IEE Proc. **130**, 623 (1983).
[2] M. V. Berry and C. Upstill, in *Progress in Optics*, edited by E. Wolf (North-Holland, 1980), Vol. 18, pp. 257–346.
[3] V. V. Korobkin, L. Ya. Polonskiĭ, L. Ya. Pononin, and L. N. Pyatnitskiĭ, Kvantovaya Élektron. (Moscow) **13**, 265 (1986) [Sov. J. Quantum Electron. **16**, 178 (1986)].
[4] M. Yu. Marin, L. Ya. Polonskiĭ, and L. N. Pyatnitskiĭ, Pis'ma Zh. Tekh. Fiz. **12**, 146 (1986) [Sov. Tech. Phys. Lett. **12**, 62 (1986)].
[5] C. Wülker, W. Theobald, and D. Ouw, AIP Conf. Proc. **18**, 121 (1994).
[6] B. Ya. Zel'dovich, N. F. Pilipetskiĭ, and V. V. Shkunov, Usp. Fiz. Nauk **138**, 249 (1982) [Sov. Phys. Usp. **25**, 713 (1982)].
[7] V. M. Volynkin, O. D. Gavrilov, and A. A. Chertkov, Pis'ma Zh. Tekh. Fiz. **12**, 409 (1986) [Sov. Tech. Phys. Lett. **12**, 167 (1986)].
[8] V. Yu. Osipov, Avtometriya, No. 5, 48 (1996).
[9] V. N. Lugovoĭ and A. M. Prokhorov, Usp. Fiz. Nauk **111**, 203 (1973) [Sov. Phys. Usp. **16**, 658 (1974)].
[10] N. I. Koroteev and I. L. Shumaĭ, *The Physics of High-Power Laser Radiation* [in Russian], Nauka, Moscow (1991), 312 pp.
[11] R. Collier, C. Burckhardt, and L. Lin, *Optical Holography* [Academic Press, New York, 1971; Mir, Moscow, 1973].
[12] B. R. Frieden (ed.), *The Computer in Optical Research: Methods and Applications* [Springer-Verlag, New York, 1980; Mir, Moscow, 1983, 488 pp.].
[13] B. Ya. Zel'dovich, V. V. Shkunov, and T. V. Yakovleva, Usp. Fiz. Nauk **149**, 511 (1986) [Sov. Phys. Usp. **29**, 678 (1986)].
[14] L. Carretero, A. Fimia, and A. Belendez, Opt. Lett. **19**, 1355 (1994).
[15] S. A. Akhmanov, M. A. Vorontsov, and V. Yu. Ivanov, JETP Lett. **47**, 707 (1988).
[16] V. V. Zosimov and L. M. Lyamshev, Usp. Fiz. Nauk **165**, 361 (1995).
[17] S. A. Akhmanov, Usp. Fiz. Nauk **149**, 361 (1986) [Sov. Phys. Usp. **29**, 589 (1986)].
[18] Yu. A. Kravtsov and Yu. I. Orlov, *Geometric Optics of Inhomogeneous Media* [in Russian], Nauka, Moscow (1980), 304 pp.
[19] B. B. Kadomtsev and V. I. Karpman, Usp. Fiz. Nauk **103**, 193 (1971) [Sov. Phys. Usp. **14**, 40 (1971)].
[20] S. N. Gurbatov, A. I. Saichev, and I. G. Yakushkin, Usp. Fiz. Nauk **141**, 221 (1983) [Sov. Phys. Usp. **26**, 857 (1983)].
[21] O. V. Rudenko, Usp. Fiz. Nauk **165**, 1011 (1995).
[22] V. G. Gorshkov, Yu. K. Danileĭko, T. P. Lebedeva, and D. A. Nesterov, JETP Lett. **45**, 243 (1987).

Translated by M. E. Alferieff

On the operating conditions of the electrical blowing module for a periodic-pulse laser based on fluorine atoms and molecules

A. K. Shuaibov

Uzhgorod State University, 294000 Uzhgorod, Ukraine
(Submitted May 29, 1997)
Zh. Tekh. Fiz. **68**, 84–87 (September 1998)

The results of an investigation of the ignition conditions and characteristics of a multiple-electrode corona discharge, intended to be used in the module which performs electrical blowing of the working media of high pressure lasers operating on fluorine atoms and molecules, in a tip–grid system are reported. The electrical and optical characteristics of corona discharges of positive and negative polarity, which were distributed along the length of a transverse discharge of lasers operating on the transitions $F(3s-3p)$ and $F_2(D'-A')$, were studied. The characteristics of corona discharges were studied in a mixture He/F_2 at atmospheric pressures. © *1998 American Institute of Physics.* [S1063-7842(98)01609-2]

INTRODUCTION

Atmospheric-pressure working mixtures He/F_2 are used quite effectively in periodic-pulse lasers emitting in the red region of the spectrum ($\lambda = 620-780$ nm) on $F(3s-3p)$.[1,2] In the vacuum ultraviolet (VUV) region this medium is the working medium for powerful lasers on $\lambda = 157$ nm $F_2(D'-A')$,[3,4] which are of great interest for applications in photochemistry and lithography. This laser has the shortest wavelength of all powerful high-pressure electric-discharge lasers ($E = 2.6$ J/liter, efficiency$=1.5\%$[4]) and it can operate in a periodic-pulse regime. When corrosive media, such as the mixture He/F_2, are used the standard mechanical systems for blowing gas mixtures through (compressors, diametric fans) have a limited service life, they are characterized by high energy consumption, and they give rise to additional contamination of the working medium of the periodic-pulse laser. High purity of the working mixture is especially important for VUV lasers operating on fluorine molecules. In this case, for pulse repetition frequencies $\leqslant 100$ Hz, electrical blowing can be used. It is based on the ''electric wind'' that arises in the external region of a corona discharge (CD).[5] Investigations of the characteristics of such CDs for the working media of N_2 and CO lasers[6] and the XeCl* laser[7] showed that in a tip–grid electrode system (ES) a CD exists in the form of point-like generation zones (GZs) and a dark exterior region. The average current I of a noncontracted CD depends strongly on the pressure and composition of the gas mixtures. The electrical blowing rate $\nu \sim I^{1/2}$ (Ref. 8) is limited by the instability of the CD and can be increased by optimizing the pressure, the composition of the gas mixtures, and the powering regime of the CD. Such investigations have not been performed for CDs in mixtures of inert gases with fluorine molecules.

The present paper presents the characteristics of a blowing module for a miniature periodic-pulse laser based on fluorine atoms and molecules which operates on a He/F_2 mixture. The current-voltage characteristics (IVCs) and the frequency characteristics of positive and negative CDs were studied. The emission spectra of the generation zones of CDs in a He/F_2 mixture and the CD current dependences of the average intensities of the radiation in the $F(3s-3p)$ lines were investigated.

EXPERIMENTAL CONDITIONS AND SPATIAL CHARACTERISTICS OF CDS

The electrode system (ES) of the CD consisted of a single row of tips and a nickel grid. The radius of curvature of a tip was equal to 0.5 mm, while the radius of the grid wires was equal to 0.15 mm. The interelectrode distance was equal to 2 cm, and the total length of the ES was equal to 11 cm. A positive or negative voltage was applied to the tips through a limiting resistance $R = 1-3$ MΩ. The other experimental conditions and the system for recording the characteristics of CDs were similar to those described in Refs. 6 and 7.

The corona discharge in a high-pressure He/F_2 mixture consisted of a red diffusion plasma medium, formed near the tip points and a dark exterior region of the CD. In contrast to a negative CD in mixtures of inert gases with HCl molecules, in the case of a CD in the mixtures He/F_2 and He/(Ar, Kr, Xe)/F_2 the GZ is continuous and its form is reminiscent of a pulsed transverse discharge. The transverse size of the GZ of a negative CD reached 0.5–1.0 cm with a length of 11 cm. The transverse dimensions of the GZ increased with voltage on the tips right up to the appearance of a streamer near one of them. The continuous character of the GZ of a CD in a He/F_2 mixture creates the prerequisites for obtaining a more uniform transverse flow of the gaseous medium than in CDs in He/Xe(Kr)/HCl mixtures. In a positive CD in a He/F_2 mixture the transverse dimensions of the GZ are two to three times smaller than for a negative CD.

The main distinction of a plasma in He/F_2 and He/(Ar, Kr, Xe)/HCl mixtures is that the rate constant for dissociative attachment of electrons to F_2 ($\nu = 0$) molecules is approximately two orders of magnitude higher than for attachment to HCl($\nu = 0$) molecules.[9,10] For this reason, at high

He/F_2 mixture pressure a large portion of the electrons is converted within the short time interval (1 ns) into negative fluorine ions.[11–13] The F^- reservoir produced is expelled by the electric field of the negatively charged tips in a direction toward the grid. In the process of diffusion of the F^- ions, electrons are detached and the detached electrons preionize the volume occupied in the next GZ. According to the data of Refs. 14 and 15, the main mechanism of ignition of a negative CD is UV preionization, and in inert gases the main source of UV preionization is diffusion of resonance radiation R. The most efficient process of electron detachment from F^- ions is photodetachment under the action of photons with $\lambda \leqslant 360$ nm.[12,13] It has been suggested that this effect be used in the emitters of periodic-pulse RF(B–X) lasers. It is called the NIAP (negative ion assisted preionization) preionization technology.[13] The sources of the radiation that destroys F^- in CDs in He/F_2 mixtures could be $\lambda = 157$ nm $F_2(D'-A')$ radiation, and in the case of $He/R/F_2$ mixtures the source could be intense spontaneous emission from the molecules RF B–X ($\lambda = 193$, 249, and 351 nm).

In a positive CD the F^- ions are neutralized by the positively charged tips, which results in the formation of a GZ which is narrower in the transverse direction. In this case the conditions for realization of the NIAP preionization of the discharge region of the GZ are suppressed. Therefore, in a CD in a He/F_2 mixture, the NIAP scheme of UV preionization is realized automatically and leads to the formation of a spatially uniform, extended GZ with transverse size $\leqslant 1$ cm.

In a CD in a He/F_2 mixture the GZ, located under the grid cathode of a laser pumped by a transverse discharge on $\lambda = 157$ nm $F_2(D'-A')$, can function simultaneously as a UV preionizer and an electrical blowing system. To optimize the blowing loop it is best to use a grid or perforated anode of a transverse discharge. In this case, the optimal geometric conditions are realized for both placement of the UV preionization and for the electrical blowing system of the laser.

ELECTRICAL CHARACTERISTICS OF CDS

The oscillographic investigations showed that the current of a positive and negative CD is pulsed and does not have a constant component. The typical shape of the CD current pulses is presented in Fig. 1. The current pulse of a negative CD had an amplitude of 2 mA (with $U = 10.4$ kV). The leading edge of the current pulses was short, and the trailing edge was extended up to 1 μs. In a positive CD the current pulse consisted of two maxima and was more prolonged. Since in a CD of definite polarity the main current carrier are ions of the same polarity, which diffuse away from the GZ toward the opposite electrode,[8,14,15] the main current carriers in a negative CD are F^- ions. The time dependence of the current of a negative CD is actually the time dependence of the density of negative ions F^-. The initial section of the current oscillogram in Fig. 1 corresponds to an increase of the F^- ion density in the region of a strong electric field (within the GZ of the CD), while the trailing edge corresponds to decrease in the number of negative ions diffusing through the exterior region of the CD. It follows from the duration of the trailing edge of the current pulse of a negative CD (0.9 μs)

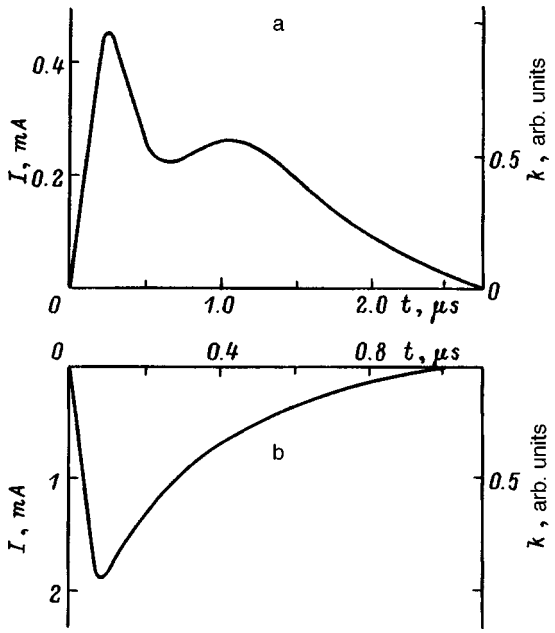

FIG. 1. Oscillograms of the current of a positive (a) and negative (b) corona discharge in the mixture $He/F_2 = 200/0.8$ kPa.

and the size of the exterior region of the CD (1.5 cm) that the average diffusion velocity of negative ions with a helium pressure of 2 atm is 1.7×10^6 cm/s. To provide such a drift velocity of F^- ions, the intensity of the electric field in the GZ must equal 20 kV/cm, which follows from data on the mobility of F^- ions in helium.[11,12] In a positive CD the main current carriers are probably positive ions F^+ and F_2^+. This is the reason for the double-hump shape of the oscillogram of the discharge current in a He/F_2 mixture.

The IVCs of CDs and the dependence of the repetition frequency of the current pulses of a negative CD on the tip voltage are presented in Fig. 2. The IVC of a CD consisted of a close to linear initial section and a sharply rising part due to streamer breakdown. For He/F_2 mixtures of the same composition and pressure the rate of current growth with

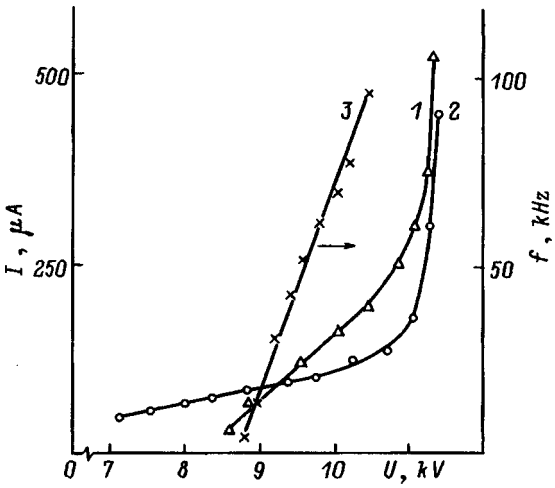

FIG. 2. Average current (*1*,*2*) and repetition frequency of the current pulses of a CD (*3*) versus the tip voltage for negative and positive CDs in a He/F_2 mixture.

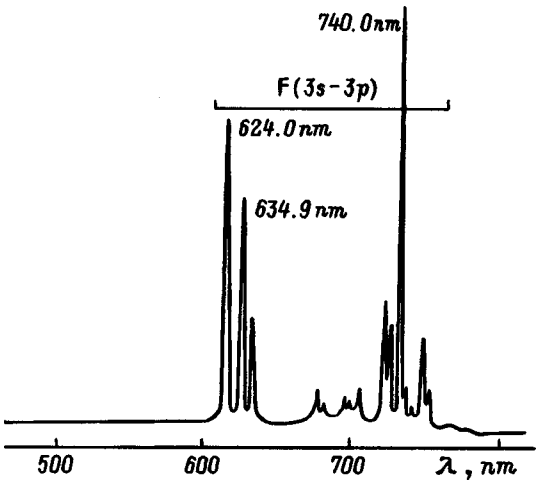

FIG. 3. Emission spectrum of the generation zone of a negative CD.

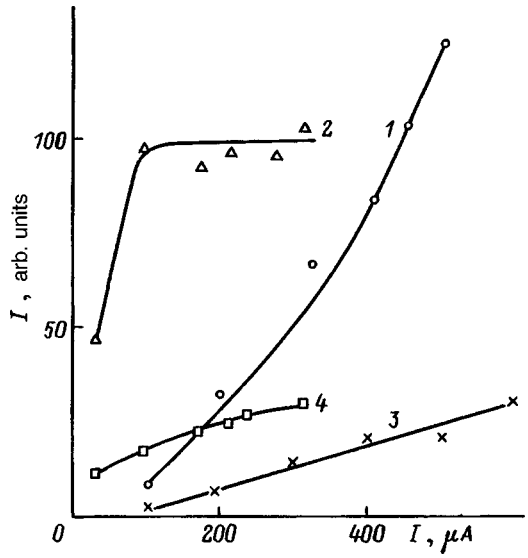

FIG. 4. Radiation intensity of the 740.0 nm F* (*1,2*) and 624.0 nm F* (*3,4*) lines versus the current of a positive and negative corona discharge.

increasing tip voltage is 1.5–2 times higher for a negative CD, but the ignition potential of a positive CD is 2–3 kV lower than of a negative CD. To obtain the maximum blowing rate of the He/F_2 mixture, a negative CD with $U=9-11$ kV is optimal. The dependences of the repetition frequencies of the current pulses on the tip voltage were linear. The highest current pulse repetition frequency was observed in a negative CD. In a positive CD with the same powering voltages, it decreased by approximately a factor of 2. When Ar, Kr, and Xe atoms were added to the He/F_2 mixture, the maximum repetition frequency of the current pulses decreased as the atomic weight of the heavy inert gas increased and was equal to 12–14 kHz in a $He/Xe/F_2$ mixture. This is due to the differences in the drift velocities of the positive R^+ and R_2^+ ions (screening the negatively charged tip) and negative F^- ions (which regulate the subsidence time of the negative charge), which determined the maximum repetition frequency of the current pulses of a negative CD.[14,15] The linearity of the IVCs is atypical for CDs and is due to the nonlinearities of CDs in inert gases. In this case, a CD acquires some of the properties of a glow discharge.[16]

The generation zone of a negative CD in a He/F_2 mixture is an extended source of not only red radiation but apparently also VUV radiation on $\lambda=157$ nm $F_2(D'-A')$ and can be used as a simple selective VUV lamp.

OPTICAL CHARACTERISTICS OF THE RADIATION IN THE GENERATION ZONE OF A CD

The spectrum of the radiation in the GZ of a CD and the dependences of the $F(3s-3p)$ lines on the current in a CD in a He/F_2 mixture are displayed in Figs. 3 and 4. The emission spectra of positive and negative CDs were the same and differed only by the intensity of the lines of the fluorine atom. The main lines in the emission spectrum of the GZ belong to the transitions $F(3s-3p)$ and were the lasing lines when the He/F_2 was mixture pumped by a high-pressure transverse discharge.[1] The highest intensity of radiation on the transitions of the fluorine atom were obtained in a negative CD, while most dependences showed an increasing character with increasing CD current (with the exception of curve *2* in Fig. 4).

The $F(3p)$ atoms in a dense electric-discharge plasma are formed efficiently in energy transfer reactions[4]

$$He^* + F_2 + (He) \rightarrow F(3p) + F + (He),$$

$$k = 8.2(-30)\ \text{cm}^6/\text{s}. \qquad (1)$$

In a negative CD the density of F^- ions, the volume of the GZ, and the intensity of the radiation on the transitions $F(3s-3p)$ are all higher than in a positive CD. In this case, together with the reaction (1), the $F(3p)$ atoms can be obtained efficiently by recombination of He^+ and F^- ions via the formation of an excimer molecule HeF*, for which a very short lifetime and rapid predissociation are characteristic.[17] The contribution of the population of $F(3p)$ by recombination, as follows from Fig. 4 and the IVC of the CD, can predominate at low tip voltages and, correspondingly, for lower effective values of the parameter E/N in the GZ of the CD.

According to numerical simulation of the kinetics of a transverse discharge in a He/F_2 mixture,[4] excited fluorine atoms with upper level energy in the range 14–15 eV make the main contribution to the population of the $F_2(D')$ state, which decays with emission of the $\lambda=157$ nm band. For this reason, the plateau in the dependence of the intensity of the $\lambda=740.0$ nm $F(3s-3p)$ line on the current in a negative CD is probably due to the loss of excited fluorine atoms in the conversion reaction

$$F(3p) + F_2 \rightarrow F_2(D') + F. \qquad (2)$$

On this basis, in the VUV region excited fluorine molecules can be observed in a negative CD with average discharge currents of 100–300 μA, but this requires a special experiment using a VUV monochromator with a corresponding system for detecting the radiation.

As one can see from the emission spectrum (Fig. 3), selective population of individual sublevels of the $3p$ states of the fluorine ion occurs in the GZ of a CD. The pulse power introduced into the GZ of a negative CD reaches 2–5 MW in a plasma volume of 5–10 cm^3. This gave a specific energy input at a level of 100 kW/cm^3. A selective source of radiation operating on $3s-3p$ transitions of the fluorine ion can be produced on the basis of the GZ of a negative CD by technical optimization of the design of the electrode system, the composition and pressure of the gas mixtures, and the power supply.

CONCLUSIONS

In summary, the investigation of the working conditions of the electric blowing module of a periodic-pulse high-pressure laser operating on $F(3s-3p)$ atoms and $F_2(D'-A')$ molecules has shown that in a corona discharge in the mixture He/F_2 a generation zone is formed in the form of a continuous plasma filament, encompassing all tips. The optimal arrangement is to use a negative corona discharge in the blowing module. The generation zone of a negative CD can be used as a simple selective emitter in the red region of the spectrum and probably on $\lambda = 157$ nm F_2^*, which can be used as a UV preionization source for a $F_2(D'-A')$ laser or as a corresponding VUV lamp. Compared with the operating conditions of the blowing module for RCl* lasers, for a CD in a He/F_2 mixture it was observed that the ignition potentials are higher and the working voltages are higher by approximately a factor of 1.5–2. The continuous character of the generation zone creates the prerequisites for obtaining a more uniform transverse flow of the gas medium in F*, F_2^*, and RF* lasers as compared with the corresponding media of periodic-pulse RCl* lasers.

I thank A. I. Dashchenko and A. I. Minya for assistance in the experiment.

[1] V. N. Lisitsyn and A. M. Razhev, Pis'ma Zh. Tekh. Fiz. **3**, 862 (1977).
[2] A. A. Serafetinides and K. R. Rickwood, Appl. Phys. B: Photophys. Laser Chem. **44**, 119 (1987).
[3] J. K. Rice, A. K. Hays, and J. R. Woodwort, Appl. Phys. Lett. **31**, 31 (1977).
[4] K. Yamada, K. Miyazaki, T. Hasama, and T. Sato, Appl. Phys. Lett. **54**, 597 (1989).
[5] A. I. Baranov, K. V. Gurkov, M. I. Lomaev *et al.*, Prib. Tekh. Éksp., No. 4, 108 (1994).
[6] A. K. Shuaibov, A. I. Minya, V. V. Zvenigorodskiĭ, and V. S. Shevera, Pis'ma Zh. Tekh. Fiz. **22**(3), 73 (1996) [Tech. Phys. Lett. **22**, 551 (1996)].
[7] A. K. Shuaibov, L. L. Shimon, and I. V. Shevera, Kvant. Elektron. (Moscow) **24**, 20 (1997).
[8] I. P. Vereshchagin, *Corona Discharges in Electronics Apparatus* [in Russian], Énergoatomizdat, Moscow (1985), 160 pp.
[9] L. G. Christophorov, Contrib. Plasma Phys. **27**, 237 (1987).
[10] D. Kigler, Z. Rozenberg, and M. Rokni, Appl. Phys. Lett. **39**, 319 (1981).
[11] J. Hsia, Appl. Phys. Lett. **30**, 101 (1977).
[12] M. R. Osborne, R. J. Winfield, and J. M. Green, J. Appl. Phys. **65**, 5242 (1989).
[13] M. R. Osborne and J. M. Green, J. Appl. Phys. **71**, 3127 (1992).
[14] É. D. Lozanskiĭ and O. B. Firsov, *Theory of Sparks* [in Russian], Atomizdat, Moscow (1975), 271 pp.
[15] Yu. P. Raĭzer, *The Physics of Gas Discharges* [in Russian], Nauka, Moscow (1987), 592.
[16] A. A. Belevtzev and L. M. Biberman, Beitr. Plasmaphys. **23**, 313 (1983).
[17] L. O. Hocker, J. Opt. Soc. Am. **68**, 262 (1978).

Translated by M. E. Alferieff

Problems of interpretation of holographic interferograms near shock wave fronts

S. V. Gribin and G. V. Ostrovskaya

A. F. Ioffe Physicotechnical Institute, Russian Academy of Sciences, 194021 St. Petersburg, Russia
(Submitted October 23, 1997)
Zh. Tekh. Fiz. **68**, 88–91 (September 1998)

A method of avoiding ambiguity in the interpretation of interferograms near a shock wave front is proposed. The method is based on combining the double-exposure schlieren method and holographic interferometry. Relations for calculating, on the basis of data obtained by analyzing double-exposure schlieren photographs, both the density at the shock wave front and the gradient of the density directly behind the front, which is necessary for calculating the shifts of the interference fringes near the shock wave front, are presented. © *1998 American Institute of Physics.* [S1063-7842(98)01709-7]

INTRODUCTION

As a rule, problems of interpretation of the interference pattern near shock wave fronts arise in interference and interference-holographic investigations of hydrodynamic processes. The sharp density jump at a wave front, together with the high velocity of the front, lead to smearing of the interference fringes and make it impossible to follow their course, which can result in an error in reading shifts by an integer number of fringes. Such ambiguity in measuring fringe shifts not only makes it impossible to calculate the density and pressure at shock front but it also results in a distortion of the density and pressure profiles behind the front.

In ordinary interferometry, the so-called ''white fringe'' method is ordinarily used to eliminate the ambiguity in the interpretation of fringes near sharp phase jumps.[1] This method requires careful tuning of the interferometer to the zeroth fringe and the use of a pulsed light source with a continuous emission spectrum. Interferometry in ''inclined beams,''[2] where the region of the phase jump is extended out on account of the deviation of the object beam from the normal to the wave front, can also be used to investigate planar shock waves.

An alternative method of solving the problem is to calculate the magnitude of the phase jump using information about the hydrodynamic parameters of the shock wave. Thus a method of calculating the jump of the interference fringes at the front of shock waves forming during flow around a body is described in Ref. 3. This method is suitable for shock fronts of arbitrary shape and permits using monochromatic laser radiation to record interferograms and holograms. A priori data on the velocity of the unperturbed gas flow were used to determine the density at the shock front.

In Ref. 4, a method based on a combination of holographic interferometry and the double-exposure schlieren method was used to eliminate the ambiguity of the interpretation of the course of interference fringes near shock fronts when determining the parameters of shock waves penetrating from air into water. In the present paper, this method is analyzed in greater detail and given a theoretical substantiation.

CALCULATION OF THE SHIFT OF INTERFERENCE FRINGES BEHIND A SHOCK FRONT

For simplicity, we confine our attention here to the case of axial symmetry. The relation between the shift $k(x)$ of the interference fringes and the radial density distribution $\rho(r)$ is given by the Abel integral equation

$$k(x)=\frac{2(n_0-1)}{\lambda}\int_x^R \frac{[\rho(r)/\rho_0-1]rdr}{\sqrt{r^2-x^2}}, \tag{1}$$

where x is the distance measured from the symmetry axis of the object, n_0 and ρ_0 are the initial refractive index and the initial density of the medium, λ is the wavelength of the probe radiation, and R is the radius of the shock front.

The density profile immediately behind the shock front can be approximated, to a first approximation, by the expression

$$\rho(r)=\rho(R)-\rho_r(R)(R-r), \tag{2}$$

where ρ_r is the derivative of the density with respect to r.

Substituting expression (2) into Eq. (1) and performing the integration, we obtain

$$k(\xi)=\frac{2(n_0-1)R}{\lambda}\left\{C(\xi)\left[\frac{\rho(R)}{\rho_0}-1\right]-D(\xi)\frac{\rho_r(R)R}{2\rho_0}\right\}, \tag{3}$$

where $\xi=x/R$, $C(\xi)=\sqrt{1-\xi^2}$,

$$D(\xi)=\sqrt{1-\xi^2}-\xi^2\ln\frac{1-\sqrt{1-\xi^2}}{\xi}.$$

Therefore, to calculate the shift of the fringes near a shock front it is necessary to know the density $\rho(R)$ and its derivative $\rho_r(R)$ at the front. The first quantity is related with the velocity N of the front by the well-known relation[5]

$$\frac{\rho(R)}{\rho_0}=\frac{(\gamma+1)N^2}{(\gamma-1)N^2+2a_0^2}. \tag{4}$$

In turn, the velocity of the front N can be measured by the double-exposure schlieren method[6] according to the distance traversed by the wave in the time between two expo-

sures. As will be shown below, $\rho_r(R)$ can also be calculated from hydrodynamic considerations using the schlieren data.

DERIVATION OF THE EQUATIONS FOR CALCULATING THE DERIVATIVE OF THE DENSITY OF A MEDIUM AT THE FRONT OF A CURVILINEAR SHOCK WAVE

The system of equations of three-dimensional gas dynamics near a shock front can be written in the form[7]

$$\rho_t+u\rho_r+\rho u_r+(A/A')u\rho=0, \quad u_t+uu_r+p_r/\rho=0,$$
$$p_t+up_r=a^2(\rho_t+u\rho_r), \tag{5}$$

where ρ is the density of the medium. p is the pressure, u is the velocity of particles in a direction normal to the shock front, $a^2=\gamma p/\rho$ is the local velocity of sound, $A(r)$ and $A'(r)$ are the cross-sectional area of the ray tube and its derivative with respect to the normal r, and $H=A'/2A$ is the average curvature of the shock front.

Quantities with subscripts are partial derivatives with respect to the time t and the coordinate r, measured in a direction normal to the front.

The system (5) is valid, specifically, for gas flows with planar, axial, and spherical symmetry near a shock front. Here H equals, respectively, 0, $1/2R$, and $1/R$, where R is the radius of curvature of the surface of the front.

The following conditions of dynamical compatibility hold at the shock front at $t=T_f(R)$:[4]

$$P(M)=\frac{P(R)}{p_0}=\frac{2\gamma M^2-\gamma+1}{\gamma+1},$$
$$D(M)=\frac{\rho(R)}{\rho_0}=\frac{(\gamma+1)M^2}{(\gamma-1)M^2+2},$$
$$V(M)=\frac{u(R)}{a_0}=\frac{2(M-1/M)}{(\gamma+1)}, \tag{6}$$

where $M=N/a_0$ is the Mach number, $N=1/(dT_f/dR)$ is the propagation velocity of the shock front, and p_0, ρ_0, and a_0 are parameters of the unperturbed atmosphere.

Thus at the shock front the unknown functions p, ρ, and u depend only on the parameter M — the Mach number of the shock front.

It is well known that the partial derivatives of any function $f(r,t)$ on a curve $t=t^*(r)$ are related by the relation

$$\frac{df}{dr}=f_r+f_t\frac{dt^*}{dr}, \tag{7}$$

where the derivative on the left-hand side is the total derivative of the function $f(r,t(r))$ with respect to the parameter r.

Applying this relation to the functions $p=p_0P(M)$, $\rho=\rho_0D(M)$, and $u=a_0V(M)$ at the shock front $t=T_f(R)$, equations relating these derivatives at the front can be obtained:

$$p_r+p_t\frac{1}{N}=p_0P_M\frac{dM}{dR},$$
$$\rho_r+\rho_t\frac{1}{N}=\rho_0D_M\frac{dM}{dR},$$

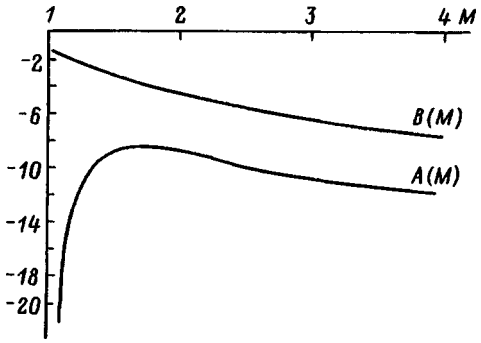

FIG. 1. The functions $A(M)$ and $B(M)$ used to calculate the density gradient ρ_r according to Eq. (9).

$$u_r+u_t\frac{1}{N}=a_0V_M\frac{dM}{dR}. \tag{8}$$

The system (8) together with Eq. (5) makes it possible to obtain analytic expressions for all partial derivatives of gasdynamic functions on a shock front, if the law of motion of the front $t=T_f(R)$ and its curvature H are known. For example, we obtain for the density gradient ρ_r

$$\frac{\rho_r}{\rho_0}=A(M)\frac{dM}{dR}+B(M)H, \tag{9}$$

where

$$A(M)=\frac{DMV_M}{(M-V)^2-P/D}+\frac{MP_M}{\gamma(M-V)[(M-V)^2-P/D]}+\frac{MD_M}{M-V},$$
$$B(M)=\frac{2DV(M-V)}{(M-V)^2-P/D}.$$

The subscript M denotes differentiation of the functions (6) so labeled with respect to the parameter M. PLots of the functions $A(M)$ and $B(M)$, necessary for calculating the derivative ρ_r, are presented in Fig. 1. The quantities dM/dR and H are taken from experiment.

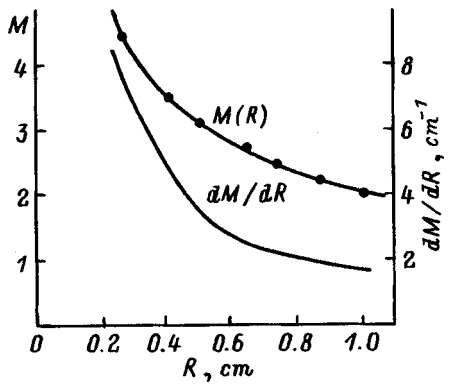

FIG. 2. Experimental dependences of the Mach number M and dM/dR on the radius R of the shock front.

TABLE I. Shock-front parameters found by the double-exposure schlieren method.

					ρ_r/ρ_0		K	
t, μs	M	dM/dR, cm^{-1}	H, cm^{-1}	ρ/ρ_0 Eq. (4)	Eq. (9)	Ref. 3	calculated from Eq. (3)	from interferogram
1.1	4.45	−8.0	2.42	4.80	76	78	1.7	1.6
2.1	3.50	−5.0	1.71	4.27	46	54	2.2	2.1
3.0	3.15	−3.5	1.41	4.00	30	42	2.6	2.5
4.7	2.75	−2.6	1.16	3.60	20	28	2.9	3.0
5.8	2.45	−2.3	1.05	3.27	17	22	2.8	3.0
7.8	2.20	−2.0	0.91	2.95	15	13	2.8	3.0
10.0	2.00	−1.5	0.79	2.67	10	8.4	2.9	2.8

ANALYSIS OF THE EXPERIMENTAL RESULTS

In Ref. 4 we obtained double-exposure schlieren photographs and holographic interferograms of a shock wave arising as a result of dielectric breakdown of air by pulsed CO_2 laser radiation. Analysis of the schlieren photographs corresponding to different times yielded the time dependence of the radius of the shock front and the propagation velocity of the shock wave. This makes it possible to construct the experimental dependence of the velocity of the front $M(R)$, presented in Fig. 2, on the radius. Figure 2 also shows the total derivative dM/dR, necessary in order to calculate the gradient ρ_r of the density and found by graphical differentiation of the function $M(R)$. The average curvature of the shock front was determined as

$$H=\frac{1}{2}\left(\frac{1}{R}+\frac{1}{R'}\right),$$

where R and R' are the principal radii of curvature of the front, which are measured directly from the schlieren photograph.

The measured values of M, dM/dR, and H for a series of times, as well as the values of the density and its gradient calculated using Eqs. (4) and (9), respectively, are presented in Table I. The table also presents the values of the density gradient which we found by the method of Ref. 3, the crux of which consists in finding ρ_r for two values of the dimensionless radius ξ_1 and ξ_2 from an equation which is the difference of the two expressions of the form (3):

$$k(\xi_1,\xi_2)=\frac{2(n_0-1)R}{\lambda}\left\{[C(\xi_1)-C(\xi_2)]\left[\frac{\rho(R)}{\rho_0}-1\right]-[D(\xi_1)-D(\xi_2)]\frac{\rho_r(R)R}{2\rho_0}\right\}, \quad (10)$$

where $k(\xi_1,\xi_2)=k(\xi_1)-k(\xi_2)$.

The equation (10) makes it possible to find $\rho_r(R)$ from the difference, measured on the interferogram, of the shifts $k(\xi_1,\xi_2)$ and the quantity $\rho(R)$, calculated from Eq. (4) using the values of the front velocity N found by the double-exposure schlieren method. It should be noted, however, that the closer the points ξ_1 and ξ_2 are to one another, the larger the error in determining $\rho_r(R)$ is. The distance between the points where the shifts $k(\xi_1)$ and $k(\xi_2)$ are measured cannot be increased by a large amount, since the linear approximation (2) used to derive Eq. (3) is valid only in direct proximity to the shock front, i.e., for values of ξ_1 and ξ_2 close to 1. On this basis, the agreement between the values of $\rho_r(R)$ found by two independent methods can be assumed to be satisfactory.

The quantities ρ/ρ_0 and the values of ρ_r/ρ_0 determined from Eq. (9) were used to calculate the shift of the fringes near the shock front. Table I gives the values of K for $\xi=0.975$, i.e., at a distance equal to $R/40$ from the front. The table also gives values of K used to solve the inverse problem — to find the radial density distribution from the fringe shifts measured on the interferogram. The fractional part of K was measured directly from the interferogram, while the

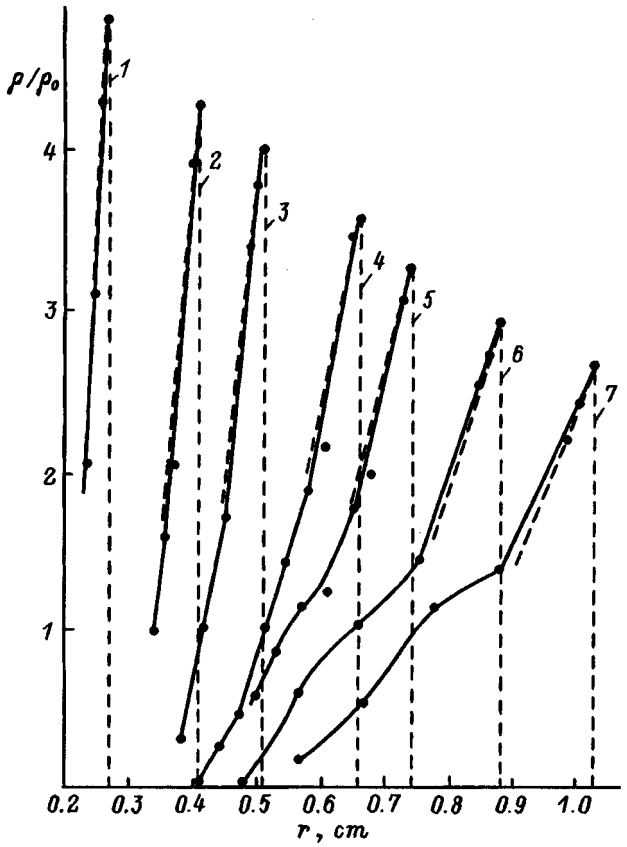

FIG. 3. Radial density distributions behind the shock front at different moments in time: *1* — 1.1, *2* — 2.1, *3* — 3.0, *4* — 4.7, 5 — 5.8, *6* — 7.8, *7* — 10.0 μs.

integer part was found so as to obtain the best agreement between the values of K calculated using Eq. (3).

The radial density distributions behind a shock front, which were obtained by analyzing the holographic interferograms corresponding to different moments in time measured from the moment of laser breakdown in air, are presented in Fig. 3. In this figure the points closest to the front were determined from the double-exposure schlieren photographs. The dashed lines correspond to the linear approximation (3) of the density profile behind the front. Therefore combining the double-exposure schlieren method with holographic interferometry made it possible to avoid the ambiguity in the interpretation of interferograms near a shock front and to obtain the density field behind the front at different stages of development of the process.

In conclusion, it should be noted that the procedure presented in this paper is suitable for studying shock waves not only in gases but also in transparent condensed media satisfying the equation of state in Tait's form,[5]

$$\frac{p+C}{p_0+C}=\left(\frac{\rho}{\rho_0}\right)^{\gamma}, \tag{11}$$

where C and γ are constants characterizing the medium.

Specifically, for water $C=3075$ kG/cm^2 and $\gamma=7.15$. The same method is also applicable for shock waves in solid materials under high pressures.[8] Analysis of the expressions for the coefficients A and B in Eq. (9) shows that the constant C is not required to calculate ρ_r behind the shock front. Only the value of the parameter γ is important.

This work was performed under State support of the leading scientific schools of the Russian Federation (Grant No. 96-15-96394).

[1] A. N. Zakhar'evskiĭ, *Interferometers* [in Russian], Oborongiz, Moscow (1952).
[2] R. Huddlestone and S. Leonard (Eds.), *Plasma Diagnostics* (Mir, Moscow, 1967).
[3] É. P. Kazandzhan and V. S. Sukhorukikh, *Optical Methods of Investigation in Ballistic Experiments* [in Russian], Nauka, Leningrad, 1979, pp. 158–170.
[4] S. V. Gribin, I. I. Komissarova, G. V. Ostrovskaya *et al.*, Zh. Tekh. Fiz. **68**(8), 39 (1998) [Tech. Phys. **43**, 912 (1998)].
[5] Yu. S. Yakovlev, *Hydrodynamics of Explosions* [in Russian], Sudpromgiz, Leningrad (1961).
[6] G. V. Dreĭden, A. P. Dmitriev, Yu. I. Ostrovskiĭ, and M. I. Étinberg, Zh. Tekh. Fiz. **53**, 311 (1983) [Sov. Phys. Tech. Phys. **28**, 191 (1983)].
[7] G. B. Whitham, *Linear and Nonlinear Waves* [Wiley, New York, 1974; Mir, Moscow, 1977].
[8] Ya. B. Zel'dovich and Yu. P. Raĭzer, *Physics of Shock Waves and High-Temperature Hydrodynamic Phenomena*, Vols. 1 and 2 [Academic Press, New York, 1966/1967; 2nd ed., Nauka, Moscow, 1966].

Translated by M. E. Alferieff

Nonlinear surface magnetic polaritons in a nonuniform magnetic field

S. V. Grimal'skiĭ, S. V. Koshevaya, and A. M. Resin

T. G. Shevchenko Kiev State University, 252601 Kiev, Ukraine
(Submitted July 8, 1996; resubmitted September 9, 1997)
Zh. Tekh. Fiz. **68**, 92–95 (September 1998)

High-frequency surface magnetic polaritons of finite amplitude propagating along the interface between a ferrite and a nonlinear insulator in a weakly nonuniform, shaft-shaped external magnetic field are investigated theoretically. The analysis is based on employment of the variational method together with bilinear relations having the form of Lorentz's lemma. It is shown that the wave dispersion and the transverse profile of a wave along the field nonuniformity depend significantly on the amplitude of the wave. © *1998 American Institute of Physics.* [S1063-7842(98)01809-1]

A great deal of interest has recently been focused on waves of finite amplitude in bounded solids.[1,2] It has been reported that surface magnetic polaritons can propagate on the interface between a nonmagnetic insulator and a ferrite [such as yttrium iron garnet (YIG)] immersed in an external magnetic field.[3,4] In such cases the wave vector and the external magnetic field lie in the plane of the interface and are mutually perpendicular. It is also known that nonlinear effects can be observed in YIG at fairly low levels of microwave power, and, in addition, the nonmagnetic insulator can be a nonlinear paraelectric such as $SrTiO_3$ and $KTaO_3$ or a ferroelectric ceramic in the paraelectric phase. Thus, in the microwave range these waves can be promising for observing nonlinear effects of the self-interaction type. In addition, the dynamics of waves in bounded ferrites can be controlled by creating a nonuniformity in the external magnetic field.[5,6] Therefore, it would be of interest to investigate the propagation of a surface magnetic polariton of finite amplitude in a weakly nonuniform external magnetic field with simultaneous allowance for magnetic and dielectric nonlinearities.

This paper describes a theoretical investigation of nonlinear surface waves (magnetic polaritons) of constant frequency propagating perpendicularly to a weakly nonuniform, shaft-shaped external magnetic field with allowance for both the magnetic and dielectric nonlinearities of the contacting media. An ordinary differential equation describing the dependence of the wave amplitude on the transverse coordinate in the plane of the interface is obtained. A numerical solution of this equation yields a nonlinear dispersion relation for waves in a nonuniform field. It is shown that the magnetic nonlinearity is dominant for this wave propagation direction. The dispersion characteristics and profile of the wave along the direction of the nonuniformity depend significantly on the amplitude of the wave at the center of the waveguide.

A surface magnetic polariton can exist on the interface between a ferrite and a nonmagnetic insulator in the case of tangential magnetization. In the linear case, it has the components (H_x, H_y, E_z) in a uniform field H_0, and the frequency ω and the wave number k are related by the dispersion relation[4]

$$\sigma_0^2-\mu^2-\frac{\sigma_0 k+\mu\tau}{p}=0, \tag{1}$$

where

$$p=\left(k^2-\frac{\omega^2}{c^2}\varepsilon_d\right)^{1/2}, \quad \tau=\left(k^2+\frac{\omega^2}{c^2}\varepsilon_f\frac{\sigma_0^2-\mu^2}{\mu}\right)^{1/2},$$

$$\sigma_0=\omega\omega_M/(\omega^2-\omega_H^2),$$

$\mu=1-\omega_H\omega_M/(\omega^2-\omega_H^2)$; $\mu_{11}=\mu_{22}=\mu$, $\mu_{12}=-\mu_{21}=i\sigma_0$, $\mu_{33}=1$, and $\mu_{13}=\mu_{23}=0$ are components of the permeability tensor of the ferromagnet (FM); $\omega_H=\gamma H_0$; $\omega_M=4\pi\gamma M_0$; γ is the gyromagnetic ratio; H_0 is the applied constant magnetic field; M_0 is the saturation magnetization; and ε_f and ε_d are the dielectric constants of the ferrite and the insulator, respectively.

It is assumed that the FM is located in the region $x>0$, that H_0 and M_0 are directed along the $0z$ axis, and that the wave vector is directed along the $0y$ axis. Furthermore, we shall consider the case of a contact between an FM and a nonlinear paraelectric ($x<0$) with a considerable dielectric constant ($\varepsilon_d\sim 10^3 \gg \varepsilon_f\sim 10^1$). In this case we can confine ourselves to consideration of retardation only in the insulator: $k>(\omega/c)\varepsilon_d^{1/2}\gg(\omega/c)\varepsilon_f^{1/2}(\sigma_0/\mu^{1/2})$, $\tau\approx k$. Then the dispersion relation (1) can be written in the simpler form

$$\sigma_0-\mu-k/p=0. \tag{2}$$

Let us consider the case where the applied magnetic field H_0 depends weakly on the transverse coordinate z in the plane of the interface and the nonuniformity has the shape of shaft ($dH_0/dz>0$ for $z<0$ and $dH_0/dz<0$ for $z>0$). We note that the influence of the small x component of the constant magnetic field, whose existence follows from the equation div $B=0$, can be neglected.[6] The propagation of a surface magnetic polariton is possible in such a system in the waveguide channel created by the field nonuniformity along the $0z$ axis in the plane of the interface, since this field nonuniformity leads to confinement of the wave energy along the $0z$ axis.[5] In the linear case this can easily be demonstrated by geometric optics. In this paper we investigate

the dispersion characteristics of a nonlinear waveguide created by the nonuniformity of the field $H_0(z)$.

Nonlinear waves in inhomogeneous structures can be analyzed using Whitham's variational method. This method calls for utilizing the stationary character of the action in choosing a trial function with allowance for the weak variation of the transverse profile of a nonlinear wave in comparison with the linear case.[7] This method has been employed to investigate nonlinear surface waves of the Damon–Eshbach type in a weakly nonuniform magnetic field without allowance for retardation,[8] as well as to analyze the phenomenon of convolution in FM fields with allowance for retardation.[9] The plan in the present work is to investigate the influence of two nonlinearity mechanisms (magnetic nonlinearity in the FM and dielectric nonlinearity in the paraelectric). Allowance for the magnetic nonlinearity in the Landau–Lifshitz equations using the variational method requires formidable calculations; therefore, below we shall use a simpler method of analysis, in which the equation describing the dependence of the wave amplitude on the transverse coordinate z in the presence of pure dielectric nonlinearity will be obtained by the variational method and the magnetic nonlinearity will be taken into account by the bilinear relations having the form of Lorentz's lemma for an electromagnetic field.[10,11]

Maxwell's equations with allowance for the dielectric nonlinearity in the paraelectric ($\varepsilon=\varepsilon_d-aE^2$, $a>0$) and the boundary conditions for the tangential components of the field H can be obtained from the variational principle for the action $S=\int\int L dV\,dt$ with the following Lagrangian:

$$8\pi L=\mathbf{E}^*\cdot\left(\varepsilon(x)-\frac{a(x)}{2}\mathbf{E}\cdot\mathbf{E}^*\right)\mathbf{E}-\mathbf{B}^*\cdot\hat{\mu}^{-1}(\omega,\mathbf{r})\mathbf{B}, \tag{3}$$

where

$$\mathbf{E}=-\frac{i\omega}{c}\mathbf{A},$$

$\mathbf{B}=\text{curl}\ \mathbf{A}$, $\mathbf{H}=\hat{\mu}^{-1}\mathbf{B}$, and $\mathbf{A}$ and $\mathbf{A}^*$ are the positive- and negative-frequency components of the vector potential.

We note that all the components of $\mathbf{A}$ for a wave in a nonuniform magnetic field $H_0(z)$ are nonzero. The main assumption is that by virtue of the weak nonuniformity of the field along the $0z$ axis the transverse profiles of the polariton components along $0x$, which is normal to the plane of the film, vary weakly in comparison to the case of a uniform field, i.e., we seek the solution for E_z in the form

$$E_z=\frac{1}{2}F(z)e^{i\omega t-iky}\begin{cases}e^{-kx}, & x>0,\\ e^{px}, & x<0,\end{cases} \tag{4}$$

where $F(z)$ is the wave amplitude, which varies slowly in comparison to the wavelength.

The dependences of A_x and A_y on x are assumed to be the same. We note that A_y and A_z are continuous at $x=0$; A_x has a discontinuity. Then, plugging (4) into (3) and performing the variation with respect to F, as well as A_x and A_y, we obtain a system of differential equations for F and $A_{x,y}$, where $A_{x,y}\sim\partial F/\partial z$. Eliminating $A_{x,y}$, we can write the equation for $F(z)$ in the form

$$\frac{d^2F}{dz^2}+\frac{2k^2p^3}{(p+k)(p^2-k^2+pk)}D(\omega,\omega_H(z),k,F)F=0, \tag{5}$$

where $D(\omega,\omega_H,k,F)=\sigma_0-\mu-k/p+(a\omega^2/2c^2p^2)F^2$ and $\omega_H=\omega_H(z)$. In a uniform field $D(\omega,\omega_H,k,F)=0$ is the nonlinear dispersion relation for a magnetic polariton with allowance for the dielectric nonlinearity.

It is significant that the field nonuniformity appears only in the form of $\omega_H(z)$ in the nonlinear dispersion relation.

If the magnetic nonlinearity in the FM is taken into account, Eq. (5) should be refined. To accomplish this, the contribution of the magnetic nonlinearity to the coefficient in front of F^2 in $D(\omega,\omega_H,k,F)$ must be determined. This coefficient can be determined in the case of a uniform external magnetic field. In the approximation used here additive contributions of the dielectric and magnetic nonlinearities appear in this coefficient. The refined nonlinear dispersion relation can be obtained most simply from the bilinear relation having the form of Lorentz's lemma for an electromagnetic field with consideration of the magnetic components of the polariton. The corresponding relation for the type of waves under consideration has the form

$$\begin{aligned}&\frac{\partial}{\partial t}\left(\frac{1}{4\pi}\varepsilon(x)\mathbf{E}_1\cdot\mathbf{E}_2^*+\frac{1}{4\pi}\mathbf{H}_1\cdot\mathbf{H}_2^*+\frac{H_0}{M_0}(m_{1x}m_{2x}^*\right.\\&\qquad\left.+m_{1y}m_{2y}^*)\right)+\frac{c}{4\pi}\text{div}([\mathbf{E}_2^*\times\mathbf{H}_1]+[\mathbf{E}_1\times\mathbf{H}_2^*])\\&\qquad-\frac{i\omega}{M_0}(H_{1y}m_{2y}^*+H_{1x}m_{2x}^*)\frac{m_x^2+m_y^2}{2M_0}\\&\qquad-\frac{i\omega}{4\pi}a(x)|\mathbf{E}_1|^2\mathbf{E}_1\cdot\mathbf{E}_2^*=0.\end{aligned} \tag{6}$$

Here $\mathbf{E}_1$, $\mathbf{H}_1$, and $m_{1x,y}$ are the positive-frequency components of the magnetic polariton with consideration of the nonlinearity; $\mathbf{E}_2$, $\mathbf{H}_2$, and $m_{2x,y}$ describe a linear monochromatic wave. The relation (6) allows us to obtain the correction to the wave frequency caused by the nonlinearity, if the wave number of the linear and nonlinear waves are assumed to be equal. This method is similar to the perturbation theory for waveguides.[11] Integrating (6) over x, we find the correction to the wave frequency caused by the dielectric and magnetic nonlinearities and the ratio between the contributions of the magnetic ($\Delta\omega_{\text{FM}}$) and dielectric ($\Delta\omega_{\text{DE}}$) nonlinearities in the correction to the frequency $\Delta\omega=\Delta\omega_{\text{FM}}+\Delta\omega_{\text{DE}}$

$$\frac{\Delta\omega_{\text{FM}}}{\Delta\omega_{\text{DE}}}=-\frac{(p+k)^3}{k(4\pi M_0)^2}\Big/\frac{a\omega^4}{2c^4p^2}. \tag{7}$$

Next, when the contribution of the dielectric nonlinearity in (5) is replaced by the sum of the contributions due to the magnetic and dielectric nonlinearities, we obtain an equation for a magnetic polariton with allowance for not only the nonlinearities in both media, but also the weak nonuniformity of the field:

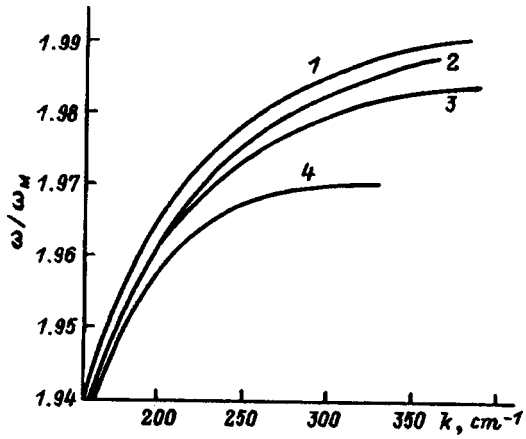

FIG. 1. Dispersion relations $k(\omega,F_0)$ for a nonlinear polariton in a weakly nonuniform magnetic field $\omega_H(z)=\gamma H_0(z)=\omega_H+\Delta\omega_H\mathrm{sech}^2qz$ when $\omega_H/\omega_M=1.4$, $\Delta\omega_H/\omega_M=0.1$, and $q=5$ cm^{-1}: *1*, *2* — $F_0(a/\varepsilon_0)^{1/2}=0.01$ (linear wave) in uniform and nonuniform fields, respectively, *3* — $F_0(a/\varepsilon_0)^{1/2}=0.05$, *4* — $F_0(a/\varepsilon_0)^{1/2}=0.1$.

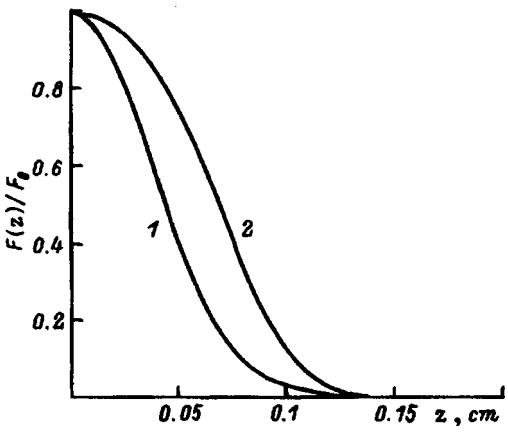

FIG. 2. Profiles of E_z along the nonuniformity of the field $H_0(z)$ $[\omega_H(z)/\omega_M=1.4+0.1\mathrm{sech}^2qz,\quad q=5\ \mathrm{cm}^{-1}]$: *1* — linear wave $[F_0(a/\varepsilon_0)^{1/2}=0.01]$, *2* — nonlinear wave $[F_0(a/\varepsilon_0)^{1/2}=0.1]$; $\omega/\omega_M=1.970$.

$$\frac{d^2F}{dz^2}+\frac{2k^2p^3}{(k+p)(p^2-k^2+kp)}\times\left(\sigma_0-\mu-\frac{k}{p}+\left(\frac{a\omega^2}{2c^2p^2}-\frac{(p+k)^3c^2}{k(4\pi M_0)^2\omega^2}\right)F^2\right)F=0. \tag{8}$$

For the lowest (symmetric with respect to z) mode the boundary conditions for F are

$$F(z=0)=F_0,\quad dF/dz(z=0)=0,\quad F(z\to\infty)\to 0, \tag{9}$$

where F_0 is the wave amplitude at the center of the waveguide (an independent parameter).

Equation (8) supplemented by the boundary conditions (9) for fixed values of ω and F_0 has nontrivial solutions for specific values of the wave number $k=k(\omega,F_0)$. The latter relation is also the nonlinear dispersion relation for a nonlinear magnetic polariton in a nonuniform magnetic field. It can be seen that the contributions of the magnetic and dielectric nonlinearities to (8) have different signs. In subsequent calculations the parameters of the paraelectric were set equal to $\varepsilon_d=2.5\times10^3$ and $a=10$ G^{-2}, and YIG with a saturation magnetization $4\pi M_0=1760$ Oe was chosen as the ferromagnetic medium.

Let us first consider the case of a small wave amplitude for a field nonuniformity of the form $(\Delta\omega_H>0)$

$$\omega_H=\omega_{H\infty}+\Delta\omega_H\ \mathrm{sech}^2qz. \tag{10}$$

It can be seen from Eq. (8) that localization of a polariton along the $0z$ axis is possible in the frequency range $(\omega_{H\infty}(\omega_{H\infty}+\omega_M))^{1/2}<\omega<\omega_{H\infty}+\Delta\omega_H+\omega_M/2$. Numerical calculations showed that in the case of a small-amplitude wave the field nonuniformity significantly alters the spectrum of the fundamental mode, and the slope of the dispersion curves decreases (Fig. 1, curves *1* and *2*). It turned out in the case of waves of finite amplitude that the main contribution is made by the magnetic nonlinearity. Since the wave profile along the nonuniformity of the external field becomes wider with increasing amplitude, this nonlinearity is defocusing. Numerical estimates showed that this conclusion is valid for amplitudes of the dielectric nonlinearity $a\leqslant 100$ G^{-2}. Its influence is confined to narrowing the frequency spectrum of the magnetic polariton from above (Fig. 1, curves *3* and *4*) and broadening the wave profile along the $0z$ axis (Fig. 2). The influence of the dielectric nonlinearity becomes more appreciable in the region where $\mu(\omega)\approx 0$, but here both the damping and the retardation in the FM must be taken into account in principle. Thus, in the waveguide under consideration, which is created by nonuniformity of the external magnetic field, the influence of nonlinearity on wave propagation is highly significant, the magnetic nonlinearity being decisive.

[1] *Nonlinear Waves in Solid-State Physics*, edited by A. D. Boardman, M. Bertolotti, and T. Twardowski (Plenum Press, New York, 1986).
[2] A. D. Boardman, M. M. Shabat, and R. F. Wallis, J. Phys. D **24**, 1702 (1991).
[3] R. W. Damon and J. R. Eschbach, J. Phys. Chem. Solids **19**, 308 (1961).
[4] M. I. Kaganov and T. I. Shalaeva, Zh. Éksp. Teor. Fiz. **96**, 2185 (1989) [Sov. Phys. JETP **69**, 1237 (1989)].
[5] A. V. Vashkovskiĭ, V. I. Zubkov, É. G. Lokk, and V. I. Shcheglov, Zh. Tekh. Fiz. **60**(7), 138 (1990) [Sov. Phys. Tech. Phys. **35**, 833 (1990)].
[6] G. N. Burlak, V. V. Grimal'skiĭ, and N. Ya. Kotsarenko, Zh. Tekh. Fiz. **59**(8), 32 (1989) [Sov. Phys. Tech. Phys. **34**, 860 (1989)].
[7] G. B. Whitham, *Linear and Nonlinear Waves*, Wiley, New York (1974); Mir, Moscow (1977).
[8] V. V. Grimal'skiĭ and Yu. G. Rapoport, Pis'ma Zh. Tekh. Fiz. **20**(9), 11 (1994) [Tech. Phys. Lett. **20**, 345 (1994)].
[9] V. Grimalsky and Yu. Rapoport, J. Magn. Magn. Mater. **140–144**, 2195 (1995).
[10] A. G. Gurevich and G. A. Melkov, *Magnetization Oscillations and Waves*, CRC Press, Boca Raton (1996).
[11] L. A. Vaĭnshteĭn, *Electromagnetic Waves* [in Russian], Sov. Radio, Moscow (1988).

Translated by P. Shelnitz

Stability of a quasineutral beam of negative ions

E. E. Barminova and A. S. Chikhachev
(Submitted March 19, 1997)
Zh. Tekh. Fiz. **68**, 96–98 (September 1998)

The stability of a beam of negative ions propagating in the parent gas is investigated. It is shown that growth of plasma oscillations with a small growth rate is possible at subcritical currents in a quasineutral regime. The influence of traveling secondary electrons, whose density is small, is also studied. The low-frequency oscillations considered pose the greatest danger to a beam whose velocity is close to the velocity of the secondary electrons. © *1998 American Institute of Physics.* [S1063-7842(98)01909-6]

The evolution of a beam of negatively charged ions (for example, H^-) over the course of a long time period has attracted the attention of both experimentalists[1] and theoreticians[2,3] owing to the possibility of employing such beams for scientific purposes and in technology.

This paper examines the instabilities of beams which can appear in the initial stage of their evolution.

After leaving the source, an ion beam enters a drift chamber containing a residual gas. Ionization of the gas by the beam produces a plasma. The density of the residual gas is of great significance for the parameters of the plasma formed. We define the critical density in the following manner:

$$n_*=\frac{v_+}{2r_0\sigma_i v_b}. \tag{1}$$

Here v_+ is the mean velocity of the positively charged secondary ions, r_0 is the radius of the beam, σ_i is the ionization cross section, and v_b is the velocity of the beam particles. It follows from qualitative arguments that if the density of the gas is less than or close to the critical value, then the space charge of the beam will be neutralized by the charge of the positive background ions, and the small number of δ electrons will not violate the quasineutrality condition $n_b \sim n_+$ (the time of flight of the secondary electrons in a beam is of the order of r_0/v_δ, where $v_\delta \sim 10^8$ cm/s). If the gas density exceeds n_*, then the beam charge is overcompensated, and a plasma beam-propagation regime is realized ($n_b \ll n_+, n_\delta$). We shall next examine the case of subcritical gas densities, assuming that the degree of neutralization of the beam charge is fixed.

1. If the mass of the positive ions neutralizing the beam charge significantly exceeds the mass of the beam ions, then, according to Ref. 4, the beam current is restricted by Pierce instability, so that the limiting current density j_P is given by the equality

$$j_P=\frac{\pi}{2}\left(\frac{2e}{m_b}\right)^{1/2}\frac{\Phi^{3/2}}{L^2}, \tag{2}$$

where $e\Phi$ is the energy of the beam particles, $e\Phi=m_b v_b^2/2$, m_b is the mass of a beam ion, and L is the length of the plasma gap.

This result was obtained in Ref. 4 from a solution of a system of hydrodynamic equations describing a wide magnetized beam.

The instability of an unmagnetized beam with a finite diameter toward oblique disturbances was studied in Ref. 5. In that study the frequencies of the axially symmetric oscillations were determined from a dispersion relation of the form

$$F(\theta,\theta_0,\beta)=0, \tag{3}$$

where

$$F(\theta,\theta_0,\beta)=2\theta\theta_0^2(\cosh\beta-e^{i\theta}\cos\theta_0)+i(\theta^2+\theta_0^2+\beta^2)e^{i\theta}\theta_0\sin\theta_0+\frac{i\sinh\beta}{\beta}\times(\theta^2(\theta^2-\theta_0^2+2\beta^2)+\beta^2(\theta_0^2+\beta^2)). \tag{4}$$

Here we have introduced the notation $\theta=\omega L/v_b$, $\theta_0=\omega_b L/v_b=\theta_b$, $\beta=kL$, and $\omega_b^2=4\pi e^2 n_b/m_b$. In addition, ω and k are, respectively, the frequency and wave vector of the oscillations: $k=(k_x^2+k_y^2)^{1/2}$ (the beam propagates along the z axis). The stability region of such a beam is broadened, and the stability threshold is raised in comparison to a Pierce beam. In the limiting case of $k=0$ and $\omega\to 0$, it follows from (3) that $\theta_0|_{z=L}=\pi$, which is equivalent to (2).

In some cases the mass of the background ions cannot be considered infinitely large (for example, if the beam propagates in the parent gas).

If the plasma ions have a finite mass, the system of hydrodynamic equations for the beam must be supplemented by equations which describe the motion of the plasma ions, as is done for a beam of electrons, whose charge is neutralized by positively charged particles of finite mass.[6,7] The same dispersion relation (3) can be obtained as a result, but in (4) we should set $\theta_0=\theta\theta_b/(\theta^2-\theta_+^2)^{1/2}$, where $\theta_+^2=4\pi e^2 n_+ L^2/m_+ v_b^2$, instead of using the equality $\theta_0=\theta_b$ for $\theta_+=0$. Here m_+ is the mass of a positive ion.

Just as in Ref. 5, in our case the dispersion relation (3) is always satisfied by the two solutions

$$\theta=\pm\theta_0+i\beta. \tag{5}$$

These solutions, however, do not describe real instability, since the density disturbance $n'\equiv 0$ if $n'|_{z=L}=0$.

Therefore, we should seek solutions which do not coincide with (5). Let $k=0$ ($\beta=0$), and let us consider the low-frequency range $\theta=\theta_+ +\delta$, where $\delta \ll \theta_+ <1$. Then, from Eq. (3) we have

$$2\theta_+(1-\cos\theta_0)+i\theta_0\sin\theta_0=0. \tag{6}$$

We find the solution of (6)

$$\theta_0=\pi-\frac{4i\theta_+}{\pi}. \tag{7}$$

Since $\theta_0^2=\theta^2\theta_b^2/(\theta^2-\theta_+^2)\sim\theta_+\theta_b^2/2\delta$, we can write

$$\delta=\frac{\theta_+\theta_b^2}{2\pi^2}\left(1+\frac{8i\theta_+}{\pi^2}\right), \tag{8}$$

and the solution of Eq. (3) is

$$\theta=\theta_+ +\frac{\theta_+\theta_b^2}{2\pi^2}+i\frac{4\theta_+^2\theta_b^2}{\pi^4}. \tag{9}$$

The solution obtained is valid for $\theta_b<\pi$. It follows from the expression for the frequency θ,

$$\theta=\theta_0\theta_b\sqrt{\theta_0^2-\theta_+^2}, \tag{10}$$

that an abrupt increase in the oscillation amplitude occurs when $\theta_b>\theta_{b\,\mathrm{cr}}=\theta_0$, signifying current collapse (the onset of aperiodic instability). In this sense $\theta_{b\,\mathrm{cr}}$ can be regarded as the limiting current of the stationary beam.

At large θ ($\theta\gg\theta_+,\theta_b$) Eq. (3) does not have solutions. If $\theta_+\to 0$, (4) yields

$$\theta_0\sin\theta_0+\beta\sinh\beta=0, \tag{11}$$

whence

$$\theta_0\simeq\pi(2s+1)+\frac{\beta\sinh\beta}{\pi(2s+1)},$$

where the integer s satisfies the inequality

$$\frac{\beta\sinh\beta}{2\pi\left(s+\frac{1}{2}\right)}\ll 1.$$

Then

$$\delta=\frac{\theta_+\theta_b^2}{2\theta_0^2}=\frac{\theta_+\theta_b^2}{2\pi^2((2s+1)+\beta\sinh\beta/\pi^2(2s+1))^2}.$$

If $\theta_+<1$ and $\beta\ll 1$, it follows from (4) that

$$\theta_0\sin\theta_0+\beta^2=2i\theta_+(1-\cos\theta_0), \tag{12}$$

and since the solution for θ_0 should be close to π [see (7)] in the case of a long-wavelength disturbance ($k\ll 1/L$), it can be concluded that a nonzero value of β leads to a small shift of the real part of the oscillation frequency (9) toward higher frequencies, while the imaginary part of θ, which is responsible for growth of the oscillations, depends mainly on the plasma frequencies of the background ions. Since it follows from (12) that

$$\theta_0\simeq\pi+\frac{\beta^2}{\pi}-\frac{4i\theta_+}{\pi},$$

the limiting beam current, according to (10), in a system with $\beta\neq 0$ is higher than the current specified by (2).

2. Let us now study the influence of traveling δ electrons present within the beam in a small density. We shall consider times that are shorter than the characteristic time for the development of instability described in Sec. 1. For simplicity, we assume that the plasma system is one-dimensional.

The density of the secondary electrons can be estimated in the following manner:

$$n_\delta\simeq n_g n_b\sigma_i v_b r_0/v_\delta. \tag{13}$$

For an energy of the H^- ions $W_H\sim 50$ keV we have $v_b\sim 3\times 10$ cm/s, and for an energy of the δ electrons $W_\delta\sim 10$ eV we have $v_\delta\sim 2\times 10^8$ cm/s. If $r_o\sim 1$ cm, $n_g\sim 10^{14}$ cm^{-3}, and the beam current $J\sim 100$ mA, then $n_b\sim 7\times 10^8$ cm^{-3}, and $n_\delta\sim 10^5$ cm^{-3}. In deriving the dispersion relation for the three-component system, in analogy to Ref. 8, we shall use a hydrodynamic description for the heavy particles, i.e., the beam ions and the plasma ions, assuming that the temperatures of these components are equal to zero, and a kinetic description for the plasma electrons, assuming that their distribution function is Maxwellian. The following relation can be obtained

$$1=\frac{\omega_+^2}{\omega^2}+\frac{\omega_b^2}{(\omega-kv_b)^2}+\frac{\omega_{pe}^2}{\omega^2-k^2v_{Te}^2}$$
$$-i\sqrt{\pi}\frac{\omega_{pe}\omega}{(kv_{Te})^3}e^{-\frac{\omega^2}{k^2v_{Te}^2}}. \tag{14}$$

We set $\omega=\Omega+i\gamma$, where Ω and γ are real. If $\gamma>0$, the oscillations are damped, and if $\gamma<0$, growth of the oscillations takes place.

If $\gamma\ll\Omega$, it follows from (14) that

$$\gamma=\frac{\sqrt{\pi}\Omega\dfrac{\omega_{pe}^2}{(kv_{Te})^3}e^{-\Omega^2/k^2v_{Te}^2}}{\dfrac{2\omega_+^2}{\Omega^3}+\dfrac{2\omega_b^2}{(\Omega-kv_b)^3}+\dfrac{2\Omega\omega_{pe}^2}{(\Omega^2-k^2v_{Te}^2)^2}}. \tag{15}$$

It can be seen from this relation that growth of the oscillations, i.e., fulfillment of the condition $\gamma<0$, is possible for $\Omega<kv_b$. In order for the denominator in (15) to become negative as $\Omega\to kv_b$, the following inequalities must be satisfied:

$$1>\frac{\Omega}{kv_b}>1-\left[\frac{1}{\alpha}\left(1-\frac{v_{Te}^2}{v_b^2}\right)\right]^{2/3},$$

$\alpha=\omega_{pe}/\omega_b$.

Under the same conditions the real part of Eq. (14) leads to the equality

$$\frac{\Omega}{kv_b}=1\pm\frac{\omega_b}{kv_b\sqrt{1-\dfrac{\omega_b^2}{k^2v_b^2}-\dfrac{\omega_{pe}^2}{k^2(v_b^2-v_{Te}^2)}}}.$$

Thus, instability occurs for values of the wave vector which satisfy the inequality

$$\frac{\omega_b}{kv_b} < \left(\frac{1}{\alpha} \left(1 - \frac{v_{Te}^2}{v_b^2} \right) \right)^{3/2} \ll 1.$$

The presence of secondary electrons in this problem leads to the growth of oscillations with the frequency $\Omega \sim kv_b - \omega_b$. The growth rate of the amplitude of these oscillations is small and tends to zero as $\omega_b \to 0$:

$$\gamma \simeq -\frac{\sqrt{\pi}}{2} \frac{\omega_{pe}^2 \omega_b (kv_b - \omega_b)}{(kv_{Te})^3} e^{-v_b^2/v_{Te}^2}.$$

The group velocity of the oscillations considered $\partial\omega/\partial k$ is close to v_b; therefore, this instability can be assigned to the discharge of drift particles. Thus, it can be concluded for a beam propagating in the parent gas in a quasineutral regime that the threshold current, beyond which there should be a dramatic increase in the oscillation amplitude, is below the Pierce current due to the participation of background ions in the oscillations. A loss of stable current propagation occurs because of the development of Pierce two-stream instability. We recall that the existence of such instability for an electron beam has been demonstrated theoretically and experimentally.[6,7,9,10]

The instability threshold of an ion beam increases when its transverse dimensions are restricted, as occurs in an electron beam.[5] Oscillations with a wavelength of the order of the beam diameter near the plasma frequency of the background ions (which was not excessively great in our case) are most dangerous for a beam.

The system does not amplify oscillations with a high frequency and is stable toward disturbances with a wavelength much smaller than the length of the flight gap. We note that weak growth of the plasma oscillations is observed at sub-Pierce currents.

If the conditions for the appearance of instability described in Sec. 1 are not present in the system, there is a possibility for the development of another, purely oscillatory instability due to the presence of secondary electrons in the system. The growth rate of these low-frequency oscillations is small. These oscillations pose the greatest danger to a beam whose velocity is close to the thermal velocity of the δ electrons.

[1] Y. Okumura, M. Hanada *et al.*, in *Production and Neutralization of Negative Ions and Beams. 5th International Symposium*, New York–Brookhaven (1990), p. 169.
[2] A. P. Naĭda and D. G. Dzhabbarov, Zh. Éksp. Teor. Fiz. **78**, 2259 (1980) [Sov. Phys. JETP **51**, 1132 (1980)]; A. P. Naĭda and V. P. Goretskiĭ, Fiz. Plazmy **11**, 394 (1985) [Sov. J. Plasma Phys. **11**, 227 (1985)].
[3] I. A. Soloshenko *et al.*, Fiz. Plazmy **20**, 810 (1994) [Plasma Phys. Rep. **20**, 730 (1994)].
[4] J. R. Pierce, J. Appl. Phys. **15**, 721 (1944).
[5] A. A. Ivanov and N. S. Putvinskaya, Zh. Tekh. Fiz. **45**, 1648 (1975) [Sov. Phys. Tech. Phys. **20**, 1049 (1975)].
[6] J. R. Pierce, J. Appl. Phys. **19**, 231 (1948).
[7] K. Yuan, J. Appl. Phys. **48**, 133 (1977).
[8] A. A. Ivanov, *Physics of a Strongly Nonequilibrium Plasma* [in Russian], Atomizdat, Moscow (1977).
[9] S. Iizuka, K. Saeki, N. Sato, and Y. Hatta, Phys. Rev. Lett. **43**, 1404 (1979).
[10] H. Shamel and H. Kolinsky, Phys. Plasmas **1**, 2359 (1994).

Translated by P. Shelnitz

Mechanism of the rf sputtering of mixed oxides

V. M. Mukhortov, G. N. Tolmachev, Yu. I. Golovko, and A. I. Mashchenko

Institute of General Physics, Russian Academy of Sciences, 117942 Moscow, Russia
(Submitted April 14, 1997)
Zh. Tekh. Fiz. **68**, 99–103 (September 1998)

New experimental data on the growth mechanisms of multicomponent $Pb(Zr,Ti)O_3$, $(Ba,Sr)TiO_3$, and Y–Ba–Cu–O films in an rf discharge plasma are presented. An investigation of the spatial distribution of the radiated intensity of the sputtered particles in the rf plasma during the deposition of films of these mixed oxides in the epitaxial state reveals general laws governing their transport from the target to the substrate, which are stipulated by features of the negative glow of the rf discharge. The roles of external and internal parameters are examined from the standpoint of describing the mechanisms of the heteroepitaxial growth of mixed oxides. © *1998 American Institute of Physics.* [S1063-7842(98)02009-1]

The conditions for the synthesis and crystallization of mixed oxides directly during the growth of thin films are often provided by the rf sputtering of ceramic targets in pure oxygen. The greatest success in this area has been achieved using an elevated oxygen pressure.[1–3] An analysis of the results of experimental studies obtained by different investigators attests to the strong dependence of the structural perfection and electrophysical properties of the films on the specific deposition conditions. The parameters for synthesizing films usually include only such macroscopic characteristics as the input rf power, the discharge current, the substrate temperature, the pressure of the working gas, and the target-substrate distance. Of course, these parameters (we shall henceforth refer to them as external parameters) apply only to a concrete film deposition machine.

Further perfection of the technology is possible only when the growth mechanisms are understood. One of the possible approaches for solving this problem is to use internal parameters, which characterize the state of the rf plasma during the sputtering of a mixed oxide. We propose the use of the spatial distribution of the radiated intensity of the sputtered components of the oxide as such a parameter.

In the present work we investigated the spatial distribution of the radiated intensity of sputtered atoms in an rf plasma during the deposition of films of mixed oxides in the epitaxial state. Conditions for growing $Pb(Zr,Ti)O_3$, $(Ba,Sr)TiO_3$, and Y–Ba–Cu–O films which permit the deposition of each of these compounds in the heteroepitaxial state were determined empirically. The composition of the oxide was chosen with the intention of proving that the growth mechanisms of the condensate are common to different mixed oxides within one deposition method and the same level of structural perfection of the films.

EXPERIMENTAL

a) Selection of conditions for depositing heteroepitaxial films. The design of the sputtering machine, the measurements of the external parameters for rf sputtering, and the methods for investigating the optical emission spectra and their spatial variation along the discharge axis were previously described.[1,2] The target in the sputtering unit was a hot-pressed ceramic of corresponding composition with a diameter of 50 mm and a thickness of 3.5 mm. The substrates used were MgO crystals.

We estimated the structural perfection of the heteroepitaxial films on the basis of data from x-ray structural investigations on a DRON-4 diffractometer. The vertical and azimuthal misorientation angles of the film crystallites, the dimensions of the coherent-scattering regions (an integral measure of the ordered defects in a film), and the microstrains (an integral measure of the unordered defects in a film) were determined.

In this paper we shall examine only the film deposition conditions under which heteroepitaxial growth takes place with a vertical misorientation angle $<0.5°$, an azimuthal misorientation angle $<3°$, coherent-scattering regions >1000 Å, and microstrains amounting to $<3\times10^{-3}$. Such structural perfection of the films can be obtained only under strictly specified deposition conditions, which can be assigned by several external parameters. The most significant such parameter is the pressure of the working gas (oxygen) in the sputtering chamber. It was established experimentally that there is a certain threshold oxygen pressure, at which heteroepitaxial film growth takes place. In particular, the threshold pressure for $Ba_xSr_{(1-x)}TiO_3$ (with $x=0.3-0.8$) is 0.3 Torr. Lowering the pressure to 0.2 Torr leads to the growth of polycrystalline films (there is no azimuthal orientation of the film relative to the substrate). The stable heteroepitaxial growth of Y–Ba–Cu–O can be achieved only at an oxygen pressure no less than 0.7 Torr. The deposition of heteroepitaxial films of $PbZr_xTi_{(1-x)}O_3$ (with $x=0.5-0.7$) requires an increase in the oxygen pressure to 1.8 Torr. The heteroepitaxial growth of all three mixed oxides indicated above at oxygen pressures above the threshold value takes place at substrate temperatures covering a fairly broad range from 580 to 650 °C. Variation of the target-substrate distance from 8 to 12 mm generally does not alter the quality of the heteroepitaxial films.

The rf power for each compound was selected empiri-

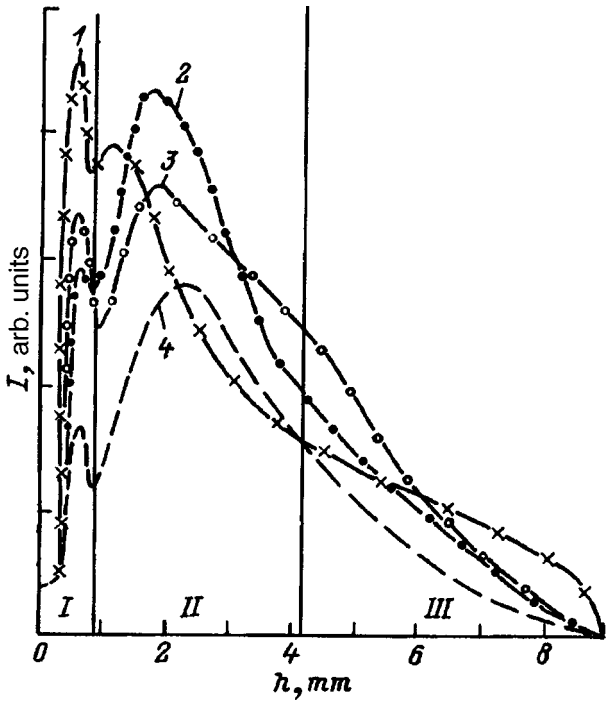

FIG. 1. Spatial distribution of the radiated intensity during the sputtering of Y–Ba–Cu–O, (Ba,Sr)TiO_3, and Pb(Zr,Ti)O_3 ceramic targets: *1* — 0 (λ = 3947 Å), *2* — Ba (λ = 4554 Å), *3* — Sr^+ (λ = 4215 Å), *4* — Cu (λ = 3273 Å); $P_{O_2} = 0.7$ Torr. The target-substrate distance $h = 8.5$ mm.

cally. To set an optimality criterion it was assumed that the electron concentration at an oxygen pressure above the critical value for each oxide must not be less than $5 \times 10^{12}\,\mathrm{cm}^{-3}$ (measurements using a symmetric double probe according to the method in Ref. 4). To stabilize the discharge and lower the probability of the appearance of current instability, the targets were preliminarily ''activated'' at a reduced (70% of the nominal value) input power ($U_{\mathrm{rf}} = 490\,\mathrm{V}$, $I_{\mathrm{rf}} = 0.8$ A). The target ''activation'' time for (Ba,Sr)TiO_3 was 15–20 min, the time for Pb(Zr,Ti)O_3 was 3.0–3.5 h, and the time for Y–Ba–Cu–O was 7–10 h. During this ''activation,'' the intensities of the lines of the sputtered atoms in the discharge increased by 15–20% even when the input power was left unchanged. It should be specially noted that the intensity growth gradients for different target components did not vary as a function of either the activation time or the input power.

b) Features of the spatial distribution of the radiated intensity of the rf plasma. The spatial distribution of the radiated intensity of the sputtered atoms and ions obeys several general laws regardless of the composition of the targets used. The main law is the spatial structuring of the discharge. This is reflected in the presence of special points on the spatial intensity distribution, which separate the space between the target surface and the substrate into the three characteristic zones shown in Fig. 1.

The first fluorescence zone is created directly by sputtering of the oxide surface. In this zone the degree of excitation of the atoms in the gas phase depends only on processes in the solid and on its surface.[2] Therefore, the maximum on the spatial intensity distribution in this region of the discharge is not determined by plasma processes. The spatial intensity distribution shown in Fig. 1 was observed for Cu* and Ba^+ during the sputtering of Y–Ba–Cu–O, for Ba^+ and Sr* in the case of (Ba,Sr)TiO_3, and for Zr^+ in the case of Pb(Zr,Ti)O_3, as well as for atomic oxygen in the case of all three oxides. Oxygen knocked out of a target can be distinguished from oxygen in the working gas on the basis of the emission spectra in just this zone of the discharge, where the excitation of lines is not determined by the discharge. Here we observed only lines corresponding to excited oxygen with an excitation potential no greater than 12.7 eV. No spectral lines with a large excitation potential, including lines of ionized oxygen, were observed in this zone. They were present in the second and third zones of the discharge, where the excitation mechanisms are already determined by plasma processes. In addition, the maxima of lines with a large excitation potential were located close to the cathode surface, indicating predominance of the electron-impact excitation mechanism.[5] The lines of Pb atoms observed during the sputtering of Pb(Zr,Ti)O_3 and the lines of Ba atoms for (Ba,Sr)TiO_3 and Y–Ba–Cu–O were extremely weak in this zone, and their intensity began to increase only beyond it. Thus, the emission spectrum in this zone of the discharge allows us to draw qualitative conclusions regarding the composition and degree of excitation of the sputtered particles.

The second fluorescence zone of the emission spectrum is created both by plasma-chemical reactions accompanying the transfer of sputtered particles through the oxygen plasma and by the excitation of atoms under the effect of direct electron impact by beam electrons accelerated in the stationary cathode field. The latter mechanism is corroborated by the fact that the higher is the excitation potential of a line, the closer are the intensity maxima of the excited atoms and ions in the second zone of the discharge to the target surface.[6]

The third zone of the discharge is characterized by a significant influence of the substrate position on the intensity of the emission lines of the sputtered atoms in the rf discharge. A characteristic feature of this influence is the vanishing of the intensity of the emission lines at the site of the substrate regardless of its position in the discharge. The oxygen lines did not exhibit a similar dependence. When the sputtering was carried out in argon, the vanishing of the emission lines of the metals was likewise not observed. To reveal the special point separating the second zone from the third, we performed a series of measurements of the spatial intensity distribution for several substrate positions relative to the target. The variation of the spatial intensity distribution for lead and ionized oxygen atoms upon variation of the target-substrate distance is shown in Fig. 2. We provisionally took the point of inflection on the plot of the spatial intensity distribution as the boundary of the third zone. Beginning at just this point, a further decrease in the distance between the substrate and the target led to intensity changes in the second zone. It can be seen from Fig. 2 that displacement of the substrate has no effect on the spatial intensity distribution of oxygen.

When the oxygen pressure created in the chamber was less than the critical value (from the standpoint of synthesizing the mixed oxide), vanishing of the intensity was noted

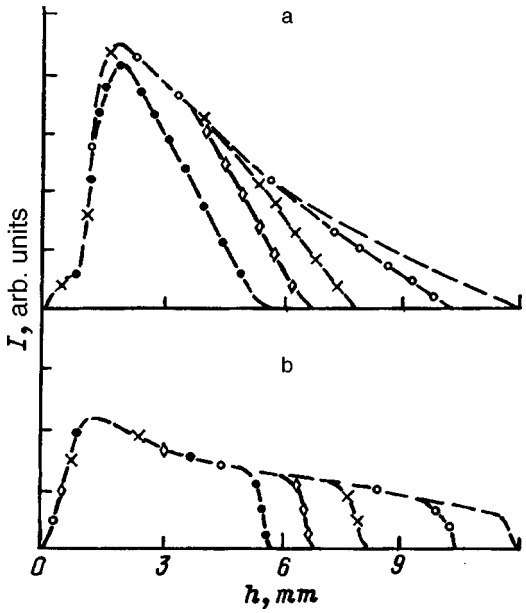

FIG. 2. Spatial distribution of the radiated intensity for lead atoms (a — $\lambda = 4057$ Å) and oxygen ions (b — $\lambda = 4415$ Å) with the substrate in various positions.

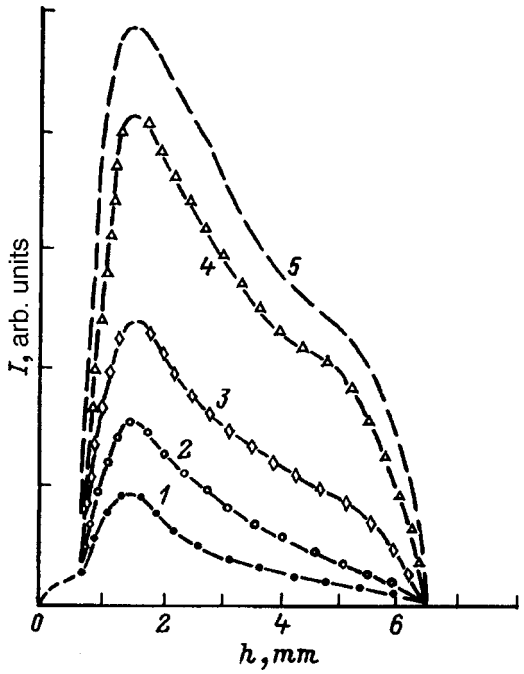

FIG. 3. Influence of the substrate temperature on the spatial distribution of the radiated intensity for lead ($\lambda = 4057$ Å, $P_{O_2} = 1.8$ Torr, $h = 6.5$ mm). T_l, °C: *1* — 570, *2* — 580, *3* — 590, *4* — 620, *5* — 640.

for only certain components. For example, the critical pressure for synthesizing $Pb(Zr_{0.53}Ti_{0.47})O_3$ was 1.8 Torr, whereas the lead component began to vanish at a pressure of 0.3 Torr for all the excited states. When Y–Ba–Cu–O was sputtered at the critical pressure of 0.7 Torr, vanishing of the lines for copper atoms was observed at 0.5 Torr.

The last general law governing the spatial intensity distribution for different oxides is the absence of lines for certain components in the emission spectra. In particular, when $(Ba,Sr)TiO_3$ and $Pb(Zr,Ti)O_3$ were sputtered there were no titanium lines in all three zones, and for Y–Ba–Cu–O there were no yttrium lines.

Moving on to a discussion of the features of the growth of each of the mixed oxides, we should stress the following. In choosing the oxides to be investigated, we included the $(Ba,Sr)TiO_3$ system because there are no highly volatile metallic components in this system. Therefore, the synthesis of this oxide in the form of films could be carried out over very broad ranges of variation of the external parameters. In particular, the structural perfection could be controlled only by varying the substrate temperature (T_l). Increasing it from 400 to 750 °C altered the orientation of the film relative to the substrate along the following sequence: polycrystalline ($T_l \geqslant 400$ °C), textured (110) film on a (100) substrate ($T_l \geqslant 480$ °C), textured (111) film on a (100) substrate ($T_l \geqslant 530$ °C), textured (100) film on a (100) substrate ($T_l \geqslant 570$ °C), heteroepitaxial film ($T_l \geqslant 630$ °C). The spatial variation of the intensity of the Ba and Sr emission lines remained the same over the entire range of variation of the substrate temperature just cited.

The other two oxides have significantly smaller ranges for variation of the substrate temperature in which their synthesis takes place. This is because they contain highly volatile metallic components of lead or copper. Figure 3 shows the influence of the substrate temperature on the character of the spatial intensity distribution of lead atoms in the case of the sputtering of $Pb(Zr,Ti)O_3$, and Fig. 4 shows the same influence for copper atoms when Y–Ba–Cu–O is deposited. In this case variation of the temperature from 580 to 650 °C did not result in violation of the stoichiometry of the components or in destruction of the conditions for heteroepitaxial

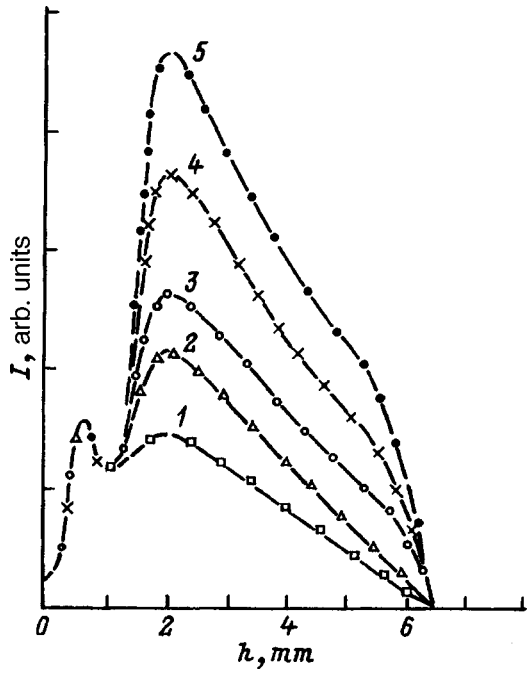

FIG. 4. Influence of the substrate temperature on the spatial distribution of the radiated intensity for copper ($\lambda = 3273$ Å) during the sputtering of Y–Ba–Cu–O ($P_{O_2} = 0.8$ Torr, $h = 6.5$ mm). T_l, °C: *1* — 550, *2* — 580, *3* — 600, *4* — 640, *5* — 660.

film growth. The synthesis of other phases with violation of the stoichiometry took place outside the temperature range just indicated. It is noteworthy that the mixed oxides of various composition and structure that we investigated are synthesized at approximately identical temperatures.

As can be seen from the curves shown above (Figs. 3 and 4), raising the substrate temperature from 570 to 580 °C led to an increase in the intensity of the spectral lines for Pb and Cu in the second and third zones by more than two fold and was accompanied by qualitative changes in the spatial intensity distribution. These changes occurred at a constant concentration of the atoms entering the discharge as a result of sputtering of the target, which was achieved by maintaining a constant intensity in the first zone. Raising the substrate temperature to 700 °C in the case of the deposition of $Pb(Zr,Ti)O_3$ or Y–Ba–Cu–O led to changes in the intensity of the Pb and Cu emission lines in the first zone and destruction of the conditions for synthesis and, of course, heteroepitaxy. Subsequent lowering of the temperature to 580 − 650 °C did not return the sputtering system to a state which ensures the conditions for synthesis despite activation of the target for many hours. Such behavior of the sputtering system attests to its indefiniteness relative to the direction of variation of the external parameters. We note that the substrate temperature is a function of two external parameters (the current in the heating element and the input rf power) and several internal parameters, such as the latent heat of crystallization of the oxide, the degree of excitation of the particles in the plasma, etc.

DISCUSSION AND CONCLUSIONS

The conventional approach to optimizing the deposition conditions of mixed oxides is to establish the relationship between the external parameters (pressure of the working gas, substrate temperature, input power, target-substrate distance, etc.) and the film properties. It is assumed that a multidimensional space of external parameters can be uniquely mapped into the space of parameters characterizing the film properties. However, when mixed oxides are sputtered, some experimental findings indicate that this is not entirely so. For example, when Y–Ba–Cu–O films were deposited, hysteretic phenomena of various kinds were observed by Katayama *et al.*[7] These investigators reported that the properties of the films depend on the sputtering history of the target, i.e., on the conditions under which it was previously sputtered. We observed a similar phenomenon when we discovered an irreversible influence of the substrate temperature on the heteroepitaxial growth of the oxides.

The modification of the target surface in response to alteration of the discharge parameters takes place over the course of several hours. The duration of the nonstationary state is probably determined by several factors: first, by the reorganization of the structure and composition of the target surface under the effects of ion bombardment, second, by the formation of metastable chemical compounds on its surface due to the condensation of particles reflected from the plasma and the substrate, and, third, by the indefiniteness of the sequence of chemical reactions taking place in the rf plasma when sputtered particles are transported through it. All this, in turn, leads to an indefinite dependence of the film properties on the external parameters.

In our opinion, the deposition of mixed oxides with a predominance of plasma-chemical processes in the growth mechanism must be approached as a complicated self-organized system. In fact, our investigation of the spatial intensity distribution revealed that a system for rf film deposition at elevated oxygen pressures can be regarded as a system having a spatial structure. The kinetic parameters (rates of the chemical reactions, initial concentrations of the particles participating in the reactions, and collision probabilities) in such a system should also depend on the spatial coordinate. In our opinion, an adequate description of such a system is possible, if we go over to internal parameters that reflect its spatial structuring. The proposed approach enables us to avoid the indefiniteness arising in the description of the film growth process in the space of external parameters. The internal parameters should be chosen such that the methods used to measure them will cause minimal disturbance of the deposition process and the parameters themselves will be informative with respect to the elementary processes accompanying the sputtering and the transport of particles from the target to the substrate. Our investigation of the fluorescent emission spectra demonstrated the possibility of correctly comparing the growth mechanisms for films differing in composition and crystal structure and revealed the general laws governing the synthesis of a mixed oxide. On this basis, the spatial distribution of the radiated intensity that we employed can be regarded as an informative internal parameter. The search for such parameters must, of course, be continued.

The sputtering of a mixed oxide under the action of oxygen ions and atoms (the latter acquire energy as a result of charge transfer in the cathode region) apparently takes place in two stages. First, the oxygen skeleton of the mixed oxide is destroyed. For just this reason, the degree of oxygen excitation has a threshold energy no greater than 12–13 eV. Destruction of the oxygen skeleton results in the passage of metallic components of various degrees of excitation, as well as, probably, their compounds with oxygen into the plasma, which comprises the second stages of the sputtering of the mixed oxide. Some of these components, such as yttrium or titanium, pass into the rf discharge plasma in the form of polyatomic compounds. Therefore, the plasma does not produce emission lines corresponding to these atoms and ions. These compounds cannot decompose in the negative glow under the action of the electron beam. The energy imparted upon electron bombardment is redistributed among their vibrational and rotational degrees of freedom, rendering them stable. Later on, just these compounds probably act as centers for cluster formation. As they move toward the substrate, the remaining metallic compounds are added to them in the second and third zones of the discharge. The external parameters assign only the conditions for the formation and evolution of specific types of clusters. The synthesis of an oxide with an assigned structure on a substrate probably corresponds to a definite type of cluster in the discharge.

When the substrate temperature is increased, additional

reflection of the highly volatile component in the compound from the surface takes place. It is manifested by an increase in the intensity of the corresponding line in the emission spectrum in the second and third zones, as can be seen from Figs. 3 and 4. In the case of $PbTiO_3$ it is the line for lead, and in the case of Y–Ba–Cu–O it is the line for copper. A further rise in temperature increases the concentration of such components in the third zone, which now surpasses the concentration needed for cluster growth. The excess concentration of the highly volatile component now enters the first zone and alters the composition of the target surface, and the self-matching of the target and substrate surfaces is destroyed. This results in a loss of the reversibility of the sputtering system toward the effect of an external parameter.

[1] V. M. Mukhortov, G. N. Tolmachev, and A. I. Mashchenko, Zh. Tekh. Fiz. **63**(11), 135 (1993) [Tech. Phys. **38**, 1001 (1993)].
[2] V. M. Mukhortov, G. N. Tolmachev, A. I. Mashchenko *et al.*, Zh. Tekh. Fiz. **62**(5), 22 (1992) [Sov. Phys. Tech. Phys. **37**, 495 (1992)].
[3] V. M. Mukhortov, Yu. I. Golovko, V. A. Aleshin *et al.*, Phys. Status Solidi A **78**, 253 (1983).
[4] O. V. Kozlov, *Electric Probe in a Plasma* [in Russian], Atomizdat, Moscow (1969), 291 pp.
[5] V. Ya. Khasilev, V. S. Mikhalevskiĭ, and G. N. Tolmachev, Fiz. Plazmy **6**, 430 (1980) [Sov. J. Plasma Phys. **6**, 236 (1980)].
[6] E. W. McDaniel, *Collision Phenomena in Ionized Gases* [Wiley, New York, 1964; Mir, Moscow, 1967, 162 pp.].
[7] T. Katayama, N. Koshizuka, T. Kitaguchi *et al.*, IEEE Transl. J. Magn. Jpn. **4**, 244 (1989).

Translated by P. Shelnitz

Optimization of a pinhole camera for neutron diffraction of a thermonuclear laser plasma

V. S. Kinchakov

Computing Center, Russian Academy of Sciences, Far-Eastern Branch, 680063 Khabarovsk, Russia
(Submitted April 2, 1997)
Zh. Tekh. Fiz. **68**, 104–109 (September 1998)

The nonstationary transport equation of DD and DT neutrons in a polyethylene wall with a cylindrical opening is solved by the Monte Carlo method. It is shown that the proposed pinhole camera lowers the requirements for brightness of a neutron source by two orders of magnitude in comparison to the existing analogs. Analytical estimates of the resolving power of the pinhole camera are given, and ways to improve it are analyzed. The region of permissible values of the parameters of the pinhole camera is constructed. Contour lines of the images of neutron point sources as functions of their number and position in the thermonuclear target are calculated. © *1998 American Institute of Physics.*
[S1063-7842(98)02109-6]

INTRODUCTION

The purpose of the present work was to investigate the characteristics of the image created by DD and DT neutrons originating from pulsed point sources and scattered by a polyethylene wall with a cylindrical opening. The criterion for selecting the wall material had previously been the value of the neutron absorption cross section. On the basis of this criterion a copper pinhole camera with a wall having a thickness of the order of 1 m was fabricated in the U.S.A.[1] However, if materials with a large elastic neutron scattering cross section, such as polyethylene, are used to fabricate a pinhole camera, the use of a time-resolved neutron detection system for the purpose of reducing the background as a result of effective slowing of the neutrons appears promising, especially in the case of scattering by nuclei of light elements. The calculations performed in the present work show that reduction of the background to reasonable values is achieved with a wall thickness of the order of 0.1 m. This permits an increase in the image brightness by two orders of magnitude in comparison with the existing analogs[2] and diminishes the difficulties in making a hole of small diameter.

Such a pinhole camera would be irreplaceable in the investigation of weak neutron sources, which cannot be ''photographed'' by ordinary pinhole cameras. Situations of this kind can arise, for example, when there is insufficient heating of the thermonuclear plasma.

NUMERICAL SIMULATION

The nonstationary integral transport equation of neutrons in a wall has been solved by the Monte Carlo method.[1–3] The program developed did not employ the traditional approximations for obtaining constants, viz., the ''multigroup'' and ''narrow-resonance'' approximations;[4] therefore, the cross sections were assigned in exact correspondence with the laws of variation with respect to the energy. Multiple scattering was taken into account. Neutron scattering by carbon and hydrogen was considered separately in Ref. 4. The total elastic scattering cross sections were taken from the ENDF/B data bank.[5] The anisotropy of the differential cross sections[6] for elastic neutron scattering by carbon was taken into account using an expansion in Legendre polynomials. In the range 0.1−3.0 MeV the cross sections were assigned by 30 points with 0.1-MeV spacing. The peak for scattering by carbon in the vicinity of 21 MeV was described separately by 20 points with 0.01-MeV spacing. The inelastic channels for the excitation of carbon nuclei by DT neutrons were taken into account using the same data bank.[5]

The neutron detection field had the form of a square divided into 1089 square cells with a side equal to $0.005 \cdot U$ cm, where U is the magnification of the image. Because of the small size of each detecting cell, the detection of neutrons in each cell was a fairly rare event. Therefore, a modification of the (direct) Monte Carlo method with statistical weights was employed to calculate the background of scattered neutrons. The probability of neutrons entering the detector was calculated at the point of each collision. These probabilities were summed over all the collisions.

The results[7] of the calculations of the background of scattered neutrons discussed were normalized to 10^{10} neu-

TABLE I. Variant with $R=13$ cm and $U=10$.

	L, cm		
T (ns)	10	7	3.5
4	1.24	1.91	2.77
8	3.14	5.04	6.09
12	4.74	7.41	9.99
16	5.99	9.32	12.84
20	7.04	11.16	15.16
24	8.06	12.90	17.33
32	9.71	15.84	21.15
40	11.00	18.11	24.04
48	12.11	19.91	26.34
60	13.40	22.07	28.98
80	14.80	24.54	32.30
100	15.61	26.17	34.42
120	16.04	27.01	35.77

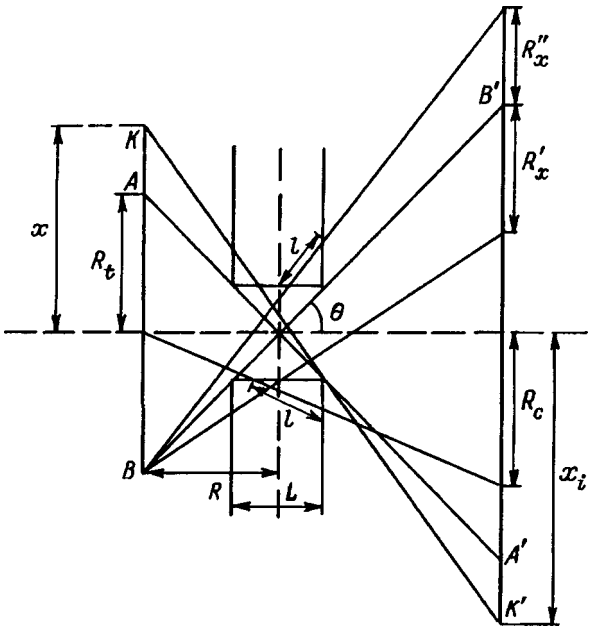

FIG. 1. Geometry of the simulated experiment.

trons per burst. The relative rms deviation of the calculations is 3%. The temperature of the DD plasma in all the calculation below was set equal to 0.002 MeV, which corresponded to broadening of the line for 0.116-MeV DD neutrons. The monochromatic approximation was adopted for DT neutrons. The results for DD neutrons are discussed below, and the case for DT neutrons will be addressed separately.

Table I presents the results of the calculation of the background of scattered neutrons as a function of the detection temperature T, the thickness L of the polyethylene wall, the magnification U of the image, and the distance R from the plasma to the midplane of the wall. The decrease in the absolute number of neutrons detected with increasing wall thickness is attributed to the multiple scattering of neutrons, as a result of which some of them pass into the rear hemisphere.

Calculations of the images of neutron point sources according to the direct scheme of the Monte Carlo method correspond to a 10% relative rms deviation in the region of the peak and do not take into account the background of scattered neutrons, which must be added to all the channels for a specific detection time. The results were normalized to 10^{10} neutrons per burst for each neutron source. Figure 1 illustrates the input data for the calculations. The diameter AB of the thermonuclear target was chosen equal to 0.05 cm. The magnification U of the image $A'B'$ was set equal to 10 in all the calculations. As follows from Fig. 1, the radius r of the hole depends linearly on the wall thickness

$$r = L \cdot R_t/(R \cdot 2). \tag{1}$$

Here R_t is the radius of the thermonuclear target. Figure 2 shows a calculation of the images of two neutron point sources located at the center and on the periphery of a thermonuclear target for a camera variant with $L=7$ cm and $R=13$ cm. Note the good resolution of the two sources and the fairly exact identification of the position of the sources. The decrease in the dimensions of the peripheral source in comparison to the central source is a consequence of the poorer observation conditions for the source on the periphery of the target. Figure 3 presents a calculation of the images of three neutron point sources located on a single line at the center of the target, on its periphery, and midway between the central and peripheral sources. For high-quality resolution of the neutron sources, the distance R from the midplane of the wall to the plasma was increased to 30 cm. The thickness L of the wall in this calculation was equal to 10 cm. The decrease in the number of neutrons in the peaks is due to the increased distance between the neutron sources and the detectors. The calculations show that the background of unscattered neutrons from one source amounts to about 35% of the amplitude of the image for a wall thickness $L=3.5$ cm, about 15% for $L=7$, and about 5% for $L=10$ cm. Thus, effective suppression of the background is achieved for a wall of thickness of 7–10 cm and a neutron detection time of 10–40 ns (Table I).

For a deuterium-tritium plasma it must be taken into account that the total interaction cross section of a neutron with hydrogen is about four times smaller than in the case of DD neutrons; therefore, the minimal wall thickness must be increased by about two and a half fold to suppress the background. This leads to a need to move the wall away from the

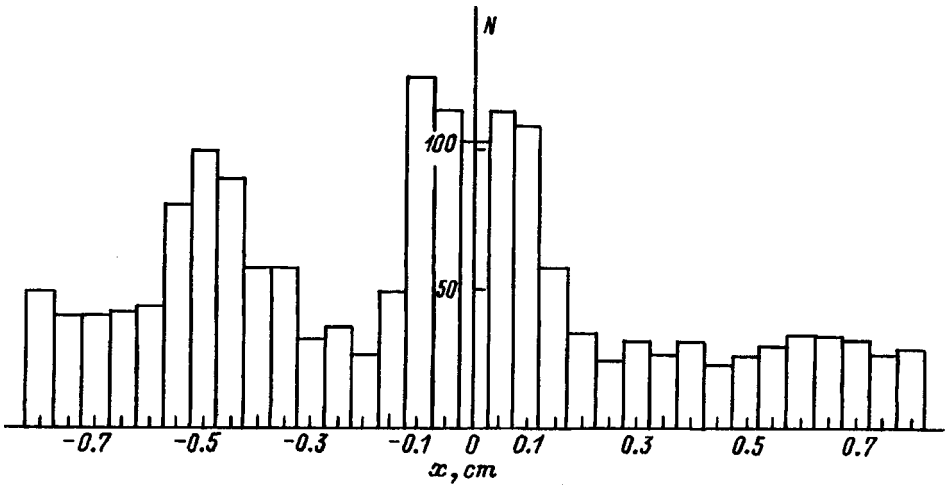

FIG. 2. Image profile along the x axis. Calculation of the case of two point sources located on the x axis at the center and on the periphery of a thermonuclear target.

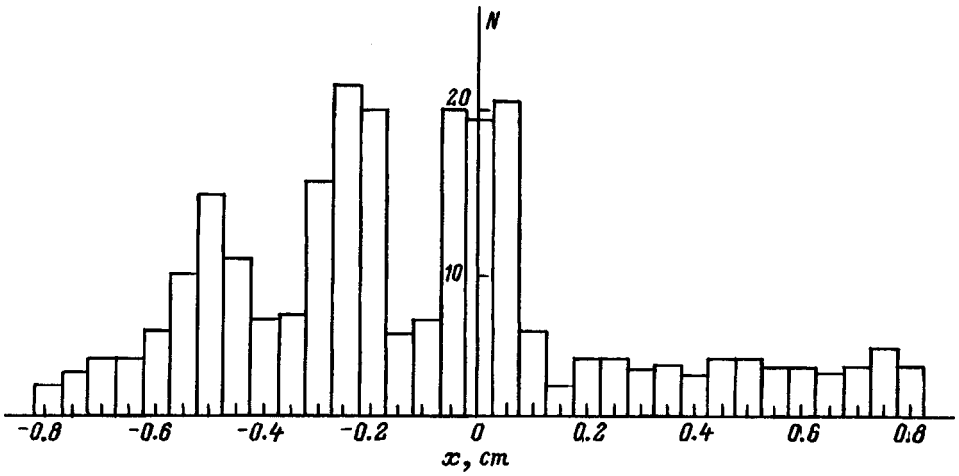

FIG. 3. Image profile along the x axis. Calculation of the case of three point sources located on the x axis at the center of a thermonuclear target, on its periphery, and midway between the first two sources.

source in order to improve the resolution and thus to stricter requirements on the brightness of the neutron source. Figure 4 presents the results of a calculation of the image of a point source of DT neutrons located at the target center and the values of the background of scattered neutrons as a function of detection time. It is seen that the cumulative background is significantly smaller than the image level even for large detection times (400 ns).

ANALYTICAL ESTIMATES OF THE RESOLUTION OF A NEUTRON PINHOLE CAMERA

The estimates presented below were obtained under the approximation (which nearly always holds)

$$\tan\theta = R_t/R \ll 1. \tag{2}$$

In addition, the background of scattered neutrons can be reduced to a minimum by selecting the detection time, and, therefore, it is not taken into account in the estimates made below.

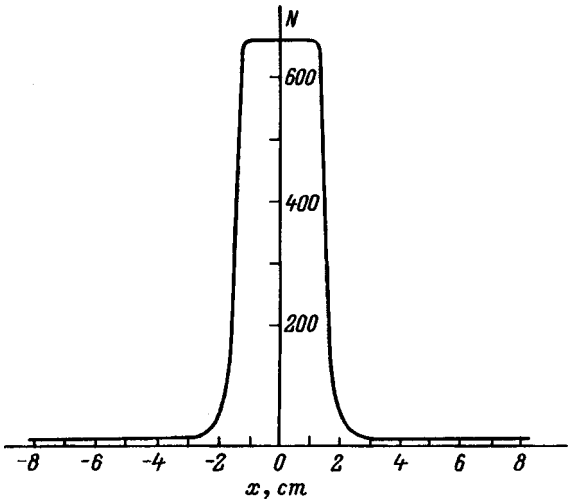

FIG. 4. Image profile along the x axis. The source of DT neutrons is located at the center of a thermonuclear target of radius $R_t = 0.5$ cm. $R = 50$ cm, $L = 30$ cm, and $U = 100$. The background of scattered neutrons for detection times of 100, 200, 300, and 400 ns equals 95.9, 112.4, 118.6, and 121.5 neutrons.

We note that the problem has cylindrical symmetry, and we specify the radius of the neutron image of a point by the condition

$$N(R_i = R_c)/N(R_i = 0) = \exp(-l/\lambda) = P_1. \tag{3}$$

Here N is the number of neutrons detected, R_i is the distance measured from the center of the image, R_c is the radius of the image of the central point, l is the path of the neutrons in the wall material, and λ is the mean free path. The choice of $P_1 = 1/3$ ensures reliable resolution of two point sources: at the point of contact between the radii of the images of two point sources the drop in the total intensity relative to the maximum intensity amounts to 40%. For the radius of the image of the central point, from condition (3) we obtain

$$R_c = r \cdot (U+1) \cdot R/R_p, \tag{4}$$

$$R_p = R + L/2 + \lambda \ln P_1. \tag{5}$$

The image of the point is the area enclosed by a circle of radius R_c. The familiar result for an optical pinhole camera follows from (4) in the approximation of an absolutely opaque wall ($\lambda = 0$).

For a point on the periphery of a target, the treatment of Eq. (3) leads to the following results: the neutron radius of the image in the direction toward the center of the plane of the image is (Fig. 1)

$$R_x' = -\lambda \ln P_1 (U+1) R_t/R_m, \tag{6}$$

$$R_m = R - L/2 - \lambda \ln P_1; \tag{7}$$

the neutron radius of the image in the direction away from the center of the plane of the image is (Fig. 1)

$$R_x'' = -\lambda \ln P_1 (U+1) R_t/R_p. \tag{8}$$

We stress that in this case the position of the neutron source on the target must be determined not from the center of the image, but with allowance for the inequality of the radii R_x' and R_x'' of the image. In the optical limit $\lambda = 0$ and $R_x' = R_x'' = 0$: the point is mapped to a point.

The resolution of the images of two point sources is given by the trivial relation

$$R_s = D/U, \tag{9}$$

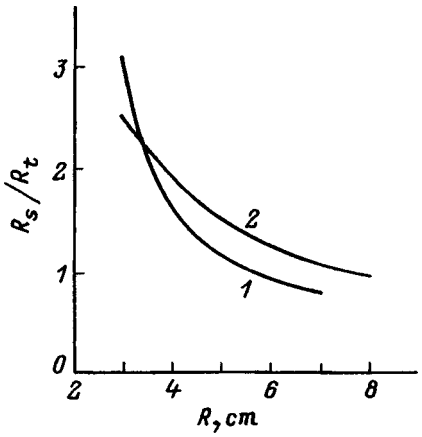

FIG. 5. Dependence of the resolving power on the distance R. L, cm: *1* — 3.5, *2* — 7.0.

where D is the sum of the radii of the images in the direction of their point of nearest approach.

It follows from Eqs. (4)–(9) that increasing the distance R from the target to the camera reduces the dimensions of the images of points and thereby improves the resolution.

In the approximation of a large magnification $U \gg 1$, for the resolution R_s of two neutron point sources we have

$$R_s/R_t = L/(2R_p) - \lambda \ln P_1/R_m. \tag{10}$$

As can be seen from Fig. 5, for a camera with a wall thickness $L=7$ cm we have $R_s \leqslant R_t$, if $R \leqslant 7$ cm. We stress that the maximum number of point sources that can be resolved by a pinhole camera in the borderline case of $R_s = R_t$ equals three, and this number can be achieved only if they are on a single straight line parallel to the plane of the camera wall. In addition, one source must be located at the center, and the other two must be located on opposite edges of the target.

Table II presents the radii of the optical and neutron images of point sources located at the center and on the periphery of a target for two camera variants, the radii of the neutron images being determined at half maximum ($P_1 = 1/2$). The table also lists the resolution of these neutron sources. It follows from Table II that the radii of the optical and neutron images differ strongly from one another for the pinhole camera with a small wall thickness L and a small distance R from the target to the midplane of the wall. The radii of the neutron images of the central and peripheral point images differ just as strongly, and $R'_x < R_c$.

As for achieving good resolution of sources in the radial direction, we should turn to pinhole cameras for which the image of a point source on the periphery of a target is flattened in this direction in comparison to the image of the central point: $R'_x/R_c \leqslant 1$. Requiring that $R > L/2 + \lambda \ln P_1$ (this condition practically always holds), we can satisfy the condition $R'_x/R_c \leqslant 1$ in two variants: 1) $R > L/2 - \lambda \ln P_1$ and $L/2 > -\lambda \ln P_1$; 2) $R < L/2 - \lambda \ln P_1$ and $L/2 < -\lambda \ln P_1$.

TABLE II. Optical and neutron radii of the images of point sources calculated from formulas (4)–(8).

L	R	R_{opt}	R_c	R'_x	R''_x	R_s
7	7	1.71	2.22	2.11	1.60	0.044
3.6	2.0	2.44	7.15	4.68	10.05	0.118

Note: The last column lists the resolution (9) of the central and peripheral neutron point sources. Calculation parameters: $U=100$, $R_t=0.05$ cm. All the values are in centimeters.

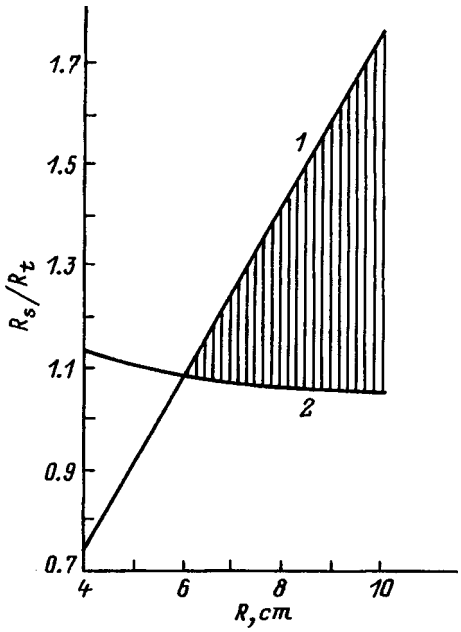

FIG. 6. Maximum (x_{max}) and minimum (x_{min}) possible distances between a neutron point source and the target center as a function of the distance R. The neutron source is located in the optically unobservable region. The hatched area covers the parameters of a pinhole camera that resolves at least a source at the center and a source on the periphery of a target provided they are located on a straight line parallel to the plane of the camera wall. $L=7$ cm; *1* — $x_{max}/(2\cdot r)$, *2* — $x_{min}/(2\cdot r)$.

An improvement in the resolving power of the pinhole camera can be also be achieved by some ''displacement'' of the neutron source into the optically unobservable region (Fig. 1). This is possible, since for some directions of motion of neutrons in the region of the hole the range in the wall material is minimal, and neutrons moving in these directions scarcely interact with the wall material. In this case the maximum possible distance x_{max} between the neutron source and the target center is determined by the maximum possible relative decrease P_2 in the brightness of the image due to neutron scattering in the wall:

$$x_{max}/r = (2R+L)/(L+\lambda \ln P_2) - 1. \tag{11}$$

The minimum distance x_{min} between the neutron source and the target center is determined by the requirement for resolution between a central source and a source located in the optically unobservable region:

$$x_{min}/r = 2R^2(U+1)/(R_p \cdot R_u), \tag{12}$$

$$R_u = UR + L/2 + \lambda \ln P_1. \tag{13}$$

In addition, the following condition must be satisfied to distinctly observe these two sources:

$$x_{max} \geqslant x_{min}. \tag{14}$$

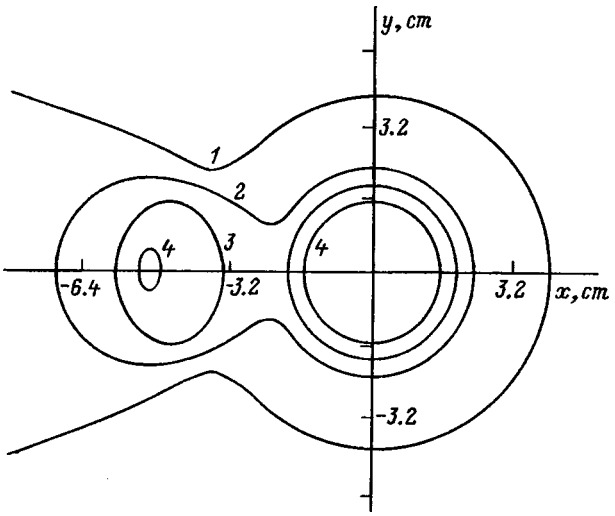

FIG. 7. Contour lines of the images of two neutron point sources. $U=100$. Normalization to 10^{10} per burst for the two neutron sources. *1* — 75.39, *2* — 177.27, *3* — 279.15, *4* — 381.03.

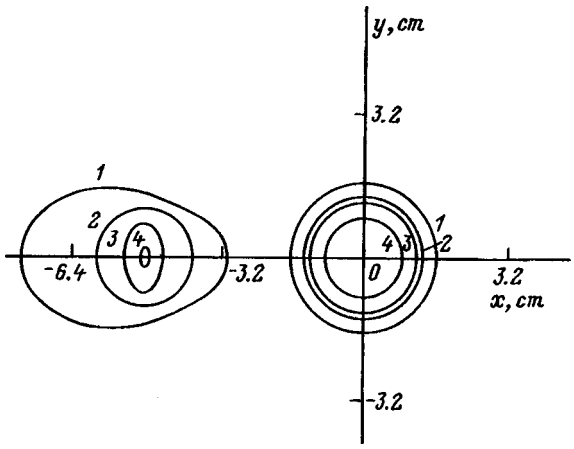

FIG. 8. Same as in Fig. 7 except that $R=14$ cm.

The condition (14) is essentially a criterion, which determines the region of permissible values of the parameters of the pinhole camera. In Fig. 6 the region of permissible values of the parameters of the pinhole camera, in which the condition (14) is satisfied, is hatched.

It can be seen from Fig. 1 that the center of the image of a neutron point source located in the optically unobservable region is specified by the straight line KK', since the range of neutrons in the wall material is greater for any other direction of motion. The distance x_i to the center of the image equals

$$x_i = x(UR + L/2)/(R - L/2). \tag{15}$$

Here x is the distance from the target center to the point source. For the radius of the image of the neutron point source we have

$$R_x = x_i - r - (x - r)R_u/R_m. \tag{16}$$

As a final step, we present the results of a calculation of the contour lines of two neutron point sources, which are located at the center and on the periphery of the target: $L=7$ cm, $R=7$ (Fig. 7), 14 cm (Fig. 8). Figures 7 and 8 reveal a decrease in the dimensions of the image as the distance between the sources and the camera wall is increased. The shape of the contour lines of the image of the central neutron source is circular, while the shape of the contour lines of the image of the peripheral source approaches an ellipse as the distance between the source and the pinhole camera is increased. It can be seen that two neutron point sources are resolved in this case provided $R \geqslant 7$ cm.

CONCLUSIONS

We have shown that the polyethylene pinhole camera with time-resolved neutron detection proposed in this paper raises the image brightness by two orders of magnitude in comparison with the existing analogs. This makes it possible to locate weaker neutron sources. Analytical estimates of the resolving power of such a camera have been made. A criterion which specifies the region of permissible values of the parameters of the neutron pinhole camera has been formulated. A modification of the direct Monte Carlo method with statistical weights significantly shortens the calculation time needed to achieve an assigned statistical accuracy.

We thank O. I. Stukov and Yu. A. Mikhaĭlov for some helpful discussions and for stimulating this work.

[1] V. A. Naumov and S. G. Rozin, *Solution of Problems in Reactor Physics by the Monte Carlo Method* [in Russian], Nauka i Tekhnika, Minsk (1978), 205 pp.
[2] G. I. Marchuk *et al.*, *The Monte Carlo Methods in Atmospheric Optics* (Springer-Verlag, Berlin–New York, 1980).
[3] G. E. Forsythe, M. Malcolm, and C. B. Moler, *Computer Methods for Mathematical Computations* [Prentice-Hall, Englewood Cliffs, NJ, 1977; Mir, Moscow, 1980, 171 pp.].
[4] L. P. Abagyan, N. O. Bazanyants, I. I. Bondarenko, and M. N. Nikolaev, *Group Constants for Designing Nuclear Reactors* [in Russian], Atomizdat, Moscow (1964), 153 pp.
[5] ENDF/B, Cross Section Evaluation Center, Brookhaven, Report BNL 50066 (1967), 467 pp.
[6] *Atlas of Effective Neutron Cross Sections of Elements* [in Russian], Atomizdat, Moscow (1955), 359 pp.
[7] V. D. Epaneshnikov, V. S. Kinchakov, Yu. A. Mikhaĭlov *et al.*, ''Passage of thermonuclear neutrons through a wall,'' [in Russian], Preprint No. 348, P. N. Lebedev Physics Institute, Academy of Sciences of the USSR, Moscow (1986), 24 pp.

Translated by P. Shelnitz

Surface damage as a result of cavitation erosion

S. N. Buravova

Institute of Structural Macrokinetics, Russian Academy of Sciences, 142432 Chernogolovka, Moscow Region, Russia
(Submitted April 16, 1997)
Zh. Tekh. Fiz. **68**, 110–114 (September 1998)

Erosion is regarded as a result of the periodic loading of a surface with spherical waves generated at the sites of the collapse of cavitation bubbles. One feature of cavitation loading is the formation of a zone of intense failure at the center of the contact surface. Damage appears a consequence of the formation of longitudinal cleavage cracks under the contact zone, which comprise a system of small annular cracks coaxial to a deep channel crack. The damage zone (blister) occupies a small fraction of the crater surface (the contact zone with the shock wave). The depth of the longitudinal cracks is an order of magnitude smaller than the thickness of the hardened layer. The hardening and erosion processes occur simultaneously.
 [S1063-7842(98)02209-0]

The dynamic failure of a solid under the action of pulsed loads differs fundamentally from quasistatic failure. This is attributed to the fact that the characteristic dimension of a dynamic load is much smaller than the sample on which it acts. Therefore, the defects responsible for damage under quasistatic conditions are ineffective. Dynamic failure has a cleavage nature and is due to the interference of unloading waves accompanying a compression pulse. The geometric factor of the arrangement of the free surfaces and the sources of unloading waves is decisive here. The examination of the mechanism of erosion wear in Ref. 1–3, which took into account the high-speed character of pulsed deformation, enabled us to reveal two types of cleavage cracks. The incubation period is characterized by the appearance of longitudinal cracks under the zone where the load is applied. The focusing of the unloading waves emanating from the lateral faces of a particle generate a channel crack, which itself becomes a source of unloading waves that lead to the formation of coaxial annular cracks. The type of damage consisting of a system of coaxial annular cracks is called multiple longitudinal cleavage fracture. The material under the contact zone fragments, and a cavity forms on the surface of the solid. Longitudinal cleavage fractures provide the main mechanism shaping the relief of the surface. The amount of material removed is insignificant in this case, and the debris consists of small, mainly equiaxial fragments. The incubation period ends when the geometry of the cavity permits the impulse appearing when a particle strikes the bottom of the cavity to pass through the lateral wall. The emergence of such impulse on the front surface and its interaction with the reflected unloading wave create a transverse zone of high tensile stresses oriented at a small angle to the surface. The loss of material in the stationary period of erosion is due to transverse cracks and takes place from a zone adjoining the contact surface. The products of wear are large plate-like chips, which exceed the fragments removed from the contact zone in size.

The unloading waves accompanying a compression pulse are responsible for damage to the obstacle. As a shock wave passes through a material, it alters its microstructure with resultant hardening of the material. Both processes, viz., erosion and hardening, occur simultaneously. The material under the contact zone within the conical surface where the compression pulse propagates undergoes hardening. In regions outside this conical surface, including the portions of the surface directly adjacent to the contact zone, the material is not subjected to any disturbance (at least in the initial stage of impact). A similar phenomenon is observed when a gas flows in a supersonic diffuser, where there is a limiting flow expansion angle, beyond which there is no flow.

The cleavage mechanism of erosion is based on an analysis of the nature of the damage appearing under dynamic loads over a broad range of disturbance amplitudes, such as plate impact (where the velocity ~ 1 km/s),[4] detonation spraying (where the velocity of the particles is $0.2-0.5$ km/s),[5] and pulsed laser irradiation (which corresponds to an impact velocity of $0.05-0.15$ km/s),[6] and on an analysis of literature data.[7] The fact that the morphology of the damage in plastic materials under high- and low-speed loads (the latter are traditionally treated as quasistatic disturbances) is identical provides evidence that the general approach to low-speed loading from the standpoint of wave mechanics is more justified.[8] The theory of the cleavage mechanism of erosion developed in Refs. 1–3 applies to the simplest cases in which the materials of the impinging body and the obstacle are identical and the contact surface of the impinging body is flat.

Since the geometric factor is decisive in the cleavage mechanism, it would be interesting to study an erodent of spherical shape (more precisely, a two-dimensional erodent with a round cross section) in the case of cavitation loading.

The experimental study of the failure of a surface under the action of collapsing bubbles reveals a qualitative similarity to liquid-drop erosion.[7] In both processes significant structural changes occur in the early incubation period, and isolated craters appear on the surface. At the center of these craters there are deep blisters of irregular shape, from which longitudinal microcracks propagate inward.[9,10] Under ex-

treme loads, as, for example, on the blades of steam turbines, the depth of the channel cracks can be as large as several drop diameters.[11] Increasing the number of loading cycles leads to the appearance of large holes on the surface.[12] Material is removed as a result of failure of the edges of such pit formations,[7,10] and pores and voids are observed under the edges. It has been established experimentally that transverse cracks are the main cause of the loss of material in the stationary period of the erosion wear of a surface.[7,13]

Several erosion mechanisms have been proposed to account for cavitation failure.[7] The generally accepted opinion, which is based on the similarity between the liquid-drop and cavitation erosion processes and the discovery of blisters at the centers of craters, is that a surface fails under the action of the cumulative jets appearing when cavitation bubbles collapse. However, such jets can appear as a result of asymmetric bubble collapse, which takes place only for bubbles located on the surface of a sample. Another possible mechanism involves shock waves generated from a bubble collapse zone. However, the appearance of craters cannot be explained using shock waves. Finally, it has been postulated that large pit formations appear under the action of a collective shock wave in the case of intense cavitation loading. Such a shock wave forms as a result of the simultaneous collapse of a cluster of bubbles. It should be noted that none of the proposed mechanisms permitted an analysis of the stress field within the solid, which determines the trajectories of the transverse cracks responsible for the loss of material upon erosion.

In this paper cavitation damage is regarded as the result of the periodic loading of a surface by spherical waves emanating from the sites where cavitation bubbles collapse.[14] The pressure in such waves is estimated to fall in the range $50-1000$ MPa.[7]

The equation describing the propagation of an individual shock wave expanding with a velocity c_1 in a medium has the form $(x-1)^2+y^2=(1+\tau)^2$, where x and y are normalized to the radius of the sphere at the moment of impact with the surface (r_0) and $\tau=(c_1t)/r_0$ is the dimensionless time. It is assumed that in the initial stage of impact the pressure at the interface P_0 is close to the values characteristic of planar impact. Then the mass velocity behind the shock-wave front in the obstacle equals $u_0=P_0/(\rho_0c_0)$, where ρ_0 and c_0 are the density and the speed of sound in the obstacle material. The pressure on the contact surface boundary P drops as the spherical wavefront expands:

$$\frac{P}{P_0}=\frac{1}{(x-1)^2+y^2}.$$

It is assumed that the disturbance acting on the obstacle $(x=0)$ ceases when the radius of the spherical wave doubles $(y=\sqrt{3})$. The rate of displacement of the contact surface boundary

$$\frac{dy}{d\tau}=\frac{\tau+1}{\sqrt{\tau^2+2\tau}}$$

is a variable quantity and varies from an infinitely large value at the initial moment of impact to the speed of sound in the undisturbed fluid medium c_1. Therefore, the reflected shock wave in the fluid is always linked to the contact surface boundary. The shock wave follows the boundary in the obstacle as long as the velocity of the latter exceeds the velocity of sound in the metal c_0. At the time

$$\tau_0=\frac{k}{\sqrt{k^2-1}}-1,$$

the shock wave separates from the contact surface boundary $(k=c_0/c_1)$, causing the formation of a centered toroidal (for spherical symmetry) or cylindrical (for a two-dimensional impinging body) unloading wave with a center at $y_0=1/\sqrt{k^2-1}$.

The propagation velocity of the shock-wave front equals $D/c_0=1+0.5\sigma_0$, and the propagation velocity of the head characteristic of the centered unloading wave equals the speed of sound in the compressed material:

$$\frac{c}{c_0}=1+\frac{n-1}{n+1}\sigma_0.$$

Here

$$\sigma_0=\frac{n+1}{2}\frac{u_0}{c_0}$$

is a small parameter, and u_0 is the exponent in the power-law dependence of the pressure on density.

For most metals k is close to 4. The coordinate where the head characteristics encounter the shock-wave front x_0 characterizes the depth at which the compression pulse decays. The value of x_0 is determined from the expression

$$x_0=\frac{y_0}{\sqrt{\left(\frac{c}{c_0}\right)^2-\left(\frac{D}{c_0}\right)^2}}=\frac{y_0}{\sqrt{\frac{n-3}{n+1}\sigma_0\left(1+\frac{3n-1}{4(n+1)}\sigma_0\right)}}.$$

When the pressure P_0 exceeds the dynamic Hugoniot elastic limit P_H, hardening of the surface layer to a depth x_0 occurs during a single passage of the shock wave. When $P_0<P_H$, hardening occurs by means of strain accumulation in repeated loadings. If the elastoplastic hysteresis ζ of the material is known, the critical number of loading cycles N_0 needed to harden the material to a depth x_0 is given by the expression

$$N_0=\frac{1}{\zeta}\left(\frac{P_H}{P_0}-1\right).$$

Table I lists the characteristics of the damaged surface layer as a function of the cavitation pressure P_0. The calculation was carried out for the following parameters: $k=4$, $\rho_0/\rho_1=2.5$,

$$\sigma_H=\frac{n+1}{2}\frac{P_0}{\rho_0c_0}=0.03,$$

$$\sigma_*=\frac{n+1}{2}\frac{P_*}{\rho_0c_0}=0.06,\quad \zeta=0.001.$$

TABLE I. Characteristics of a surface layer damaged by cavitation loading.

P_0, MPa	844	703	562	422	281	158	141	70.5
V_0, m/s	750	625	500	375	250	140	125	62.5
σ_0	0.0375	0.0313	0.0250	0.0188	0.0125	0.0070	0.0063	0.0031
$N_0\times10^{-3}$	0.001	0.001	0.200	0.600	1.400	3.286	3.800	8.600
x_0	2.981	3.266	3.652	4.216	5.164	6.901	7.303	10.328
$\Psi_0=90°$	11.2	10.2	9.1	7.9	6.4	4.8	4.5	3.2
			$y_0=0.2582,\quad y_1=0.1947$					
$N_*\times10^{-3}$	54.771	72.313	101.458	156.744	289.794	690.526	818.665	2318.350
L_0	0.4365	0.4391	0.4415	0.4434	0.4452	0.4464	0.4465	0.4466
L_1	0.1074	0.1081	0.1087	0.1091	0.1096	0.1098	0.1099	0.1101
			$y_2'=0.1349,\quad y_3'=0.0855, y\quad''_3=0.1842,\quad y_4'=0.0501$					
$N_{**}\times10^{-3}$	5.401	6.682	8.600	11.800	18.200	33.285	37.440	75.800
L_2'	0.0926	0.0945	0.0963	0.0981	0.0999	0.1015	0.1018	0.1026
L_3'	0.0765	0.0780	0.0795	0.0810	0.0825	0.0838	0.0840	0.0845
L_3''	0.0162	0.0165	0.0168	0.0172	0.0175	0.0178	0.0179	0.0180
L_4'	0.0548	0.0559	0.0570	0.0581	0.0592	0.0601	0.0602	0.0606

For comparison, the table also lists the values of the velocity V_0 of a liquid drop which creates the same pressure in the obstacle upon impact as does a cavitation shock wave. It can be seen from the table that the thickness of the hardened layer rises as the pressure drops. This dependence is attributed to the decrease in the difference between the propagation velocity of the shock-wave front and the speed of sound in the compressed material. At low pressures the unloading overtakes the shock-wave front after a longer time. However, a low pressure requires multiple repetition of the loading cycles before structural changes will occur in the material. Table I lists the values of the expansion angle Ψ_0 of the conical surface within which the compression pulse propagates[1–3] $\tan\Psi_0=(1-0.5\sigma_0)/\sqrt{\sigma_0}$. For media with a high dynamic stiffness, such as metals, the angle Ψ_0 is close to $\pi/2$, but as P_0 rises, the divergence of the flow behind the shock-wave front increases.

The damage to the hardened surface layer is caused by the interference of the counterpropagating centered unloading waves. Focusing the unloading waves creates a channel-like zone of tensile stresses on the symmetry axis ($y=0$). For unloading waves originating in free space the intensity of the tensile stresses is determined by the divergence of the flow behind the shock-wave front. The angle of deflection of the portion of the shock-wave front disturbed by unloading from the initial orientation $\alpha=\sqrt{\sigma_0}-\sqrt{\sigma}$ is a small quantity.

The expansion velocity in the interference zone v_0 equals

$$\frac{v_0}{c_0}=\frac{u}{c_0}\alpha=\frac{2}{n+1}\sigma_0^{3/2}(1-\sqrt{m})m.$$

Here $m=\sigma/\sigma_0$. This expression for $v_0(m)$ has an extremum at $m=4/9$. For an undisturbed flow $\sigma=\sigma_0$, $\alpha=0$, and $v_0=0$; on the tail characteristic of an unloading wave $\sigma=0$, but $\alpha=\sqrt{\sigma_0}$; therefore, $v_0=0$. The maximum value of the expansion velocity

$$\frac{v_0}{c_0}=\frac{8}{27}\frac{\sigma_0^{3/2}}{n+1},$$

is probably somewhat overestimated, since the ''support'' from the compression waves appearing on the interface at $y>y_0$ was not taken into account.

The small degree of divergence of the flow specifies the low tensile stresses in the interference zone, which differ strongly in magnitude from the cleavage strength of the material P_*. A channel crack forms in a dynamic fatigue regime. The critical number of loading cycles N_* needed to generate a crack on the surface of a solid is specified by the expression

$$N_*=\frac{1}{\zeta}\left(\frac{u_*}{v_0}-1\right),$$

where

$$u_*=\frac{P_*}{p_0c_0}.$$

A subsequent increase in the number of cycles in the supercritical range leads to growth of the crack into the material. For a channel crack the depth L_0 is given by the expression[2,3,8]

$$L_0=y_0\tan\arccos\frac{u_*}{v_0(1+\zeta N)}=y_0\sqrt{\frac{\zeta N_*}{\zeta N_*+1}\left(\frac{N}{N_*}-1\right)}.$$

The growth of a channel crack alters the character of the subsequent loading, since it itself becomes a source of an unloading wave. As a result of the interference of two counterpropagating centered unloading waves with sources at $y=0$ and $y=y_0$, an annular zone of tensile stresses is generated at $N>N_*$. A loss of continuity takes place soonest on the surface at the solid at $y_1=(y_0+k\tau_0)/2$ when $N=2N_*$. Subsequent cavitation loading leads to the growth of the first-generation annular crack and the formation of a new

centered unloading wave. The new wave with a center at y_1 influences the channel crack by ''wedging it open.'' The influence of the unloading wave emanating from y_0 ceases.

The dynamic ''wedging open'' of a crack under the action of cyclic loads differs fundamentally from the quasistatic process, which is accompanied by deepening of the crack. Because the coordinate y_1 where the annular crack is formed is smaller than y_0, the new unloading wave cannot deepen the previously formed crack. After the annular crack appears, growth of the channel crack ceases, and the maximum depth L_0, to which cleavage damage extends is achieved when $N=2N_*$. The dynamic character of the damage of the obstacle under the action of cyclic loads is manifested in the growth of the number of longitudinal annular cracks, and crack deepening takes place during the formation of each new generation of cracks. Each new growing crack terminates the growth of the crack of the previous generation.

The first-generation annular crack, like the channel crack, is determined by the divergence of the flow, and its maximum depth equals

$$L_1=(y_0-y_1)\sqrt{\frac{\zeta N_*}{1+\zeta N_*}}.$$

As can be seen from Table I, the critical number of cycles N_* depends significantly on the cavitation pressure, while the maximum penetration depth into the obstacle scarcely depends on P_0.

The channel crack is oriented strictly in the longitudinal direction by virtue of the symmetric arrangement of the counterpropagating unloading waves generating it. The annular cracks exhibit a slight deviation. The banks of longitudinal cracks, like free surfaces oriented toward a shock disturbance, generate a centered unloading wave, which lowers the pressure in the shock wave to $P=P_0/4$.[1–3,8] The remainder of this pressure is removed by a lateral unloading wave. The expansion velocity ω_0 in the interference zones of the unloading waves, whose sources are longitudinal cracks, differs from the expansion velocity caused by the divergence of the flow behind the shock wave:

$$\omega_0=\frac{2}{n+1}\frac{\sigma_0}{4}c_0.$$

The critical number of cycles N_{**} needed to generate the annular cracks of the second and ensuing generations is given by the expression

$$N_{**}=\frac{1}{\zeta}\left(\frac{u_*}{\omega_0}-1\right).$$

The coordinate for formation of the annular crack of a new generation by neighboring unloading waves with centers at y_a and y_b is specified by the expression $y_{ab}=0.5(y_a+y_b+k\tau_b-k\tau_a)$, and its penetration depth is given by the expression

$$L_{ab}=0.5(y_b-y_a-k\tau_b+k\tau_a)\sqrt{\frac{\zeta N_{**}}{1+\zeta N_{**}}}.$$

As can be seen from Table I, erosion appears earlier on the peripheral portions of the failure zone. The diameter of the failure zone y_0 is a small fraction of the diameter of the contact zone $y=\sqrt{3}$. As the annular cracks continue to appear, their coordinates shift toward the center, and their penetration depths decrease.

Thus, the physical model of cavitation damage as a result of the periodic loading of a surface with shock waves generated by the collapse of bubbles is capable of accounting for the experimentally observed formation of deep blisters in the surface craters. As for the other two proposed models of cavitation loading, damage can take place due to cumulative jets. However, the specific conditions needed for asymmetric bubble collapse do not make this mechanism decisive.

The theory that pit formations are a result of a collective shock wave is apparently erroneous. The formation of a multiple-front shock wave upon the simultaneous impact of several particles[3] leads to alteration of the damping law of the combined wave. The duration of action of such a wave increases, causing an increase in the thickness of the hardened layer. However, for the loads which are realized in cavitation erosion ($u_0/c_0\lesssim 0.02$), the increase in the thickness of the hardened layer is not significant. Cleavage damage depends on the presence of unloading waves and, therefore, does not depend on the lifetime of the combined shock wave. In cases where the simultaneous collapse of a very large number of bubbles takes place and a nearly planar shock wave forms, the conditions for the appearance of unloading waves vanish and longitudinal erosion does not appear. The formation of large pits on a surface under intense cavitation loading should be attributed to a significant increase in the number of shock waves acting on the contact zone per unit time rather than to the action of a combined shock wave.

[1] S. N. Buravova, Pis'ma Zh. Tekh. Fiz. **15**(17), 63 (1989) [Sov. Tech. Phys. Lett. **15**, 689 (1989)].
[2] S. N. Buravova, Zh. Tekh. Fiz. **62**(8), 58 (1992) [Sov. Phys. Tech. Phys. **37**, 859 (1992)].
[3] S. Buravova, Wear **157**, 359 (1992).
[4] G. A. Adadurov, A. F. Belikova, and S. N. Buravova, Fiz. Goreniya Vzryva No. 4, 95 (1992).
[5] A. F. Belikova, S. N. Buravova, Yu. N. Kiselev, and É. A. Mironov, Fiz. Khim. Obrab. Mater. No. 4, 100 (1989).
[6] A. F. Belikova, S. N. Buravova, A. A. Goncharov, and Fed'ko, Poverkhnost' No. 10, 134 (1989).
[7] C. M. Preece, in *Erosion*, edited by C. M. Preece (Academic Press, New York, 1979), p. 268.
[8] S. N. Buravova, A. A. Goncharov, and Ju. N. Kiselev, Tribol. Int. **29**, 359 (1996).
[9] R. Brown, S. Kosco, and E. J. Jun, Wear **88**, 181 (1983).
[10] I. Hansson, J. Klæstrap Kristensen, and K. A. Mørch, J. Phys. D **11**, 891 (1978).
[11] J. E. Field, M. B. Lesser, and J. P. Dear, Proc. R. Soc. London, Ser. A **401**, 225 (1985).
[12] E. P. Georgievskaya, in *Cavitation Erosion of Propellers* [in Russian], Sudostroenie, Leningrad (1978), p. 129.
[13] A. W. Ruff and S. M. Wiederhorn, in *Erosion (Treatise on Materials Science and Technology, Vol. 16)*, C. M. Preece (Ed.), Academic Press, New York (1979), pp. 69–126; Mir, Moscow (1982), pp. 80–139.
[14] S. Buravova, in *High Pressure Science and Technology*, W. A. Trzecia Kowski (Ed.), World Scientific, Warsaw (1995), pp. 944–946.

Translated by P. Shelnitz

Features of the use of the photorefractive method for the local contactless determination of the thermal diffusivity

A. L. Filatov

Institute of Radio Engineering and Electronics, Russian Academy of Sciences, 141120 Fryazino, Moscow Region, Russia

(Submitted December 2, 1996; resubmitted June 20, 1997)
Zh. Tekh. Fiz. **68**, 115–118 (September 1998)

The main difference between the proposed method and the methods previously used is the modified relative arrangement of the pump and probe beams. Beams which cross in the sample are used. This provides for local measurements along with the possibility of investigating any point in a sample. The main differences between the methods for determining the thermal diffusivity in insulators and in semiconductors are revealed and explained on the basis of an analysis of theoretical and experimental results. © *1998 American Institute of Physics.* [S1063-7842(98)02309-5]

INTRODUCTION

The determination of the thermal properties of different materials is still an important area of modern physics. The 14th European Conference on Thermophysical Properties, which was held in France in September of 1996, demonstrated the steady interest in this subject. One of the practical applications of thermal investigations is the design of composite materials with assigned thermal properties. Studies involving the determination of the thermal properties of small objects (of the order of 10 μm)[1] and the local determination of these properties in structures already created[2] have been conducted in this area.

The photorefractive method may be convenient for such investigations.[3] It is based on an investigation of the optical inhomogeneity appearing near the site of absorption of intensity-modulated pump radiation using a laser probe beam. Similar optical methods have already found broad application in the determination of thermal properties. However, none of them simultaneously offers both the possibility of performing local measurements and a capability of investigating any region in the bulk of a sample. In the interference[4] and photothermodeformation[5] methods the surface of the sample is used to deflect and reflect the probe beam. Therefore, despite the possibility of performing local measurements, these methods cannot be used to investigate the bulk of a sample. Methods based on the standard mirage effect[6] permit the performance of measurements at any site in a sample. However, they do not ensure that the measurements are local, since the interaction distance between the probe beam and the optical inhomogeneity is chosen as large as possible in them in order to increase the signal-to-noise ratio.

The photorefractive method permits local determination of the thermal diffusivity in any region of the sample. This is achieved by using a modification of the mirage effect with the smallest possible interaction distance between the probe beam and the optical inhomogeneity, i.e., with pump and probe beams which cross in the bulk of the sample. A diagram of the paths of the beams in the photorefractive method is shown in Fig. 1. The pump beam *1* is weakly absorbed in the medium after it traverses the distance z from the sample surface *2*. The probe beam *3* passes perpendicularly to the pump beam at a distance x from it and is deflected on the optical inhomogeneity *4* by an angle Θ.

The physical basis of the photorefractive method is that the absorption of the intensity-modulated pump radiation in the bulk of the sample periodically produces gradients of the temperature, the strain, and the concentration of free carriers (in semiconductors) near the site of absorption. These gradients, in turn, lead to the periodic appearance of optical inhomogeneity. The parameters of this inhomogeneity contain information on the optical, mechanical, thermal, and other properties of the medium. They can be determined from the deflection of the probe beam passing near the site of absorption of the pump radiation.

The principal measurements in the photorefractive method are determinations of the dependences of the amplitude and phase of the deflection angle of the probe beam on the distance between the beams for a fixed modulation frequency of the pump beam. Sometimes the dependences on modulation frequency are investigated for a fixed distance between the beams.

THEORY AND METHODS

The deflection angle Θ of the probe beam has two components (Θ_x, Θ_z), one of which is perpendicular, while the other is parallel to the pump beam. Their magnitude is determined by the magnitude of the corresponding refractive index gradients:

$$\Theta = \begin{pmatrix} \Theta_x \\ \Theta_z \end{pmatrix} = \frac{1}{n^{\mathrm{opt}}} \int_{-\infty}^{\infty} dy \begin{pmatrix} \dfrac{\partial n^{\mathrm{opt}}}{\partial x} \\ \dfrac{\partial n^{\mathrm{opt}}}{\partial z} \end{pmatrix}, \tag{1}$$

where n^{opt} is the refractive index of the medium for the probe radiation.

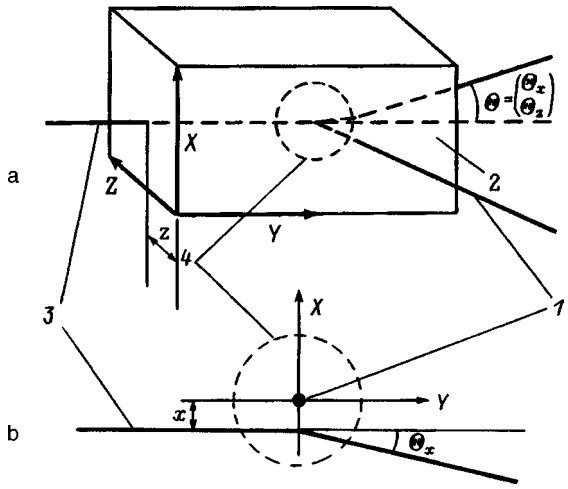

FIG. 1. Diagram of the paths of the beams in the photorefractive method: a — three-dimensional image, b — two-dimensional image (projection onto the XY plane).

A detailed derivation of the formula for calculating the deflection angle in the case of a semiconductor medium was given in Ref. 3. The dependence of the refractive index on temperature and carrier concentration was taken into account in it. Let us utilize Eq. (14) from Ref. 3

$$\Theta_x = C_1 \exp(-\beta z) \int_0^\infty d\xi\, \xi W_0 \sin(\xi x/(D\tau)), \tag{2}$$

where

$$W_0 = \frac{1-\alpha(\xi^2 - B^2 - i\Omega/\Omega_0) + Q(\xi^2 - B^2 - i\Omega)}{(\xi^2 - B^2 - i\Omega/\Omega_0)(\xi^2 + 1 - B^2 - i\Omega)},$$

$$\alpha = -\frac{\kappa}{E_g D}\left(\frac{\partial n^{\text{opt}}}{\partial n}\right)\left(\frac{\partial n^{\text{opt}}}{\partial T}\right)^{-1},$$

$B = \beta(D\tau)^{1/2}$, $\Omega_0 = \chi/D$, $\Omega = \omega\tau$, $\omega = 2\pi f$, $Q = (h\nu - E_g)/(\gamma E_g)$, C_1 is a constant, β is the absorption coefficient for the pump radiation, z is the distance from the sample surface to the region under investigation, f is the modulation frequency of the pump radiation, χ is the thermal diffusivity, κ is the thermal conductivity, τ is the lifetime of the charge carriers, E_g is the gap width of the semiconductor, $h\nu$ is the photon energy of the pump radiation, and γ is the quantum efficiency.

After setting the lifetime of the charge carriers equal to zero, from Eq. (2) we can easily obtain the expression for insulators

$$\Theta_x = C_2 \exp(-\beta z) \exp(\sqrt{-i\omega/\chi}\, x). \tag{3}$$

An analysis of Eq. (3) reveals a procedure for determining the thermal diffusivity in insulators by the photorefractive method. The values of $\Theta_x(x,z,\omega)$ for $z = \text{const}$ and $\omega = \text{const}$ measured at two or more distances between the pump and probe beams uniquely specify the parameter sought. In addition, a modification of this procedure, in which the value of this parameter is determined from the function $\Theta_x(\omega)$ for $z = \text{const}$ and $x = \text{const}$ is possible.

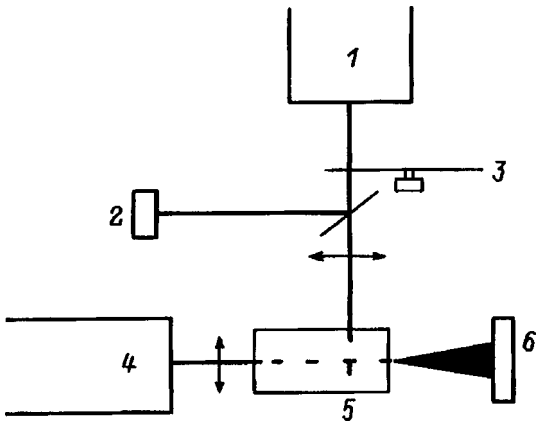

FIG. 2. Block diagram of the experimental apparatus: *1* — pump laser, *2* — power control, *3* — modulator, *4* — probe laser, *5* — sample, *6* — position-sensitive photodiode.

Despite the cumbersome nature of expression (2), the procedure for determining the thermal diffusivity in semiconductors is practically the same as in insulators. However, in this case low pump radiation modulation frequencies must be used. It was noted in Ref. 3 that predominance of the ''electronic'' influence over the ''thermal'' influence is observed at high frequencies in silicon, and vice versa. The concepts of high and low frequencies are easily defined and explained by comparing the characteristic times for charge carriers (τ) and thermal processes ($1/\omega$). At low pump radiation modulation frequencies ($\tau\omega < 1$) a large portion of the photoexcited carriers recombine during the modulation period. At high frequencies, $\tau\omega > 1$, the charge carriers do not manage to recombine and make a contribution to the photorefractive effect over the course of the entire period.

The magnitude of the photorefractive effect can be estimated using a simplified model. The characteristic length of the effect is the thermal length $L = \sqrt{2\chi/\omega}$, and the characteristic time is the reciprocal of the angular frequency $1/\omega$. When radiation is absorbed in a sample, the temperature of a volume $\Delta V = \pi L^2/\beta$ increases by $\Delta T = P\beta/\pi L^2 \omega \rho C_p$, where P is the pump radiation power, ρ is the density, and C_p is the heat capacity of the sample. A gradient of the refractive index $\Delta n^{\text{opt}}/L = (dn^{\text{opt}}/dT)(\Delta T/L)$, on which deflection of the probe beam takes place, also appears. For example, for silicon, in which $dn^{\text{opt}}/dT = 2.5 \times 10^{-4}\ \text{K}^{-1}$ (Ref. 7), $\beta = 10\ \text{cm}^{-1}$ (Ref. 8), $C_p = 0.648$ J/(gK) (Ref. 9), $\chi = 0.85\ \text{cm}^2/\text{s}$ (Ref. 10), and $\rho = 2.33\ \text{g/cm}^3$ (Ref. 9), 1-mW radiation modulated at a frequency of 1 Hz causes deflection by an angle of 3×10^{-9} rad, according to the estimate made.

EXPERIMENTAL APPARATUS

An experimental apparatus, which can be described by the block diagram in Fig. 2, was assembled to determine the thermal diffusivity by the photorefractive method. An Nd:YAG laser with a wavelength of 1.06 μm served as the source of the pump radiation. The probing was performed by the output of a He–Ne laser with a wavelength of 1.5 μm. The experiments were performed mainly on samples of silicon, in which the probe radiation is scarcely damped, and the

absorption coefficient for the pump radiation equals $10\,\mathrm{cm}^{-1}$ (Ref. 8). The constriction diameters of the probe and pump beams in their interaction zone were about 50 μm. The relative arrangement of the beams was varied by moving the lens that focuses the pump beam. A mechanical interrupter provided for pump radiation modulation frequencies in the range from 10 to 2000 Hz. The deflection angle of the probe beam was determined by a position-sensitive photodiode. The differential signal from the photodiode was amplified and detected by a synchronous detector with quadratic channels.

Because of the short interaction length between the probe beam and the optical inhomogeneity, special attention was focused on the noise and the sensitivity of the apparatus during its creation. It was found that the irremovable sources of noise, which determine the sensitivity, are fluctuations of the intensity and angle of inclination of the probe beam. For good non-Russian models of He–Ne lasers[11] these fluctuations are of the order of $10^{-9}\,\mathrm{rad/Hz^{1/2}}$. For the He–Ne laser used in our apparatus, which was based on the mass produced LGN-208 model, they amount to $5\times10^{-9}\,\mathrm{rad/Hz^{1/2}}$. Achieving such a limiting sensitivity required minimizing the mechanical noise.

The relative vibrations of the lasers, lenses, sample, and position-sensitive photodetector were the main source of mechanical noise in the apparatus. The probe part of the system (the He–Ne laser, the focusing lens for the probe beam, the sample, and the position-sensitive photodetector) were especially sensitive to vibrations. Therefore, all of its elements were placed on an optical bench and rigidly fastened to it. Beside vibrations, other sources of noise and interference were discovered. The movement of air, which always occurs in the room, led to deviations of the probe beam and, therefore, to additional noise in the apparatus. The scattering of the probe beam on dust particles caused sudden surges in the signal. Therefore, the path of the probe beam was shielded by boxes.

RESULTS AND DISCUSSION

To ascertain the details of the procedure for determining the thermal diffusivity in semiconductors, we investigated a series of samples of single-crystal silicon with different lifetimes. The samples had characteristic linear dimensions of order 1 cm. All the samples gave approximately the same value for the thermal diffusivity, viz., $0.82\,\mathrm{cm^2/s}$, which is close to the values of this parameter obtained by the thermodeformation method ($0.81\,\mathrm{cm^2/s}$, Ref. 5) and to the tabulated value ($0.85\,\mathrm{cm^2/s}$, Ref. 10). On the basis of a treatment of the experimental results, the accuracy of the photorefractive measurements was of the order of 10%.

Figure 3 presents experimental and calculated values of the phase and amplitude of the photorefractive signal in a silicon sample ($\tau=0.62$ ms, $D=17\,\mathrm{cm^2/s}$) as a function of the distance between the pump and probe beams. The solid lines are theoretical curves calculated from Eq. (3), and the points are experimental results. The figure reveals good quantitative agreement between the theoretical and experimental curves for all modulation frequencies.

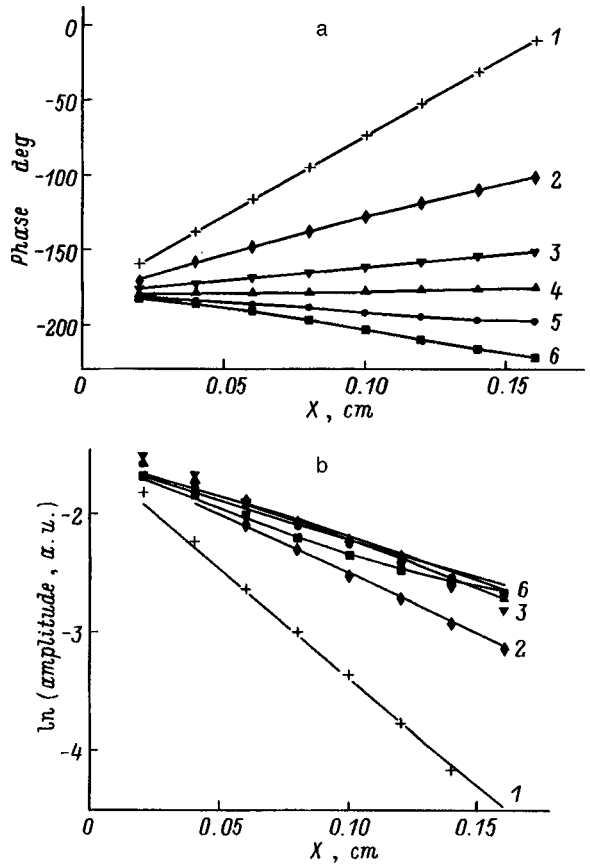

FIG. 3. Experimental and calculated values of the phase (a) and amplitude (b) of the photorefractive signal. f, Hz: *1* — 1800, *2* — 560, *3* — 180, *4* — 60, *5* — 20, *6* — 10.

At high frequencies the character of the curves is determined by the electronic parameters and scarcely depends on the thermal properties of the samples (curves *1* and *2*). The phase and amplitude dependences are straight lines, whose slope is determined by the lifetime and diffusion coefficient of the photoexcited carriers.[3] As the modulation frequency at which the product $\tau\omega$ becomes close to unity decreases, the thermal processes begin to compete with the electronic processes (curves *3–5*). At the same time, the influence of the modulation frequency on the amplitude dependence weakens, the slope of the phase dependence begins to decrease, and its sign changes when the frequency is decreased further. To understand the behavior of the curves in this frequency range, attention should be focused on the fact that an increase in the concentration of free carriers in silicon leads to an increase in the refractive index, while an increase in temperature leads to a decrease.

After the slope changes sign the phase dependence gradually cease to have the form of straight lines (curve *6*). A zone with a fairly strong influence of the electronic processes continues to exist near the site of absorption of the pump radiation. As the distance between the pump and probe beams is increased, the concentration of photoexcited carriers decreases strongly, and the slope of the phase dependence begins to be determined mainly by the value of the thermal diffusivity.

It can be seen from the foregoing analysis that the pho-

torefractive method can be applied successfully to the local contactless determination of the thermal diffusivity at any point in the volume of an insulator or semiconductor. The parameters which specify the locality of the method are the constriction diameter of the probe beam and the thermal length $L_t=(2\omega/\chi)^{1/2}$, over which the thermal properties of the material are averaged. In addition, for semiconductors there are restrictions on the position of the region investigated relative to the sample surface. Surface recombination begins to influence the photorefractive method as the surface is approached to within a distance of the order of the diffusion length of the charge carriers. However, despite these restrictions, the photorefractive method can find broad application in laboratory investigations of the thermal properties of various materials.

[1] P. Echegut, ''Microscopic approach of thermooptical properties,'' in *14th ECTP (European Conference on Thermophysical Properties)*, Lyon-Villeurbanne, France (1996), p. 55.

[2] D. Schwingel, R. Taylor, and J. Wigren, in *Conference Book of 14th ECTP (European Conference on Thermophysical Properties)*, Lyon-Villeurbanne, France (1996), p. 101; High Temp.–High Press. **30**, 253 (1998).

[3] A. Filatov, V. Mirgorodsky, and V. Sablicov, Semicond. Sci. Technol. **8**, 694 (1993).

[4] H. Dersch and N. M. Amer, Appl. Phys. Lett. **47**, 292 (1985).

[5] V. I. Mirgorodsky, G. A. Orlova, and A. L. Filatov, Zh. Tekh. Fiz. **62**, 180 (1992) [Sov. Phys. Tech. Phys. **37**, 333 (1992)].

[6] V. I. Mirgorodskiĭ, E. V. Novichikhin, V. A. Sablikov *et al.*, Zh. Tekh. Fiz. **64**, 174 (1994) [Tech. Phys. **39**, 210 (1994)].

[7] G. E. Jellison Jr. and H. H. Burke, J. Appl. Phys. **60**, 841 (1986).

[8] W. C. Dash and R. Newman, Phys. Rev. **99**, 1151 (1955).

[9] I. V. Grigor'ev and E. Z. Meĭlikhov, *Physical Quantities. A Handbook* [in Russian], Énergoizdat, Moscow (1991).

[10] I. K. Kikoin, *Tables of Physical Quantities. A Handbook* [in Russian], Atomizdat, Moscow (1976), 1232 pp.

[11] M. Olmstead, N. Amer, S. Kohn *et al.*, Appl. Phys. A **32**, 141 (1983).

Translated by P. Shelnitz

Investigation of the thermodynamic and physical characteristics of a thermomagnetic engine with a gadolinium working element

K. N. Andreevskiĭ, A. G. Mandzhavidze, I. G. Margvelashvili, and S. V. Sobolevskaya

Institute of Physics, Georgian Academy of Sciences, 380077 Tbilisi, Georgia
(Submitted August 19, 1997)
Zh. Tekh. Fiz. **68**, 119–122 (September 1998)

A quantitative description of the thermodynamic characteristics of thermomagnetic engines is given. Expressions for the work and efficiency of a thermomagnetic engine as a function of the thermal and magnetic properties of the working material are obtained. Experimental results obtained on a laboratory model of such an engine are presented. © *1998 American Institute of Physics.* [S1063-7842(98)02409-X]

INTRODUCTION

The possibility of creating thermomagnetic generators which operate under a regime with periodic heating and cooling of a ferromagnet in the presence of an external magnetic field and transform thermal energy from a hot reservoir into electrical or mechanical energy was considered in Refs. 1–9. The overwhelming majority of such experimental devices employ working elements composed of rare-earth magnets that have specific magnetic properties:[10–12] comparatively low values of the Curie temperature θ (from room temperature to 100 °C), abrupt temperature dependences of the magnetization in an external magnetic field near the point of the magnetic phase transition, etc. However, the publications cited were devoted predominantly to a description of the technical principles; at the same time, the literature scarcely offers any publications devoted to the physical (particularly, the thermodynamic) basis of thermomagnetic generators and engines.

THERMODYNAMICS OF A MAGNETOTHERMAL ENGINE

The following cycle (Fig. 1) was chosen to quantitatively estimate the thermodynamic characteristics of magnetothermal engines that utilize the variation of the magnetization of a ferromagnet in response to variation of its temperature under the influence of a heat pulse in the presence of an external polarizing magnetic field. In the first step (AB) (an adiabatic process) the rapid introduction of a polarizing magnetic field H causes the evolution of heat due to the magnetocalorific effect. This effect is much stronger in many rare-earth magnets near the Curie point than in Fe, Co, and Ni;[12] therefore, the change in the temperature of the magnet in fairly strong fields (of the order of several tenths of a tesla) can be very significant (in Fig. 1 $H_0=0$, $T_B>T_A$).

In the second step (BC) a quantity of heat Q_1 is imparted to the magnet at $H=\text{const}$. As a result, its temperature rises from T_B to T_C, and the magnetization decreases from $j(T_B)$ to $j(T_C)$. In the third step (CD) (an adiabatic process) the polarizing magnetic field is removed. In this step heat is absorbed reversibly, and the temperature of the magnet drops to T_D.

Finally, in the fourth step of the cycle (DA) the excess heat Q_2 is removed from the magnet, and its temperature decreases to T_A, i.e., the magnet returns to its original state.

The work performed by the magnet during one cycle, $A=|Q_1|-|Q_2|$, was calculated using the well known relations between the thermodynamic and magnetic characteristics of the working material.[13–15] The following expressions were obtained for the work and efficiency:

$$A=mC_p(T_c-T_B)(1-\exp[-(kH^2/2C_p)]), \tag{1}$$

$$\eta=A/Q_1=1-\exp(-kH^2/2C_p). \tag{2}$$

Here m is the mass of the magnet, C_p is the specific heat in the absence of a magnetic field, k is the coefficient in the expansion of the magnetization j in a small parameter. After some simple transformations, the expression (2) can be brought into the form

$$\eta=1-T_A/T_B=(T_B-T_A)/T_B. \tag{3}$$

We represent the work as a function of the temperatures at the coldest (T_A) and warmest (T_C) points of the cycle

$$A=mC_p(1-\exp[-kH^2/2C_p]) \times(T_C-T_A\exp[-kH^2/2C_p]). \tag{4}$$

From the condition $A>0$ and the positive value of the expression in the first set of parentheses we obtain the inequality

$$T_c-T_A\exp[kH^2/2C_p]>0, \tag{5}$$

from which follows a bound on the magnetic field

$$H<(2C_p/k)\ln(T_C/T_A). \tag{6}$$

The physical meaning of this bound is that when the magnetic field exceeds the quantity on the right-hand side of (6), the reversible evolution of heat due to the magnetocalorific effect raises the temperature of the magnet to $T_B>T_C$, and the transfer of heat from the hot reservoir to the magnet consequently ceases.

In order to quantitatively estimate the work of the magnet during a single cycle for various values of the magnetic field H and the temperature of the cold reservoir T_A, the value of k was found empirically. It follows from the

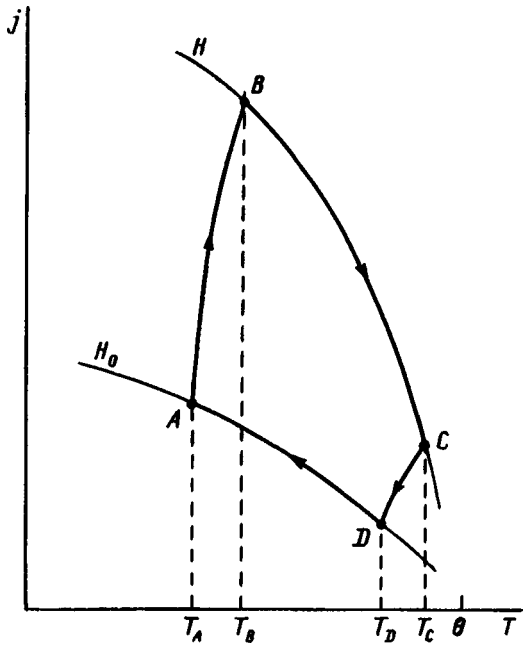

FIG. 1. Dependence of the magnetization j of a ferromagnet on its temperature T in different fields: $H_0=0$ and $H=\text{const}$.

temperature dependence of the specific magnetization of gadolinium[11] that for $H=0.2$ T the product $kH=-(\partial j/\partial T)_{H,P}$ amounts to about $2.7\times10^{-7}\,\text{T}\cdot\text{m}^3/\text{kg}\cdot\text{K}$, and, accordingly, $k=1.33\times10^{-6}\,\text{m}^3/\text{kg}\cdot\text{K}$. The lattice specific heat, which, according to Dulong and Petit's law, equals $25\,\text{J/mol}\cdot\text{K}$, which gives $C=1.6\times10^2\,\text{J/kg}\cdot\text{K}$ for Gd, served as an approximate value of C_p.

The plots calculated from (4) of the dependence of the work (per gram of Gd) on the strength of the external magnetic field H for various temperatures of the cold reservoir and $T_C=291$ K are presented in Fig. 2. The calculations show that the work increases with magnetic field up to a certain value $H=H^*$, and then as H increases, the work decreases and vanishes at the value of H specified by (6).

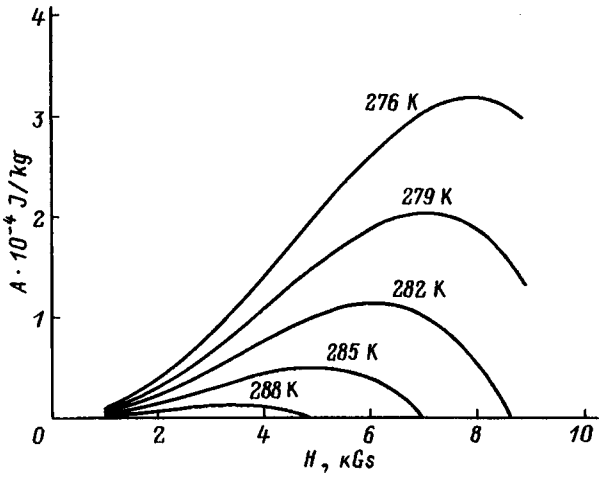

FIG. 2. Plots of the dependence of the work (per gram of Gd) on the strength of the external magnetic field H calculated from Eq. (4) for various temperatures of the cold reservoir and $T_C=291$ K.

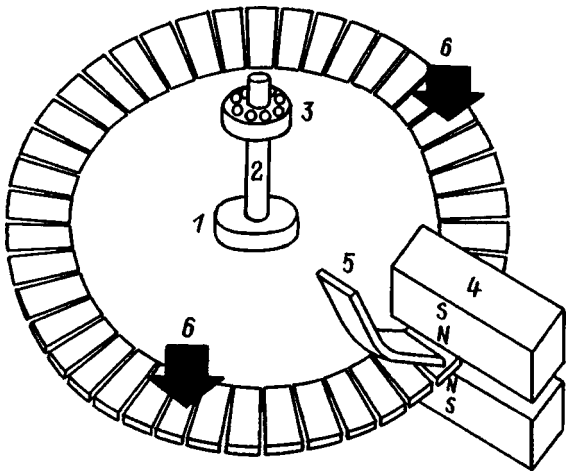

FIG. 3. Schematic representation of a model of a magnetothermal engine: *1* — rotor, *2* — shaft, *3* — ball bearing, *4* — magnets, *5* — supply of hot water, *6* — cooling zone.

The maximum value of the work $A(H^*)$ is greater, the lower is the temperature T_A of the cold reservoir.

EXPERIMENTAL RESULTS

The main working element in the magnetothermal engine is the rotor (Fig. 3), which is fashioned in the form of a disk (*1*) from a thermally nonconducting material (Perspex) mounted on Duralium shaft *2* with the possibility of rotation in the horizontal plane on ball bearing *3*. Along the rim of the disk there are plane-parallel gadolinium plates, which form a circular ring of thickness 1 mm. As the disk rotates, the gadolinium plates pass between like poles of permanent magnets *4*, which are mounted symmetrically relative to the rotation plane and create a nonuniform magnetic field at the entrance to the gap between them, which is also symmetric relative to the rotation plane. In the initial state, where the temperature of all the gadolinium plates is the same and equal to the temperature of the surrounding medium, the magnetic field of magnets *4* exerts two forces on the plates, $\mathbf{F}_1$ and $\mathbf{F}_2$, which are equal in magnitude and oppositely directed and which hold disk *1* in a state of rest. The force acting on an element of a magnet of mass dm is equal in magnitude to

$$dF=j\,dm(\partial H/\partial x), \tag{7}$$

where $\partial H/\partial x$ is the magnetic field gradient along the force lines.

When the engine operates, hot water is supplied along copper pipes *5* to the gadolinium plates passing through the gap between the poles of the magnets as the disk rotates. The heating of the plates lowers their magnetization, and, as a result, the returning force $\mathbf{F}_2$ at the exit from the region of action of the magnetic field is considerably smaller in absolute value than the force $\mathbf{F}_1$ acting on the magnet at the entrance to the gap (Fig. 4). If the total moment of the forces $\mathbf{F}_1$ and $\mathbf{F}_2$ and of the force of the load on the disk shaft $\mathbf{F}_\text{L}$ is nonzero, the disk undergoes accelerated rotation, as a result of which the next plates of the working elements are brought into the heating zone. The plates leaving the region of action

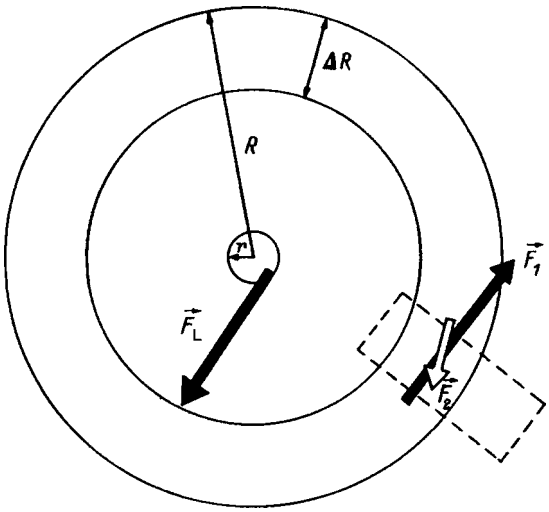

FIG. 4. Forces exerted on a plate by the magnetic field ($\mathbf{F}_1$ and $\mathbf{F}_2$) and the load ($\mathbf{F}_L$) acting on the shaft.

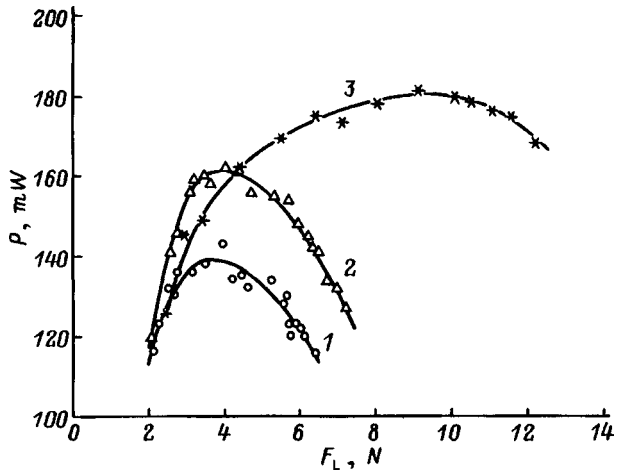

FIG. 5. Dependence of the power of the engine on the load on the shaft.

of the magnetic field enter the zone where they are cooled by cold water, which is supplied to the surface of the plates along copper pipes *6*. Since the heating zone is located only in the gap between the poles of the permanent magnets and since the cooling zone covers practically all of the remainder of the disk, it can be assumed that the gadolinium plates have been uniformly cooled to the temperature T_D of the cold water at the entrance to the gap. During accelerated rotation of the disk, the residence time of the plates in the heating zone shortens. Therefore, the plates are heated to a lower temperature, and the force $\mathbf{F}_2$ acting on them at the exit from the gap increases in absolute value. Ultimately, if the flow rates of the hot and cold water are constant and the load $\mathbf{F}_L$ remains unchanged, the total moment of the forces becomes equal to zero, and a stationary rotation regime with a practically constant angular velocity is established.

In the engine design under consideration a configuration of permanent magnets, in which their like poles are opposite one another, was chosen. The choice of this configuration was stipulated by the following arguments. A nonuniform field at the entrance to the gap between the magnets with maximum possible uniformity in the heating zone is needed for efficient operation of the engine. In addition, the force $\mathbf{F}_1$, which is caused by the nonuniformity of the field at the entrance, must have the largest possible component in the required direction of motion of the working elements. A field with a solenoidal structure satisfies these requirements nearly ideally.

An examination of various configurations of the permanent magnets revealed that orientation of the magnets with unlike poles opposite one another does not satisfy the requirements stated above. In fact, although the requirement for uniformity of the field in the heating zone is satisfied in this case; nevertheless, the orientation of the force lines in the direction perpendicular to the rotation plane of the disk creates forces directed at large angles to the to the rotation plane at the entrance to the gap, and the resultant force lying in the rotation plane is very small.

When the permanent magnets are arranged with parallel magnetic moments, the configuration of the magnetic field is similar to a solenoidal one. However, in this case the magnetic field is drawn out of the central region adjacent to the rotation plane of the disk both at the entrance to the gap and within it, and, therefore, the resultant force $\mathbf{F}_1$ drawing the magnetic elements into the gap is also small. In the case of the arrangement of the permanent magnets with like poles opposite one another (antiparallel orientation of the magnetic moments), despite the significant nonuniformity of the field in the gap, the configuration of the field at the entrance to the gap is nearly solenoidal and provides for the maximum value of the advancing force $\mathbf{F}_1$ in comparison to other arrangements of the magnets.

The radius of the disk in the experimental model of the magnetothermal engine $R=0.09$ m, the width of the circular ring of gadolinium working elements $\Delta R=0.02$ m, and the radius of the disk shaft $r=0.005$ m. The maximum magnetic field strength at the entrance to the gap is $\sim 1.5-2$ T. Figure 5 shows experimental plots of the dependence of the stationary power measured in tests of the experimental model on the load on the disk shaft $\mathbf{F}_L$. Curves *1* and *2* are plots of these dependences for an experimental model containing one pair of permanent magnets oriented with like poles opposite one another and thus one heating zone. The temperature of the cold water is about 16 °C, and the temperature of the hot water is 54 °C (curve *1*) and 68 °C (curve *2*). Increasing the load $\mathbf{F}_L$ at values close to zero leads to a rise in the net power to a certain maximum value and to a drop at higher values of $\mathbf{F}_L$.

The increase in power with the load at small values of $\mathbf{F}_L$ apparently occurs, because, as $\mathbf{F}_L$ is increased and, accordingly the angular velocity of the disk decreases, the working elements manage to be heated to a higher temperature in the gap between the magnets. The temperature distribution across the thickness of each plate is then more uniform. In addition, as the angular velocity drops, the role of the dissipative factors diminishes.

The drop in power at higher values of $\mathbf{F}_L$ is evidently attributable to the fact that the plates in the gap manage to be heated across their entire thickness to temperatures exceeding the Curie point when the angular velocity ω decreases

below a certain value. Therefore, when ω decreases further, the amount of work performed by the engine during a fixed time interval drops.

Curve *3* in Fig. 5 shows the dependence of the power on load for a similar engine containing two pairs of magnets and thus two heating zones for the working elements, which are positioned symmetrically relative to the rotation axis at opposite ends of a diameter of the disk. The temperature of the cold and hot water are equal to 15 and 66 °C, respectively. It is seen that the introduction of an additional pair of magnets increases both the maximum net power of the engine and the width of the working range of loads. In this case doubling of the maximum power of the engine could be expected, but a smaller effect is observed experimentally because the total flow rate of hot water for the two pairs of magnets remained practically the same as in the case with one pair. This is equivalent to a twofold decrease in the flow rate of hot water per pair of magnets.

CONCLUSIONS

1. Expression for the work and efficiency of a magnetothermal engine have been obtained on the basis of known relations from thermodynamics and the theory of magnetism. It has been shown that the work depends in a complex way on the strength of the external magnetic field: it rises with increasing H up to a certain maximum value and then drops.

2. The configuration of the external magnetic field has been optimized to obtain the maximum value of the force acting on the working material.

3. The testing of a laboratory model of such an engine has yielded the dependences of the power on load for various temperatures of the hot and cold reservoirs.

[1] H. E. Stauss, J. Appl. Phys. **30**, 1622 (1959).
[2] J. Elliot, J. Appl. Phys. **30**, 1774 (1959).
[3] M. Ohboshi, H. M. Kabayashi, T. Katayama *et al.*, J. Appl. Phys. Jpn. **15**, 2019 (1976).
[4] I. S. Petrenko and V. A. Finkel', Zh. Tekh. Fiz. **50**, 2421 (1980) [Sov. Phys. Tech. Phys. **25**, 1416 (1980)].
[5] A. L. Tyurin, Candidate's dissertation, Ashkhabad (1988).
[6] K. K. Boboshko, ''Magnetothermal engine'' [in Russian], USSR Inventor's Certificate (Patent) No. 1,295,027.
[7] A. P. Nikolaĭchuk, ''Magnetothermal engine'' [in Russian], USSR Inventor's Certificate (Patent) No. 1,341,377.
[8] A. G. Mandzhavidze, V. S. Bedbenov, and A. Yu. Shtaerman, ''Device for converting solar energy into mechanical energy'' [in Russian], USSR Inventor's Certificate (Patent) No. 1,453,998.
[9] A. G. Mandzhavidze and V. S. Bedbenov, ''Magnetothermal engine,'' USSR Inventor's Certificate (Patent) No. 1,414,046.
[10] K. P. Belov, *Rare-Earth Magnets and Their Application* [in Russian], Nauka, Moscow, 1980.
[11] K. P. Belov, M. A. Belyanchikova, V. Z. Levitin, and S. A. Nikitin, *Rare-Earth Ferro- and Antiferromagnets* [in Russian], Nauka, Moscow, 1965.
[12] K. P. Belov, *Magnetothermal Phenomena in Rare-Earth Magnets* [in Russian], Nauka, Moscow, 1990.
[13] S. A. Shmatko and Yu. V. Usov, *Structure and Properties of Metals and Alloys. A Handbook* [in Russian], Naukova Dumka, Kiev, 1987.
[14] Yu. B. Rumer and M. Sh. Ryvkin, *Thermodynamics, Statistical Physics, and Kinetics* [Mir, Moscow, 1980; Nauka, Moscow, 1977, 552 pp.].
[15] I. P. Bazarov, *Thermodynamics* [Vysshaya Shkola, Moscow, 1976; Pergamon Press, Oxford, 1964].

Translated by P. Shelnitz

BRIEF COMMUNICATIONS

Schottky barrier UV photodetectors based on zinc selenide

V. P. Makhniĭ

Chernovtsy State University, 274012 Chernovtsy, Ukraine
(Submitted April 10, 1997)
Zh. Tekh. Fiz. **68**, 123–125 (September 1998)

The results of investigations of the properties of UV photodetectors based on zinc selenide are presented. The influence of the parameters of the diode structure, the temperature, and the voltage on the main characteristics and parameters of the photodetectors is considered.
 [S1063-7842(98)02509-4]

In recent years the problem of detecting and quantitatively evaluating UV radiation has become especially critical. This is due primarily to the drastic deterioration in the ecological situation: ozone holes, the sun's activity, etc. On the other hand, the more extensive use of sources of UV radiation in science and technology, medicine, and the national economy calls for the development of functional measuring devices, whose main element is a photodetector. One of the promising types of UV detectors is the Schottky photodiode. A surface potential barrier provides for effective separation of the charge carriers generated in this region as a result of the absorption of photons with an energy $\hbar\omega$, which is appreciably greater than the gap width E_g. Such detectors are presently fabricated mainly from Si and broad-band III–V compounds.[1,2] The employment of broader-band materials would permit the creation of selective UV detectors, which can operate without additional light filters that cut off the long-wavelength portion of the spectrum. The main technical characteristics and parameters of metal ZnSe photodiodes are described below, and the influence of various factors, viz., bias voltage, temperature, doping level in the substrate, etc., on them is investigated.

Single-crystal wafers of low-resistivity *n*-ZnSe having a thickness of 0.4–0.5 mm served as the original substrates. Semitransparent barrier contacts were created by thin (10–20 nm) nickel films, which are characterized by sufficiently large and uniform transmission in the spectral range investigated.[3] In addition, this metal forms a high [at least 1.2 eV at 300 K (Ref. 4)] potential barrier with *n*-ZnSe and has good adhesion and electrical conductivity.[5] The configuration and dimensions of the photosensitive areas were assigned by a molybdenum mask during deposition of the semitransparent metallic layers. Indium ohmic contacts were made on the opposite side of the semitransparent substrate. The structures were placed in standard cases for semiconductor photodetectors with a leucosapphire window for the entry of UV light. The effective area of the photodiodes varied in the range $10^{-2}-10^{-1}$ cm^2.

The investigations in Ref. 4 showed that the barrier height φ_0 of a Ni–ZnSe contact depends on the doping level in the substrate and increases from 1.2 to 2.0 eV as the free-electron concentration decreases from 10^{17} to 10^{15} cm^{-3}. At the same time, the dark current density J_0 at room temperatures varied in the range $10^{-16}-10^{-23}$ A/cm^2. The photosensitivity spectrum of the diodes at zero bias has the form of a broad band in the range 0.20–0.47 μm (Fig. 1). The typical values of the monochromatic current sensitivity S_λ at $\lambda_{\max}=0.42-0.44$ μm fall in the range 0.1–0.15 A/W, which corresponds to a quantum efficiency of 0.3–0.4 electrons/photon. The dynamic range of linearity of the current-voltage characteristic covers at least six orders of magnitude, and the fill factor of the optical load characteristic varies in the range 0.6–0.9. Because of the small value of J_0, the sensitivity threshold $P_{\min}$ in a single frequency interval Δf was estimated using the formula $P_{\min}=J_0/\sqrt{\Delta f}S_\lambda^{\max}$, and its value for the structures investigated is $10^{15}-10^{22}$ W·cm^{-2}·Hz$^{-1/2}$. Therefore, Schottky barriers based on zinc selenide can serve as threshold photodetectors for the UV portion of the spectrum.

Let us now consider the influence of various factors on some parameters and characteristics of the photodetectors. We first note that in the $\pm 60\,^\circ$C temperature range the short-wavelength sensitivity remains practically fixed at $\lambda \leqslant 0.4$ μm. This is due to the fact that high-energy photons with $\hbar\omega > E_g$ are actually absorbed on the surface. The temperature shift of the long-wavelength edge of the spectrum amounts to $\approx 7\times 10^{-4}$ eV/K and is close to the temperature coefficients for the variation of φ_0 and E_g. Increasing T from 20 to 60 °C leads to increases in the dark current and the sensitivity threshold by approximately an order of magnitude.

The investigations showed that the form of the photosensitivity spectrum and the absolute value of S_λ depend on the doping level in the substrate and the reverse bias V. We note that the rate of variation of $S_\lambda/(V)$ increases with decreasing λ (Fig. 2). An increase in the doping level in the substrate leads to a decrease in the absolute values of the ratio $S_\lambda(V)/S_\lambda(V_0)$ for $\lambda=\text{const}$ without altering the general form of the $S_\lambda(V)$ curve. These findings can be attributed to the influence of image forces. In such a structure (see the inset in Fig. 2) the photocarriers generated in the region $0-X_m$ are not separated by the barrier field, and they drift toward the surface and recombine on it without making any contribution to the photocurrent. The thickness X_m of this

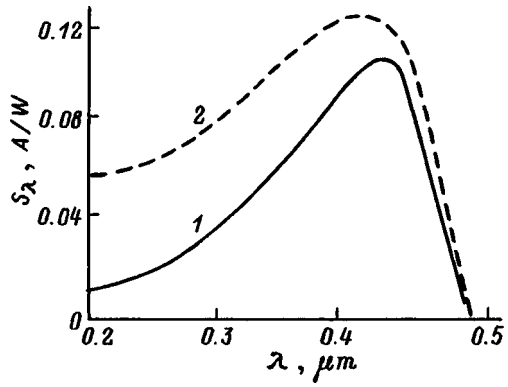

FIG. 1. Photosensitivity spectra of a Ni–ZnSe diode at $V=0$ (*1*) and -6 V (*2*). $T=300$ K.

''dead'' layer is approximately equal to the distance from the interface to the point with maximum potential and, according to Ref. 6, is given by the expression

$$X_m=\frac{1}{4}\left[\frac{e^2}{2\pi\varepsilon\varepsilon_0 N_d(\varphi_0-eV)}\right]^{1/4}, \tag{1}$$

where ε is the dielectric constant of the semiconductor, ε_0 is the permittivity of free space, and N_d is the concentration of ionized donors.

On the other hand, the ''dead'' layer can be represented as a filter with a transmission

$$T_\lambda=\exp(-\alpha\cdot X_m), \tag{2}$$

where α is the absorption coefficient, which increases with decreasing λ.

The optical transmission of such a filter for a specific value of N_d increases with decreasing α and increasing V. Therefore, an increase in the reverse bias at $\lambda=$ const should lead to an increase in the sensitivity of the diode, as is observed experimentally (Fig. 2). At a certain value V_0, S_λ reaches its maximum value, which is determined by the parameters φ_0 and N_d of the structure, by the density of surface

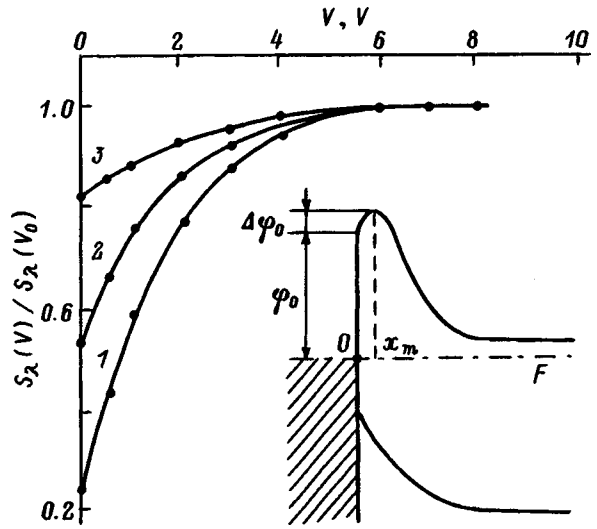

FIG. 2. Dependence of the ratio $S_\lambda(V)/S_\lambda(V_0)$ on the reverse bias on a Ni–ZnSe diode at $\lambda=0.20$ (*1*), 0.30 (*2*), and 0.45 μm (*3*) and $V_0=6$. Inset — energy diagram of the diode.

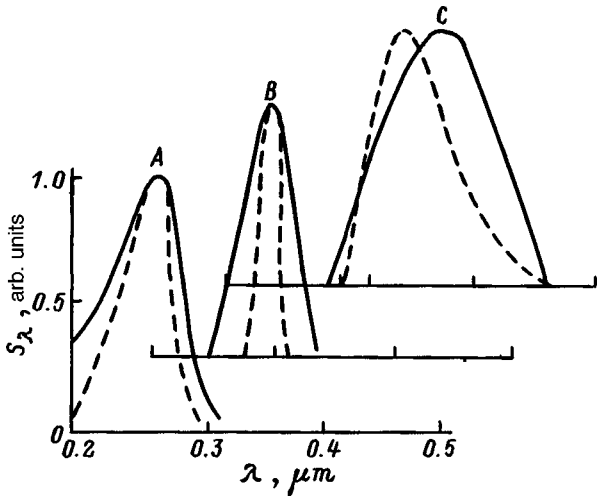

FIG. 3. Photosensitivity spectra of a Ni–ZnSe diode with various filters (solid curves) and bands corresponding to the bactericidal (A), erythemal (B), and suntan (C) regions of the spectrum (dashed curves).

states, and by the reflectivity of the barrier contact. Operation of the photodiode at reverse biases close to V_0 permits a significant increase in sensitivity in the short-wavelength region of the spectrum in comparison to S_λ at $V=0$ (Fig. 1). A further increase in sensitivity can be achieved by optimizing the technology for fabricating the structure (by selecting the material and thickness of the barrier contact and the transmitting coating, as well as by adjusting the treatment of the substances to lower the rate of surface recombination).

In conclusion, we note that the photosensitivity spectrum of ZnSe diodes covers all the principal biologically active ranges of UV light: A — the bactericidal range (0.20–0.28 μm), B — the erythemal range (0.28–0.32 μm), and C — the suntan range (0.32–0.45 μm).[7] Bands A, B, and C can be isolated by employing appropriate filters.[8] The photosensitivity spectra in each of these bands in Fig. 3 have been normalized at their maxima to unity.

Thus, the photodetectors developed can find application in instruments and devices intended for detecting, monitoring, and measuring the dose and power of UV light.

[1] V. I. Stafeev and I. D. Anisimova, Fiz. Tekh. Poluprovodn. **28**, 462 (1994) [Semiconductors **28**, 281 (1994)].
[2] I. D. Anisimova, I. M. Vikulin, F. A. Zaitov, and Sh. D. Kurmashev, *Semiconductor Photodetectors: Ultraviolet, Visible, and Near-Infrared Regions of the Spectrum* [in Russian], Radio i Svyaz', Moscow (1984), 216 pp.
[3] K. L. Chopra and S. R. Das, *Thin Film Solar Cells* [Plenum Press, New York (1983); Mir, Moscow (1986), 435 pp.].
[4] V. P. Makhniĭ and V. V. Mel'nik, Fiz. Tekh. Poluprovodn. **29**, 1468 (1995) [Semiconductors **29**, 764 (1995)].
[5] A. I. Kurnosov, *Materials for Semiconductor Devices and Integrated Microcircuits* [in Russian], Vysshaya Shkola, Moscow (1980), 327 pp.
[6] E. H. Roderick, *Metal-Semiconductor Contacts* [Clarendon Press, Oxford (1980); Radio i Svyaz', Moscow (1982), 378 pp.].
[7] V. P. Rvachev, *Introduction to Biophysical Photometry* [in Russian], Izd. L'vovskogo Univ., (1966), 378 pp.
[8] V. P. Makhniĭ and V. V. Mel'nik, Ukrainian Patent No. 9,412,810 (20 December 1994).

Translated by P. Shelnitz

Determination of the surface potential of a dielectric layer on a target bombarded by an ion beam

G. G. Bondarenko, A. I. Bazhin, A. P. Korzhavyĭ, V. I. Kristya, and R. D. Aitov

Moscow State Institute of Electronics and Mathematics, 109028 Moscow, Russia
(Submitted February 25, 1997)
Zh. Tekh. Fiz. **68**, 126–128 (September 1998)

The electric field at the surface of a charge spot created by an ion beam on a dielectric coating of a target is calculated. An expression is obtained which relates the surface potential of the insulator to the potential of the collector corresponding to saturation of the collector secondary-electron current. It permits determination of the potential drop across the oxide layer of a cold cathode without introducing complications in the construction of the experimental apparatus.
 [S1063-7842(98)02609-9]

Metallic cold cathodes with a dielectric oxide film on the working surface are employed in many gas-discharge devices.[1,2] Their emission properties depend on the electric field created in the insulator by the surface charge formed as a result of ion bombardment of the cathode in the discharge. The known methods for measuring the surface potential of a dielectric layer irradiated by charged particles call for the introduction of an additional probe beam[3,4] or movable parts in the apparatus.[5,6]

The electric field at the surface of a charge spot created by an ion beam on a dielectric coating of a target is calculated in this paper. An expression, which relates the surface potential of the insulator to the potential of the collector corresponding to saturation of the collector secondary-electron current, is obtained. It permits determination of the potential drop on the oxide layer of a cold cathode without complicating the design of the experimental apparatus. A similar problem was considered in Ref. 7, but the relations obtained in that work have a fairly cumbersome form, which makes it difficult to use them in investigations of the emission properties of cold cathodes.

When a target with a dielectric coating is bombarded by an ion beam, a charge spot forms on its surface. The distribution of the charge density $\sigma(r)$ in it is similar to the distribution of the current density in the beam and is usually Gaussian:[8]

$$\sigma(r)=\sigma_0 \exp\left(-\frac{r^2}{r_e^2}\right), \tag{1}$$

where r is the distance from the center of the spot and r_e is the effective radius of the spot.

Let the z axis be directed along a normal to the target (Fig. 1). In this case the $z=0$ plane is the boundary between the metallic coating and the insulator, the $z=H$ plane is the surface of the dielectric layer with a dielectric constant ε, and the secondary-electron collector is located in the $z=H+L$ plane. The transverse dimensions of the target and the collector are assumed to be much greater than L so that we can neglect the edge effects, and the potential of the collector relative to the substrate φ_c significantly exceeds the contact potential difference on the boundaries of the media. The electric field potential in the insulator is denoted by φ_1, and the potential outside the insulator is denoted by φ_2. Then, if the beam current I_p is small enough that its perveance $I_p/\varphi_b^{3/2}$ (φ_b is the potential corresponding to the energy of the beam particles) does not exceed $10^{-9}A/V^{3/2}$ (Ref. 9), the distribution of the potential in the system is described by the Laplace equations

$$\Delta\varphi_1=0, \quad \Delta\varphi_2=0 \tag{2}$$

with the boundary conditions

$$\varphi_1(r,0)=0, \quad \varphi_1(r,H)=\varphi_2(r,H),$$

$$\frac{\partial\varphi_2}{\partial z}(r,H)-\varepsilon\frac{\partial\varphi_1}{\partial z}(r,H)=-\frac{\sigma(r)}{\varepsilon_0},$$

$$\varphi_2(r,H+L)=\varphi_c, \tag{3}$$

where ε_0 is the permittivity of free space.

Solving the boundary-value problem (1)–(3) by separation of variables, we find the expression for the normal component of the electric field at the target surface

$$E_z(r,z)=-\frac{\partial\varphi_2}{\partial z}=-\frac{\varphi_c\varepsilon}{H+\varepsilon L}+\frac{\sigma_0(\varphi_c)r_e^2}{2}\int_0^\infty \times\frac{\lambda\exp(-\lambda^2 r_e^2/4)\cosh[\lambda(L+H-z)]J_0(\lambda r)}{[\coth(\lambda L)+\varepsilon\coth(\lambda H)]\sinh(\lambda L)}d\lambda, \tag{4}$$

where $J_0(x)$ is the Bessel function of order 0.

It can be seen from (4) that at small values of φ_c there is a field at the center of the spot which prevents some of the secondary electrons from escaping to the collector. As φ_c increases, the number of such electrons decreases, and when a certain value $\varphi_c=\varphi_{c0}$ is achieved, at which the condition $E_z(0,H)=0$ is satisfied, all the electrons impinge on the collector, i.e., saturation of the secondary current occurs. The quantity $\sigma_0(\varphi_c)$ reaches its maximum value $\sigma_0(\varphi_{c0})$ at $\varphi_c=\varphi_{c0}$. It follows from (4) that

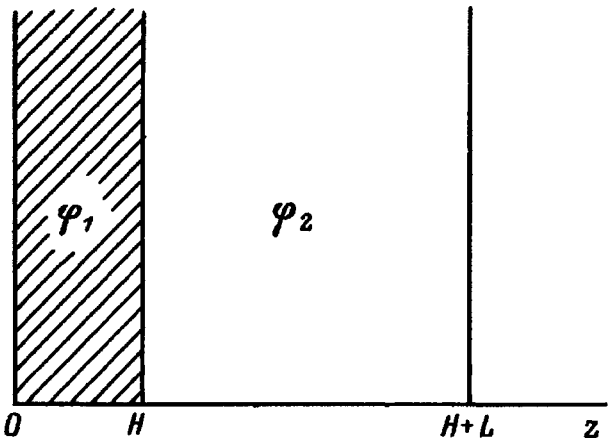

FIG. 1. Diagram of the electrode gap.

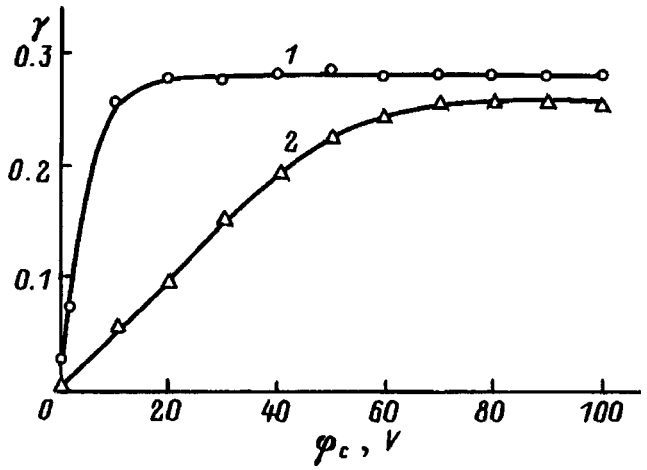

FIG. 2. Experimental dependence of the ratio γ of the collector secondary-electron current to the ion-beam current on the collector potential φ_c for samples obtained under cathodic (*1*) and anodic (*2*) oxidation regimes.

$$\varphi_{c0}=\frac{(H+\varepsilon L)\sigma_0}{2\varepsilon_0\varepsilon}\int_0^\infty \frac{t\exp(-t^2/4)dt}{1+\varepsilon\tanh(tL/r_e)\coth(tH/r_e)}. \tag{5}$$

Taking into account the characteristic values of the quantities appearing in (5) $r_e\sim10^{-3}$ m, $L\sim10^{-2}$ m, and $H\sim10^{-8}$ m and neglecting the terms of order H/L and $H/r_e\sim10^{-5}-10^{-6}$, we obtain

$$\varphi_{c0}=\frac{\varphi_h L}{2t_e}\left\{\int_0^\infty t^2\exp(-t^2/4)dt+\int_0^\infty t^2\exp(-t^2/4)\times[\coth(tL/r_e)-1]dt\right\}, \tag{6}$$

where $\varphi_h=\sigma_0(\varphi_{c0})H/(\varepsilon_0\varepsilon)$ is the potential at the center of the spot in the regime of complete collection of the secondary current, which is the working regime for cold cathodes.

The first of these integrals equals $2\sqrt{\pi}$, and the second, as can easily be shown, does not exceed $\sqrt{\pi}(r_e/L)^2$, i.e., when $r_e/L\ll1$, the expression (6) takes the form

$$\varphi_{c0}=\frac{\sqrt{\pi}\,\varphi_h L}{r_e}, \tag{7}$$

whence it follows that

$$\varphi_h=\frac{r_e}{\sqrt{\pi}\,L}\varphi_{c0}. \tag{8}$$

Therefore, after experimentally determining the potential φ_{c0}, at which saturation of the collector current occurs, we can use (8) to find the surface potential of the dielectric layer at the center of the charge spot created by the beam.

Experimental investigations were performed on samples prepared from pure aluminum with an oxide film on the surface, which was obtained by treating them in an oxygen glow charge. The thickness of the oxide was measured by an ellipsometric technique. The distance L from the sample to a flat 100 mm diam collector was equal to 10 mm. A beam of He^+ ions with an energy of 300 eV and $r_e=1.8$ mm was used. Under these conditions there is no appreciable spreading of the charge over the cathode surface[8], and there are no regions with a significantly different work function on it, which can have an effect on the form of the dependence of the secondary-electron current on the collector potential.[1]

Figure 2 shows measured plots of the dependence of the ratio $\gamma=I_s/I_p$ of the collector secondary-electron current I_s to the ion-beam current I_p on the collector potential φ_c for a sample obtained under a cathodic oxidation regime (curve *1*, $H=8\times10^{-9}$ m) and for a sample obtained under an anodic oxidation regime (curve *2*, $H=3.5\times10^{-8}$ m). The values of φ_{c0} for them are equal to 20 and 90 V, respectively, and, as follows from (8), the surface potentials φ_h equal 2.0 and 9.0 V. The field strength in the insulator $E_h=\varphi_h/H$ is then equal to 3×10^8 V/m, which is consistent with the known[6,10] estimates of the field in aluminum oxide at which the injection of electrons from the substrate needed to maintain stationary charging of the sample surface under the conditions of ion bombardment occurs.

Thus, the relation (8) obtained in the present work permits the determination of the surface potential of the oxide layer in investigations of the emission properties of cold cathodes without complicating the design of the apparatus.

[1] L. N. Dobretsov and M. V. Gomoyunova, *Emission Electronics*, Israel Program for Scientific Translations, Jerusalem (1971).
[2] R. D. Aitov, A. P. Korzhavyĭ, and V. I. Kristya, Obz. Élektron. Tekh., Ser. 6, No. 5, 1 (1991).
[3] V. Ya. Upatov, Radiotekh. Elektron. **2**, 184 (1957).
[4] O. N. Kryutchenko and A. E. Chizhikov, Élektron. Tekh., Ser. 4, No. 4, 62 (1987).
[5] A. Ibragimov, Zh. Tekh. Fiz. **54**, 401 (1984) [Sov. Phys. Tech. Phys. **29**, 239 (1984)].
[6] O. N. Kryutchenko, A. F. Mannanov, A. A. Nosov *et al.*, Poverkhnost', No. 6, 93 (1994).
[7] L. A. Serebrov and S. A. Fridrikhov, Radiotekh. Elektron. **5**, 1680 (1960).
[8] V. Ya. Upatov, Radiotekh. Elektron. **39**, 967 (1994).
[9] P. T. Kirstein, G. S. Kino, and W. E. Waters, *Space-Charge Flow* [McGraw-Hill, New York (1967); Mir, Moscow (1970), 600 pp.].
[10] H. Kanter and W. A. Feibelman, J. Appl. Phys. **33**, 3580 (1962).

Translated by P. Shelnitz

Fluctuation of the delay time of nonhysteretic Josephson junctions during a linear current rise

I. N. Askerzade

Institute of Physics, Azerbaijan Academy of Sciences, 370143 Baku, Azerbaijan
(Submitted May 19, 1997)
Zh. Tekh. Fiz. **68**, 129–130 (September 1998)

The influence of thermal fluctuations on the delay time of nonhysteretic Josephson junctions during a linear rise in the current through them is investigated in two cases: a) during a slow rise, and b) at a high rate of increase. © *1998 American Institute of Physics.*
[S1063-7842(98)02709-3]

It is known that consideration of the superconducting component of the current through a Josephson junction leads to an additional delay in the transition process from the superconducting state to the resistive state.[1] For nonhysteretic junctions the delay time τ_D can make a significant contribution to the total time of the transition process.

Despite the significant progress that has been made in creating Josephson junctions with a large delay[2] and in developing basic Josephson single-quantum logic elements,[3] the effects of thermal fluctuations on the delay time have not yet been investigated. In view of this, the fluctuations of the delay time τ_D during a linear rise in the current through a nonhysteretic junction are calculated in this paper.

We assume that nonhysteretic junctions are described by a linear resistive model with sources of thermal white noise in their normal resistances R. The dynamics of a nonhysteretic junction are described by the equation[1]

$$\dot{\varphi}+\sin\varphi=i+i_f, \tag{1}$$

where the phase φ, the time τ, and the current i are measured, respectively, in units of $\Phi_0/2\pi$, $\Phi_0/2\pi I_cR$, and I_c (I_c is the critical current of the junction, and Φ_0 is the magnetic flux quantum).

The fluctuation current i_f obeys the relations

$$\langle i_f\rangle=0; \quad \langle i_f i_{f\tau}\rangle=2\gamma\delta(\tau), \tag{2}$$

where $\langle\ldots\rangle$ denotes averaging over an ensemble, γ is the thermal energy in units of $\Phi_0 I_c/2\pi$, and $\delta(\tau)$ is a Dirac delta function.

The asymptotic expressions for the solution of Eq. (1) in the absence of noise for a linear rise in the current through the junction, i.e., for $i=\alpha\tau$ [$\lambda=(dI/dt)\Phi_0/2\pi I_cR$ is the dimensionless current rise rate] were presented in Ref. 1:

$$\tilde{\varphi}=\begin{cases} -(-2\alpha\tau)^{1/2} & \text{for}\ \tilde{\varphi}\to-\infty, \quad (3a)\\ C_1\alpha^{2/3}(\tilde{\tau}-C_2\alpha^{-1/3}) & \text{for}\ \tilde{\varphi}\simeq 0, \quad (3b)\\ (2/(C_3\alpha^{-1/3}-\tilde{\tau}))^{1/3} & \text{for}\ \tilde{\varphi}\to\infty, \quad (3c)\end{cases}$$

where $\tilde{\tau}=\tau-\alpha^{-1}$, $\tilde{\varphi}=\varphi-\pi/2$, and $C_1=1.25$, $C_2=1.21$, and $C_3=2.9$ are constants.

The quantity $\tau_D=C_3\alpha^{-1/3}$ is the mean value of the delay time.

Let us consider the case in which the current through the junction varies slowly at a rate

$$\alpha\ll(1-i^2)^{1/2}, \quad \gamma^{3/2}. \tag{4}$$

In this case the fluctuations do not have sufficient time to produce thermal activation of the system through the energy barrier $\Delta u=2^{5/2}(1-i^2)^{3/2}/3$, where the barrier height is measured in units of $\Phi_0 I_c/2\pi$. For the probability of a transition to the resistive state we use the known expression[1]

$$q(t)=1-\exp\left\{-\int_{-\infty}^{t}\tau_L^{-1}\,dt'\right\}, \tag{5}$$

where $\tau_L=\tau_L(I(t))$ is the lifetime of the metastable state of the nonhysteretic junctions, for which we have the expression[4]

$$\tau_L^{-1}=(1-i^2)^{1/2}\cdot e^{-\Delta u/\gamma}/2\pi. \tag{6}$$

As a result of the integration of (5) with allowance for (6) in the case of small fluctuations $\gamma\ll 1$ we have

$$q(\tau)=1-\exp\{-C_o e^{-2^{5/2}(1-\alpha\tau)^{3/2}/3\gamma}\}, \tag{7}$$

where $C_0=\gamma/4\pi\alpha$.

Using (7), in analogy to Ref. 5, we can find the dispersion of the delay time

$$\sigma^2(\tau_D)=(3\gamma\ln C_0/2^{5/2})^{4/3}/6\alpha^2, \tag{8}$$

which coincides with Eq. (22) in Ref. 5, where the only difference is in the expression for C_0.

In the opposite limit of large rise rates of the current through the junction, which corresponds to the reverse of the inequality (4), only slight variation of the transition process occurs under the effect of fluctuations. To find $\sigma^2(\tau_D)$ in this limit, we linearize Eq. (1) with respect to small increments $\delta\varphi$:

$$\delta\dot{\varphi}-\tilde{\varphi}(\tilde{\tau})\cdot\delta\varphi=i_f, \tag{9}$$

whose formal solution has the form

$$\delta\varphi(\tilde{\tau})=\int_{-\infty}^{\tilde{\tau}} i_f e^{\int_{\tilde{\tau}'}^{\tilde{\tau}}\tilde{\varphi}(x)\,dx}\,d\tilde{\tau}'. \tag{10}$$

The value of $\delta\varphi$ for $\tilde{\tau}\to\tau_D$ is proportional to the variation of the delay time τ_D, and, therefore, for the dispersion of the delay time with allowance for Eq. (3b) in the region of inertial motion we can write

$$\sigma^2(\tau_D)=2\gamma B^2 e^{a\tilde{\tau}^2-2ab\tilde{\tau}}\int_{-\infty}^{\tilde{\tau}} e^{-(a\tilde{\tau}'^2-2ab\tilde{\tau}')}\,d\tilde{\tau}', \qquad (11)$$

where $a=C_1\alpha^{2/3}$, $b=C_2\alpha^{-1/3}$, and B is the proportionality factor between $\delta\varphi$ and $\delta\tau_D$, which can be determined for $\tilde{\tau}\to\tilde{\tau}_D$ by differentiating (3c). Thus,

$$\sigma^2(\tau_D)=D_0\gamma\alpha^{-11/9}. \qquad (12)$$

Using the asymptotic formulas (3), we can calculate D_0. It is approximately equal to 11.9. Formula (12) differs appreciably from (8): in particular, the dependence of $\sigma^2(\tau_D)$ on α is weak.

[1] K. K. Likharev, in *Introduction to the Dynamics of Josephson Junctions* [in Russian], Nauka, Moscow (1985), 320 pp.
[2] A. L. Gudkov, V. K. Kornev, and V. I. Makhov *et al.*, Pis'ma Zh. Tekh. Fiz. **14**, 1127 (1988) [Sov. Tech. Phys. Lett. **14**, 495 (1988)].
[3] K. K. Likharev, O. A. Mukhanov, and V. K. Semenov, in *SQUID'85*, H. D. Hahlhohm and H. Lubbing (Eds.), W. de Gruyter, Berlin (1985), pp. 1103–1108.
[4] J. Kurkijarvi, Phys. Rev. **66**, 325 (1972).
[5] O. V. Snigirev, Radiotekh. Elektron. No. 29, 2216 (1984).

Translated by P. Shelnitz

Inductance in a system of doubly connected, ideally diamagnetic bodies

A. I. Spitsyn

Kharkov State Technical University of Radio Electronics, 310726 Kharkov, Ukraine
(Submitted June 3, 1997)
Zh. Tekh. Fiz. **68**, 131 (September 1998)

General relations for the inductances of a system of doubly connected, ideally diamagnetic bodies with currents circulating through them are found with consideration of the induced current densities in the individual bodies due to the influence of their mutual shielding. © *1998 American Institute of Physics.* [S1063-7842(98)02809-8]

When problems concerning the interaction of ideally diamagnetic bodies[1,2] and the diagnostics of media consisting of an assigned system of loops[3] are considered, the need to determine the inductances of a system of doubly connected, ideally diamagnetic bodies of arbitrary shape arises in the problem of ascertaining the radiation pattern. In this paper we find general relations for the mutual inductances of a system of n doubly connected, ideally diamagnetic bodies with the currents I_i $(i=1,2,\ldots,n)$ circulating through them. Beside these bodies, the system also contains other singly connected, ideally diamagnetic bodies.

For a clearer understanding, we repeat the derivation in Ref. 4 of the magnetic energy of bodies for the specific case under consideration. With allowance for the relations $\mathbf{B}=\mathrm{curl}\mathbf{A}$, $\mathrm{curl}\mathbf{H}=\mathbf{j}$, and $\mathrm{div}\mathbf{H}=0$, the integral for the magnetic energy $w=\int_v \mathbf{B}\cdot\mathbf{H}\,dv/2$ can be divided into surface and volume integrals. Since the field does not penetrate into an ideally diamagnetic conductor, the volume integral $\int_v \mathbf{j}\cdot\mathbf{A}\,dv=0$, and because of the tendency of the integral over an infinitely distant surface to vanish, the surface integral reduces to integration only over the surfaces of the bodies present $w=\int_s \mathbf{A}\cdot\mathbf{J}\,dS/2$, where $\mathbf{J}=\mathbf{H}\times\mathbf{n}$ is the surface current density and $\mathbf{n}$ is an internal normal to the surface of the body. Let $\mathbf{A}^{(i)}$ and $\mathbf{J}^{(i)}$ comprise a solution for the system that satisfies the ideal boundary conditions for the total current in the ith doubly connected body I_i and $I_k=0$ when $k\neq i$. We use $\mathbf{J}_m^{(i)}$ to denote the corresponding value of the current density in the mth body for the total current I_i in the ith body and $I_k=0$ when $k\neq i$. Owing to the linearity of the electrodynamic equations and the corresponding boundary conditions for bodies with the currents I_i $(i=1,2,\ldots,n)$ in them, $\mathbf{A}=\Sigma_i\mathbf{A}^{(i)}$ and $\mathbf{J}=\Sigma_i\mathbf{J}^{(i)}$. If we take into account that $\mathbf{A}^{(i)},\mathbf{J}^{(i)}\sim I_i$, the total magnetic energy can be represented by the relation $w=\Sigma_{i,k}L_{ik}I_iI_k/2$, where

$$L_{ik}=\frac{1}{I_iI_k}\int_s \mathbf{A}^{(i)}\cdot\mathbf{J}^{(k)}\,ds. \tag{1}$$

It follows from the equality $\int_v \mathbf{B}^{(i)}\cdot\mathbf{H}^{(k)}\,dv=\int_v \mathbf{H}^{(i)}\cdot\mathbf{B}^{(k)}\,dv$ that $L_{ik}=L_{ki}$. Since $s=\Sigma_m s_m$, then, going over to summation over the surfaces S_m of the individual bodies in (1), we find $L_{ik}=1/(I_iI_k)\Sigma\int_{sm}\mathbf{A}_m\cdot\mathbf{J}_m\,ds$.

The following statement holds. If a surface current $I=\int_C \mathbf{J}\cdot d\mathbf{l}_n$, where C is a contour enclosing an arbitrary transverse section at any point in the conductor, $d\mathbf{l}_n=\mathbf{n}_0 dl$, and $\mathbf{n}_0$ is the unit vector on the surface of the conductor normal to the element dl of the contour C, flows through a transverse section along a doubly connected, ideally diamagnetic body of arbitrary shape and if $\Phi=\int_L \mathbf{A}\cdot d\mathbf{l}$ for any contour L which surrounds the cavity and lies completely on the surface of the body, the surface integral over the entire surface s of the body is $\int_s \mathbf{A}\cdot\mathbf{J}\,ds=\Phi I$. This statement can be proved by dividing the surface s of the body into a network that consists of current lines on the surface of the body and lines orthogonal to them and taking the integral $\int_s \mathbf{A}\cdot\mathbf{J}\,ds$. On the basis of this relation, only the term with $m=k$ remains in the sum over m, i.e.,

$$L_{ik}=\frac{1}{I_iI_k}\int_{s_k} \mathbf{A}_k^{(i)}\cdot\mathbf{J}_k^{(k)}\,ds=\frac{\Phi_{ki}}{I_i}, \tag{2}$$

since the total induced current in the kth body, where $i\neq k$, equals zero, and Φ_{ki} is the magnetic flux caused by the current I_i through the cavity of the kth body. The value of L_{ik} for $i=k$ depends on the relative positions of the bodies. The general relation for the magnetic energy of a system of bodies can be represented in the generally accepted form $w=1/2\Sigma_k\Phi_kI_k$, where $\Phi_k=\Sigma_i\Phi_{ki}$. The energy conservation law for the potential energy of the system yields the general relation $U=\Sigma_k s_kI_k\Phi_k$ (Ref. 1), where $s_k=1$, if the flux $\Phi_k=\mathrm{const}$ is conserved in the kth ideally diamagnetic body, and $s_k=-1$, if the conditions for the flow of a constant current $I_k=\mathrm{const}$ through it are created.

[1] A. I. Spitsyn, Zh. Tekh. Fiz. **63**(4), 145 (1993) [Tech. Phys. **38**, 337 (1993)].
[2] A. I. Spitsyn, Zh. Tekh. Fiz. **63**(12), 1 (1993) [Tech. Phys. **38**, 1037 (1993)].
[3] S. Gavil, A. Mor, and M. Weinstein, J. Franklin Inst. **325**, 595 (1988).
[4] L. D. Landau and E. M. Lifshitz, *Electrodynamics of Continuous Media*, 1st ed., Pergamon Press, Oxford (1960), 531 pp.

Translated by P. Shelnitz

On the intensity of shock-initiated magnetoelastic oscillations arising in iron borate single crystals during pulsed magnetizing or magnetization-switching processes

O. S. Kolotov, A. P. Krasnojon, and V. A. Pogozhev

M. V. Lomonosov Moscow State University, 119899 Moscow, Russia
(Submitted July 8, 1997)
Zh. Tekh. Fiz. **68**, 132–133 (September 1998)

The intensities of magnetoelastic oscillations accompanying pulsed 180° and 90° magnetization switching of iron borate single crystals as well as pulsed magnetization of the crystals from a demagnetized state (with zero total magnetic moment) are compared for the first time. The amplitude A_1 of the oscillations of the signal obtained from the experimental sample by the induction method is adopted as a measure of the intensity of the magnetoelastic oscillations. It is found that for the same pulse heights of the magnetic field H exciting the magnetization-switching or magnetizing process, the amplitudes A_1 of the oscillations observed in 90° magnetization-switching and initial-magnetization processes have practically the same value, which is $\sqrt{2}$ times smaller than the amplitude of the oscillations obtained in 180° magnetization switching (reversal). It is concluded on the basis of the result obtained that the intensity of the magnetoelastic oscillations is virtually independent of the initial state of the single crystal and is determined mainly by the energy density $\Delta\mathbf{M}\cdot\mathbf{H}$ acquired by the magnetic subsystem of the crystal from the external field ($\Delta\mathbf{M}$ is the change in magnetization). Hence it follows that when iron borate is used in fast modulators for Mössbauer γ rays it is preferable to use the 90° magnetization-switching regime rather than the magnetization regime as has been done until very recently. © *1998 American Institute of Physics.* [S1063-7842(98)02909-2]

Iron borate ($FeBO_3$) is one of the fastest-responding of known magnetic materials.[1] This property is used in fast modulators for Mössbauer γ rays.[2,3] However, the weak easy-plane ferromagnet $FeBO_3$ is characterized by a strong magnetoelastic interaction,[4,5] and during magnetizing/magnetization-switching processes magnetoelastic oscillations are excited in it at a frequency determined by the thickness of the sample and the propagation velocity of shear waves (in the direction of the c axis).[6–8] This circumstance makes it difficult to use $FeBO_3$ in pulsed setups. Earlier modulators for Mössbauer γ rays[2,3] have employed the pulsed magnetization of $FeBO_3$ single crystals. In the initial state (in the absence of external magnetic fields) the single crystal is divided into a large ($\geqslant 15-20$) number of domains, and its average magnetization is close to zero.[5,9] In choosing this regime, it was assumed that because the changes in magnetization in different domains are not in phase with one another, the intensity of the magnetoelastic oscillations will be lower than in the case of other, switching processes. However, special investigations comparing the intensities of the oscillations accompanying different processes were not performed. At the same time, such investigations are needed not only to choose the optimal operating regime for modulators but also for understanding the physics of the magnetizing/switching processes.

In the present paper the intensities of the oscillations arising during pulsed magnetization and during 180° and 90° magnetization switching are compared. The last two processes were initiated by a fast (in a time <1 ns) change in the direction of the external magnetic field **H** (by 180° and 90°, respectively) with a simultaneous increase in the absolute magnitude of the field. The indicated processes are all characterized by the same direction of the magnetization in the final state so as to avoid ambiguity when comparing the intensity of the oscillations.

The experimental single-crystal wafers of $FeBO_3$ were irregular polygons with a transverse size of 3–8 mm and ranged in thickness from 24 to 110 μm.

An induction setup with time resolution ~ 1 ns was used.[10] The signal from a longitudinal sensing loop was detected. The amplitude A_1 of the signal oscillations, observed after the main stage of the magnetizing/switching process was completed,[7,8] was taken as the measure of the intensity of the magnetoelastic oscillations.

The dependence of the intensity of the oscillations on the amplitude H of the field pulse was investigated. The position of the sample was the same in all magnetizing/switching processes. The results obtained are illustrated for the example of a 110 μm thick sample and a field H_s required for in-plane technical saturation of the sample (2.1 Oe) and an average period of the magnetoelastic oscillations of 56 ns.

The dependences $A_1(H)$ are presented in Fig. 1. One can see that as the field intensity H increases, the intensity of the magnetoelastic oscillations at first increases and then starts to decrease. For $H>15$ Oe the amplitude of the oscillations becomes comparable to the noise of the apparatus. For all three regimes the maximum intensity of the oscillations is reached approximately at the same field intensity $H=H^*$. On the basis of earlier investigations of the 180° magnetization-switching regime,[7,11] this result can be ex-

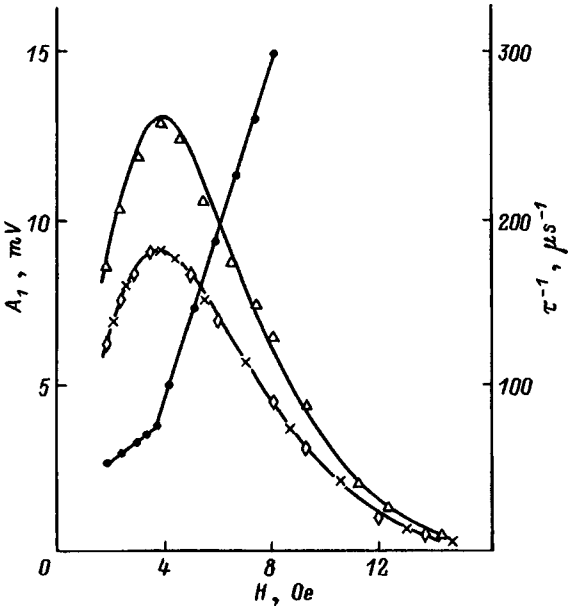

FIG. 1. 90° pulsed magnetization switching curve $(\cdot)$ $\tau^{-1}(H)$ and curves of the amplitude A_1 of the oscillations versus the amplitude H of the magnetic field pulse: $\triangle$ — 180° magnetization switching, $\diamond$ — 90° magnetization switching, $\times$ — magnetization from a demagnetized state.

plained as follows. The initial growth in the intensity is due to an increase in the energy density $\Delta\mathbf{M}\cdot\mathbf{H}$ obtained by the magnet from the external field. Here $\Delta\mathbf{M}$ is the change in magnetization as a result of the magnetizing/switching process. At the same time, as the field intensity increases, the duration τ of the main (initial) stage of the magnetizing/switching process decreases, and for its characteristic value $\tau=\tau^*=15\pm2$ ns, which is virtually independent of the period of the magnetoelastic oscillations and the type of process, the lagging of the phonon subsystem of the single crystal from the magnon subsystem starts to have an effect. In the ferromagnetic resonance technique, this effect has been termed ''freezing'' of the crystal lattice.[4,5] The time τ^* achieved for H close to H^* (3.5–4 Oe for the samples investigated) corresponds to a kink in the pulsed magnetization switching (or initial magnetization) curves, representing the dependence of the reciprocal of the duration of the magnetizing/switching process on the field intensity H. As an example, the curve $\tau^{-1}(H)$ obtained with 90° magnetization switching is presented in Fig. 1.

One can see that the sharp increase in the rate of magnetization switching in fields $H>H^*$ is due to the decrease in energy losses to excitation of magnetoelastic oscillations. Another important result is that the intensity of the oscillations in the case of 90° magnetization switching and magnetization from a demagnetized state are close to one another. Therefore the pulsed magnetization regime, in reality, has no advantages over the 90° magnetization switching regime. However, the latter regime makes it possible to obtain a high degree of modulation of the Mössbauer γ-radiation. It also follows from the results presented that the intensity of the oscillations is virtually independent of the initial state of the sample and is determined mainly by the quantity $\Delta\mathbf{M}\cdot\mathbf{H}$. Indeed, the energy of the magnetoelastic oscillations is proportional to A_1^2, and for this reason the intensity in the case of 180° magnetization switching should be $\sqrt{2}$ times higher than in the case of the two other processes. Turning to the figure, one can see that the indicated ratio is close to 1.4. For the other samples which we investigated it ranged from 1.35 to 1.5.

In summary, it is desirable to employ the 90° magnetization-switching regime in Mössbauer γ-ray modulators. To decrease the intensity of the magnetoelastic oscillations the magnetization switching time must be decreased to $\sim$1.5–2 ns. Then the ''freezing'' of the crystal lattice will be adequate.

We thank G. V. Smirnov and Yu. V. Shvyd'ko for a valuable discussion.

[1] O. S. Kolotov, V. A. Pogozhev, and R. V. Telesnin, Phys. Status Solidi A **72**, K197 (1982).
[2] G. V. Smirnov, Yu. V. Shvyd'ko, O. S. Kolotov, V. A. Pogozhev *et al.*, Zh. Eksp. Teor. Fiz. **86**, 1495 (1984) [Sov. Phys. JETP **59**, 875 (1984)].
[3] Yu. V. Shvyd'ko, K. P. Aleshin, O. S. Kolotov, V. A. Pogozhev *et al.*, Preprint No. IAE-3932/14 [in Russian], I. V. Kurchatov Institute of Atomic Energy, Moscow, 1984.
[4] E. A. Turov and V. G. Shavrov, Usp. Fiz. Nauk **140**, 429 (1983) [Sov. Phys. Usp. **26**, 593 (1983)].
[5] R. Diehl, W. Jantz, B. I. Nolang, and W. Wettling, Curr. Top. Mater. Sci. **11**, 241 (1984).
[6] O. S. Kolotov, V. A. Pogozhev, G. V. Smirnov, and Yu. V. Shvyd'ko, Fiz. Tverd. Tela (Leningrad) **29**, 2544 (1987) [Sov. Phys. Solid State **29**, 1471 (1987)].
[7] O. S. Kolotov, Kim En Hen, A. P. Krasnozhon, and V. A. Pogozhev, JETP Lett. **58**, 53 (1993).
[8] O. S. Kolotov, A. P. Krasnozhon, and V. A. Pogozhev, Fiz. Tverd. Tela (St. Petersburg) **38**, 1017 (1996) [Phys. Solid State **38**, 565 (1996)].
[9] G. B. Scott, J. Appl. Phys. **7**, 1574 (1974).
[10] O. S. Kolotov, V. A. Pogozhov, and R. V. Telesnin, *Methods and Apparatus for Investigation of the Pulsed Properties of Thin Magnetic Films* [in Russian], Moscow State University Press, Moscow (1970), 192 pp.
[11] O. S. Kolotov, Kim En Khen, A. P. Krasnozhon, and V. A. Pogozhev, Fiz. Tverd. Tela (St. Petersburg) **36**, 231 (1994) [Phys. Solid State **36**, 127 (1994)].

Translated by M. E. Alferieff

Dynamical equations of an ensemble of defects in the presence of disoriented substructures

Yu. V. Grinyaev, N. V. Chertova, V. E. Panin

Institute of Strength Physics and Materials Engineering, Siberian Branch of the Russian Academy of Sciences, 634021 Tomsk, Russia
(Submitted January 13, 1998)
Zh. Tekh. Fiz. **68**, 134–135 (September 1998)

It has been established experimentally that during a deformation process the defect structure of materials evolves from a single distribution of the defects to an ensemble of interacting particles which consists of nondisoriented or disoriented substructures, depending on the magnitude of the deformation. The conditions for the existence of disoriented defect substructures are examined on the basis of a field description of the dynamics of an ensemble of defects, and a generalization of previously known dynamical equations of nondisoriented defect substructures to the case of disoriented substructures is obtained. These equations show which quantities characterize the field of defects in the presence of disoriented substructures.
 [S1063-7842(98)03009-8]

The physics of mesomechanics, which has been undergoing intensive development during the last ten years, is based on the concept of scale levels of deformation and fracture.[1,2] The choice of a scale level to study is determined by the investigator's ''filter.'' For example, phenomena occurring during microscale deformations are studied in electron-microscopic investigations,[3] while mesoscale phenomena are studied in optico-television investigations.[4,5] Correlating the results observed during deformation on different scale levels made it possible to arrive at the conclusion that isolated defects (microscale dislocations, macroscale shear bands, and so on) appear near the yield stress, and then, as the deformation increases, ensembles of interacting defects, representing diverse substructures, are formed. In some deformation interval, irrespective of the method of loading and the material under investigation, the observed substructures can be divided into two classes: nondisoriented and disoriented substructures.[3] The phenomenon of scale invariance, which presumes that deformation on different levels develops similarly, makes it possible to introduce the concept of a defect at an arbitrary scale as a source of a displacement ''jump'' of different magnitudes and to make use of the deformation regularities studied on one scale to analyze the behavior of the material on a different scale. A system of equations describing a continuum of defects, which represents an ensemble of nondisoriented substructures, was obtained in Ref. 6. In the present paper we propose a system of dynamical equations for an ensemble of defects in the presence of disoriented substructures. Since the system of equations derived is a generalization of the results of obtained in Ref. 5, we shall give a brief exposition of the main tenets of this work.

According to Ref. 6, a continuum of defects that consists of an ensemble of interacting defects can be treated as an independent subsystem of the deformable solid. This gives a basis for proposing a model of a deformable body representing a mixture of two continua, one of which is a material medium–elastic continuum and the other is a continuum of defects. The elastic continuum, which is absorbs the stresses from external actions and defects of the material, is characterized by effective stresses

$$\sigma=\sigma^{\text{ext}}+\sigma^{\text{int}} \tag{1}$$

and an effective momentum

$$\rho\mathbf{V}=\rho\left(\mathbf{V}^{\text{int}}+\frac{\partial\mathbf{u}}{\partial t}\right), \tag{2}$$

where σ^{ext} is the external applied stress, σ^{int} is the internal stress related with the defects in the material, $\mathbf{V}^{\text{int}}$ and $\partial\mathbf{u}/\partial t$ are the rates of the displacements that are due to, respectively, the flux of defects and external action, and ρ is the density of the medium.

The continuum of defects consists of a mechanical field with stresses: α is the dislocation density tensor and I is the dislocation flux density tensor and is characterized by the energy of the cores of the defects and their inertial properties. The proposed model makes it possible to write the dynamical field equations for an ensemble of defects as

$$B\nabla\cdot I=-\rho\mathbf{V},\quad \nabla\cdot\alpha=0,$$

$$\nabla\times I=\frac{\partial\alpha}{\partial t},\quad S\nabla\times\alpha=-B\frac{\partial}{\partial t}I-\sigma, \tag{3}$$

where B and S are unknown constants of the theory, which characterize the inertial properties of the defects and the energy of a unit dislocation and the symbols $(\cdot)$ and $(\times)$ denote scalar and vector products.

The equation of dynamic equilibrium

$$\frac{\partial}{\partial t}\rho\mathbf{V}=\nabla\cdot\sigma \tag{4}$$

is the condition for the compatibility of Eqs. (3).

When disoriented fragments form in a subsystem of defects on any scale, the mechanical fields of the defects are

characterized by a strong nonuniformity and by the presence of internal stresses of alternating sign. The sign-alternating or nonoriented internal stresses, designated in what follows as σ_d^{int}, can be taken into account by introducing dipole configurations in the field of defects. Lattice curvature having a sign-alternating character was discussed in a similar manner in Ref. 7. The sign-alternating character of nonoriented internal stresses makes it possible to assume that

$$\int_s d\mathbf{s}\cdot\sigma_d^{\text{int}}=0, \tag{5}$$

where the integral extends over any full cross section of the deformable body.

Oriented stresses satisfy the equation

$$\int_s d\mathbf{s}\cdot\sigma_0^{\text{int}}=\mathbf{f},$$

where $\mathbf{f}$ is the force with which one part of the material interacts with another part through a section S.

In the general case

$$\sigma^{\text{int}}=\sigma_d^{\text{int}}+\sigma_0^{\text{int}}. \tag{6}$$

Since the condition (5) holds for an arbitrary section of the deformed body, the equality

$$\sigma_d^{\text{int}}=\frac{1}{2}\nabla\times M \tag{7}$$

holds.

It can be shown that the tensor M equals

$$M=r\times\sigma_d^{\text{int}}, \tag{8}$$

where r is the radius vector of the point considered.

It follows from Eq. (7) that dipole configurations of defects, determining the appearance of disoriented substructures in a deformable body, lead to the appearance of moments of the stresses.

The displacement of dipole ensembles or bound defects will give rise to a sign-alternating momentum $\rho\mathbf{V}_d^{\text{int}}$, which will satisfy the equation

$$\int_w \rho\mathbf{V}_d^{\text{int}}dw=0, \tag{9}$$

where the integration extends over the entire volume w occupied by the deformable body.

In contrast to bound defects, free defects produce a nonzero total momentum

$$\int_w \rho\mathbf{V}_s^{\text{int}}dw\neq 0.$$

The combination $\rho\mathbf{V}^{\text{int}}=\rho(\mathbf{V}_d^{\text{int}}+\mathbf{V}_s^{\text{int}})$ of the integrands in the last two equalities determines the momentum of a material point due to the flux (2) of defects. Since the condition (9) holds for a body of any shape, we have

$$\rho\mathbf{V}_d^{\text{int}}=-\nabla\cdot\rho, \tag{10}$$

according to which a tensor P of rank 2 can be represented as a dyadic product

$$P=\mathbf{r}\rho\mathbf{V}_d^{\text{int}}, \tag{11}$$

where $\mathbf{r}$ is the radius vector.

The quantity P is the dipole of the momentum. The antisymmetric part of the dipole is the moment of momentum density or the angular momentum density.

In the absence of external loads, free defects, and oriented stresses, the equation (4) of dynamical equilibrium becomes

$$\frac{\partial}{\partial t}\rho\mathbf{V}_d^{\text{int}}=\nabla\cdot\sigma_d^{\text{int}} \tag{12}$$

or, taking account of the relation (9),

$$-\nabla\frac{\partial}{\partial t}P=\nabla\cdot\sigma_d^{\text{int}}. \tag{13}$$

Hence nonoriented internal stresses can be determined to within the curl of a certain tensor in the form of the equality

$$\sigma_d^{\text{int}}=-\frac{\partial P}{\partial t}+\frac{1}{2}\nabla\times M, \tag{14}$$

which signifies that the tensor of nonoriented internal stresses can be due to mobile and static dipole ensembles of defects. Taking account of Eqs. (6), (9), (10), and (14), the field equations describing the dynamics of an ensemble of defects in the presence of disoriented substructures can be written in the form

$$\nabla\cdot(BI-P)=-\rho\left(\mathbf{V}_s^{\text{int}}-\frac{\partial u}{\partial t}\right),\quad \nabla\cdot\alpha=0,$$

$$\nabla\times I=\frac{\partial\alpha}{\partial t},$$

$$\nabla\times\left(S\alpha+\frac{1}{2}M\right)=-\frac{\partial}{\partial t}(BI-P)-\sigma_0^{\text{int}}-\sigma^{\text{ext}}. \tag{15}$$

[1] V. E. Panin (Ed.), *Physical Mesomechanics and Computer-Aided Design of Materials* [in Russian], Nauka, Novosibirsk (1995) Vol. 1, 298 pp.
[2] V. E. Panin, in *Abstracts of the International Conference ''Mesofracture 96,''* Institute Strength Physics and Materials, Tomsk (1996) pp. 14–15.
[3] N. A. Koneva and E. V. Kozlov, Izv. Vyssh. Uchebn. Zaved. Fiz., No. 2, 89 (1990).
[4] V. E. Panin, S. V. Panin, and A.I. Mamaev, Dokl. Akad. Nauk SSSR **350**, 35 (1996).
[5] V. E. Panin, Izv. Vyssh. Uchebn. Zaved. Fiz., No. 11, 6 (1995).
[6] Yu. V. Grinyaev and V. E. Panin, Dokl. Akad. Nauk SSSR **353**, 37 (1997).
[7] A. D. Korotaev, A. N. Tyumentsev, V. Ch. Gonchikov, and A. I. Olemskoĭ, Izv. Vyssh. Uchebn. Zaved. Fiz., No. 3, 81 (1991).

Translated by M. E. Alferieff

Study of nanocrystalline nickel films deposited in a nitrogen atmosphere

V. S. Zhigalov, G. I. Frolov, V. G. Myagkov, S. M. Zharkov, and G. V. Bondarenko

L. V. Kirenskiĭ Institute of Physics, Siberian Branch of the Russian Academy of Sciences, 660036 Krasnoyarsk, Russia

(Submitted December 8, 1997)
Zh. Tekh. Fiz. **68**, 136–138 (September 1998)

It is shown that high-speed condensation methods can be used to prepare nickel nitride films in the nanocrystalline state. The phase composition of the condensate formed exhibits a strong dependence on the substrate temperature. © *1998 American Institute of Physics.* [S1063-7842(98)03109-2]

The study of the structural–energy state of nitrogen in solid solution and in nonstoichiometric metal nitrides Me–N of the ''interstitial phase'' type based on fcc metals (Me stands for Fe, Ni, etc.) continues to be an urgent metallophysical task in the development of high-nitrogen alloys. Such metal nitrides remain the subject of extended study as model objects on which information can be obtained about the correlation of crystal structure, electronic structure, and physical properties as a function of the nitrogen concentration. At the same time, limitations of the experimental data about the structure and properties of Me–Ni alloys force the authors of these models to turn to the works of the 1940s.[1,2]

In recent years in connection with the development of methods of preparing nanocrystalline materials,[3] the possibilities of creating large amounts of various alloys have broadened. First of all, this is a function of the fact that the chemical activity of these materials manifests a strong dependence on the size of the crystallites.[4]

The present paper examines the properties of films of nickel nitride and the processes accompanying their synthesis. To prepare these films, we used the method of pulsed plasma sputtering. Earlier we showed that with the help of this technique it is possible to prepare nanocrystalline films of $3d$ metals with unusual properties.[5–8] The starting vacuum was 10^{-6} Torr. Spectrally pure nitrogen, whose pressure was varied from 5×10^{-5} to 10^{-2} Torr, was then admitted to the sputtering chamber. The substrate temperature at the outset of sputtering was always 20 °C. The condensation rate of the Ni films in a pulse of 100 μs duration was 10^4-10^5 A/s. We used cover glasses of 0.2 mm thickness as the substrate. The thickness of the investigated films varied within the range 45.0–70.0 nm.

We studied the phase composition and magnetic properties (magnetization M_s) in the prepared samples as functions of the nitrogen partial pressure in the chamber. The results obtained are presented in Table I. We also determined the state of the substrate after the preparation process. The magnetization was measured at room temperature.

The films prepared at $P=10^{-6}$ Torr had a metallic lustre, an undeformed surface, and zero magnetization. At $P=10^{-4}$ Torr the samples also had a metallic lustre, but were strongly deformed, and $M_s=415$ Js. Starting from a pressure of 2×10^{-4} Torr, two pronounced regions were observed on the sample: in its center a light-colored region, with metallic luster but strongly deformed, and along its edges, a dark, undeformed region [Fig. 1a]. The light-colored region had a large magnetization while the dark region was practically nonmagnetic. The films prepared at $P=10^{-2}$ Torr were homogeneous and nonmagnetic. Samples with similar properties were prepared at 10^{-3} Torr, when sputtering is performed with interruptions.

To examine the structure of the films, we performed an electron-microscope analysis. Figure 1b displays electron diffraction patterns and photographs of the microstructure from different regions of film 3, prepared at 10^{-3} Torr. The central part of the film has fcc structure with lattice parameter $a=0.352$ nm, and size of the crystallites $0.2-0.4$ μm. Taking into account the large magnetization, it is possible to identify this region as a phase of pure Ni. The second part of the sample has hcp structure with lattice parameters $a=0.266$ mm and $c=0.429$ nm, and size of the crystallites <10.0 nm. The lattice parameters and zero magnetization suggest that this region is nickel nitride with the formula Ni_3N (Ref. 1).

Film 1 had a hcp phase with lattice parameters $a=0.264$ nm and $c=0.433$ nm. We identified it as a phase of pure Ni. The properties of these films are discussed in Ref. 8. In sample 2 we observed fcc structure with lattice parameters characteristic of pure Ni. Films 4 and 5 are nickel nitride with the formula Ni_3N.

As was noted above, in some of the samples the substrate was strongly deformed, which speaks of the presence of a high temperature at the time of formation of the conden-

TABLE I.

Sample No.	P_N, Torr	Phase composition	M_s, Js	State of substrate
1	10^{-6} (without nitrogen)	hcc (Ni)	0	Not deformed
2	10^{-4}	fcc (Ni)	415	Deformed
3	10^{-3}	fcc (Ni)	415	Partially deformed
		hcc (Ni_3N)	0	
4	10^{-3} *	hcc (Ni_3N)	0	Not deformed
5	10^{-2}	hcc (Ni_3N)	0	Not deformed

*The film was prepared with evaporation interruption every 15–20 s.

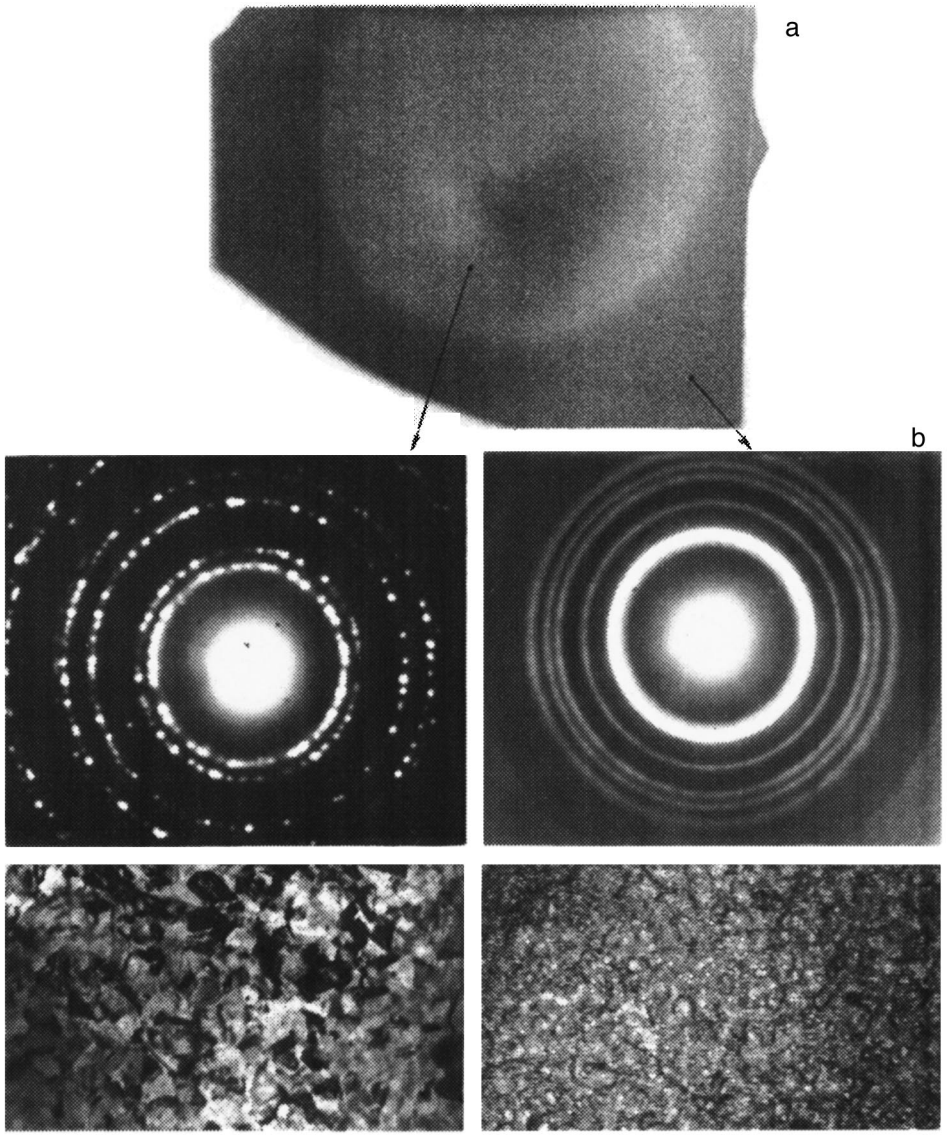

FIG. 1. Electron-microscopic analysis of a Ni–N_2 film prepared at a pressure of 10^{-3} Torr: a — photograph of the sample; b — electron diffraction patterns and microphotographs; left — of the central part, right — from the periphery of the sample.

sate. In order to pursue this question in more detail, we performed an analysis of the temperature dynamics in the substrates during the film deposition process. Toward this end, we sputtered Pd–Cu film thermocouples on the substrate. The results are plotted in Fig. 2. During the first few minutes, when deposition of the condensate takes place, the substrate temperature was raised to $T=470-570$ K. This is because the high flux density of the evaporated material carries with it a large amount of heat, which is then liberated to the substrate. After switching off the plasma the substrate temperature stays unchanged for some time and then begins to fall according to an exponential (films 1 and 4).

A different picture is observed for film 2: as the temperature is raised to $T\sim 470$ K, a jumplike increase in the temperature occurs. Due to the finite response time of the thermocouple it was not possible to measure it exactly. However, the strong deformation of the substrate indicates that $T>770$ K. We attribute this sudden increase in the temperature to the liberation of heat accompanying the decomposition of nickel nitride. As follows from Ref. 1, the phase transition Ni_3N–Ni_4N takes place at $T=460-470$ K. Due to

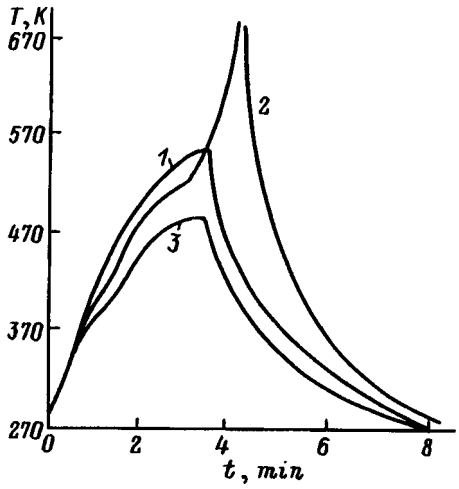

FIG. 2. Time scans of the temperature in nickel films deposited in a 10^{-6} Torr vacuum (*1*) and in a nitrogen atmosphere at a pressure of 10^{-4} (*2*), 10^{-2} (*3*).

the accompanying liberation of heat, an abrupt growth of the temperature takes place, and at $T=610-620\,\mathrm{K}$ the nickel nitride decomposes with liberation of the fcc phase of Ni.

Thus, in order to prepare nickel nitride (Ni_3N) films using the proposed technique, it is necessary to avoid raising the substrate temperature to temperatures $T>460\,\mathrm{K}$. In our case, this was achieved both by raising the nitrogen pressure in the vacuum chamber (film 5), which leads to a decrease in the condensation rate and a corresponding decrease in T, and by interrupting the sputtering process (film 4). In film 3, in which we simultaneously observed regions with different structure, the decomposition temperature was reached only in the center of the sample. Thus, on the periphery of the film the nickel nitride phase was preserved. The small size of the crystallites on the periphery ($<10.0\,\mathrm{nm}$) would seem to indicate that the nanocrystallinity of the films is one of the reasons for the formation of the nickel nitride phase.

[1] R. Bernier, Ann. Chim. (Paris) No. **66**, 104 (1951).
[2] N. Terao, J. Phys. Soc. Jpn. **15**, No. 2, 227 (1960).
[3] W. Siegel, Nanostruct. Mater. No. **3**, 1 (1993).
[4] M. L. Cohen and W. D. Knight, Phys. Today **43**, No. 12, 42 (1990).
[5] G. I. Frolov, O. A. Bayukov, V. S. Zhigalov *et al.*, JETP Lett. **61**, 63 (1995).
[6] V. G. Myagkov, L. I. Kveglis, and G. I. Frolov, Izv. Ross. Akad. Nauk **59**(2), 152 (1995).
[7] G. I. Frolov, V. S. Zhigalov, A. I. Pol'skiĭ *et al.*, Fiz. Tverd. Tela (St. Petersburg) **38**, 1208 (1996) [Phys. Solid State **38**, 668 (1996)].
[8] S. M. Zharkov, V. S. Zhigalov, and G. I. Frolov, Fiz. Met. Metalloved. **81**, 170 (1996).

Translated by Paul F. Schippnick

Temperature dependence of the current–voltage characteristic in a model of the conductivity of a metal–insulator–metal structure with a carbonaceous active medium

V. M. Mordvintsev and V. L. Levin

Institute of Micro-Electronics, Russian Academy of Sciences, 150007 Yaroslavl, Russia
(Submitted January 13, 1998)
Zh. Tekh. Fiz. **68**, 139–141 (September 1998)

A new mechanism is proposed for the processes taking place in metal–insulator–metal structures with a nanometer-sized insulating gap. The dependence of the theoretical current–voltage characteristic on the substrate temperature is analyzed and compared with experimental results.
 [S1063-7842(98)03209-7]

Basing ourselves on extensive experimental material[1] on electroformed diodes with metal–insulator–metal structure (MIM structures) and carbonaceous conducting paths exhibiting *N*-shaped static current–voltage characteristics, in Ref. 2 we proposed a new mechanism for the processes taking place in such objects. The essential elements of the proposed mechanism include, in particular, a nanometer-sized insulating gap structure and electron tunneling-limited current through the cathode potential barrier. On the basis of such a mechanism, in Refs. 3 and 4 we developed conductivity models of MIM structures with a carbonaceous active medium, in which a region with negative differential resistance appears due to the presence of inner feedback loops in the system and mechanisms of transparency modulation in the cathode barrier. We showed that these processes are accompanied by self-formation of a nanostructure in the carbonaceous medium, and that the electroforming can be considered as a process of self-organization of the insulating nanogap in the carbonaceous conducting medium[5] in the presence of a strong local electric field. The present paper analyzes the dependence of the theoretical current–voltage characteristic on the substrate temperature predicted by this model and compares the calculated results with the available experimental data.

As follows from the experimental data on electroformed MIM structures,[1] the current in them in the ''on'' (low-resistance) state with *N*-shaped current–voltage characteristic is to first order independent of the substrate temperature. This fact was one of the arguments in favor of the tunneling mechanism of conductivity posited in the model.[3,4] Other such arguments were the nanometer-sized width of the insulating gap formed in the carbonaceous conducting medium, measured with the help of a scanning tunneling microscope[2,6] and the corresponding high field strengths in the insulating gap for actually used voltages (from one to ten volts), which allows one here to speak of such a structure as a nano-MIM diode.[3]

The fact that in the mechanism[2] on which the respective models are based the temperature T of the formed insulator (FI) located in the insulating gap (and consisting of a composite material of the sort ''conducting particles in an insulating matrix,'' see Fig. 1) plays an important role (the reaction rate constant of disappearance of particles of the carbonaceous conducting phase depends on it exponentially) creates the impression that the model should give a strong dependence of the current density j in the structure on the substrate temperature T_0. However, in actual fact this is not the case.

Figure 1 plots the current–voltage characteristics of a MIM structure with a carbonaceous active medium calculated according to the model developed in Ref. 4, for two widely spaced temperatures T_0. In contrast to the model data,[4] the calculation was carried out for a parameter set giving characteristics close to those experimentally observed. In particular, this pertains to the position of the maximum of the current–voltage characteristic and the values of the current density which in a refined estimate should have an order-of-magnitude value of 10^6 A/cm^2 at the maximum. The latter allows us to adopt a value of the constant $C = 10^{-9}$ cm^3/deg·W which is more reasonable from physical considerations in the heat balance equation used in the model

$$T - T_0 = CE_{fd} j, \tag{1}$$

where E_{fd} is the field strength in the formed insulator.

Due to the poor thermal contact of the formed insulator with the surface of the substrate and the relatively high thermal conductivity of the latter, the assumption is made that all other elements of the MIM structure besides the formed insulator are at the temperature T_0. The values of the remaining model parameters are $\phi = 3.5$ eV and $\phi_a = 3.5$ eV (the heights of the potential barriers, whose meaning is clear from the inset to Fig. 1); $Q = 3$ eV, $f = 10^{13}$ s^{-1} (the activation energy and pre-exponential coefficient in the expression for the reaction rate constant of the disappearance of particles of the conducting carbonaceous phase); $\sigma = 10^{-22}$ cm^2 (the effective cross section of formation of the particles of the carbonaceous conducting phase of organic molecules upon electron impact); $\alpha = 0.6$, $\nu_k = 0.4$ [the maximum possible concentration (volume fraction) of the particles of the carbonaceous conducting phase and the percolation threshold in the formed insulator]; $b = 0.1$ nm (a constant characterizing the divergence of the electron flux); $l = 3$ nm (the thickness of the formed insulator perpendicular to the anode–cathode

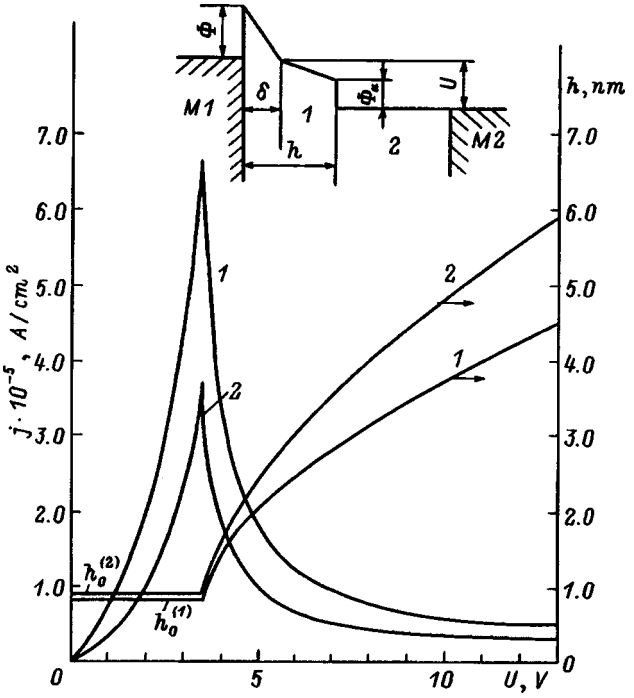

FIG. 1. Calculated curves of the dependence of the current density j and width h of the insulating gap on the voltage U on a MIM structure for substrate temperature T_0: *1* — 300, *2* — 800 K. Inset shows a simplified potential diagram of the MIM structure: M_1 — cathode, *1* — PD (photodetector), *2* — CCM, M_2 — anode.

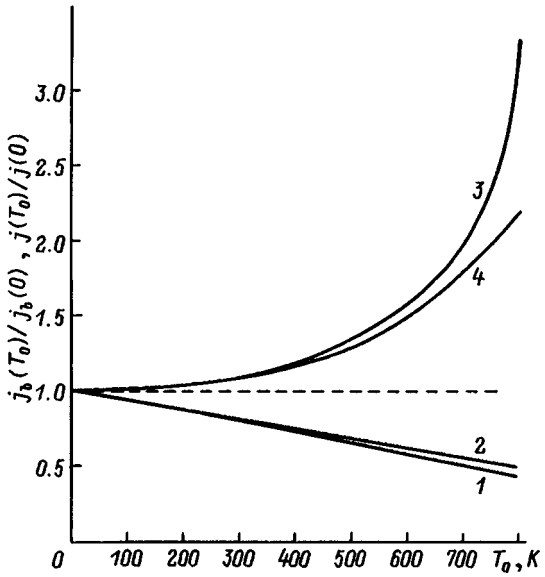

FIG. 2. Calculated curves of the dependence on the substrate temperature T_0 of the current-density ratios: *1* — $j(T_0)/j(0)$, calculated according to the model developed in Ref. 4 for $U=\phi$ without account of formula (2); *2* — like *1*, but with formula (2) taken into account, $\beta=8\times10^{-4}$ eV·K; *3* — $j_b(T_0)/j_b(0)$ in accordance with formula (2) calculating according to the model developed in Ref. 4, i.e., with variable δ; $U=\phi$, model parameters as in *2*; *4* — $j_b(T_0)/j_b(0)$ in accordance with formula (2), $\beta=8\times10^{-4}$ eV·K, $U=\phi$, $\delta=0.84$ nm.

direction); and, finally, $w=0.2$ [a constant determining the effective value of the parameter C in Eq. (1) for small thickness of the formed-insulator region].

In the analysis of the temperature dependence it is necessary to make a fundamental distinction between states of the structure corresponding to segments of the current–voltage characteristic before and after the maximum ($U=\phi$). Let us first consider the case $U>\phi$. Under these conditions the temperature T of the formed insulator reaches 1500 K while in the MIM structure feedback loops operate which lead, in particular, to mobility of the effective anode (see Fig. 1, inset), whose role is played by the carbonaceous conducting medium (CCM). The latter is a connected conducting cluster of particles of the carbonaceous conducting phase (their concentration falls exponentially with growth of the temperature T), formed when the percolation threshold is reached in part of the region initially occupied by the formed insulator. Therefore, the width of the insulating gap h is a variable and grows with increase of the voltage on the MIM structure (Fig. 1). The falling branch of the current–voltage characteristic corresponds to an increase in the width δ of the cathode potential barrier with growth of U.

The nature of the dependence of the current density j on the substrate temperature T_0 is clear from Eq. (1). Taking into account that E_{fd} and T vary weakly due to the fact that feedback loops are acting in the structure, equilibrating changes in T and j, and also that T stands inside the exponential in the expression for the concentration of particles of the carbonaceous conducting phase, one can expect an almost linear decrease of j with growth of T_0. As follows readily from Eq. (1), as T_0 varies from liquid-nitrogen temperature to room temperature (the range in which experimental data are available) noting that at $T\approx1500$ K the decrease in the current amounts to about 15%. Results of exact calculation for the maximum value of the current–voltage characteristic ($U=\phi$) and the above values of the model parameters are shown in Fig. 2 (curve *1*). They completely confirm the rough estimate obtained above.

Experimental data[7] for the voltages U on the electroformed MIM structure near the maximum of the current–voltage characteristic and higher did not reveal a temperature dependence upon comparison of the liquid-nitrogen and room-temperature curves. However, if we taken into account the low reproducibility of the current values in this voltage range even for constant T_0, which is usually characterized by a 10−15% spread, then we can hardly expect to observe the predicted model dependence in such a narrow temperature interval. A reliable answer can be obtained only by increasing the substrate temperature to temperatures significantly above room temperature, which would allow one to expect an approximately twofold decrease in the current upon varying T_0 from 100 to 800 K (Fig. 2).

One more factor that can have an affect on the function $j(T_0)$ is the well-known temperature dependence of the tunneling current density j_b in a potential barrier of constant width and height,[8] associated with smearing of the electron energy distribution in the cathode near the Fermi level of the metal, which was not taken into account in the model

$$\gamma=\frac{j_b(T_0)}{j_b(0)}=\frac{\pi CkT_0}{\sin(\pi CkT_0)}=\frac{\beta B\delta\phi^{-0.5}T_0}{\sin(\beta B\delta\phi^{-0.5}T_0)}. \qquad (2)$$

The last equality is valid for $U \geqslant \phi$, i.e., a triangularly shaped barrier. In this case $C = B\delta/(2\phi)^{0.5}$, where B is the constant inside the exponential in the expression for the tunneling current, k is the Boltzmann constant, and $\beta = 1.92 \cdot 10^{-4}$ eV·K. It was shown in Ref. 9 that the characteristic shape of the dependence of the quantity γ on the voltage U on the structure, which has its maximum at $U = \phi$, is well confirmed experimentally; however, the absolute values here significantly exceed the theoretical values, which comprise a maximum of tens of a percent. In order to take this experimental fact into account, in the calculations based on the model developed in Ref. 4 we formally assigned β the value $\beta = 8 \times 10^{-4}$ eV·K in expression (2). This gave a wide range of variation of values of γ (curve *3* in Fig. 2); however, even such an artificial enhancement of the dependence $\gamma(T_0)$, as can be seen, has almost no effect on the temperature dependence $j(T_0)$ (curve *2* in Fig. 2). This result is unique for the above-mentioned reasons, which being the cause of the smallness of the variations of E_{fd} and T, and is also connected with the variability of the quantities h and δ in the model.

In the case $U < \phi$ the carbonaceous conducting medium (CCM) fills the entire region of the formed insulator while inside the potential barrier the dissociation of carbon-containing molecules due to electron impact and, consequently, the formation of particles of the carbonaceous conducting phase are impossible. Therefore we have a potential barrier of constant width $\delta = h = h_0$, which is fixed at the value $U = \phi$ (Fig. 1). Such an object has the usual tunneling current–voltage characteristic (the growing branch in Fig. 1), whose temperature dependence is given by expression (2). Figure 2 plots the corresponding curve (curve *4*) for the constant value $\delta = 0.84$ nm obtained by lowering the voltage to $U = \phi$ at the constant temperature $T_0 = 300$ K, calculated for the same value $U = \phi$.

It is important to note that for small values of U the reproducibility of the current measurements in electroformed MIM structures is significantly higher than for $U \geqslant \phi$. This made it possible with high accuracy to obtain the experimental temperature dependence of the current[7] for $U = 1.5$ V, in very good agreement with formula (2), for a total increase in the current of 10% with growth of the temperature from 90 to 300 K. Such a result is an additional confirmation of the validity of the ideas contained in the model.[4]

We wish to express our gratitude to S. A. Krivelevich for a discussion that initiated the present work.

[1] H. Pagnia and N. Sotnik, Phys. Status Solidi A **108**(11), 11 (1988).
[2] V. M. Mordvintsev and V. L. Levin, Zh. Tekh. Fiz. **64**(12), 88 (1994) [Tech. Phys. **39**, 1249 (1994)].
[3] V. M. Mordvintsev and V. L. Levin, Zh. Tekh. Fiz. **66**(7), 83 (1996) [Tech. Phys. **41**, 679 (1996)].
[4] V. M. Mordvintsev and V. L. Levin, Zh. Tekh. Fiz. (in press).
[5] K. A. Valiev, V. L. Levin, and V. M. Mordvintsev, Zh. Tekh. Fiz. **67**(11), 39 (1997) [Tech. Phys. **42**, 1275 (1997)].
[6] H. Pagnia, N. Sotnik, and W. Wirth, Int. J. Electron. **69**(1), 25 (1990).
[7] J. G. Simmons and R. R. Verderber, Proc. R. Soc. London, Ser. A **301**, 77 (1967).
[8] A. Modinos, *Field-, Thermionic-, and Secondary-Electron Emission Spectroscopy* [in Russian], Nauka, Moscow (1990), 319 pp.
[9] J. G. Simmons, in *Handbook of Thin-Film Technology*, edited by L. I. Maissel and R. Glang (McGraw-Hill, New York, 1970), 764 pp.

Translated by Paul F. Schippnick